Chemistry Meets DNA Nanostructures

by

Anqin Xu

B. S. in Chemistry, Peking University, China, 2013

Submitted to the Graduate Faculty of the

Kenneth P. Dietrich School of Arts and Sciences in partial fulfillment

of the requirements for the degree of

Doctor of Philosophy

University of Pittsburgh

2019

UNIVERSITY OF PITTSBURGH

KENNETH P. DIETRICH SCHOOL OF ARTS AND SCIENCES

This dissertation was presented

by

Anqin Xu

It was defended on

October 7, 2019

and approved by

Raúl Hernández Sánchez, PhD, Assistant Professor, Department of Chemistry

Tara Meyer, PhD, Professor, Department of Chemistry

Lei Li, PhD, Associate Professor, Department of Chemical and Petroleum Engineering

Dissertation Director: Haitao Liu, PhD, Associate Professor, Department of Chemistry

Chemistry Meets DNA Nanostructures

Anqin Xu, PhD

University of Pittsburgh, 2019

Since N. C. Seeman proposed the first DNA tile structure, the concept of using DNA to construct mechanically robust nanostructure got remarkably developed in the past 40 years. Arbitrary 2D and 3D DNA nanostructures have been designed and synthesized, with size ranging from nanometer to micrometer scale. These DNA nanostructures, with the abundant varieties of modifications available, have demonstrated their applications in biosensing, drug delivery and nanofabrication.

In this dissertation, I have demonstrated several approaches to chemically modify DNA nanostructures that are motived by their potential applications. Chapter 2 focuses on the effect of chemical modification of DNA nanostructures on the nanoscale pattern transfer using HF etching of SiO_2. The unmodified DNA templates produced negative-tone patterns on SiO_2 substrate with *ca.* 27 nm in depth (high contrast) and *ca.* 22 nm in width (high resolution). Streptavidin molecules were able to locally promote the HF etching reaction, increasing the vertical contrast of the transferred pattern by 35%. Chapter 3 reports the investigation of the stability and reusability of DNA nanostructure templates after the HF etching negative-tone pattern transfer process. With the help of fluorescence microscopy and a polymerase chain reaction (PCR) system, it was confirmed that DNA nanostructures could be preserved after pattern transfer reaction and be potentially reused for future nanofabrication process. Chapter 4 presents the deposition of DNA nanostructures onto highly oriented pyrolytic graphite (HOPG) from an aqueous buffer solution. The factors that affected the deposition process were investigated and the DNA nanostructures

were used as templates for site-selective chemical vapor deposition (CVD) of SiO_2 on HOPG. Chapter 5 demonstrates the design and synthesis of a photochemical active DNA tetrahedron structure with sub-10 nm size through an easy, one-step annealing reaction. This photochemical active DNA tetrahedron can be potentially applied for selective and controlled molecule encapsulation and delivery using UV light activation. I hope this dissertation will provide more insight into the applications of DNA nanostructures and will serve as a stepping stone for the future development of DNA nanotechnology.

Table of Contents

List of Tables

List of Figures

Preface

First and foremost, I would like to take this opportunity to express my sincere gratitude to my research advisor Prof. Haitao Liu for all of his support and guidance during my entire Ph.D. career at University of Pittsburgh. He led me into the world of DNA nanotechnology, which I have been in love with for the past 6 years. He also taught me a lot of thinking and scientific skills and guided me to be a real scientist. His knowledge, attitude and passion about science inspired me deeply during my graduate study and always encouraged me to be a better scientist. Thanks for everything you have done for me.

I would like to thank Prof. Seth Horne and Prof. Alexander Deiters, for their time and support as my comprehensive exam committee members. I would also like to thank Prof. Tara Meyer, Prof. Raúl Hernández Sánchez and Prof. Lei Li, for their time and support as my Ph.D. defense committee members.

I am also grateful to all my collaborators Prof. Alexander Deiters, Prof. Minhee Yun, Prof. Feng Xiong, Prof. Lei Li, Dr. James Hemphill, Dr. Pei Liu, Dr. Andrew Kozbial, Mohammad Sharbati for their support on research projects and experiment instruments. I would like to specially thank Dr. Joel Gillespie and Dr. Esta Abelev for their time teaching and helping me on various characterization techniques during the past six years.

I also want to thank all of my former and current group members: Prof. Shichao Zhao, Dr. Cheng Tian, Dr. Zhiting Li, Dr. Feng Zhou, Dr. Karen B. Ricardo Figueroa, Dr. Hyojeong Kim, Dr. Muhammad Salim, Dr. Liwei Hui, Justin Hurst, Min A Kim, Christopher Kurpiel, Dong Wang, Nathan Tolman, Ruobing Bai and undergraduate researchers Ashley Pop, Tom Napp, for their help

and suggestion on my research projects. Without your scientific and mental support, I cannot achieve what I have right now. Thank you all and best wishes for your future career.

I would like to give special thanks to my advisor as an undergraduate researcher, Prof. Meiping Zhao at Peking University in China. Without her, I would not have so much love and passion for science to pursue graduate study. I would like to thank her for being an important mentor in my life.

Finally, the dissertation would not be possible without the support from my family. My parents, Yongze Xu and Ying Dai, have always supported me and encouraged me to pursue my dream. They deserve the most credits. I would also like to express my deepest appreciation to my dear husband, Peixin Zheng. He is always my strongest backing and driving force to never give up. His support is always the best gift in my life.

1.0 Introduction

1.1 Development of DNA Nanostructures

Deoxyribonucleic acid, or more generally known as its abbreviation 'DNA', was identified and isolated for the first time in late 1860s by Swiss physiological chemist Friedrich Miescher.[1] In 1953, about 90 years after discovery of DNA, the double helix structure of DNA was revealed by American biologist James Watson and English physicist Francis Crick.[2] However, DNA was only regarded as the genetic information carrier at that moment.[3] No one would have imagined that DNA can be such an important tool in material science in the 21st century. The story all started in 1982 when N. C. Seeman first proposed that DNA could be used to build covalently joined three-dimensional networks by combining individual structures using simple sticky end base pairing.[4] The concept of using DNA to construct mechanically robust nanostructure formed at that moment and got remarkably developed during the past 40 years.[3, 5-11]

The construction of DNA nanostructures is based on the principle that single strands of DNA can self-assemble into double helices by complementary base paring through a convenient thermal annealing process. Based on Watson-Crick base paring rule, adenine (A) always pairs with thymine (T) and guanine (G) always pairs with cytosine (C) via hydrogen bonding.[2] This intrinsic property of DNA makes it possible for researchers to predict the intermolecular interactions between different DNA single strands with different sequences. Through precise design of nucleotide sequences, DNA molecules can be controlled to associate with each other to construct complex structures. The following section provides an overview of the development of DNA nanostructures in the past four decades.

1.1.1 Self-assembled DNA tile structures

In 1982, with the idea of using DNA-based structures as the skeleton frame templates to arrange other molecules (*e.g.*, proteins) into well-ordered lattices for crystallography, N. C. Seeman reported the first self-assembled mechanically robust DNA tile structure.[4] Four single DNA strands were designed with complementary sticky ends so that they could be associated into a four-way branched junction – a Holliday junction (**Figure 1(a)**, left).[12-13] Multiple branched DNA junctions could be programmed with unique sticky ends and self-assembled into 2D arrays (**Figure 1(a)**, right).[12] To further increase the stability of DNA tiles and enable the construction of larger DNA nanostructures,[14-15] a mechanically robust double-crossover DNA tile was demonstrated in 1993 by introducing crossover strands that were partially complementary to each of the two parallel DNA double helices.[16] Since then, more complex DNA tiles were designed to self-assemble through hybridization into the desired structures, either a crystalline array or a larger closed object. A variety of framework-like DNA nanostructures[17] have been created using the tile structure as repeating unit,[13, 18-27] including nanoribbons (**Figure 1(b)**)[21] and triangular nanotubes (**Figure 1(c)**).[24]

The design of DNA tile structures soon expanded into three dimensions. These 3D structures were also based on the branched junctions between different DNA single strands. The branched junctions serve as the vertices while the hybridized strands serve as the edges of the structures.[8] The structures are floppy just as a cage made by ligated ropes.[11, 14, 28] Some examples of these DNA nanostructures include a cube (1991, **Figure 1(d)**),[29] a truncated octahedron (1994, **Figure 1(e)**),[30] a tetrahedron(2004),[31] an octahedron from one DNA single strand (2004)[32] and a tetrahedron from one DNA single strand (2009).[33] With the development of more rigid tile structures like 3-[34] and 5-point-star motifs,[35] different types of 3D DNA nanostructures with higher

complexity have been demonstrated, such as 3D DNA lattice (**Figure 1(f)**)[36] and polyhedrons (*e.g.*, icosahedron) (**Figure 1(g)**).[35]

Recent development in tile-based DNA nanostructures revealed the possibility of constructing complex shapes from single-stranded DNA tiles.[37-43] In the first design from Wei and co-workers in 2012,[37] each single-stranded tile consisted of a 42-nt DNA strand with four domains of 10-11 bases. Each domain was a complementary sticky end that could bind to one of the tile's four local neighbors through Watson-Crick base pairing self-assembly process. Each single-stranded tile acted as a 3 nm-by-7 nm pixel on the 310-pixel molecular canvas. To construct a DNA nanostructure with a desired shape on the 'canvas', a mixture of the single strands corresponding to the covered part of the shape (existing pixels) were mixed and processed through one-pot thermal annealing process. The single strands corresponding to the uncovered part of the shape (non-existing pixels) were excluded. The strategy managed to synthesize 107 distinct and complex 2D DNA nanostructures including numbers, letters and emojis (**Figure 1(h)**).[37] In addition, the idea has been extended and applied to the construction of 3D DNA nanostructures in which each building unit was a 'DNA brick' of 32 nucleotides.[39] Similar to 2D single-stranded DNA tile, each DNA brick was a LEGO-like model with four domains (two heads and two tails) of 8 nucleotides that were complementary to its four neighbors. The DNA brick acted as a 2.5 nm-by-2.5 nm-by-7 nm voxel on the 1000-voxel '3D molecular canvas'. The inclusion and exclusion of each voxel strand led to the formation of a DNA nanostructure of certain shape through single-step thermal annealing process (**Figure 1(i)**).[39] The single-stranded tile methods have demonstrated their capability to form multiple 2D and 3D DNA nanostructures, such as a teddy bear cavity structure, with a molecular weight of as large as 0.5-GDa.[41] These single-stranded tile methods opened a new chapter in DNA nanotechnology and provided an innovative approach for

the construction of almost arbitrary shaped DNA nanostructures with only short synthetic strands, which eliminates the size and sequence limitation from long viral DNA strand in the design of DNA origami nanostructures (**1.1.2**).

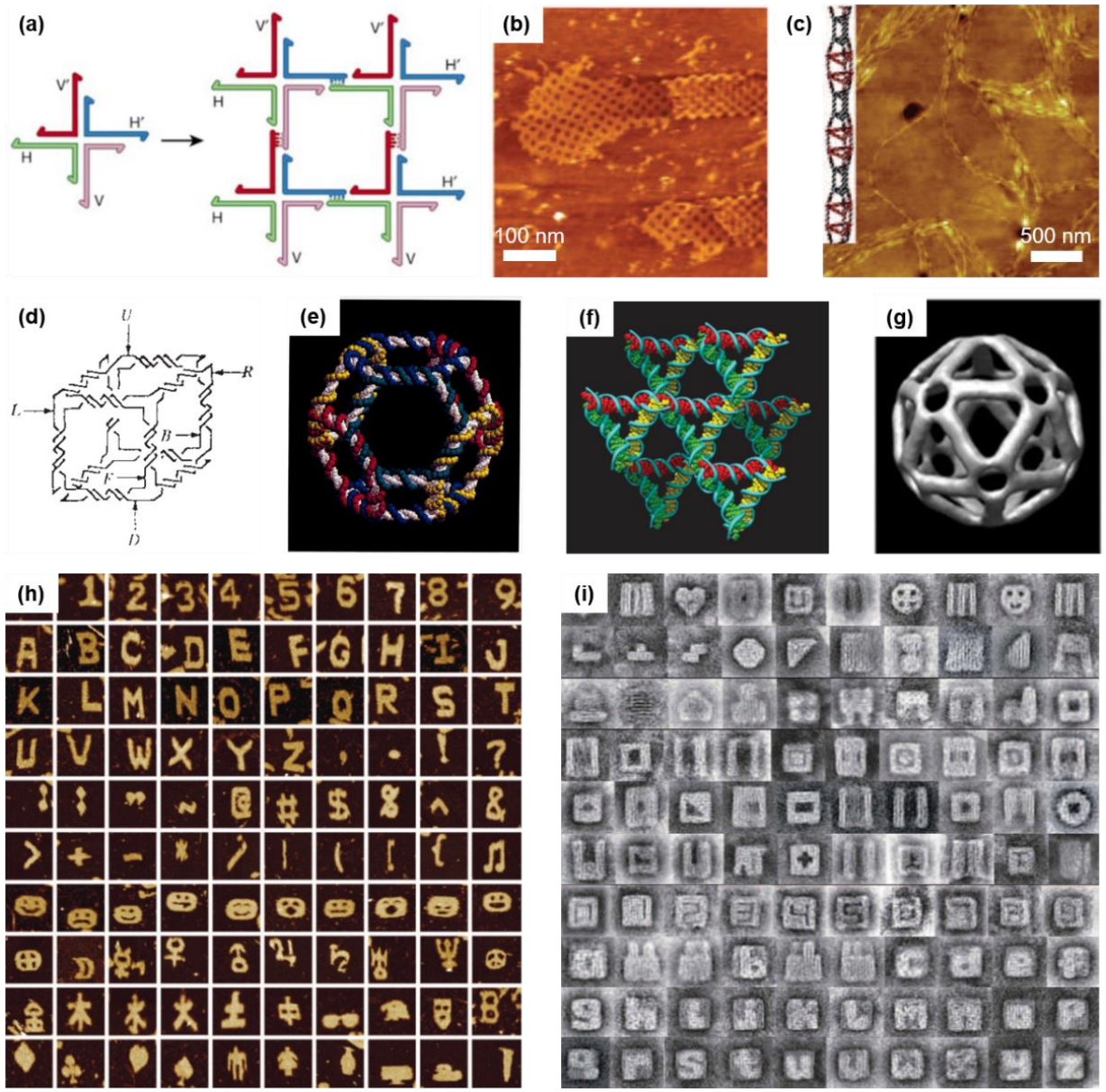

Figure 1. Examples of self-assembled DNA tile structures. (a) A branched DNA molecule with a Holliday junction and the self-assembly of four branched DNA molecules into a larger structure via complementary sticky ends. (b) AFM image of DNA nanoribbons. (c) AFM image of DNA triangular nanotubes. Inset shows the design of the structure with alternative large and small triangular sections. (d) A 3D DNA cube. (e) A DNA truncated octahedron. (f) 3D DNA lattice formed by tensegrity triangles. (g) A DNA icosahedra formed by sticky-ended five-point-star motifs. (h) AFM images of self-assembled DNA single stranded tiles. (i) TEM images of self-assembled 3D DNA bricks. Reprinted with permission from: (a) Reference 12, copyright © 2003, Springer Nature; (b) Reference 21, copyright © 2003, American Association for the Advancement

1.1.2 DNA origami nanostructures

The early-stage DNA nanostructures were often called ‘unscaffolded structures’ as compared to the recently developed DNA origami nanostructures in which a long scaffold DNA strand was used. In 2006, P. W. K. Rothemund first introduced the idea of ‘scaffolded DNA origami’ as a new method to assemble DNA nanostructures.[44] In the typical process, a viral genomic scaffold ss-DNA strand (*e.g.*, M13mp18, which is 7249 nucleotides in length) is selected and the corresponding short synthetic staple ss-DNA strands (10-50 nucleotides in length) are designed with the help from a computer software.[44-47] The staple strands are complementary to multiple regions of the scaffold so that they can direct the folding of the scaffold into desired shapes to achieve maximum hydrogen bonding through base pairing (**Figure 2(a)**).[3, 44] The resulting DNA nanostructures are roughly 100 nm in diameter and have a spatial resolution of as low as 2 nm, which is determined by the helix geometry of the natural B-DNA structure.[17, 47]

Scaffolded DNA origami nanostructures share some important advantages with the self-assembled DNA tile structures mentioned above. First, the formation of scaffolded DNA origami is achieved through a simple, single-step, one-pot thermal annealing process with few errors and relatively high yield. Second, the method doesn’t require accurate stoichiometry control and only little amount of defected by-products form in the system so the purification step is significantly simplified. Third, the idea provides a possibility to create almost all kinds of 2D or 3D shapes, leading to more varieties in the field of DNA nanotechnology.[3, 44] In the past 13 years, arbitrary 2D or 3D DNA origami nanostructures have been designed and synthesized, including a 2D smiley face (**Figure 2(b)**),[44] a 2D eleven-layer concentric square frame (**Figure 2(c)**),[48] a 3D nanoflask (**Figure 2(d)**),[48] a tetrahedron molecular container[49] and a 3D railed bridge.[50]

The traditional DNA origami nanostructures have limited sizes (usually within 100 nm scale) due to the preset length of the viral scaffold strand. Scientist have been making every effort to expand DNA origami nanostructure into micrometer scale for fulfillment of the realistic need of industrial nanopatterning applications. The most straightforward idea was to introduce a longer scaffold strand. A 26-kb single-stranded DNA fragment was prepared by long-range PCR amplification and used to construct a super-sized DNA origami nanostructure of 239.6 nm by 108.6 nm.[51] An alternative method to scale up DNA origami was to increase the size and molecular weight of staple strands. The traditional short synthetic staples could be replaced by DNA tiles[52] or even DNA origamis[53] to achieve a nanostructure in 300-nm range (**Figure 2(e)**). To simplify the design and synthesis process, another popular idea was to connect multiple DNA origami nanostructures together by extending staple strands with suitable complementary sticky ends. Endo and co-workers reported the first method to self-assemble DNA origami nanostructures (named 'jigsaw pieces') into 1D array through programmed sticky ends and shape matching.[54] Then similar strategies were developed to scale up origami nanostructures in 2D space (*e.g.*, a 3 × 3 assembly, **Figure 2(f)**).[55-56] Using DNA origami nanostructures as tiles, infinite 2D arrays have also been demonstrated via bottom-up fabrication through complementary base pairing (**Figure 2(g)**).[57] At the same time, Woo and co-workers published a different approach to arrange DNA origami nanostructures via blunt-end stacking interactions including binary codes and shape complementarity.[58] It was also reported that 2D DNA origami lattices could be self-assembled through stepwise precise control of surface diffusion by regulating the concentrations of cations (Mg^{2+} and Na^{+}) on the mica surface (**Figure 2(h)**).[59] Besides 2D nanostructures, 3D DNA polyhedras of 20-60 MDa have also been synthesized through hierarchical self-assembly of precisely designed stiff three-arm-junction DNA origami tripods (**Figure 2(i)**).[60] The successful

construction of larger DNA origami nanostructures provides solid foundation for their broader applications in material science.

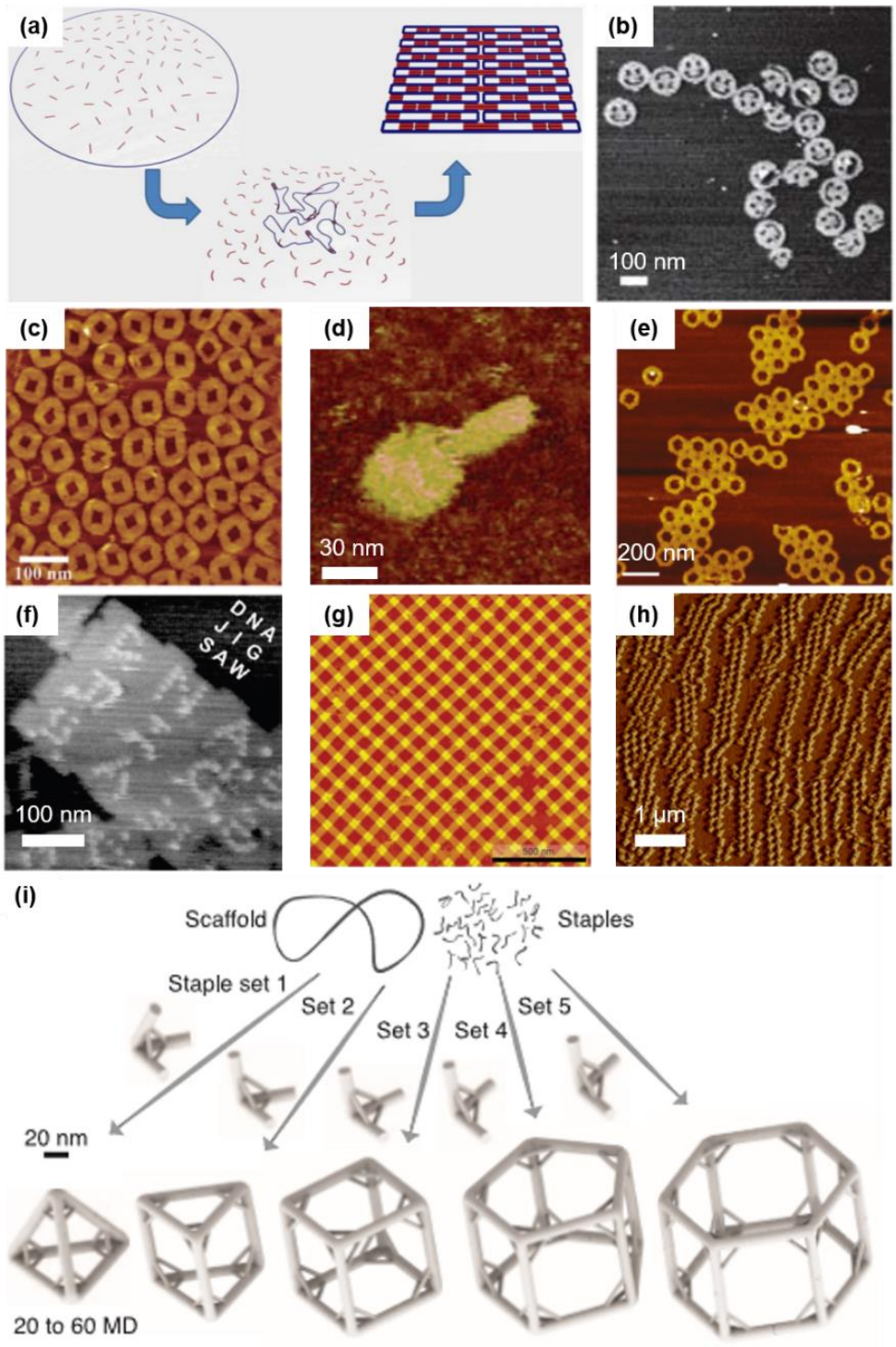

Figure 2. DNA origami nanostructures. (a) Scaffolded DNA origami formation of a two-dimensional rectangular structure. (b) AFM image of 2D DNA smiley faces. (c) AFM image of eleven-layer concentric DNA square frames. (d) AFM image of a 3D DNA nanoflask. (e) AFM image of 3 × 3 hexagonal staple tiles assembled into superstructures. (f) AFM image of 2D origami

array formed from ‘jigsaw’ pieces. (g) AFM image of an infinite 2D origami array. (h) Tapping amplitude AFM image of origami checkerboard lattices on a mica surface. (i) 3D DNA polyhedras self-assembled from stiff, tunable DNA tripods. Reprinted with permission from: (a) Reference 3, copyright © 2010, Elsevier, Ltd.; (b) Reference 44, copyright © 2006, Springer Nature; (c)(d) Reference 48, copyright © 2011, American Association for the Advancement of Science; (e) Reference 53, copyright © 2011, American Chemical Society; (f) Reference 55, copyright © 2011, American Chemical Society; (g) Reference 57, copyright © 2011, Wiley-VCH Verlag GmbH & Co. KGaA, Weinheim; (h) Reference 59, copyright © 2014, Springer Nature; (i) Reference 60, copyright © 2014, American Association for the Advancement of Science.

1.2 Modification and Functionalization of DNA Nanostructures

DNA nanostructures have shown the advantages of high programmability and complexity and have been demonstrated as arbitrary 1D, 2D or 3D shapes.[61] The structural rigidity and ease of synthesis have qualified DNA nanostructures as one of the most promising materials for biotechnology and material science.[62] However, the properties of DNA nanostructures are intrinsically inert and uniform and the functionality of DNA is limited.[63-64] The modification and functionalization of DNA nanostructures is essential and critical to alter their chemical, optical and electronic properties, either globally or locally, which leads to the broad applications in diverse fields of science.[64]

Multiple techniques have been developed for integration of different materials and molecules onto DNA nanostructures. The most popular method is to introduce modification into the oligonucleotides, which are used to synthesize DNA nanostructures at a later stage. Numerous standard modifications for oligonucleotides are commercially available, such as fluorophores and quenchers, chemical functional groups (*e.g.*, amino, thiol, azide, etc.), biotin and cholesterol.[65] These modifications can be attached to either 3' end, 5' end or internal position of an oligonucleotide strand to achieve the easy detection of signals, the attachment of other molecules including metal nanoparticles or proteins, and the alternation of surface properties. Due to the limited chemical reactions available on the oligonucleotide strands, a lot of molecules are attached to oligonucleotides through two-step reaction like click chemistry or other interactions, such as the attachment of gold nanoparticles via gold-thiol reaction,[66-67] the attachment of protein via alkyne-azide reaction[63] and the attachment of streptavidin via streptavidin-biotin interaction.[68] Because the sequence of each oligonucleotide strand in the design of a DNA nanostructure is unique, the position of modification in the structure can be precisely controlled. Even if a hydrocarbon chain

spacer is usually required between the nucleotide and the modification, the freedom of the positional control is only limited to several nanometers. Based on this principle, a series of DNA nanostructure modifications have been reported, mostly for protein modifications.[21, 69-73] Yan and co-workers reported the arrangement of streptavidin molecules into 2D arrays through the modification of biotin molecules onto DNA tiles (**Figure 3(a)**).[21] Chhabra and co-workers also reported a method to align two aptamers alternatively in the design of a 2D DNA array, which enables the generation of multiprotein nanoarrays (**Figure 3(b)**).[69] Mastroianni and co-workers successfully used a DNA pyramid to group gold nanoparticles in a chiral manner (**Figure 3(c)**).[73]

The direct modification of oligonucleotides that are used to build DNA nanostructures is straightforward and convenient. The construction of DNA nanostructures can be achieved using the same one-step thermal annealing method. However, it comes with the stringent requirement that the modified molecule must be compatible with the thermal process (*i.e.*, as high as 95 °C). Meanwhile, if the same modification needs to be applied at multiple positions on the DNA nanostructure, each modified oligonucleotide must be prepared separately, which means high cost and high complexity. The similar thing happens when the position of modification needs to be changed within the DNA nanostructure. The development of DNA origami nanostructures introduces a complete set of staple strands which can be used as a platform for the arrangement of different molecules. It is not uncommon the modification is required at multiple locations and at different locations so that the effects can be compared. With this background in mind, the modification of DNA origami nanostructures is often achieved through extension of one or many staple strands.[63] Then a functionalized oligonucleotide strand with complementary sequence can be added to hybridize with the extended part of the staple strand. This method gives the modified system higher capacity for variable modifications at multiple sites. The only drawback of the

method is the precision of modification is sacrificed because of the spatial freedom of the extended double helix. Following this approach, many modification and organization systems on DNA nanostructures are developed for different molecules such as quantum dots, metal nanoparticles, carbon nanotubes, proteins, enzymes, etc.[74-89] Some examples include arrangement of six gold nanoparticles on triangular DNA origami (**Figure 3(d)**),[75] attachment of two nanotubes perpendicular to each other on triangular DNA origami (**Figure 3(e)**),[77] enzyme cascade organized on rectangular DNA origami (**Figure 3(f)**)[78] and shaping of liposomes with lipid-modified DNA nanocages (**Figure 3(g)**).[89] With the help of complementary sticky ends and a DNA origami platform, Knudsen and co-workers also managed to route individual polymers into desired shapes (**Figure 3(h)**).[90]

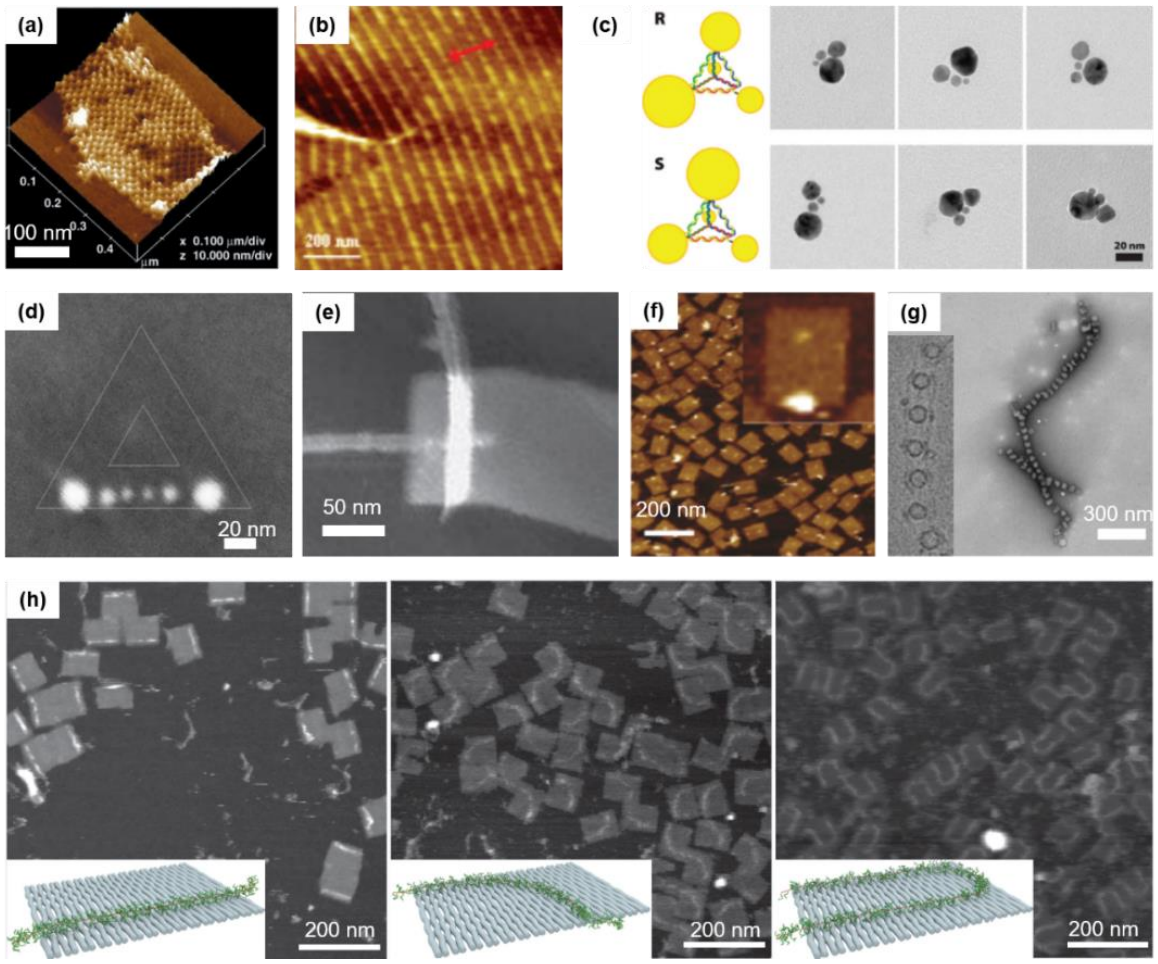

Figure 3. Modification and functionalization of DNA nanostructures. (a) AFM image of self-assembled streptavidin arrays via biotin modifications on 2D DNA arrays. (b) AFM image of periodic 2D multiprotein nanoarrays by aptamers attached on DNA tiles. (c) Diagram and TEM images of gold nanoparticles on chiral DNA pyramidal nanostructures. (d) SEM image of six-AuNP linear structures organized by triangular DNA origami. (e) AFM image of a cross-junction of two carbon nanotubes on rectangular DNA origami. (f) AFM image of DNA nanostructure-directed co-assembly of two enzymes. Inset shows the magnified AFM image of one DNA origami platform with two enzymes attached. (g) TEM image of DNA-nanocage-controlled formation of liposomes. Inset shows the magnified image. (h) AFM images of polymer immobilization on DNA origami. Different shapes of origami-polymer hybrids were used in three cases. Insets show the corresponding shape designs. Reprinted with permission from: (a) Reference 21, copyright © 2003, American Association for the Advancement of Science; (b) Reference 69, copyright © 2007, American Chemical Society; (c) Reference 73, copyright © 2009, American Chemical Society; (d)

Reference 75, copyright © 2010, American Chemical Society; (e) Reference 77, copyright © 2009, Springer Nature; (f) Reference 78, copyright © 2012, American Chemical Society; (g) Reference 89, copyright © 2017, Springer Nature; (h) Reference 90, copyright © 2015, Springer Nature.

A very special case of internal modification on oligonucleotide is the replacement of a nucleotide with a functional linker, such as 2-aminopurine (fluorescent analog of dG and dA)[91] or deoxyUridine (analog of dT, subject to enzyme removal).[92] One specific functional linker of interest is the photo-cleavable linker (moiety).[93] Insertion and photo-activation of the linker can lead to photo-regulation of oligonucleotide function and thus the structural or functional change of DNA nanostructure. Upon irradiation, the chemical bonds in the photo-cleavable linker can be cleaved, leading to the cleavage of the DNA strand at the position of the photo-cleavable linker. Several approaches have been designed to control the deactivation and activation of the system using the photo-cleavable linkers (**Figure 4(a)**).[94] In the first approach, the functional oligonucleotide is cleaved and thereby deactivated upon irradiation. This is the most straightforward approach to achieve the photochemical control of the function of oligonucleotides.[95] In the second approach, instead of inserting photo-cleavable linkers inside the functional strand, researchers link the functional strand with a partially complementary inhibitor strand containing a photo-cleavable linker.[93, 96-97] Before exposure to light, the duplex between functional strand and inhibitor strand is stable so the system stays inactive. After irradiation and cleavage of the photo-cleavable linker, the functional strand is released and becomes active. A third approach is designed to simplify the second approach in which two ends of a linear oligonucleotide are linked by a photocleavable moiety to create a circular oligonucleotide.[98-99] The circular oligonucleotide remains inactive before irradiation due to their structural inflexibility. Upon irradiation, the photocleavable linker gets cleaved and the functional strand becomes linear, enabling duplex formation with target strand.[98-99] The structural regulation of DNA nanostructure via light has been reported in several cases. Kohman and co-worker reported a novel strategy to trigger large-scale structural reconfiguration within a spherical DNA origami nanostructure via the

cleavage of inserted photo-labile spacers located within the crossover of the staple strands (**Figure 4(b)**).[100] The spacers were cleaved with light irradiation and the origami spheres were transformed to two tethered hemispheres, which can be potentially used for molecule release and delivery. Tohgasaki and co-workers reported a similar photoactive DNA pyramid nanocapsule and successfully demonstrated its biocompatible activation in cells (**Figure 4(c)**).[101] Others have also reported the release of proteins and other cargos upon light irradiation of their photocleavable linker attachment to DNA nanostructure hosts.[102-103] However, the photocleavable linkers were inserted as an extension to the oligonucleotide strands so the configuration of DNA nanostructures remained unchanged after UV activation. Using the principle that azobenzene can be switched reversibly between the *trans*- and *cis*- isomers by UV lights at different wavelengths,[104] some groups have developed other methods to manipulate the shape and configuration of DNA nanostructures with light. Yang and co-workers managed to assemble multiple hexagonal DNA origamis into various 2D oligomeric nanostructures under visible light and dissemble the system under UV light.[105] Kuzyk and co-workers achieved the configuration switching of two DNA origami nanostructures by incorporation of azobenzene in the linkage and irradiation by light (**Figure 4(d)**).[106] An interesting photo-controlled nanomachine was published in 2015 based on the photoactivated reaction between pyrene modifications and disulfide modifications, which led to the light-driven walking behaviors of DNA strand on DNA tile platform (**Figure 4(e)**).[107] Light has been widely used by chemists as an experimental element to provide energy and regulate reactions. With all the methods provided to regulate modified DNA nanostructures with light, we can expect DNA nanostructures to be more widely used in biomedical applications.

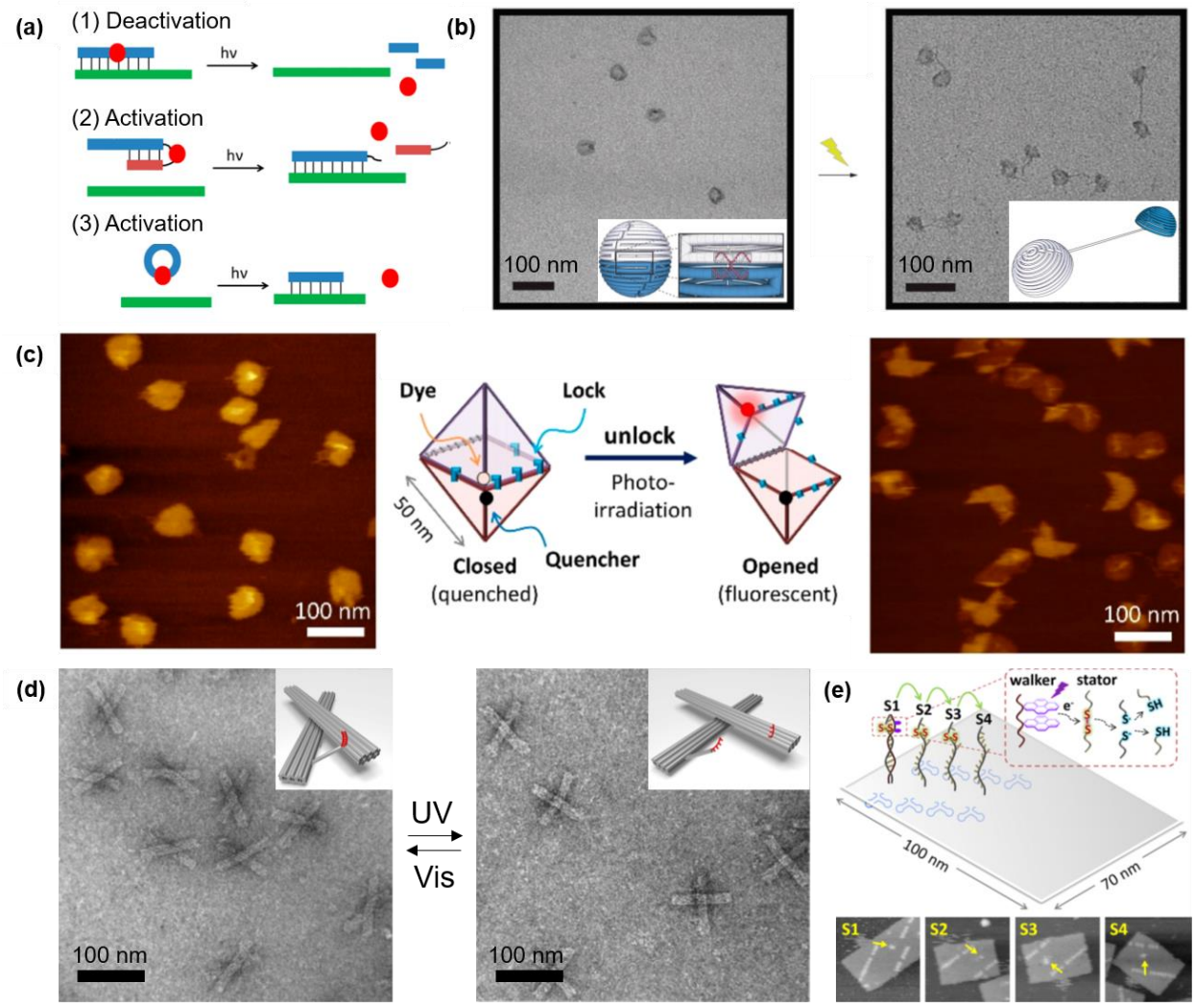

Figure 4. Photochemical control of DNA nanostructures. (a) Different approaches to regulate photocleavable linker modified oligonucleotide hybridization with light. (b) TEM images of the closed and open spherical DNA nanostructures before and after light irradiation. Insets show the corresponding diagrams. (c) Diagram and AFM images of photocaged DNA nanocapsule at closed and open forms. (d) TEM images of light-induced conformation changes of DNA origami nanostructures. Inset show the corresponding diagrams of locked and relaxed states. (e) Schematic illustration and AFM images of the light-driven walking system on DNA origami platform. Reprinted with permission from: (a) Reference 94, copyright © 2014, American Chemical Society; (b) Reference 100, copyright © 2015, Royal Society of Chemistry; (c) Reference 101, copyright © 2019, American Chemical Society; (d) Reference 106, copyright © 2016, Springer Nature; (e) Reference 107, copyright © 2015, American Chemical Society.

1.3 Stability of DNA Nanostructures

Although the past 40 years has witnessed significant development of DNA nanotechnology, one major concern of DNA nanostructures for bioengineering and material science applications is their low thermal and chemical stability, especially under harsh conditions. There are two contexts when discussing the stability of DNA nanostructures. One is the stability of hydrogen bonding of DNA double helices, which correlates to denaturation of DNA. The other is the stability of covalent chemical bonds in the single-stranded DNA chain, which correlates to degradation of DNA. The following sections provide a short review of stability of DNA nanostructures under various conditions.

1.3.1 Thermal stability of DNA nanostructures

The average length of a staple strand in a DNA origami design is 30 nucleotides. The length of DNA strand used for construction of unscaffolded DNA nanostructures varies from case to case. The average melting temperature of 30-bp ds-DNA is 65 °C,[108] which also depends on the sequences of the strands and the chemical environment. The addition of Mg^{2+} in the buffer solution for synthesis of DNA nanostructures can stabilize the hydrogen bonding and increase the melting temperature.[109] The standard synthesis procedure of a DNA nanostructure usually has a denaturation temperature of 95 °C, at which all the DNA double strands are expected to de-hybridize and the entire DNA nanostructure is dissociated. When DNA nanostructures are used for fabrication purpose, where high temperature is usually required, DNA nanostructures are often deposited on a substrate such as mica or silicon wafer (SiO_2/Si). It has been reported that the deposition of DNA nanostructures on a dry substrate provided additional electrostatic support and

helped DNA nanostructures maintain their overall shapes at a much higher temperature on both SiO_2/Si substrate (**Figure 5**)[110] and mica substrate.[111] The overall shapes of DNA nanostructures could be maintained at up to 200 °C in air.[110-111] Then the thickness of DNA nanostructures started to decrease beyond that temperature, indicating the leftover triangular patterns on the substrate could be the inorganic residues from decomposition of DNA nanostructures,[112] which is consistent with the previous reported results characterized by thermogravimetric analysis (TGA).[113-114] It is generally safe to expect DNA nanostructures to be intact at temperatures lower than 150 °C. Removal of DNA nanostructures from substrates can usually be achieved by heating the samples to high temperature (*e.g.*, 400 °C), followed by rinsing the surfaces with water.[112]

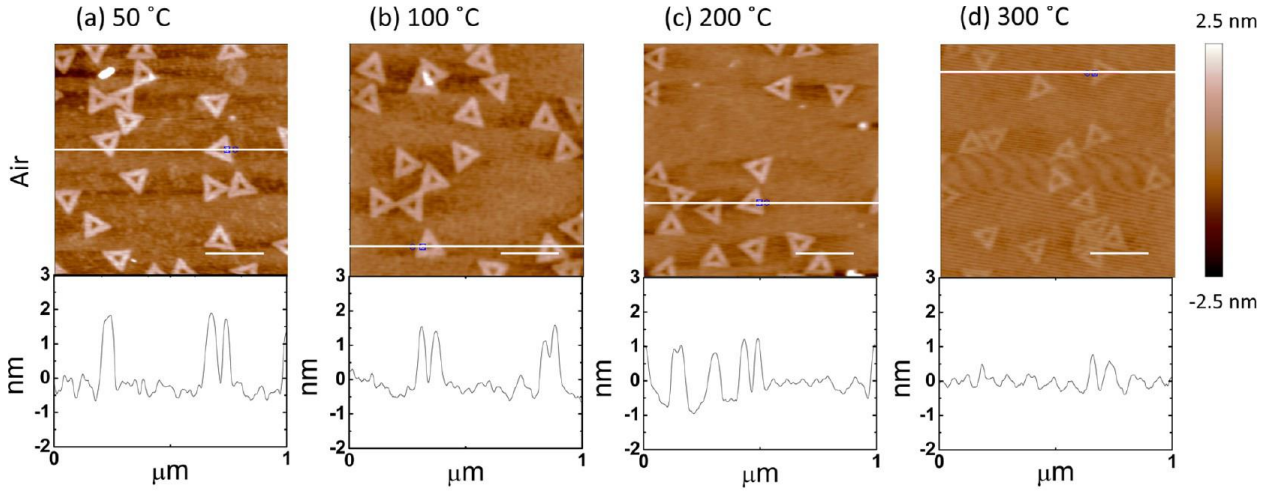

Figure 5. Thermal stability of DNA nanostructures on SiO_2/Si substrate in air. AFM images of triangular DNA origami nanostructures heated at (a) 50 °C, (b) 100 °C, (c) 200 °C, and (d) 300 °C for 10 min. White horizontal lines on the AFM images indicate where the cross sections were determined. Scale bars denote 250 nm. Reprinted with permission from Reference 110, copyright © 2014, American Chemical Society.

1.3.2 Chemical stability of DNA nanostructures

The synthesis of DNA nanostructures usually happens in a buffer solution with a pH of 8 and high concentration of Mg^{2+}. The addition of Mg^{2+} can shield the negative charges of nucleotide backbones and stabilize the hydrogen bonding[109] and thus allow the DNA double helices to form, which leads to the self-assembly of DNA nanostructures. As organic materials, dried DNA nanostructures could also be devastated after 15 min of UV/O_3 treatment,[110] which is also commonly used as a method to remove DNA templates after nanofabrication process. In this section, we will focus on the stability of DNA nanostructures in various pH and Mg^{2+} environments.

The hydrolysis of DNA can occur in either acidic or basic environments, usually under extreme pH. DNA hydrolysis can happen at three locations, phosphodiester backbone, DNA bases and glycosidic bonds connecting the nucleotides to the DNA backbone.[110, 115] It was discovered that all three types of hydrolysis have the minimum reaction rates around neutral pH.[110] For acidic pH range, depurination (hydrolysis of glycosidic bonds only) happens more easily than hydrolysis of phosphodiester backbone.[116] The depurination rate constant relies highly on the sequence of the DNA strand because the hydrolysis is much more facile at purines than at pyrimidines.[117] When deposited on SiO_2/Si substrate, the shapes of triangular DNA origami nanostructures started to change after 10 s immersion when the pH reached 4 in the acidic range or 12 in the basic range (**Figure 6(a)**).[110]

High magnesium ion (Mg^{2+}) concentration of 10-20 mM is considered a critical requirement for synthesis of DNA nanostructures. However, this high concentration is often incompatible with biomedical applications of DNA nanostructures.[118-119] It has also been reported that Na^+ and other monovalent cations could help increase the melting temperature of ds-DNA and stabilize the double helix structure.[120] Using DNA origami nanostructures as an example, replacing

Mg^{2+}-containing buffer with pure water through filtering/washing cycles didn't significantly affect the overall stability of DNA nanostructures.[118] However, defective DNA origami nanostructures were observed at such low concentration of Mg^{2+} (less than 1 μM) (**Figure 6(b)**). Rinsing the as-deposited SiO_2/Si substrate with water suggested the similar result. Much lower surface density of DNA origami nanostructures was also observed, resulting from the weaker electrostatic forces between DNA nanostructures and SiO_2 substrate due to the removal of Mg^{2+} from the surface (**Figure 6(c)**).[110] After immersed in NaCl solution for 10 s, it was observed that triangular DNA origami nanostructures deposited on SiO_2/Si substrate partially disintegrated (**Figure 6(d)**).[110] This was mainly due to the low ionic strength of the solution. Meanwhile, the DNA origami nanostructures showed an increased height and less shape damage in 0.2 M NaCl solution, which is consistent with the previous report that Na^+ could replace Mg^{2+} in the minor groves of DNA double helices.[120] Removal of Mg^{2+} from TAE (Tris-acetic acid-EDTA) buffer resulted in severe damage of DNA origami nanostructures while mixture solution of Na_2HPO_4 buffer and NaCl provided enough support to stabilize DNA nanostructures (**Figure 6(e)**).[119] In summary, it is critical to provide enough concentration of Mg^{2+} in the application system for DNA nanostructures. Otherwise a much higher ionic strength should be provided with Na^+ or other cations. Some other methods have been developed to stabilize DNA nanostructures in low-Mg environment, such as oligolysine coating of DNA nanostructures.[121]

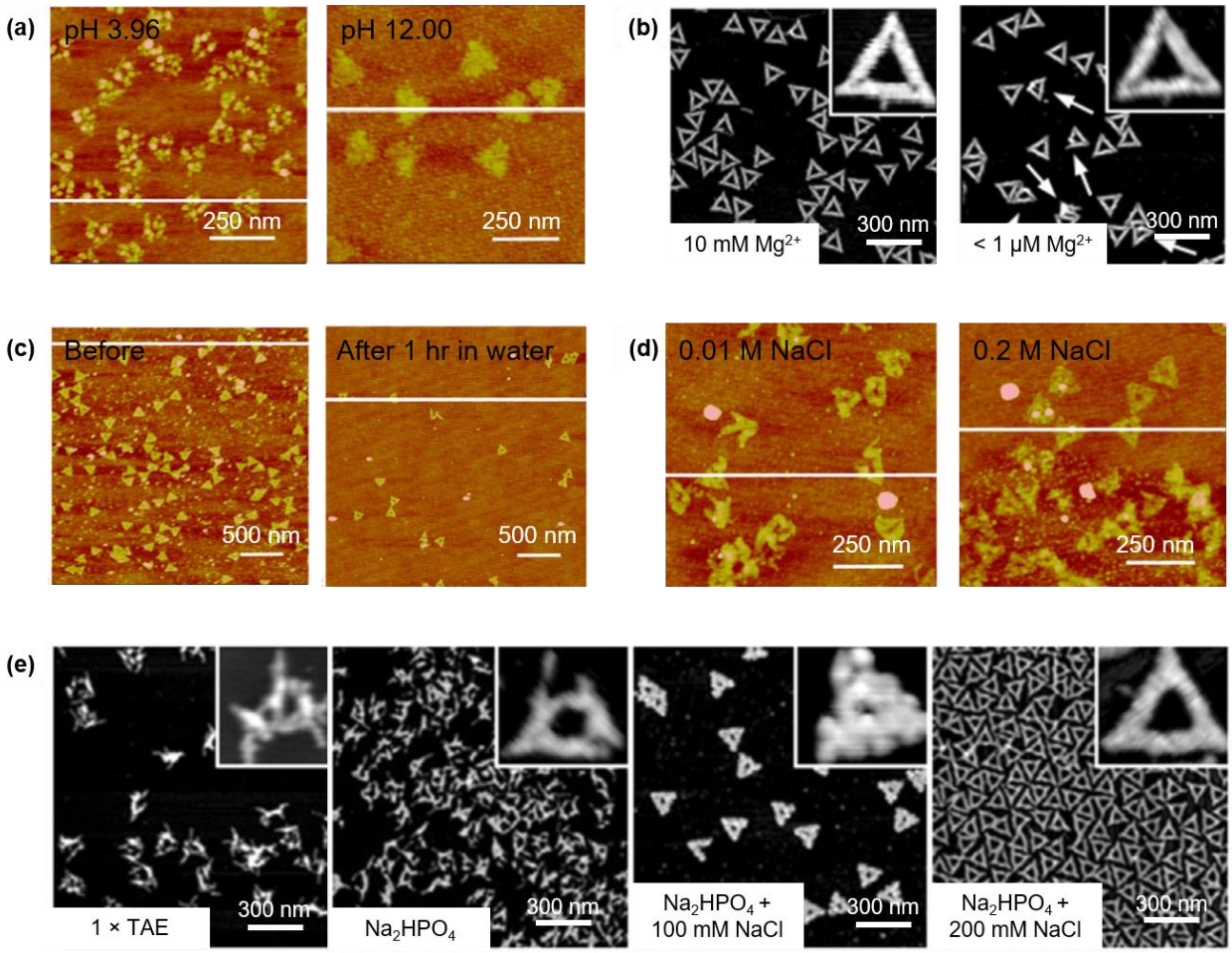

Figure 6. Stability of triangular DNA origami nanostructures in various chemical environments. (a) AFM images of as-deposited DNA nanostructures after 10 s immersion in pH 3.96 and pH 12.00 solution on SiO_2/Si substrate. (b) AFM images of DNA nanostructures in 1 × TAE buffer containing 10 mM $MgCl_2$ and after applying three filtering/washing cycles with pure water (Mg^{2+} concentration < 1 μM). (c) AFM images of as-deposited DNA nanostructures before and after 1 hr immersion in pure water on SiO_2/Si substrate. (d) AFM images of as-deposited DNA nanostructures after 10 s immersion in 0.01 M and 0.2 M NaCl solution on SiO_2/Si substrate. (e) AFM images of DNA nanostructures in different solutions. Reprinted with permission from: (a)(c)(d) Reference 110, copyright © 2014, American Chemical Society; (b)(e) Reference 118, copyright © 2018, Wiley-VCH Verlag GmbH & Co. KGaA, Weinheim.

1.3.3 Hydrofluoric acid (HF)-induced DNA damage

Hydrofluoric acid (HF) is not a strong acid, but it is a highly corrosive acid, which can be used to manufacture semiconductors and many other materials.[122-124] It is also an important chemical for silicon dioxide (SiO_2) nanofabrication using DNA nanostructures as templates. Hydrofluoric acid, when fully hydrolyzed, will generate hydrogen ion (H^+) and fluoride ion (F^-). The effect of H^+ to the DNA origami nanostructures was discussed previously in **1.3.2**. The acidity (p*K*a) of HF is 3.189 (25 °C, zero ionic strength).[125] To reach pH 4, the acidic pH for deformation of DNA nanostructures, approximately 0.12 mM HF is needed, which is a relatively low concentration. F^- is considered more hazardous to human beings, especially in the form of HF. HF can cause severe damage to most organic tissues because of the chelation reaction between F^- and calcium ion (Ca^{2+}) and magnesium ion (Mg^{2+}),[126-128] making HF a more dangerous acid than most other acids. Even if there were many reports of burns by HF and the treatment in animals, there were few reports of how HF interacts with cells or molecules down to the μm or nm level.

Seo and co-workers first investigated the toxicity of HF at the cellular level by comet assay.[122] Comet assay, also known as single cell gel electrophoresis (SCGE), is an uncomplicated and sensitive technique for the detection of DNA damage at the level of the individual eukaryotic cell.[129] In comet assay method, a single cell was exposed to damaging factor and then a gel electrophoresis was performed. An image was obtained to measure the olive tail moment (OTM) which is the product of tail length and DNA percentage in the tail.[130-131] A healthy and undamaged cell shows a sphere shape with an OTM value of 0. However, with more DNA damage induced, the OTM value increases. Seo and co-workers found that HF caused DNA damage in a concentration-dependent manner. HF at 90 μg/mL (4.5 mM) induced DNA damage five times more than in the PBS control in 5 min in ice (**Figure 7(a)**).[122] It was also reported that the DNA

damage by HF might be due to the generation of reactive oxygen species (ROS),[122] which means that the damage was not related to the backbone structures of DNA but only affected the bases of nucleotides.

Catania and co-workers also investigated the hydrolysis of DNA induced by HF.[132] Their work focused on the damage of phosphodiester bonds as well as the bonds between the sugar rings and bases. It was reported that DNA could be completely hydrolyzed by 48% liquid HF at 50 ℃ with Thymine (Thy), Guanine (Gua), Adenine (Ade), Cytosine (Cyt), partial deoxycytidine (dC) and minor amount of 5-Methylcytosine (5-MeCyt) left detected by high-performance liquid chromatography (HPLC) (**Figure 7(b)**). The backbone structures of DNA were completely broken up under the conditions.

To the best of my knowledge, there is no detailed report investigating the HF-induced damage to DNA nanostructures in a nanofabrication process. Also, it is unclear whether DNA damage happens when low concentration of HF presents under milder conditions or in gas phase.

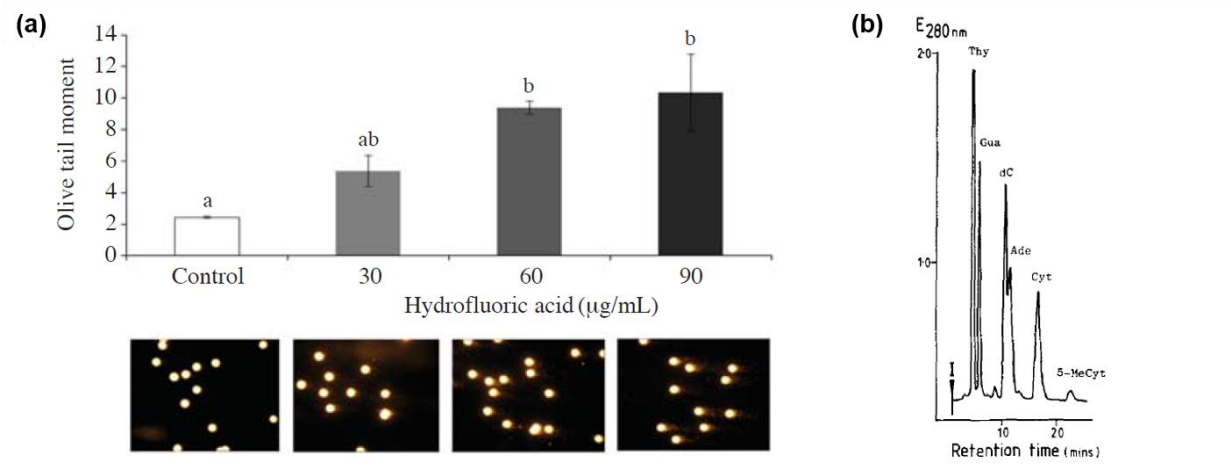

Figure 7. (a) Concentration dependent HF-induced DNA damage measured by comet assay with olive tail moment. (b) HPLC elution profile of DNA hydrolyzed using 48% HF (50 ℃, 4 hr). Reprinted with permission from: (a) Reference 122, copyright © 2013, Korean Society of Environmental Risk Assessment and Health Science and Springer Science Business Media Dordrecht; (b) Reference 132, copyright © 1987, Elsevier, Inc.

1.4 Applications of DNA Nanostructures

Over the past 40 years, DNA nanotechnology has attracted extensive attentions from many research communities.[133] The development of DNA nanotechnology has provided arbitrary 1D, 2D or 3D DNA nanostructures with a size range from nanometer to micrometer. These DNA nanostructures, with the abundant varieties of modifications available, can be synthesized precisely with 'bottom-up' self-assembly approaches and exhibit the functions that are not found for DNA in nature.[7] The remarkable structural properties and biocompatibility of DNA nanostructures have qualified them as important materials for the applications of biosensing, drug delivery and nanofabrication.[134] Recent progress in DNA synthesis technology has lowered the cost of DNA to $200 per gram,[135] making DNA nanostructures one of the best candidates for large-scale applications.

1.4.1 DNA nanostructures as biosensors

DNA nanostructures, which are in nature biomolecules, demonstrated their first and most intuitive applications in biological applications including diagnostics and therapeutics.[136] There is a critical need to develop biosensors for ultra-sensitive and simple detection of target analytes including protein, peptide, DNA and RNA.[137] DNA-based biosensors have provided internal sequence pairing for detection of DNA or RNA targets and external modifications for detection of other biomolecules, making them one of the best tools for early stage and ultra-sensitive diagnose of various diseases. DNA nanostructures inherit the advantages from oligonucleotides as biosensors and offer the possibility to create integrated flatforms for multi-channel detection at the same time. DNA nanostructures also provide innovative amplification methods and output signal

types,[137] indicating broader applications in biosensing field. In the past 20 years, DNA nanostructure-based biosensors have been applied for the detection of various biomolecules with optical, electrochemical or topographical signals.

Most of the DNA nanostructure-based biosensors are based on specific molecular interactions. As a demonstration for nucleic acid detection, Ke and co-workers reported the first read-out sensor in 2008, in which they used rectangular DNA origami nanostructures to construct nucleic acid probe tiles for label-free microRNA hybridization.[138] By extending the staple strands in the DNA nanostructure, they were able to create a set of 20 nucleotide long single stranded probes on the surface of DNA nanostructure. When RNA targets, which were complementary to DNA probes, hybridized to the probes and captured onto the origami surface, a topography change could be easily detected by atomic force microscopy (AFM) (**Figure 8(a)**). Another DNA nanostructure based electrochemical biosensor for the detection of microRNA has also been developed recently.[139] Similar methods have also been applied to detect DNA[140] and single-nucleotide polymorphism (SNP) genotyping.[141-142] Instead of topographical signals, conformational change has also been utilized in DNA sequence detection.[143-144]

DNA nanostructures have also been widely used for the detection of proteins. The types of proteins that can be detected are limited due to the interaction types between proteins and DNA. Proteins must be able to interact directly with DNA (aptamers) or with common modifiers on DNA (biotins, fluoresceins, etc.).[134] Using 'DNA origami pliers' or 'DNA origami forceps', which consisted of two levers of ~ 170 nm long connected at a fulcrum, and different ligand modifications, various single-molecule organic targets (*e.g.*, streptavidin and Immunoglobulin G) (**Figure 8(b)**),[143] inorganic targets (*e.g.*, metal ions),[143] and environmental signals (*e.g.*, pH)[145] could be visualized by AFM and quantified by fluorescence measurement due to the conformational change

of the DNA origami nanostructures.[143] Other protein detection systems have been developed based on the interaction between aptamer and platelet-derived growth factor (PDGF) monitored in real time by optical tweezers,[146] the interaction between aptamer and the malaria biomarker *Plasmodium falciparum* lactate dehydrogenase (P*f*LDH) or Thrombin visualized by topography change,[81, 147] the interaction between prostate-specific antigen (PSA) and detection antibody characterized by a rolling circle amplification (RCA) system and absorbance spectrophotometry,[148] and the interaction between biotin and streptavidin characterized by conformational change.[144] DNA origami nanostructures have also provided platforms to study enzyme cascade. Glucose oxidase (GOx) and horseradish peroxidase (HRP) were attached onto DNA origami platform and the best distance for the highest efficiency was determined.[78, 149]

Unscaffolded DNA nanostructures have also been widely used as platforms for biosensors. DNA tetrahedron nanostructure, as one of the simplest 3D DNA nanostructures, is the most popular DNA material for biosensing. DNA tetrahedron nanostructure is a rigid and robust structure suitable for precise alignment of linear or stem-loop probes on a solid-phase surface.[137] Electrochemical biosensors have been developed for the detection of DNA,[150] microRNA,[151] proteins (*e.g.*, thrombin),[150, 152] cocaine (**Figure 8(c)**)[153], ions (*e.g.*, protons and Hg^{2+})[154] and adenosine triphosphate (ATP)[154] by attaching DNA tetrahedron nanostructures on gold substrates.

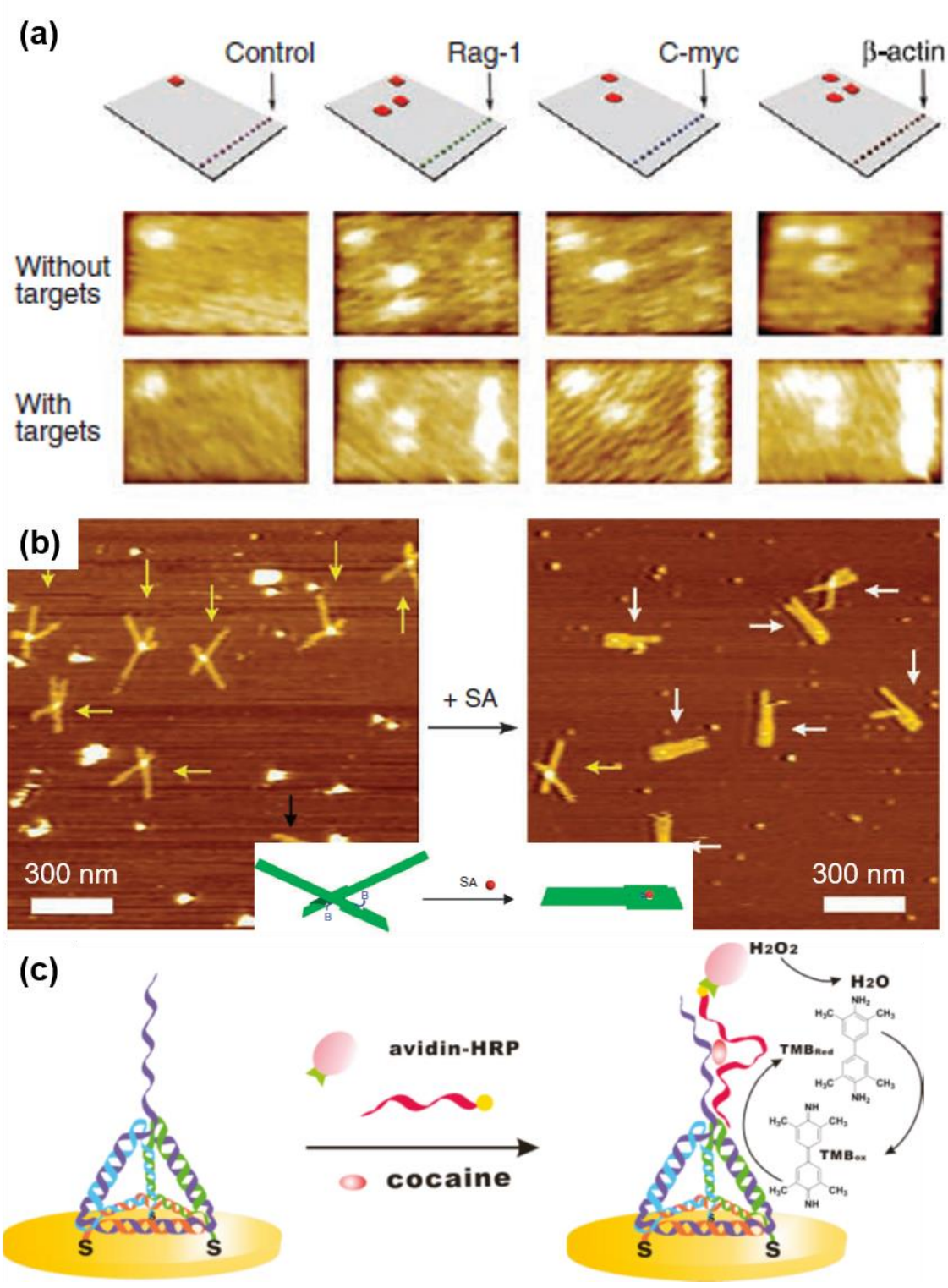

Figure 8. Examples of DNA nanostructures as biosensor. (a) (Top) Topographic illustration of the bar-coded tile designs. The top left corners of the tiles are modified with one to three groups of topological features that form distinctive bar codes for each tile. Each tile carries a line of probes

positioned near the right edge of the tile to optimize target-binding efficiency. (Middle and Bottom) Typical zoom-in AFM images of the bar-coded tiles without targets (Middle) and with targets (Bottom). Each type of tile is readily identified by its bar code. (b) AFM images of streptavidin (SA) pinching by biotinylated DNA pliers. After SA addition (right), DNA pliers selectively pinched exactly one SA tetramer and closed into the parallel closed form. Inset shows the schematic illustration of SA pinching. (c) Scheme for an aptamer-based electrochemical cocaine sensor using tetrahedron-decorated gold electrodes. The presence of cocaine fused extended strand (purple) and biotinylated strand (red). This binding process is transduced to electrochemical signals via the specific binding of avidin-HRP conjugates to the biotin tag. HRP catalyzed electro-reduction of hydrogen peroxide (H_2O_2) in the presence of 3,3',5,5'-tetra-methylbenzidine (TMB) to generate quantitative signals. Reprinted with permission from: (a) Reference 138, copyright © 2008, American Association for the Advancement of Science; (b) Reference 143, copyright © 2011, Springer Nature; (c) Reference 153, copyright © 2011, American Chemical Society.

1.4.2 DNA nanostructures for drug delivery

The field of nanomedicine requires the fabrication of nanoscale objects to serve as delivery cages for a variety of therapeutic cargos including small molecules, proteins and nucleic acids. DNA nanostructures are natural biopolymers with outstanding biocompatibility and biodegradability, making them applicable for *in vivo* cellular delivery in cancer and enzyme replacement therapy.[155-159] Recent progress suggested that DNA nanostructures can readily pass through the membrane barrier and become internalized by cell, with certain modified labels[160] or with certain geometries.[161-163] Meanwhile, it has been suggested that DNA nanostructures can maintain their structural stability in physiological conditions with presence of nucleases.[164-165] Surface modification and labelling methods have also been developed to enhance the stability of DNA nanostructures of different sizes and shapes.[121, 166] DNA nanostructures have been demonstrated to serve as drug molecule carrier for small molecules (*e.g.*, doxorubicin),[167-169] nucleic acids (*e.g.*, small interfering RNA, aptamers or CpG oligodeoxynucleotides)[154, 162, 170-171] and proteins (*e.g.*, antigen-binding antibody fragments or catabolite activator protein).[172-173]

DNA tetrahedron is a small 3D DNA nanostructure for drug delivery and therefore more cost-effective and more liable. DNA tetrahedron nanostructure was employed for efficient delivery of doxorubicin into drug-resistant breast cells.[169] Doxorubicin is a type of anti-cancer drug and can intercalate into DNA duplexes. Doxorubicin-loaded DNA tetrahedron nanostructures were easily loaded into the drug-resistant breast cancer cells as well as the wild-type control cells without additional transfection agents (**Figure 9(a)**). The drug release significantly and efficiently inhibited the multidrug resistance (MDR) cell growth (**Figure 9(b)**). Integrating aptamer to identify tumor cells and doxorubicin drugs onto a single DNA tetrahedron nanostructure, selective drug delivery can be achieved as a ‘sense and treat’ nanodevice (**Figure 9(c)**).[174]

Despite the advances in the development of drug delivery systems using DNA nanostructures as carriers, there is still long way to go before DNA nanostructures can be applied for clinical treatments. There are concerns about the stability of DNA nanostructures in complex intercellular and cellular environments, toxicity of exogenous DNA, biocompatibility of modifications on DNA nanostructures for cargo encapsulation and sensitivity of detection signals.[134, 158] With the rapid development in DNA nanotechnology, these challenges will likely be overcome in the future.

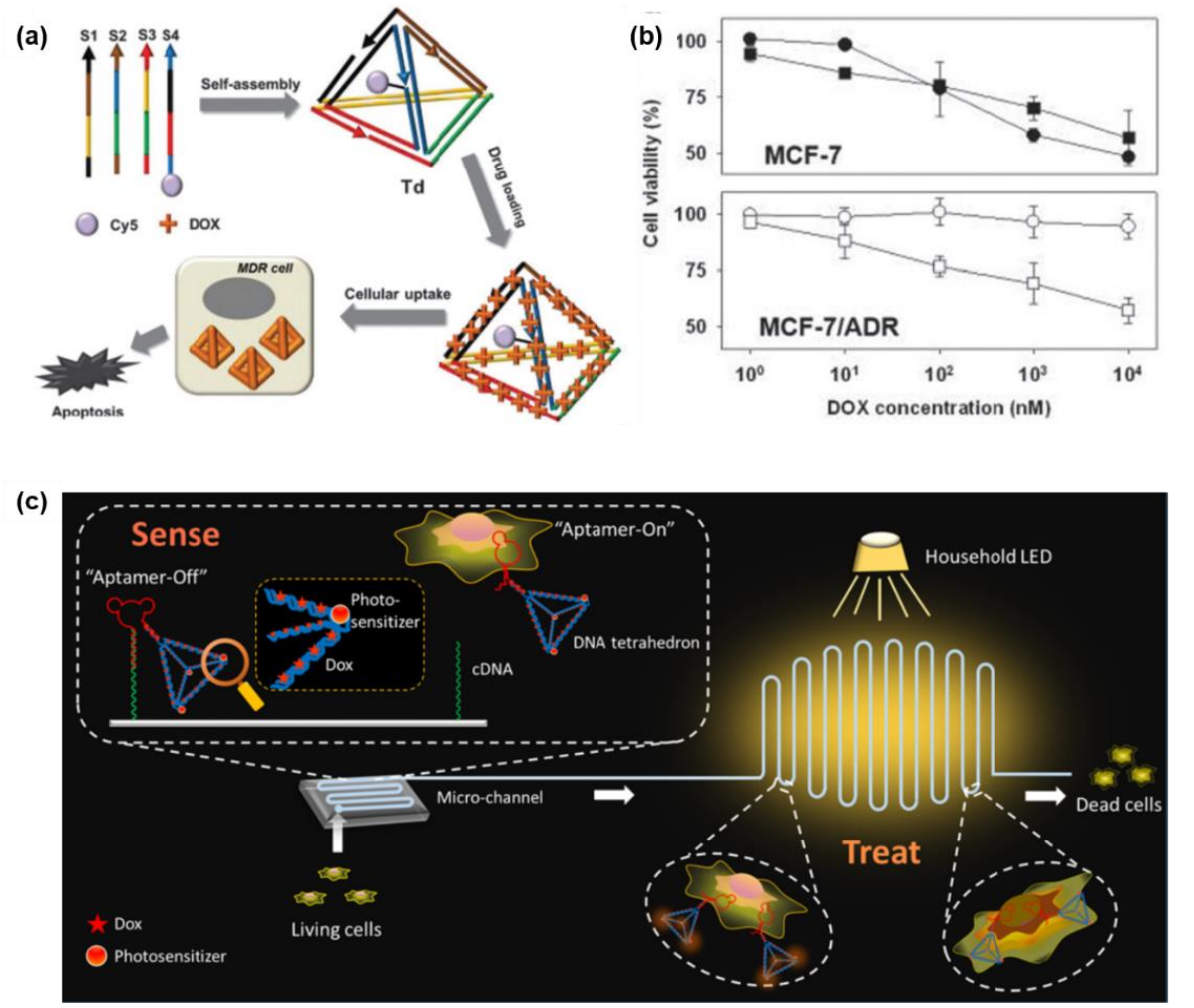

Figure 9. Doxorubicin (DOX) delivery systems using DNA tetrahedron nanostructure. (a) Schematic diagram of the DOX-loaded DNA tetrahedron and its cytotoxic effect for multidrug resistance drugs. (b) Cytotoxicity of DOX (circles) and DOX-loaded DNA tetrahedron nanostructures (squares) in drug-sensitive MCF-7 breast cancer cells and doxorubicin-resistant (MCF-7/ADR) breast cancer cells. (c) Illustration of the 'sense-and-treat' DNA nanodevice for synergetic destruction of circulating tumor cells. Reprinted with permission from: (a)(b) Reference 169, copyright © 2013, Royal Society of Chemistry; (c) Reference 174, copyright © 2016, American Chemical Society.

1.4.3 DNA nanostructures for nanofabrication

With the advantages of high resolution, low cost and shape arbitrariness, DNA nanostructures have been widely used in nanofabrication, *i.e.* patterning of different substrates including but not limited to metals, carbon materials, oxides, semiconductor materials and polymers, which are later used as micromechanical devices, optical devices or microfluidic chips. Pattern transfer is a process to copy the shapes of the templates to other materials. The traditional patterning methods in industry are optical lithography and electron-beam lithography. Polymer resist is patterned with these lithography methods and then the resulting patterns are transferred into an underlying substrate by etching or material growth.[175] The current technique allows the fabrication of semiconductor chips with feature sizes as small as 7 nm.[175-176] However, these fabrication processes leads to high capital and operational costs and potential problem with material incompatibility (especially for many organic and biological materials). At the same time, the template cost of DNA-based nanofabrication is less than $6 per m^2 assuming that monolayer amount of material is used, which is relatively low compared to other traditional materials, making even larger-scale applications possible.[11] Modifications on DNA nanostructures also provide the potential compatibility for various materials and substrates. However, there are also some downsides for DNA nanostructures as patterning templates. Typical pattern transfer methods to etch through a substrate layer or to deposit inorganic layers onto the template usually involve harsh chemical reaction conditions, at which the stability of DNA is limited. Also, most DNA nanostructures (especially the widely-used 2D DNA origami structures) is much thinner than the traditional photoresist polymer and the interaction between DNA and substrate is via weak electrostatics and van der Waals forces. As a result, DNA nanostructures could be easily lifted off from the surface in a traditional pattern transfer process and cannot provide thorough protection to

the surface. Considering the advantages and disadvantages of DNA nanostructures as patterning templates, researcher have developed numerous novel patterning methods for DNA nanostructure templates in much milder conditions.

Metallization is one of the earliest and most widely used approaches of DNA-templated patterning. The negatively charged backbone of DNA and the nitrogenated nucleobases provide a variety of binding sites for metal ions via electrostatic or coordination interactions.[177] First example of solution phase metallization of λ-DNA with silver (Ag) was reported by Braun and co-workers in 1998.[178] Since then, the metallization of different metals, such as Ag, Pt, Cu and Au on DNA strands[179-180] and DNA nanostructures[181-184] has been reported. Jin and co-workers utilized gold or silver metalized DNA origami nanostructures as masks for plasma etching-based pattern transfer to graphene (**Figure 10(a)**).[182] Instead of metallization of the entire DNA nanostructure, site-specific metallization methods of DNA nanostructure were also reported by several studies. The site specification was achieved by extending staple strand(s) in DNA nanostructures and modifying the ends with metal binding sites.[87-88, 185] Pearson and co-workers provided an example to selectively attach gold nanoparticles and fabricate conductive wires within nanometer scale resolution (**Figure 10(b)**).[185] Metallization is a critical step to improve the chemical stability of DNA nanostructures through plasma-based etching processes. However, one significant shortcoming with DNA metallization methods is that the metal coatings produces were nonconformal, leading to a significant loss of resolution.

DNA nanostructures also provide the templates for deposition of other materials. Surwade and co-workers developed a method to pattern inorganic oxides using DNA nanostructure templates through room-temperature one-step chemical vapor deposition (CVD) process.[186] Both negative-tone and positive-tone patterns of SiO_2 with ultra-high resolution were achieved by

controlling the experimental conditions (**Figure 10(c)**). Liu and co-workers also developed methods to coat DNA nanostructures uniformly with SiO_2 via Stöber method (**Figure 10(d)**).[187]

DNA nanostructures have also been used for etch-based pattern transfers. High-resolution etching and patterning of SiO_2 using unmodified DNA nanostructures as templates was demonstrated by Surwade and co-workers and will be discussed in detail later in **1.4.4**.[188] Using the existing SiO_2 patterns as a hard mask, high-contrast and high-resolution etching of Si can be achieved through plasma etching process (**Figure 10(e)**).[112]

The development of DNA nanotechnology has also demonstrated the application of DNA nanostructures for patterning of polymers[189] and carbon materials (*e.g.*, highly oriented pyrolytic graphite – HOPG and graphene).[182, 190] Tian and co-workers developed a polymer imprinting technique in which DNA nanostructures can directly print patterns onto a layer of spin-coated polymer substrate (**Figure 10(f)**).[189] Coating of Al_2O_3 improves the mechanical stability of the DNA nanostructures, making the imprinting masks reusable.[191]

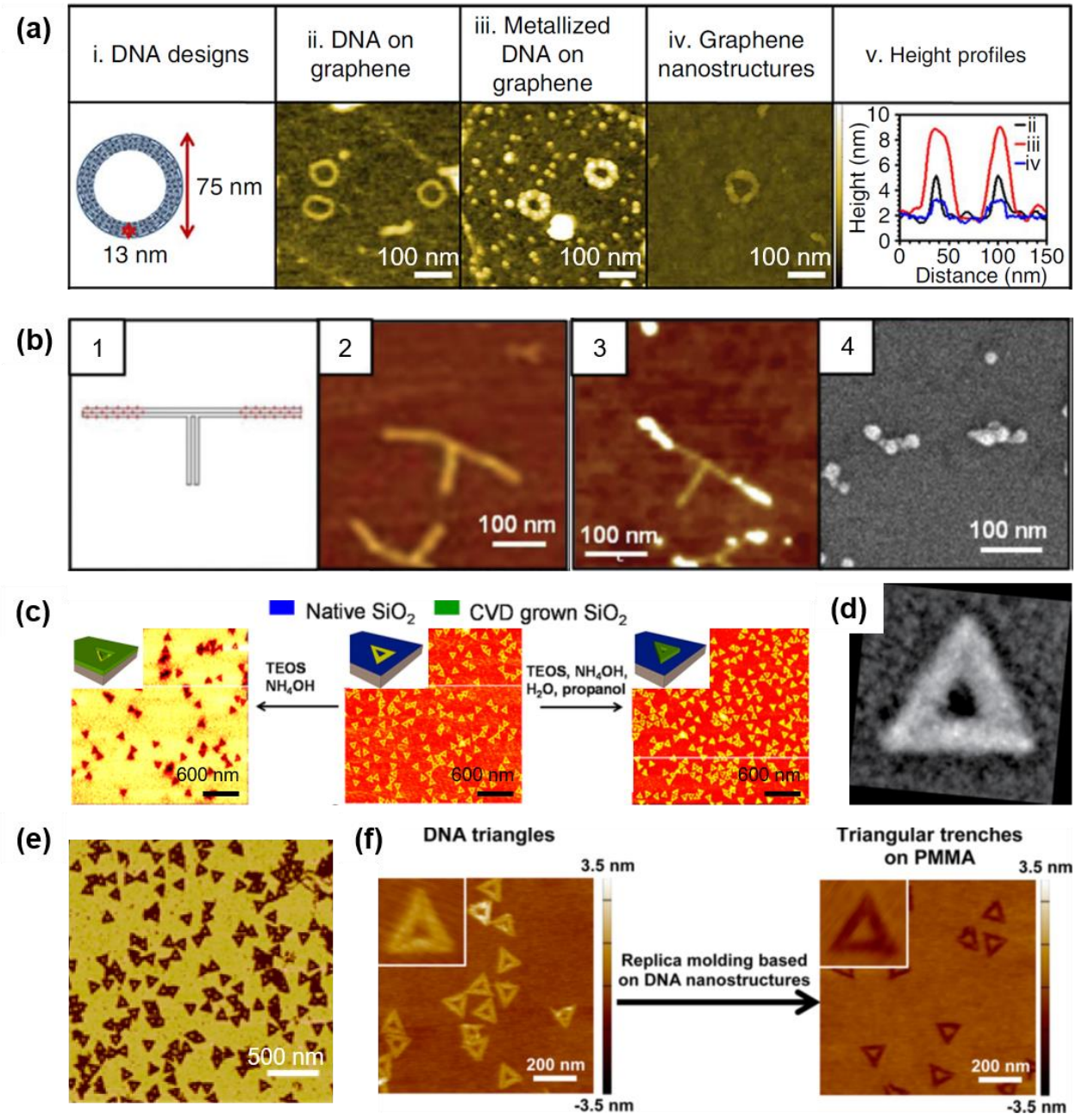

Figure 10. Nanofabrication using DNA nanostructures as templates. (a) Nanopatterning of graphene via metallized DNA structures that encode and transfer spatial information. Panel (i) shows the ring-shaped DNA origami nanostructure design. Panel (ii)-(iv) show the AFM images of the DNA templates immobilized on graphene, the metallized templates on graphene and the final etched graphene shapes. Panel (v) is a typical height profile of the nanostructure in column (ii)-(iv). (b) Images of the 'T' shaped DNA origami with a programmed gap between site-selective regions of metallization. Panel (1) shows the design of the structure with the red markings as the

locations of metal attachment. Panel (2) and (3) are the AFM images of the unseeded and seeded 'T' DNA origamis. Panel (4) is the SEM image of the 'T' DNA origami with a gap following metallization. (c) (Middle) AFM image of DNA origami nanostructures on SiO_2/Si substrate. (Left and Right) AFM images of DNA-templated CVD growth of inorganic oxide (SiO_2) showing negative-tone or positive-tone patterns under different reaction conditions. Insets show the corresponding cartoon representations. (d) SEM image of a silica-coated triangular DNA origami nanostructure. (e) AFM image of triangular patterns on Si substrate using etched SiO_2 as a hard mask and plasma etching. (f) Fabrication of poly(methyl methacrylate) (PMMA) stamp by replication over the triangular DNA origami nanostructures. AFM images are presented for DNA nanostructures on SiO_2/Si substrate and triangular patterns on PMMA stamp. Insets show the magnified images. Reprinted with permission from: (a) Reference 182, copyright © 2013, Springer Nature; (b) Reference 185, copyright © 2012, American Chemical Society; (c) Reference 186, copyright © 2013, American Chemical Society; (d) Reference 187, copyright © 2018, Springer Nature; (e) Reference 112, copyright © 2015, American Chemical Society; (f) Reference 189, copyright © 2017, American Chemical Society.

1.4.4 Vapor-phase HF etching of SiO_2

In 2011, our group reported a nanoscale negative-tone pattern transfer method from DNA nanostructure to SiO_2.[188] DNA nanostructures could modulate the vapor-phase etching of SiO_2 at the single-molecule level and as a result, a faithful pattern could be transferred from the DNA nanostructures to the inorganic substrate, *i.e.* SiO_2. The vapor-phase etching of SiO_2 by hydrogen fluoride (HF) gas is based on the thermodynamically favorable reaction between SiO_2 and HF gas to produce SiF_4 and H_2O:

$$SiO_2(s) + 4HF(g) \rightarrow SiF_4(g) + 2H_2O(g)$$

Water is the catalyst in this reaction to help the reactants overcome the kinetic barrier. Due to the fact that water is both catalyst and product of the etching reaction, as the reaction progresses on the substrate, the surface water concentration increases and as a result, the reaction rate increases. The surface etching reaction is autocatalytic. The etching rate of SiO_2 is positively correlated with the concentration of surface-adsorbed water. If the amount of surface-adsorbed water is not uniform throughout the whole surface, a surface with different thicknesses of SiO_2 will be generated after HF etching reaction.

In our previous research, it was shown that DNA nanostructures could modulate the vapor-phase etching of SiO_2 at the single-molecule level by changing the amount of water adsorbed near itself, leading to direct negative-tone and positive-tone pattern transfers from DNA nanostructures to SiO_2 at nanometer resolution (**Figure 11(a)**). After optimization of pattern transfer conditions, the method could reproducibly produce patterns with sub-10 nm resolution (**Figure 11(b)**)[192] or high vertical contrast (>10 nm, with sub-20 nm resolution).[112]

In the follow-up studies, inorganic salt (*e.g.*, sodium chloride – NaCl), graphene oxide and also protein (*e.g.*, albumin) were all proved to promote hydrofluoric acid (HF) etching of silicon

dioxide layer on silicon wafer, creating negative-tone patterns on the silicon wafer (**Figure 11(c)**).[193]

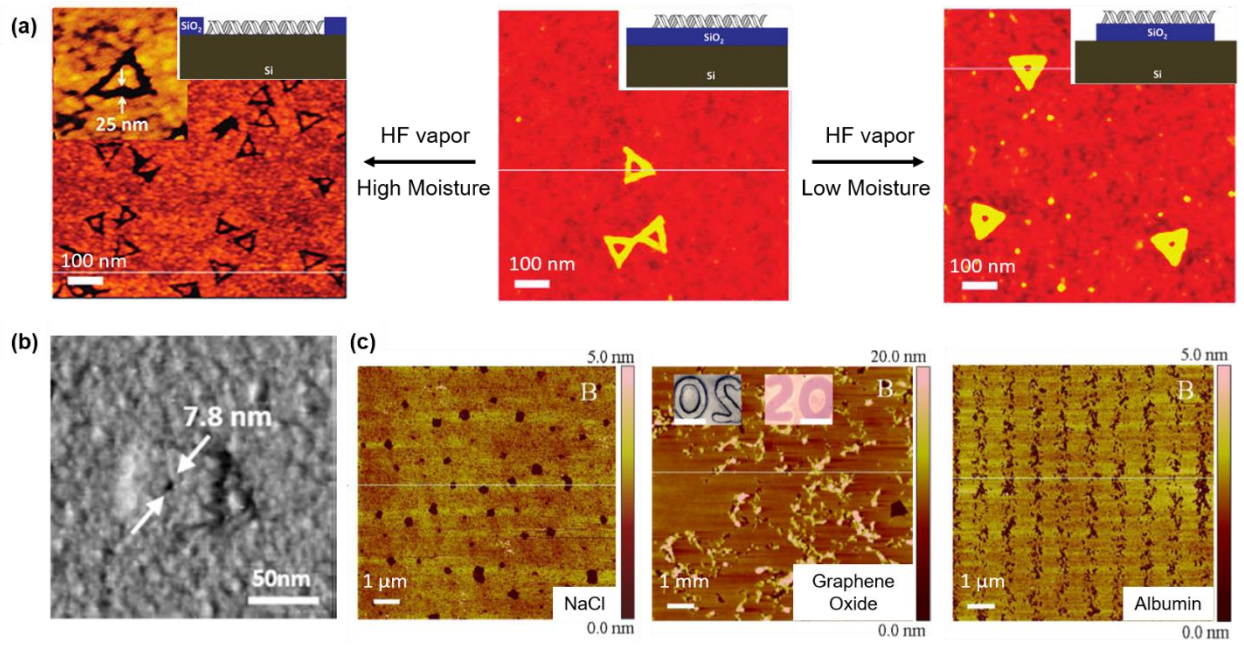

Figure 11. Vapor-phase HF etching of SiO_2. (a) (Middle) AFM image of triangular DNA origami nanostructures on SiO_2 surface. (Left and Right) AFM images of negative-tone and positive-tone triangular patterns produced on SiO_2 substrate under different etching conditions. Insets show the corresponding cartoon representations. (b) AMF phase image of SiO_2 substrate etched with DNA origami templates showing sub-10 nm resolution. (c) AFM images of negative-tone patterns created by different inorganic and organic molecules. Insets in graphene-templated image show the optical microscopy images of polydimethylsiloxane (PDMS) stamp (for graphene oxide deposition) and SiO_2/Si substrate after HF etching process. Reprinted with permission from: (a) Reference 188, copyright © 2011, American Chemical Society; (b) Reference 192, copyright © 2016, American Chemical Society; (c) Reference 193, copyright © 2015, IOP Publishing Ltd.

1.4.5 Limitations of DNA nanostructures for nanofabrication

It has been almost four decades since the concept of DNA nanotechnology was first coined. DNA nanostructures have been utilized in various state-of-the-art nanofabrication applications. With all the great potentials of high resolution, low cost and high programmability, there are still challenges and limitations ahead. Apart from the concern of thermal and chemical stability as discussed in **1.3**, the major problem for DNA nanofabrication is the deterministic organization of DNA nanostructures. In an industrial application, the locations and orientations of DNA nanostructure templates must be precisely controlled. Pioneering work on the lithography-directed self-assembly of DNA nanostructures was based on the predefined patterns created by e-beam lithography or deep ultraviolet lithography.[194-196] The deposition of DNA nanostructures was guided by the predefined patterns due to size matching and surface modification. However, these methods require high-cost lithography techniques, which are indeed what DNA-based lithography is trying to replace. Recent progress has applied DNA-based nanofabrication method for antifouling applications, in which the placement and alignment of DNA nanostructures is not a critical issue.[197] Another challenge for DNA-based nanofabrication is the compatibility with a wider variety of materials. New pattern transfer methods and mechanisms must be developed within the limited DNA-stable environmental conditions. Meanwhile, defects always present in the preparation of DNA nanostructures so the fabrication method must be able to tolerate high defect densities.[175] With these challenges and concerns solved in the future, we hope that DNA nanostructures will open up more opportunities for nanofabrication.

2.0 DNA-Based 3D Lithography Using 2D Templates

2.1 Chapter Preface

Materials contained in this chapter were submitted for publication as a research article.

List of Authors: Anqin Xu, Ashley N Pop, Hyojeong Kim and Haitao Liu

Author Contributions: A.X. and H.L. designed and directed the experiments. A.X. conducted the experiments with help from A.N.P for synthesis of DNA origami nanostructures (**2.3.4**) and pattern transfer from negative SiO_2/Si substrate to positive PLLA film (**2.3.8**) and H.K. for **2.3.8**. All authors discussed the results. A.X. and H.L. wrote the manuscript with input from all authors.

2.2 Introduction

There is a growing need of creating 3D complex nanostructures for applications in nano/micro-electronics, energy, and biomedical engineering.[198-205] Current approaches to 3D nanofabrication heavily rely on multiple cycles of photolithography (*i.e.*, layer-by-layer patterning),[199] which is time-consuming and cost-inefficient. Photolithography is inherently 2D in nature because the contrast of its pattern transfer is defined by the presence or absence of a photoresist layer. During the pattern transfer, the part of the substrate that is covered by photoresist will be etched to the same depth, producing a uniform vertical contrast. To produce 3D patterns (*i.e.*, variable vertical contrast) using 2D templates in one step will require a new pattern transfer mechanism that can produce contrast variation within the template. Here we demonstrate this capability using chemically-modified DNA nanostructure templates.

Since the concept of DNA nanostructures was created by N. Seeman in 1982,[4] DNA materials have been constructed into arbitrary shaped 2D and 3D nanostructures with a theoretical precision of approximately 2 nm.[14, 29-32, 37, 39, 206-207] Starting in 2006,[44] scaffolded DNA origami opened a new era in DNA self-assembly, providing an entirely new class of template for bottom-up nanofabrication. DNA origami nanostructures can serve as platforms for assembly of metal nanoparticles,[74-75] carbon nanotubes,[77] quantum dots[76] and biological molecules.[69, 79-81] Of particular relevance to this study, DNA origami nanostructures have been utilized as nanoscale lithography templates to pattern many materials including but not limited to metals,[88, 182-184] semiconductors[186, 188] and carbon materials.[84, 190, 195, 208]

DNA nanostructure is a versatile and low-cost template for high resolution lithography. DNA-based lithography is a bottom-up fabrication method yet it offers access to designer patterns that previously only top-down fabrication methods can provide. DNA-based fabrication has

already demonstrated sub-10 nm resolution,[192] which is on par with what the state-of-the-art optical, electron or X-ray lithography can offer. Compared with these competing technologies, DNA-based lithography has a unique advantage in the overall cost. It does not require expensive instruments that are typically required for optical, electron or X-ray lithography.[209-213] Recent advances in bio-based manufacturing has pushed the cost of DNA nanostructure to as low as \$0.2/mg, or \$0.3/m^2 for a monolayer amount of 2D DNA template.[133, 135] At this price tag, DNA-based lithography is potentially economical for high resolution patterning over very large areas (>> m^2).

However, the existing DNA-based lithography methods produce patterns of homogeneous vertical contrast, *i.e.*, they are 2D in nature like the mainstream photolithography. Here, we show that DNA-based lithography, when using DNA nanostructure templates with site-specific modifications, produces digitally-controlled vertical contrasts after pattern transfer to a SiO_2 substrate. This is the first demonstration of using 2D DNA templates to produce 3D nanoscale patterns.

2.3 Experimental Section

2.3.1 Materials

(100)-oriented silicon wafers with 300 nm of thermal oxide layer (SiO_2/Si substrates) were purchased from University Wafers, USA. 2-Amino-2-(hydroxymethyl)-1,3-propanediol (Trizma base or Tris, ≥ 99.9%), acetic acid (≥ 99.7%), ethylenediaminetetraacetic acid (EDTA, ≥ 99%), magnesium acetate tetrahydrate (≥ 99%), sulfuric acid (95.0%-98.0%), hydrogen peroxide solution (30% wt. % in water), streptavidin, hydrofluoric acid (HF, 48%), potassium hydroxide (reagent grade, 90%, flakes), poly(*L*-lactide) (PLLA) (viscosity ~2.0 dL/g, 0.1 % (w/v) in chloroform (25 °C)), dichloromethane (99.5%) and acetone (ACS reagent, ≥ 99.5%) were purchased from Sigma-Aldrich, USA and used as received without further purification. Ethanol (200 proof) was purchased from Fisher Scientific, USA. Streptavidin was dissolved in water and the concentration was determined by 280 nm UV absorbance measured by NanoDrop 2000c spectrophotometer (Thermo Scientific™, USA). Polydimethylsiloxane (PDMS) was fabricated with Sylgard 184 silicone elastomer kit (Dow Corning, Midland, MI, USA). Water (18.2 MΩ·cm) was filtered by a water purification system (Barnstead MicroPure Standard, Thermo Scientific™, USA) and used throughout the entire experiment for the preparation of chemical solutions and in the cleaning of the experimental apparatus.

2.3.2 DNA materials

M13mp18 single stranded phage DNA was purchased from Bayou Biolabs and used as the scaffold DNA strand for DNA origami nanostructure synthesis. Synthetic DNA strands were

purchased from Integrated DNA Technology, Inc. The complete sequence profile of all 232 staple strands is listed in **2.3.3 DNA Sequence Profile**. In the design of modified triangular-shaped DNA origami nanostructure, 21 of the staple strands were replaced with corresponding extended strands (**Table 1**). BiotinMultiT strand (3'–/3Bio/ – TTTTTTTTTTTTTTT – 5') was also purchased from Integrated DNA Technology, Inc. and purified with high-performance liquid chromatography (HPLC) by the manufacturer. All the DNA samples were used as received without further purification.

Table 1. Information of 21 new staple strands to construct modified DNA origami nanostructure.

#	Name	Plate #	Position	New Sequence (5' – 3')
1	t1s14i	2	D2	AAAAAAAAAAAAAAATAGCTGTGAGAAAATGTGTAGGTAAAGATACAACTTT
2	t1s16i	2	E2	AAAAAAAAAAAAAAATAGCTGGCATCAAATTTGGGGCGCGAGCTAGTTAAAG
3	t1s18i	2	F2	AAAAAAAAAAAAAAATAGCTTTCGAGCTAAGACTTCAAATATCGGGAACGAG
4	t3s14e	2	F5	AAAAAAAAAAAAAAATAGCTCAATATGACCCTCATATATTTTAAAGCATTAA
5	t3s16e	2	G5	AAAAAAAAAAAAAAATAGCTCATCCAATAAATGGTCAATAACCTCGGAAGCA
6	t3s18g	2	H5	AAAAAAAAAAAAAAATAGCTAACTCCAAGATTGCATCAAAAAGATAATGCAGATACATAA
7	t5s14e	2	F8	AAAAAAAAAAAAAAATAGCTTTAATGCCTTATTTCAACGCAAGGGCAAAGAA
8	t5s16e	2	G8	AAAAAAAAAAAAAAATAGCTTTAGCAAATAGATTTAGTTTGACCAGTACCTT
9	t5s18g	2	H8	AAAAAAAAAAAAAAATAGCTTAATTGCTTTACCCTGACTATTATGAGGCATAGTAAGAGC
10	t7s16e	2	D11	AAAAAAAAAAAAAAATAGCTTAAAGCTATATAACAGTTGATTCCCATTTTTG
11	t7s18g	2	E11	AAAAAAAAAAAAAAATAGCTCGGATGGCACGAGAATGACCATAATCGTTTACCAGACGAC
12	t9s18g	4	F1	AAAAAAAAAAAAAAATAGCTTGCTGTAGATCCCCCTCAAATGCTGCGAGAGGCTTTTGCA
13	t-1s14e	4	H3	AAAAAAAAAAAAAAATAGCTATTTTCTGTCAGCGGAGTGAGAATACCGATAT
14	t-1s16e	4	B4	AAAAAAAAAAAAAAATAGCTATTCGGTCTGCGGGATCGTCACCCGAAATCCG
15	t-1s18g	4	D4	AAAAAAAAAAAAAAATAGCTCGACCTGCGGTCAATCATAAGGGAACGGAACAACATTATT
16	t-3s14e	4	C8	AAAAAAAAAAAAAAATAGCTGTTTTGTCAGGAATTGCGAATAATCCGACAAT
17	t-3s16e	4	D8	AAAAAAAAAAAAAAATAGCTGACAACAAGCATCGGAACGAGGGTGAGATTTG
18	t-3s18e	4	E8	AAAAAAAAAAAAAAATAGCTTATCATCGTTGAAAGAGGACAGATGGAAGAAAAATCTACG
19	t-5s16e	4	D11	AAAAAAAAAAAAAAATAGCTAACAGCTTGCTTTGAGGACTAAAGCGATTATA
20	t-5s18g	4	E11	AAAAAAAAAAAAAAATAGCTCCAAGCGCAGGCGCATAGGCTGGCAGAACTGGCTCATTAT
21	t-7s18g	3	A2	AAAAAAAAAAAAAAATAGCTAAAACACTTAATCTTGACAAGAACTTAATCATTGTGAATT

2.3.3 DNA sequence profile

Complete sequence profile of all 232 staple strands to construct triangular-shaped DNA origami nanostructure (without modification) is listed below.[44]

Plate number: 1

t10s17c, A1, TTAAATATGCA

t10s27c, A2, ATACCGAACGA

t10s7c, A3, TAGCACCATTA

t12s19c, A4, GGATAGCGTCC

t12s29c, A5, GTAGCAATACT

t12s9c, A6, AACAAAGTTAC

t6s13c, A7, CTATTTTTGAG

t6s23c, A8, ACCATATCAAA

t6s3c, A9, TATAAACAGTT

t8s15c, A10, CCAAAAACATT

t8s25c, A11, AGACTTTACAA

t8s5c, B1, CCACCAGAGCC

t-11s18e, B2, ATAAGGCTTGC

t-11s28e, B3, ACTATTAAAGA

t-11s8e, B4, TCAAGATTAGT

t-5s12e, B5, TGTAGCATTCC

t-5s22e, B6, GTGGGAACAAA

t-5s2e, B7, TTAATTAATTT

t-7s14e, C1, TTTAATTGTAT

t-7s24e, C2, CGGTGCGGGCC

t-7s4e, C3, TTAATTTCATC

t-9s16e, C4, ACTACGAAGGC

t-9s26e, C5, ATGAGTGAGCT

t-9s6e, C6, CTGTCCAGACG

Plate number: 2

t1s24i, A3, CCTGATTAAAGGAGCGGAATTATCTCGGCCTC

t2s11g, A4, AGAAAAGCCCCAAAAAGAGTCTGGAGCAAACAATCACCAT

t2s27f, A5, GGACATTCACCTCAAATATCAAACACAGTTGA

t3s20g, A6, CGCCAAAAGGAATTACAGTCAGAAGCAAAGCGCAGGTCAG

t4s11g, A7, GCAAATATTTAAATTGAGATCTACAAAGGCTACTGATAAA

t4s27f, A8, TGACCTGACAAATGAAAAATCTAAAATATCTT

t5s20g, A9, AACACTATCATAACCCATCAAAAATCAGGTCTCCTTTTGA

t6s7f, A11, ATTAAAGGCCGTAATCAGTAGCGAGCCACCCT

t7s28g, A12, CTATTAGTATATCCAGAACAATATCAGGAACGGTACGCCA

t1s10g, B2, GACGGGAGAATTAACTCGGAATAAGTTTATTTCCAGCGCC

t1s26i, B3, GCAAATCACCTCAATCAATATCTGCAGGTCGA

t2s13g, B4, ACAGTCAAAGAGAATCGATGAACGACCCCGGTTGATAATC

t2s3g, B5, TTTGATGATTAAGAGGCTGAGACTTGCTCAGTACCAGGCG

t3s24e, B6, TAATCCTGATTATCATTTTGCGGAGAGGAAGG

t4s13g, B7, CGTTCTAGTCAGGTCATTGCCTGACAGGAAGATTGTATAA

t4s3g, B8, TTTAACGGTTCGGAACCTATTATTAGGGTTGATATAAGTA

t5s24e, B9, AATGGAAGCGAACGTTATTAATTTCTAACAAC

t6s15g, B10, ATAAAGCCTTTGCGGGAGAAGCCTGGAGAGGGTAG

t7s10g, B11, ATAAGAGCAAGAAACATGGCATGATTAAGACTCCGACTTG

t7s30g, B12, GAATCCTGAGAAGTGTATCGGCCTTGCTGGTACTTTAATG

t1s12i, C2, TCATATGTGTAATCGTAAAACTAGTCATTTTC

t1s28i, C3, CGACCAGTACATTGGCAGATTCACCTGATTGC

t2s15f, C4, ATAGTAGTATGCAATGCCTGAGTAGGCCGGAG

t2s5f, C5, CCGGAACCCAGAATGGAAAGCGCAACATGGCT

t3s26e, C6, TTATCTAAAGCATCACCTTGCTGATGGCCAAC

t4s15f, C7, CAGGCAAGATAAAAATTTTTAGAATATTCAAC

t4s5f, C8, CTCAGAGCATATTCACAAACAAATTAATAAGT

t5s26e, C9, TAATAGATCGCTGAGAGCCAGCAGAAGCGTAA

t6s17f, C10, TAAGAGGTCAATTCTGCGAACGAGATTAAGCA

t7s14e, C11, ATGACCCTGTAATACTTCAGAGCA

t7s4e, C12, GCCGCCAGCATTGACACCACCCTC

t11s18h, D1, AATACTGCGGAATCGTAGGGGGTAATAGTAAAATGTTTAGACT

t1s14i, D2, GTGAGAAAATGTGTAGGTAAAGATACAACTTT

t1s2i, D3, CGGGGTTTCCTCAAGAGAAGGATTTTGAATTA

t2s17f, D4, AACCAGACGTTTAGCTATATTTTCTTCTACTA

t2s7f, D5, AAAGACAACATTTTCGGTCATAGCCAAAATCA

t3s28g, D6, AGAGATAGTTTGACGCTCAATCGTACGTGCTTTCCTCGTT

t4s17f, D7, GATTAGAGATTAGATACATTTCGCAAATCATA

t4s7f, D8, GGAGGGAATTTAGCGTCAGACTGTCCGCCTCC

t5s28g, D9, GAATACGTAACAGGAAAAACGCTCCTAAACAGGAGGCCGA

t7s16e, D11, TAAAGCTATATAACAGTTGATTCCCATTTTTG

t7s6e, D12, AGAGCCGCACCATCGATAGCAGCATGAATTAT

t11s28h, E1, TCTTTGATTAGTAATAGTCTGTCCATCACGCAAATTAACCGTT

t1s16i, E2, GGCATCAAATTTGGGGCGCGAGCTAGTTAAAG

t1s30g, E3, TTGACGAGCACGTATACTGAAATGGATTATTTAATAAAAG

t2s1g, E4, GATAAGTGCCGTCGAGCTGAAACATGAAAGTATACAGGAG

t3s10g, E5, GTCAGAGGGTAATTGATGGCAACATATAAAAGCGATTGAG

t3s30g, E6, AGAATCAGAGCGGGAGATGGAAATACCTACATAACCCTTC

t4s1g, E7, TAGCCCGGAATAGGTGAATGCCCCCTGCCTATGGTCAGTG

t5s10g, E8, GATAACCCACAAGAATGTTAGCAAACGTAGAAAATTATTC

t5s30g, E9, TTAAAGGGATTTTAGATACCGCCAGCCATTGCGGCACAGA

t6s25g, E10, TCAATAGATATTAAATCCTTTGCCGGTTAGAACCT

t7s18g, E11, CGGATGGCACGAGAATGACCATAATCGTTTACCAGACGAC

t7s8g, E12, CACCGTCACCTTATTACGCAGTATTGAGTTAAGCCCAATA

t11s8h, F1, CAGAAGGAAACCGAGGTTTTTAAGAAAAGTAAGCAGATAGCCG

t1s18i, F2, TTCGAGCTAAGACTTCAAATATCGGGAACGAG

t1s4i, F3, AGCGTCATGTCTCTGAATTTACCGACTACCTT

t2s21g, F4, CCTGATTGCTTTGAATTGCGTAGATTTTCAGGCATCAATA

t3s14e, F5, CAATATGACCCTCATATATTTTAAAGCATTAA

t3s4e, F6, TGTACTGGAAATCCTCATTAAAGCAGAGCCAC

t4s21g, F7, GCGCAGAGGCGAATTAATTATTTGCACGTAAATTCTGAAT

t5s14e, F8, TTAATGCCTTATTTCAACGCAAGGGCAAAGAA

t5s4e, F9, CCTTGAGTCAGACGATTGGCCTTGCGCCACCC

t6s27f, F10, CAATATTTGCCTGCAACAGTGCCATAGAGCCG

t7s20g, F11, GATAAAAACCAAAATATTAAACAGTTCAGAAATTAGAGCT

t1s20g, G2, GAATACCACATTCAACTTAAGAGGAAGCCCGATCAAAGCG

t1s6i, G3, TTCATAATCCCCTTATTAGCGTTTTTCTTACC

t2s23g, G4, TGGCAATTTTTAACGTCAGATGAAAACAATAACGGATTCG

t3s16e, G5, CATCCAATAAATGGTCAATAACCTCGGAAGCA

t3s6e, G6, CACCGGAAAGCGCGTTTTCATCGGAAGGGCGA

t4s23g, G7, GATTATACACAGAAATAAAGAAATACCAAGTTACAAAATC

t5s16e, G8, TTAGCAAATAGATTTAGTTTGACCAGTACCTT

t5s6e, G9, TCAGAACCCAGAATCAAGTTTGCCGGTAAATA

t7s24e, G11, ACAATTCGACAACTCGTAATACAT

t8s17g, G12, TAATTGCTTGGAAGTTTCATTCCAAATCGGTTGTA

t1s22i, H2, TCGGGAGATATACAGTAACAGTACAAATAATT

t1s8i, H3, ATGGTTTATGTCACAATCAATAGATATTAAAC

t2s25f, H4, AAGGAATTACAAAGAAACCACCAGTCAGATGA

t3s18g, H5, AACTCCAAGATTGCATCAAAAAGATAATGCAGATACATAA

t3s8g, H6, CATTCAACAAACGCAAAGACACCAGAACACCCTGAACAAA

t4s25f, H7, TAGGAGCATAAAAGTTTGAGTAACATTGTTTG

t5s18g, H8, TAATTGCTTTACCCTGACTATTATGAGGCATAGTAAGAGC

t5s8g, H9, TTGACGGAAATACATACATAAAGGGCGCTAATATCAGAGA

t6s5g, H10, CAGAGCCAGGAGGTTGAGGCAGGTAACAGTGCCCG

t7s26e, H11, TTGAGGATGGTCAGTATTAACACCTTGAATGG

Plate number: 3

t-6s23f, A1, CGGCGGATTGAATTCAGGCTGCGCAACGGGGGATG

t-7s18g, A2, AAAACACTTAATCTTGACAAGAACTTAATCATTGTGAATT

t-8s17c, A3, GGCAAAAGTAAAATACGTAATGCC

t-5s2e-t6s23c-3T, A6, TTAATTAATTTTTTACCATATCAAA

t-5s22e-t6s13c-3T, A7, GTGGGAACAAATTTCTATTTTTGAG

t-6s25c, B1, TGGCGAAATGTTGGGAAGGGCGAT

t-7s20g, B2, ACCTTATGCGATTTTATGACCTTCATCAAGAGCATCTTTG

t-8s25f, B3, TCTTCGCTATTGGAAGCATAAAGTGTATGCCCGCT

t-9s30g, B4, CGATGGCCCACTACGTATAGCCCGAGATAGGGATTGCGTT

t-7s4e-t8s25c-2T, B6, TTAATTTCATCTTAGACTTTACAA

t-7s24e-t8s15c-2T, B7, CGGTGCGGGCCTTCCAAAAACATT

t-6s27f, C1, TGTCGTGCACACAACATACGAGCCACGCCAGC

t-8s27c, C3, GCGCTCACAAGCCTGGGGTGCCTA

t-9s6e-t10s27c-1T, C6, CTGTCCAGACGTATACCGAACGA

t-9s26e-t10s17c-1T, C7, ATGAGTGAGCTTTTAAATATGCA

t-6s3f, D1, TCCCTTAGAATAACGCGAGAAAACTTTTACCGACC

t-7s28g, D2, TTCCAGTCCTTATAAATCAAAAGAGAACCATCACCCAAAT

t-8s5f, D3, TTCTGACCTAAAATATAAAGTACCGACTGCAGAAC

ts-rem1, D4, GCGCTTAATGCGCCGCTACAGGGC

t-11s8e-t12s29c-0T, D6, TCAAGATTAGTGTAGCAATACT

t-11s28e-t12s19c-0T, D7, ACTATTAAAGAGGATAGCGTCC

t-6s5c, E1, GTTTGAAATTCAAATATATTTTAG

t-7s30g, E2, CAAGTTTTTTGGGGTCGAAATCGGCAAAATCCGGGAAACC

t-8s7c, E3, TCAGCTAAAAAAGGTAAAGTAATT

t-5s12e-t6s3c-3T, E6, TGTAGCATTCCTTTTATAAACAGTT

t-6s7f, F1, AATAGATAGAGCCAGTAATAAGAGATTTAATG

t-9s10g, F3, ACGCTAACGAGCGTCTGGCGTTTTAGCGAACCCAACATGT

t-7s14e-t8s5c-2T, F6, TTTAATTGTATTTCCACCAGAGCC

t-7s10g, G1, GCCAGTTACAAAATAATAGAAGGCTTATCCGGTTATCAAC

t-7s8g, G2, GCGCCTGTTATTCTAAGAACGCGATTCCAGAGCCTAATTT

t-9s16e-t10s7c-1T, G6, ACTACGAAGGCTTAGCACCATTA

t-8s15f, H2, CGGTTTATCAGGTTTCCATTAAACGGGAATACACT

t-9s20g, H3, TGGTTTAATTTCAACTCGGATATTCATTACCCACGAAAGA

t-11s18e-t12s9c-0T, H6, ATAAGGCTTGCAACAAAGTTAC

Plate number: 4

t8s27g, A1, CGCGAACTAAAACAGAGGTGAGGCTTAGAAGTATT

t9s28g, A2, TAAAACATTAGAAGAACTCAAACTTTTTATAATCAGTGAG

t-1s14i, A4, CAACAGTTTATGGGATTTTGCTAATCAAAAGG

t-1s24i, A5, AGGAAGATGGGGACGACGACAGTAATCATATT

t-1s4i, A6, TTTAACCTATCATAGGTCTGAGAGTTCCAGTA

t-2s17f, A7, ATTGTGTCTCAGCAGCGAAAGACACCATCGCC

t-2s7f, A8, TCAATAATAGGGCTTAATTGAGAATCATAATT

t-3s28g, A9, GTTTGCGTCACGCTGGTTTGCCCCAAGGGAGCCCCCGATT

t-4s17f, A10, GTACAACGAGCAACGGCTACAGAGGATACCGA

t-4s7f, A11, CCCATCCTCGCCAACATGTAATTTAATAAGGC

t-5s28g, A12, TTAATGAAGTTTGATGGTGGTTCCGAGGTGCCGTAAAGCA

t9s30h, B2, GCCACCGAGTAAAAGAACATCACTTGCCTGAGCGCCATTAAAA

t-1s16e, B4, ATTCGGTCTGCGGGATCGTCACCCGAAATCCG

t-1s26e, B5, GCCAGTGCGATCCCCGGGTACCGAGTTTTTCT

t-1s6e, B6, TTAGTATCGCCAACGCTCAACAGTCGGCTGTC

t-2s1g, B7, AAAACAAAATTAATTAAATGGAAACAGTACATTAGTGAAT

t-3s10g, B8, AACGTCAAAAATGAAAAGCAAGCCGTTTTTATGAAACCAA

t-3s30g, B9, TAGAGCTTGACGGGGAGTTGCAGCAAGCGGTCATTGGGCG

t-4s1g, B10, GAGCAAAAGAAGATGAGTGAATAACCTTGCTTATAGCTTA

t-5s10g, B11, TCCCAATCCAAATAAGATTACCGCGCCCAATAAATAATAT

t8s7g, C1, AGCCATTTAAACGTCACCAATGAACACCAGAACCA

t9s6e, C2, CCATTAGCAAGGCCGGGGGAATTA

t-12s19h, C3, CCTGACGAGAAACACCAGAACGAGTAGGCTGCTCATTCAGTGA

t-1s16i, C4, GCCGCTTTGCTGAGGCTTGCAGGGGAAAAGGT

t-1s26i, C5, CTCTAGAGCAAGCTTGCATGCCTGGTCAGTTG

t-1s6i, C6, AGTATAAAATATGCGTTATACAAAGCCATCTT

t-2s21g, C7, GCTCATTTTTTAACCAGCCTTCCTGTAGCCAGGCATCTGC

t-3s14e, C8, GTTTTGTCAGGAATTGCGAATAATCCGACAAT

t-3s4e, C9, GATTAAGAAATGCTGATGCAAATCAGAATAAA

t-4s21g, C10, GTTAAAATTCGCATTAATGTGAGCGAGTAACACACGTTGG

t-5s30g, C12, CTAAATCGGAACCCTAAGCAGGCGAAAATCCTTCGGCCAA

t9s10h, D1, TATCTTACCGAAGCCCAAACGCAATAATAACGAAAATCACCAG

t9s8g, D2, GAGCCAGCGAATACCCAAAAGAACATGAAATAGCAATAGC

t-12s29h, D3, ACGTGGACTCCAACGTCAAAGGGCGAATTTGGAACAAGAGTCC

t-1s18g, D4, CGACCTGCGGTCAATCATAAGGGAACGGAACAACATTATT

t-1s28g, D5, TTTCACCAGCCTGGCCCTGAGAGAAAGCCGGCGAACGTGG

t-1s8g, D6, TTTCCTTAGCACTCATCGAGAACAATAGCAGCCTTTACAG

t-2s23g, D7, GTAACCGTCTTTCATCAACATTAAAATTTTTGTTAAATCA

t-3s16e, D8, GACAACAAGCATCGGAACGAGGGTGAGATTTG

t-3s6e, D9, CACCGGAATCGCCATATTTAACAAAATTTACG

t-4s23g, D10, GGATAGGTACCCGTCGGATTCTCCTAAACGTTAATATTTT

t-5s16e, D11, AACAGCTTGCTTTGAGGACTAAAGCGATTATA

t-5s6e, D12, GTGTGATAAGGCAGAGGCATTTTCAGTCCTGA

t9s16e, E1, ACTAAAGTACGGTGTCGAATATAA

t-10s17h, E2, ACCAACCTAAAAAATCAACGTAACAAATAAATTGGGCTTGAGA

t-12s9h, E3, TGCTATTTTGCACCCAGCTACAATTTTGTTTTGAAGCCTTAAA

t-1s18i, E4, GCGCAGACTCCATGTTACTTAGCCCGTTTTAA

t-1s28i, E5, CCTTCACCGTGAGACGGGCAACAGCAGTCACA

t-1s8i, E6, CAAGTACCTCATTCCAAGAACGGGAAATTCAT

t-2s25f, E7, ACGTTGTATTCCGGCACCGCTTCTGGCGCATC

t-3s18g, E8, TATCATCGTTGAAAGAGGACAGATGGAAGAAAAATCTACG

t-3s8g, E9, AGCATGTATTTCATCGTAGGAATCAAACGATTTTTTGTTT

t-4s25f, E10, AGTTGGGTCAAAGCGCCATTCGCCCCGTAATG

t-5s18g, E11, CCAAGCGCAGGCGCATAGGCTGGCAGAACTGGCTCATTAT

t-5s8g, E12, ACAAGAAAGCAAGCAAATCAGATAACAGCCATATTATTTA

t9s18g, F1, TGCTGTAGATCCCCCTCAAATGCTGCGAGAGGCTTTTGCA

t-10s27h, F2, AACTCACATTATTGAGTGTTGTTCCAGAAACCGTCTATCAGGG

t-1s10e, F3, AGAGAATAACATAAAAACAGGGAAGCGCATTA

t-1s20e, F4, ACAGGTAGAAAGATTCATCAGTTGAGATTTAG

t-1s2i, F5, CCTTTTTTCATTTAACAATTTCATAGGATTAG

t-2s11g, F6, CCTCAGAACCGCCACCCAAGCCCAATAGGAACGTAAATGA

t-2s27f, F7, CCAGGGTGGCTCGAATTCGTAATCCAGTCACG

t-3s20g, F8, TTAATAAAACGAACTAACCGAACTGACCAACTCCTGATAA

t-4s11g, F9, AGGTTTAGTACCGCCATGAGTTTCGTCACCAGGATCTAAA

t-4s27f, F10, CGCGCGGGCCTGTGTGAAATTGTTGGCGATTA

t-5s20g, F11, ACCAGTCAGGACGTTGGAACGGTGTACAGACCGAAACAAA

t-6s13f, F12, ACAGACAGCCCAAATCTCCAAAAAAAAATTTCTTA

t9s20h, G1, AAAGAAGTTTTGCCAGCATAAATATTCATTGACTCAACATGTT

t-10s7h, G2, ACGACAATAAATCCCGACTTGCGGGAGATCCTGAATCTTACCA

t-1s12i, G3, AGGGATAGCTCAGAGCCACCACCCCATGTCAA

t-1s22i, G4, CGCGTCTGATAGGAACGCCATCAACTTTTACA

t-1s30e, G5, CGAGAAAGGAAGGGAAGCGTACTATGGTTGCT

t-2s13g, G6, AGACGTTACCATGTACCGTAACACCCCTCAGAACCGCCAC

t-2s3g, G7, AGAGTCAAAAATCAATATATGTGATGAAACAAACATCAAG

t-3s24e, G8, TGTAGATGGGTGCCGGAAACCAGGAACGCCAG

t-4s13g, G9, AGCGTAACTACAAACTACAACGCCTATCACCGTACTCAGG

t-4s3g, G10, ACATAGCGCTGTAAATCGTCGCTATTCATTTCAATTACCT

t-6s15c, G12, CGAGGTGAGGCTCCAAAAGGAGCC

t9s26e, H1, ACCACCAGCAGAAGATGATAGCCC

t-1s14e, H3, ATTTTCTGTCAGCGGAGTGAGAATACCGATAT

t-1s24e, H4, CAGTTTGACGCACTCCAGCCAGCTAAACGACG

t-1s4e, H5, TTATCAAACCGGCTTAGGTTGGGTAAGCCTGT

t-2s15f, H6, CACGCATAAGAAAGGAACAACTAAGTCTTTCC

t-2s5f, H7, ACTAGAAATATATAACTATATGTACGCTGAGA

t-3s26e, H8, GGTTTTCCATGGTCATAGCTGTTTGAGAGGCG

t-4s15f, H9, TAGTTGCGAATTTTTTCACGTTGATCATAGTT

t-4s5f, H10, GTTAAATACAATCGCAAGACAAAGCCTTGAAA

t-5s26e, H11, TGCTGCAAATCCGCTCACAATTCCCAGCTGCA

t-6s17f, H12, ACCCCCAGACTTTTTCATGAGGAACTTGCTTT

2.3.4 Synthesis of triangular-shaped DNA origami nanostructures

Triangular-shaped DNA origami nanostructures were synthesized using a previously published method[44, 188] by mixing 8.60 µL of M13mp18 single stranded phage DNA solution (1 mg/mL, equivalent to 454 nM), 15.0 µL of DNA staple strands (mixture of 300 nM for each strand), 77 µL of DI water, and 181 µL of a TAE/Mg buffer. The TAE/Mg buffer solution contains the following reagents with their corresponding concentrations: 40 mM trizma base, 20 mM acetic acid, 12.5 mM magnesium acetate and 1 mM EDTA. The thermal cycler (MiniCycler™, MJ Research, Canada) quickly heated the mixture solution up to 95 ˚C, then annealed it to 20 ˚C at a cooling rate of 1 ˚C/min. Then at room temperature DNA origami nanostructure sample solution (*ca.* 280 µL) was divided equally and transferred into two separate 30 kDa MW centrifugal devices

(Nanosep Centrifugal Devices with Omega Membrane, Pall Corporation, Port Washington, NY). Additional *ca.* 400 µL of TAE/Mg buffer solution was filled into each centrifugal device and the mixtures were centrifuged at a speed of 6000 rpm using a single speed benchtop microcentrifuge (Fisher Scientific, USA) to remove the excess DNA staple strands. The DNA solution was centrifuged until 1/4 of the original volume (*ca.* 140 µL) was left on top to ensure that the sample wasn't completely dry. The process of adding buffer and centrifuging was repeated five times in total. The final DNA origami nanostructure sample was stored in TAE/Mg buffer inside a plastic vial at 4 ˚C. The prepared DNA origami solution has a concentration of 13.8 nM at 100% yield. The practical concentrations varied between 2 nM to 4 nM in different batches of samples, based on the estimation from 260 nm absorbance values by UV-Vis spectrophotometer (Nanodrop 2000c, Thermo Scientific™, USA).

2.3.5 Modification of streptavidin onto DNA nanostructures

Triangular-shaped DNA origami nanostructures were synthesized using M13mp18 single stranded phage DNA and 232 short staple strands. To achieve the modification of streptavidin onto triangular-shaped DNA origami nanostructure, 21 discrete staple strands were selected on one liner side of the structure and each staple strand was extended with a spacer strand containing a 5-mer random sequence nucleic acid chain and 15 adenine nucleotides (**Table 1**, **Figure 12(a)**). A complementary DNA strand with 15 thymine nucleotides and biotin modifier on 3' end was designed and used to attach biotin molecules onto the DNA nanostructure. With 21 of the original staple strands replaced by the 21 corresponding extended staple strands (**Table 1**, **Figure 12(b)**) in the staple strands mixture, triangular-shaped DNA origami nanostructures with biotin were synthesized using the aforesaid method by mixing 8.60 µL of M13mp18 single stranded phage

DNA solution (1 mg/mL, equivalent to 454 nM), 15.0 μL of DNA staple strands (300 nM for each strand), 18.5 μL of BiotinMultiT DNA strand (25.6 μM), 58 μL of DI water and 181 μL of a TAE/Mg buffer. The annealing and purification methods were performed in the same way. The BiotinMultiT DNA strand here was in 5 times excess compared to the extended staple strands to ensure the complete modification of biotin on the DNA nanostructure. Then the DNA samples were mixed with streptavidin in TAE/Mg buffer solution. Concentration of DNA origami nanostructures was determined from 260 nm absorbance values from UV-Vis spectrophotometer. Streptavidin concentration was set to 10 times excess compared to biotin modifiers to ensure complete modification of streptavidin onto DNA nanostructures. The solution was mixed thoroughly in a 600 μL microcentrifuge tube and set aside at room temperature for at least 1 hr to achieve best interaction between biotin and streptavidin. To purify the mixture and to remove all the excess streptavidin in the solution, the mixture (usually *ca.* 200 μL) was transferred into a 100 kDa MW centrifugal devices (Nanosep Centrifugal Devices with Omega Membrane, Pall Corporation, Port Washington, NY). Additional buffer was added to fill the solution to the top of the centrifugal device for a total *ca.* 600 μL. The solution was centrifuged at a speed of 6000 rpm using a single speed benchtop microcentrifuge to remove excess free streptavidin. The centrifuging process stopped when the volume was back to *ca.* 200 μL. The process of adding buffer and centrifuging was repeated two times to eliminate the concentration drop of the DNA nanostructures. The triangular-shaped DNA origami nanostructures with streptavidin modification were prepared freshly before use to eliminate the aggregation of DNA nanostructures due to the interaction between biotin and streptavidin molecules.

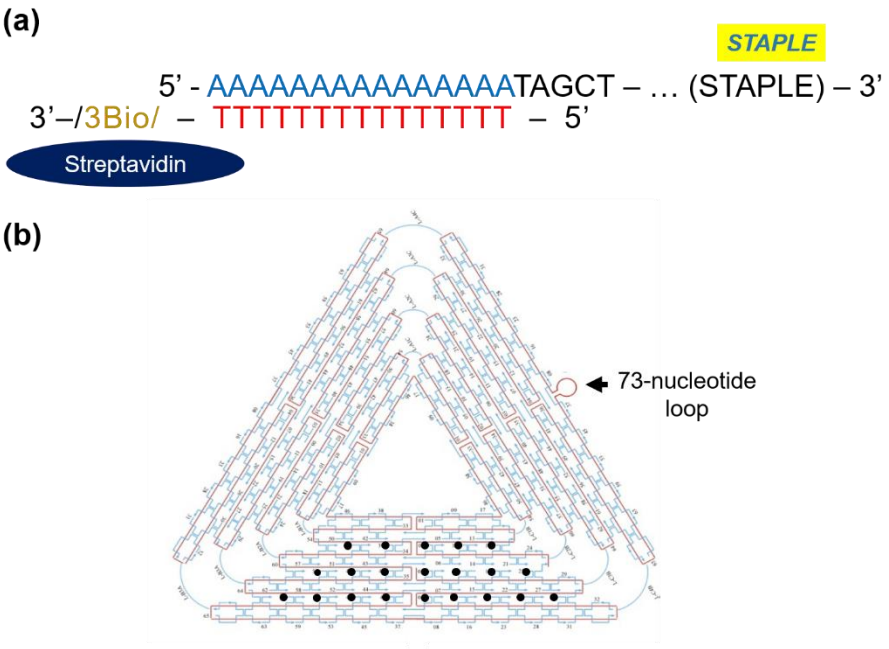

Figure 12. Modification of streptavidin onto triangular-shaped DNA origami nanostructures: (a) Design of staple extension and attachment of biotin-streptavidin system. (b) Scheme of 21 modification positions on the DNA nanostructure. Template in (b) is reprinted and adapted with permission from Reference 74, copyright © 2013, American Chemical Society.

2.3.6 Deposition of DNA samples onto SiO_2/Si substrates

A SiO_2/Si substrate (0.4 cm × 0.8 cm size) was cleaned by immersing it in a newly piranha piranha solution (3/7 (v/v) 30% hydrogen peroxide/ 98% sulfuric acid solution) in a covered glass petri dish on a 50 ˚C heating plate for 30 min. *Warning: Piranha solution is a strong oxidizing reagent and can detonate unexpectedly; extra caution in handling is required.* The substrate was then thoroughly washed with water and dried with a N_2 stream. DNA origami nanostructures (20 µL) was pipetted onto the clean and dry SiO_2/Si substrate and left in a plastic petri dish without interruption for 30 min. A wet Kimwipe was inserted between the cover and the bottom of the

plastic petri dish to maintain humidity inside and reduce evaporation of water from DNA sample. After 30 min, the substrate was dried with a N_2 stream. Then the substrate was immersed into a 9/1 (v/v) ethanol/water solution for 5 s to remove salt impurities and dried again using a N_2 stream. To ensure complete removal of the salt residues, the immersion and drying steps were repeated two times.

2.3.7 HF etching of SiO_2 with DNA templates

After deposition of sample, the SiO_2/Si substrate was transferred into a home-built HF etching system for further HF etching reaction. *Warning: Hydrofluoric acid (HF) is a highly corrosive liquid and a contact poison to human bodies; extra caution in handling is required.* Schematics of the etching setup and details of the etching chamber are shown in **Figure 13**. The system consists of 2 plastic containers – one with water and the other one with 48% HF solution, 3 mass flow controllers and an etching chamber. The mass flow controllers were all purchased from Omega Engineering, Inc. and the model numbers are: USA – FMA-3704 (for HF carrier gas, range 0 - 100 standard cubic centimeter per minute (sccm)), FMA-5510 (for H_2O carrier gas, range 0 - 200 sccm) and FMA-5510 (for dry N_2, range 0 - 200 sccm). The home built etching chamber consists of a stainless steel tube, a stainless steel sample holder, a heating tape (KH-203/5-P, Omega Engineering, Inc., USA) and a temperature controller (CNi3222-C24, Omega Engineering, Inc., USA). The temperature detector is located inside the aluminum heating block to obtain precise control of the temperature of the tube. The fluctuation of the temperature was less than 0.3 ˚C within the etching period. HF solution was regularly replaced to maintain a consistent output partial pressure of HF. The exhausted gas from the system was absorbed by saturated potassium hydroxide (KOH) solution to remove any HF and then vented to the ambient.

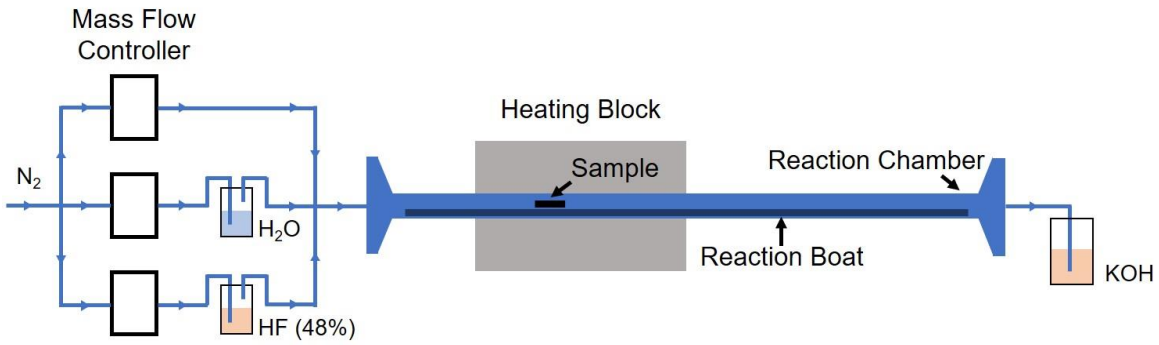

Figure 13. Schematics of the home-built vapor phase HF etching setup.

The SiO_2/Si substrate was placed onto the reaction boat at the marked position and transferred into the heating block (**Figure 13**). The position was selected based on the preliminary results (**2.4.5**), in which multiple positions in the heating block were tested and the one with most consistent outcomes was picked. Vapors of HF and water were supplied by passing N_2 gas through the respective containers so there were totally three streams of N_2 gas in the system – pure N_2 gas, N_2 gas saturated with HF vapor and N_2 gas saturated with water vapor, which were controlled by the three mass flow controllers, respectively. Note that hydrofluoric acid used here was a 48% solution so the N_2 gas stream with HF vapor also contained water vapor. Three streams of gas combined before entering the chamber and went through the reaction chamber continuously. The flow rates of the three streams of N_2 gas carrier determine the partial pressure of each reagent. Based on the previous research (**2.4.4**), the best working condition for the HF etching reaction was [35 °C, N_2 flow rate = 55 sccm, N_2-carried H_2O flow rate = 15 sccm, N_2-carried 48% HF flow rate = 10 sccm, reaction time 20 min] in order to achieve high contrast and high resolution. This condition was used throughout the experiments except otherwise specified.

In a typical HF etching process, after the SiO_2/Si substrate was locked in the reaction chamber, pure N_2 gas stream and N_2 gas with water vapor stream were first introduced into the

chamber for 20 min to achieve equilibrium of water between the substrate surface and the gas flow. N_2 gas carrier for HF vapor was shut off during this preparation process. Then all three streams were introduced together into the reaction chamber for the set reaction time. After 20 min, the N_2 gas carriers for water vapor and HF vapor were immediately shut off. Only high flow rate (*ca.* 180 sccm) of pure N_2 gas was used to clean up any leftover HF on SiO_2/Si substrate and in the reaction system before the substrate was taken out. The sample was washed by water, acetone and then water again (30 s for each step) after reaction and then dried using a N_2 stream. To remove the organic residues on the substrate, the sample was heated in a 400 ˚C furnace in air for 1 hr and rinsed with water for 1 min and then dried using a N_2 stream (**Figure 14**, cleaning step).

2.3.8 Pattern transfer from negative SiO_2/Si substrate to positive PLLA film

Due to the intrinsic accuracy limitation of Atomic Force Microscopy (AFM) technique for scanning negative patterns, PLLA film was used to achieve pattern transfer to positive patterns from the negative-tone patterns on the etched SiO_2/Si substrate. PLLA solution was made by dissolving 3% (w/w) PLLA into dichloromethane. SiO_2/Si substrate, cleaned and heated following the aforesaid procedure, was further cleaned by piranha solution. The substrate was immersed in a newly piranha piranha solution (3/7 (v/v) 30% hydrogen peroxide/ 98% sulfuric acid solution) in a covered glass petri dish on a 50 ˚C heating plate for 30 min. *Warning: Piranha solution is a strong oxidizing reagent and can detonate unexpectedly; extra caution in handling is required.* The substrate was thoroughly washed with water and dried with a N_2 stream. Freshly-cleaned substrate was then fixed onto the spin coater and spin coated by 3% PLLA solution at 4,000 rpm for 30 s. The spin-coating process was repeated three times to achieve an appropriate thickness of film.

PDMS precursor was mixed with curing agent at a 10:1 mass ratio. The prepolymer mixture was vigorously blended by hand for at least 5 minutes and degassed in a vacuum desiccator. The mixture was poured over a piranha solution cleaned prime grade silicon wafer. The wafer with the mixture was placed in the vacuum desiccator to further degas air bubbles. The PDMS prepolymer on the silicon wafer was cured for 1 hr at 60 ˚C in the oven. The thickness of the resulting PDMS film was *ca.* 1-2 mm. The PDMS film, cut into 0.7 cm × 1.0 cm size, served as a supporting layer to help peel off the thin PLLA film from the SiO_2/Si substrate. With the flat side of PDMS film stuck to top surface of PLLA film, 10 μL of water was added between the PLLA film and the SiO_2/Si substrate. The PLLA film was easily separated from SiO_2/Si substrate and the positive features were exposed for analysis (**Figure 14**).

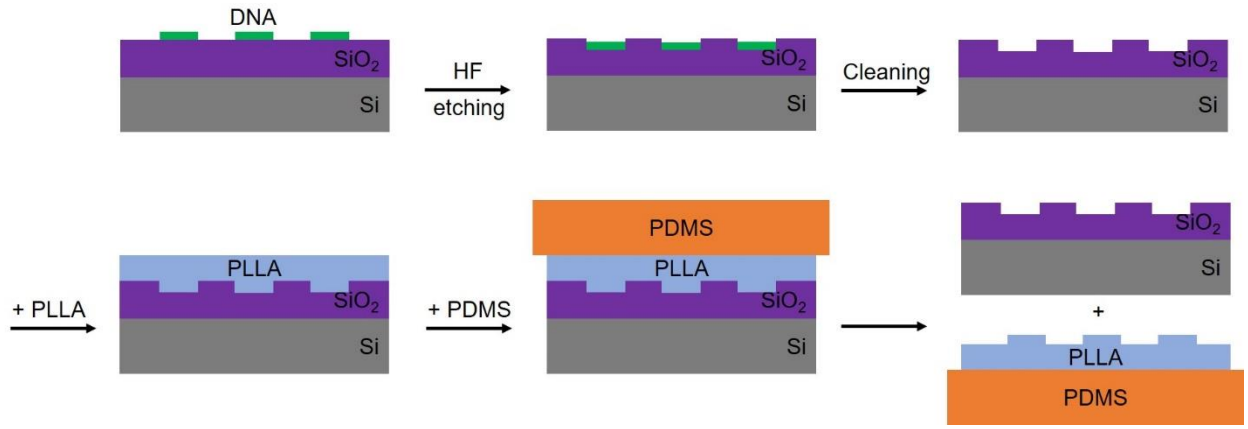

Figure 14. HF etching and PLLA pattern transfer process.

2.3.9 Atomic Force Microscopy (AFM) characterization

Throughout the study, surface morphologies of the samples were monitored using an Asylum MFP-3D Atomic Force Microscope (Oxford Instruments, UK) by AC mode in air with HQ:NSC15/Al BS AFM probes (325 kHz, 40 N/m) purchased from μmasch (NanoAndMore, USA). Images were analyzed by Igor Software (Version 6.3.7.2) equipped with Asylum Research package. Without special annotation, all images were collected at a scan rate of 0.5 Hz and 512 data points per line with the scan size identified by scale bars.

2.3.10 Scanning Electron Microscopy (SEM) characterization

SEM images of the SiO_2/Si substrates were taken by a Zeiss Sigma 500 VP Analytical FE-SEM system (Zeiss, Germany) with 1.00 kV EHT and SE2 detector at University of Pittsburgh Nanoscale Fabrication and Characterization Facility. Resolution of SEM images was set to 1024 × 768. No coating process was performed on the SiO_2/Si substrates in order to maintain the original morphology of the patterns. To reduce the surface charging effect, a different etching condition [35 °C, N_2 flow rate = 70 sccm, N_2-carried H_2O flow rate = 0 sccm, N_2-carried 48% HF flow rate = 10 sccm, reaction time 20 min] was used to prepare the samples for SEM measurements. The SiO_2/Si substrates etched by this condition had shallower negative-tone patterns and less influence from charging effect was observed on the SEM images.

2.4 Results and Discussion

2.4.1 DNA-mediated HF etching of SiO_2

The pattern transfer used in this work is based on the HF vapor etching of SiO_2, which is an autocatalytic reaction catalyzed by H_2O adsorbed on the SiO_2 surface. The overall reaction between the vapor phase HF and the SiO_2 substrate is shown by equation **1**:

$$SiO_2(s) + 4HF(g) \rightarrow SiF_4(g) + 2H_2O(g) \qquad [\mathbf{1}]$$

Different mechanisms have been proposed for this reaction[214-216] and the generally acceptable explanation is that water is a catalyst of the reaction.[217] The reaction is initiated by condensation of HF and H_2O in the gas phase onto the SiO_2 surface and goes through a two-step process (equation **2** and **3**). As more water is produced in the final etching step (equation **3**) than initially consumed in the deprotonation step (equation **2**), this reaction is autocatalytic in nature.

$$6HF + 3H_2O \rightarrow 3HF_2^- + 3H_3O^+ \qquad [\mathbf{2}]$$

$$3HF_2^- + 3H_3O^+ + SiO_2 \rightarrow 2HF + SiF_4 + 5H_2O \qquad [\mathbf{3}]$$

The etching rate of SiO_2 is positively correlated with the amount of water locally adsorbed on the substrate surface. Further, the autocatalytic process will amplify the small difference in the amount of water adsorbed on the surface, increasing the etching selectivity as the etching progresses. In our previous research, we showed that DNA nanostructures could modulate the vapor-phase etching of SiO_2 at the single-molecule level by changing the amount of water adsorbed near itself. We showed that a molecular-scale pattern could be transferred from the DNA nanostructure to the SiO_2 substrate.[188] This pattern transfer method produced negative patterns with sub-10 nm resolution (**Figure 11(b)**)[192] or high vertical contrast (>10 nm, with sub-20 nm resolution).[112] In later studies, other hydrophilic materials, such as inorganic salt (*e.g.*, NaCl),

graphene oxide and protein (*e.g.*, albumin) were all shown to promote HF etching of SiO_2 etching, creating negative-tone patterns on silicon wafer.[193]

DNA origami nanostructure provides numerous sites for site-specific chemical modifications. By introducing chemical functional groups onto DNA origami nanostructures, one can locally change the water-adsorption capability of the DNA nanostructure, therefore locally changing its catalytic activity in the HF-etching reaction. We hypothesize that if such a modified 2D DNA nanostructure is used as the template for HF-etching of SiO_2, 3D nanoscale pattern can be created on the SiO_2 surface after a single step of pattern transfer (**Figure 15**).

To test this hypothesis, we used triangular-shaped DNA origami nanostructure as a model to study the effect of introducing streptavidin on the vertical contrast of DNA-mediated HF-etching of SiO_2. The triangular-shaped DNA origami nanostructure was selected due to its unique structural features. Each triangular-shaped DNA origami nanostructure provides three identical linear sides and a central void. The modification was performed on only one of the three linear sides and its effect on the pattern transfer was assessed by comparing the contrast of pattern transfer of the three sides within the same DNA nanostructure. Streptavidin is a commonly used water-soluble protein in molecular biology, known for its strong and specific non-covalent binding to biotin. We incorporated biotin-modified DNA strands into the DNA nanostructure, allowing site-specific attachment of streptavidin.

The modified DNA nanostructure was used as the template for negative-tone pattern transfer to SiO_2, in which DNA nanostructures promoted the etching of SiO_2.[188] Our previous research has identified the optimum etching conditions,[112] under which the DNA nanostructures created uniform triangular-shaped trenches on the SiO_2 surface. Streptavidin molecules were

expected to increase the adsorption of water vapor, which should locally increase the depth of the negative-tone pattern (**Figure 15**).

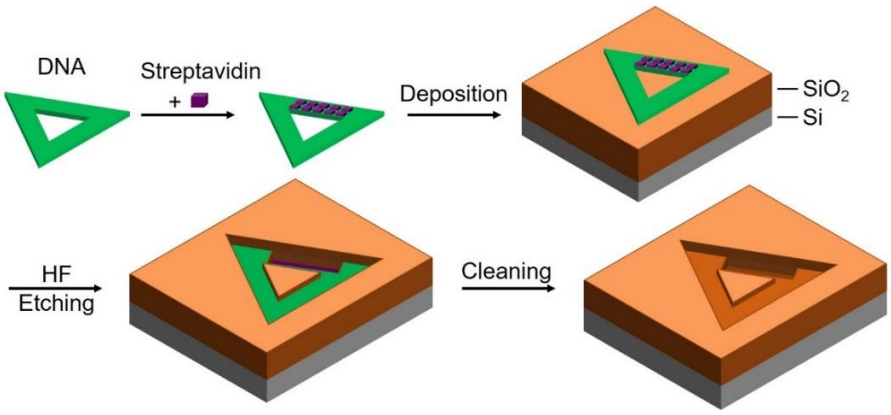

Figure 15. HF etching and pattern transfer process of the DNA nanostructures with streptavidin modification.

2.4.2 Modification of streptavidin onto DNA nanostructures

Triangular-shaped DNA origami nanostructures were synthesized using M13mp18 single stranded phage DNA and 232 short staple strands. On one side of the DNA nanostructure, 21 discrete staple strands were selected and extended to serve as the attaching points for the complementary biotin-modified DNA strands (**2.3.2**). The biotin-modified DNA nanostructures were then mixed with excess streptavidin in buffer solution and finally purified by membrane centrifugal filtration.

Figure 16 compares the AFM images of DNA origami nanostructures without and with modification, presented using two color maps to highlight the topography features. It was observed that with only biotin modifiers (**Figure 16(b)**), the modified DNA nanostructures did not show

significant topography difference compared to their unmodified counterparts (**Figure 16(a)**); in both cases, the three sides showed similar heights. Addition of streptavidin (**Figure 16(c)** before purification and **Figure 16(d)** after purification) altered the topography profiles with one side significantly higher than the other two. Note that the loose round dots in **Figure 16(c)** represent the free streptavidin molecules. **Figure 16(e)** compares the statistical distribution of the heights for different types of DNA origami nanostructures. For each type of DNA nanostructure, 40 structures were randomly selected and three height values were measured for the three sides of each DNA nanostructure. We observed that for the DNA nanostructures with streptavidin modification, the height histogram shows two groups of heights which were significantly different from each other. The height difference between the two groups was about 0.8 nm and the population of the higher group was roughly half of that of the lower group. We conclude that the streptavidin increased the apparent height of the DNA nanostructure by 0.8 nm. **Figure 16(d)** also showed that almost 100% of the analyzed DNA nanostructures had successful streptavidin modification. Note that we did not resolve individual streptavidin on the DNA nanostructure, likely due to the small distance between the modification site (< 10.6 nm) and large size of the dried streptavidin molecule (*ca.* 11.1 nm).[218]

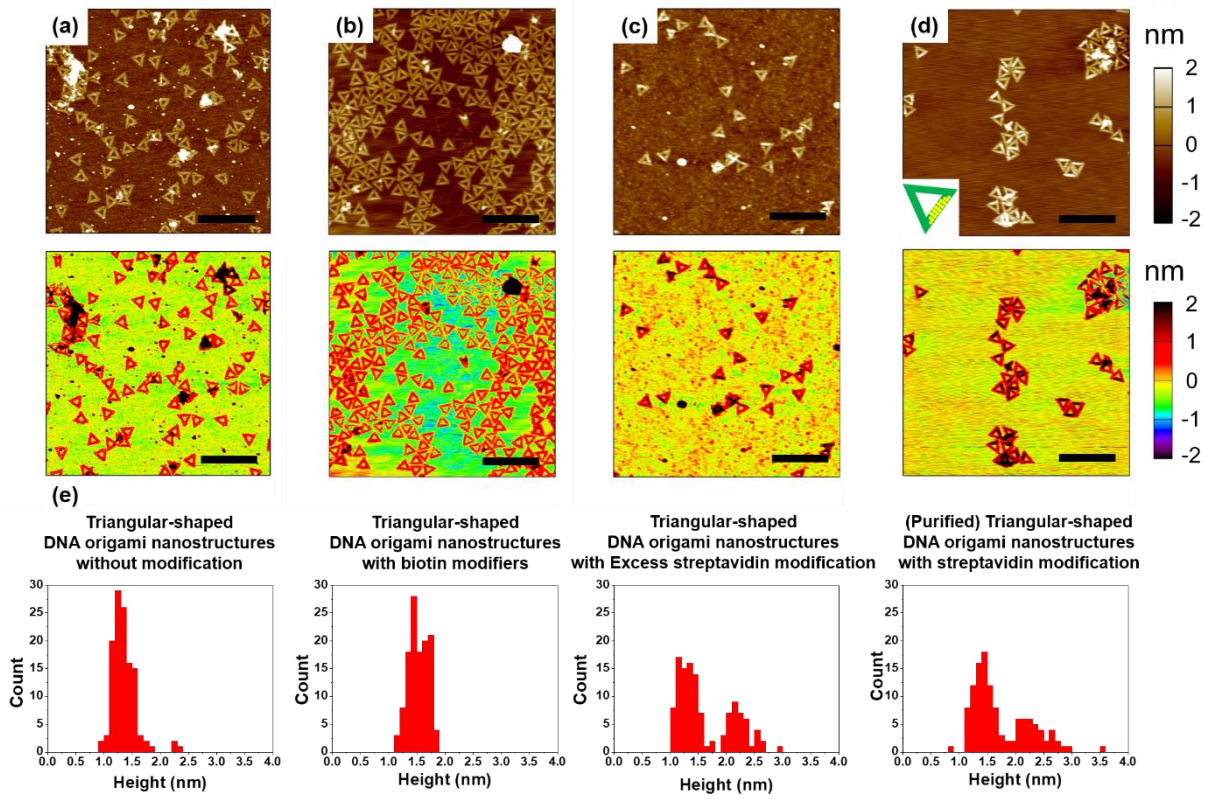

Figure 16. Modification of DNA nanostructure using streptavidin. AFM image of triangular-shaped DNA origami nanostructures (a) without modification, (b) with biotin modifiers, (c) with excess streptavidin modification and (d) with streptavidin modification after purification. The images are shown in two color scales. Scale bars denote 500 nm. Inset of (d) shows the design of streptavidin modification on the DNA nanostructure. (e) Statistical histograms of height distributions of the three linear sides of the DNA nanostructures. The height was measured at the center of the side of the DNA nanostructure.

2.4.3 Calculation of partial pressure of each reagent after mixing in the etching chamber

The containers of water and HF solution and also the tubes to deliver gas into the etching chamber were all stored at room temperature (20-25 °C average). At 20°C, the saturation vapor pressure of H_2O is 2339 Pa.[219] The equilibrium vapor pressure of 48% HF solution is 2666 Pa of HF and 666 Pa of H_2O.[112] From our previous studies, we can assume that N_2 gas got into equilibrium with the liquid phase after bubbling through the containers. The total pressure inside the etching chamber was around 1 atm since the system was balanced with outer atmosphere.

The partial pressure of each vapor inside the chamber was proportional to the flow rate of N_2 through its container. For pure N_2 gas = 55 sccm, N_2 gas with HF vapor = 15 sccm and N_2 gas with water vapor = 10 sccm, the partial pressure was calculated as followed:

H_2O: $p_{H2O} = 15/80 \times 2339 + 10/80 \times 666 = 522$ Pa.

HF: $p_{HF} = 10/80 \times 2666 = 333$ Pa.

For pure N_2 gas = 70 sccm, N_2 gas with HF vapor = 10 sccm and N_2 gas with water vapor = 0 sccm, the partial pressure was calculated as followed:

H_2O: $p_{H2O} = 10/80 \times 666 = 83$ Pa.

HF: $p_{HF} = 10/80 \times 2666 = 333$ Pa.

As expected, when the flow rate of N_2 gas with HF vapor was kept constant, the increase of flow rate of N_2 gas with water vapor will increase the partial pressure of water vapor in the chamber, leading to higher etching rate. If the 333 Pa (2.5 mmHg) HF partial pressure in the etching chamber reaches an equilibrium with the SiO_2/Si substrate surface at 35 °C, an equivalent 25-30% HF solution is condensed on the substrate surface for etching reaction.[220]

2.4.4 Selection of best working condition for HF etching reaction

Our previous research proposed two best working conditions for HF etching reaction to achieve high-resolution, high-contrast pattern transfer. The two conditions were [35 °C, p_{HF} = 333 Pa, p_{H2O} = 658 Pa, reaction time 20 min] and [35 °C, p_{HF} = 333 Pa, p_{H2O} = 1090 Pa, reaction time 20 min].[112] To reduce the surface roughness and to potentially highlight the contrast resulted from the modification effect, we selected the milder condition [35 °C, p_{HF} = 333 Pa, p_{H2O} = 658 Pa, reaction time 20 min] in our experiment. The HF etching setup was rebuilt with new tubing, parts and reagents to eliminate possible residues from previous experiments. At the same time, the line of 2-proponal was eliminated based on the previous results. The partial pressure values were converted into the flow rates in the system for easy operation purpose. Considering that the average room temperature was higher than 20 °C, less amount of water was used to reduce surface roughness. The selected working condition was [35 °C, N_2 flow rate = 55 sccm, N_2-carried H_2O flow rate = 15 sccm, N_2-carried 48% HF flow rate = 10 sccm, reaction time 20 min]. In our follow-up experiments, the selected working condition showed consistent results with high contrast and high level of shape preservation.

2.4.5 Selection of best working position for HF etching reaction

In the HF etching setup, the heating block provided heat through a heating pad wrapped outside the metal cylinder and a millimeter-size temperature sensor was placed between the reaction chamber and the heating block for temperature feedback and control. Due to the fully enclosed design of the reaction chamber and the possible uneven heating from the heating pad, we performed a series of experiments at different positions inside the reaction chamber to determine

the best position for experiment consistency. Four different positions were selected on the reaction boat as shown in **Figure 17**. Here, position #3 indicated the center of the heating block. The position of the temperature sensor was slightly toward upstream (left) side of the chamber from the center position so that two positions were selected on this side. The distance between each two adjacent positions was 1 cm. Position #1, #3, #4 all showed inconsistency throughout the multiple parallel samples prepared (**Figure 18**). Several AFM images showed incomplete shape preservation with the central voids invisible after etching. We attributed this inconsistency to the temperature variation inside the reaction chamber. Position #2 showed the best consistency and was selected for all the experiments (**Figure 19**). We inferred that Position #2 was indeed the closest position of the four on the reaction boat to the temperature sensor so that the 35 °C temperature setting was maintained throughout the experiment.

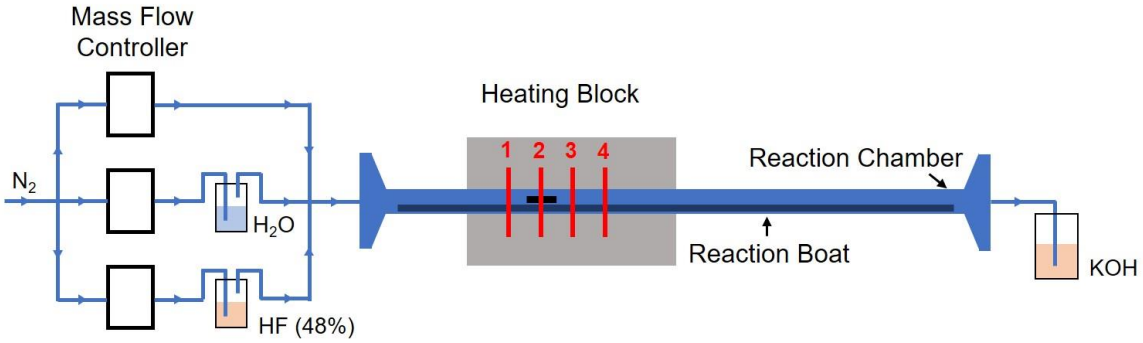

Figure 17. Schematics of the home-built vapor phase HF etching setup and four sample positions.

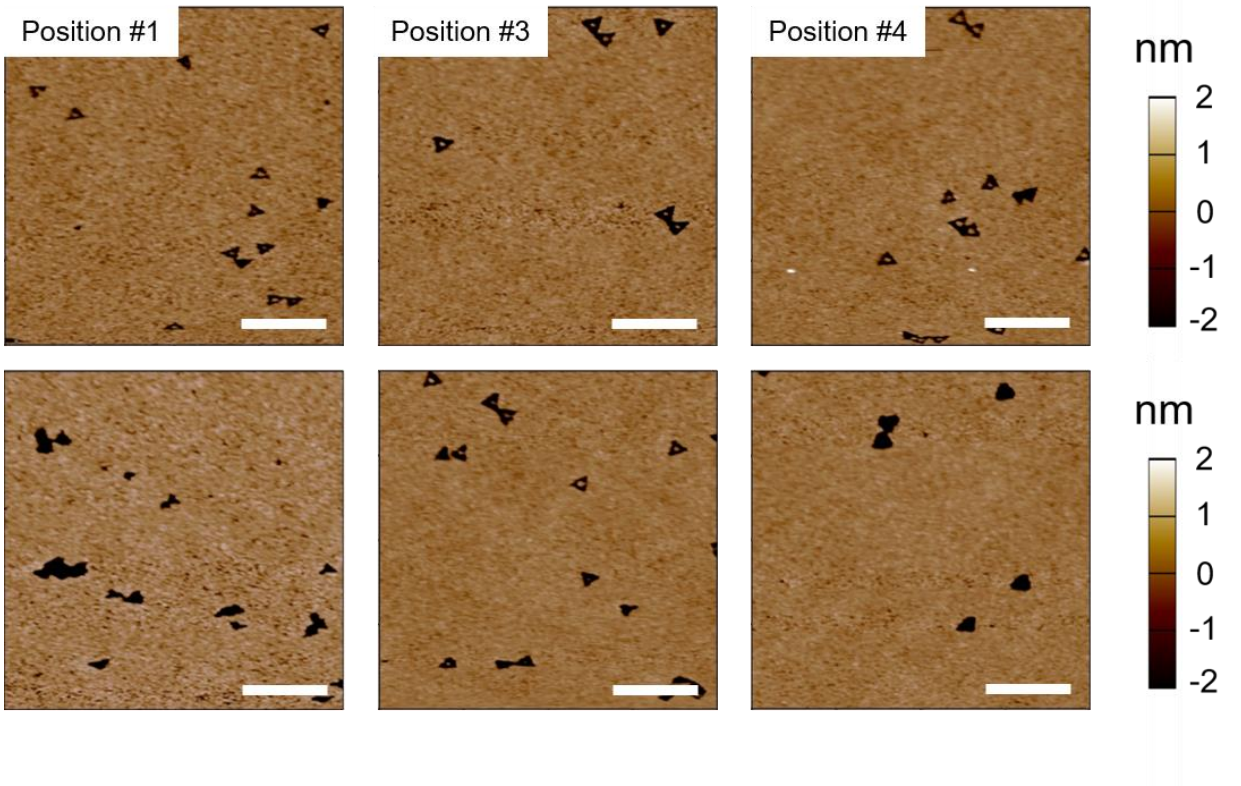

Figure 18. AFM images of etched SiO_2/Si substrates at different positions. Scale bars denote 500 nm.

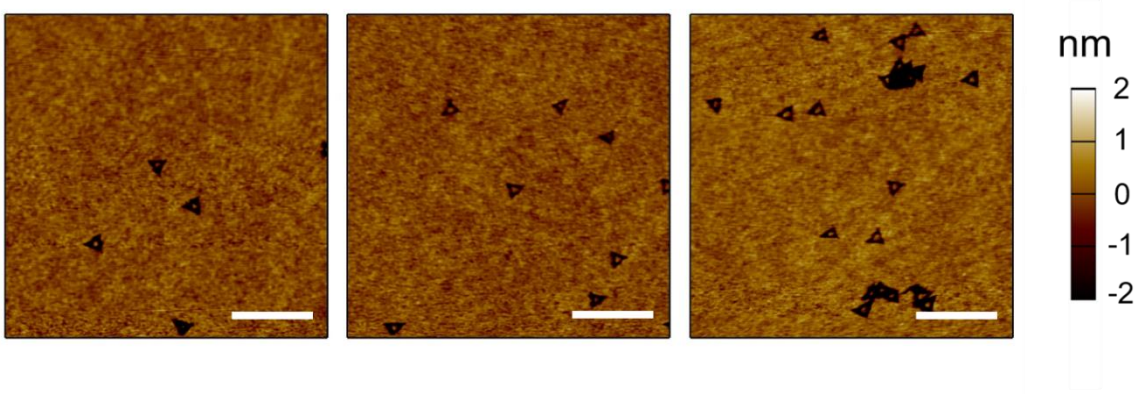

Figure 19. AFM images of etched SiO_2/Si substrates at Position #2 (best position). Scale bars denote 500 nm.

2.4.6 Effect of modification on the depth of the patterns measured directly from negative-tone patterns on SiO_2/Si substrates

SiO_2/Si substrates were deposited with DNA nanostructures, without or with streptavidin modification, and then etched with HF vapor. We followed a previously developed method to quantitatively investigate the enhancement effect of DNA on the HF vapor etching reaction.[112] We analyzed the vertical contrast by measuring the etching depth at the apexes and used the obtained values for comparison between different samples. Here the depths of the linear side centers were also acquired for the triangular patterns. A specific linear side center depth was measured by drawing a cross section across the opposite apex and the center and reading the peak value from the profile.

We found that under our experimental condition, streptavidin modified DNA nanostructures (**Figure 20(c)-(d)**) showed similar behaviors in the HF vapor etching process compared to the DNA nanostructures without modification (**Figure 20(a)-(b)**). Both unmodified and streptavidin-modified DNA nanostructures produced negative-tone patterns on SiO_2. Box plots (**Figure 20(e)**) showed the statistical comparison between different groups of depth data. For the SiO_2/Si substrates etched by each type of DNA nanostructures, 40 negative-tone triangular patterns were randomly selected and analyzed. In each box plot, the hollow square indicates the average of the data and the box defines the 25% percentile and 75% percentile positions of the data. The whisker range represents the section that is within one standard deviation higher and lower than the average, beyond which the outliers are plotted. We observed large variation of depth values (ranged from 2 to 20 nm) between multiple triangular patterns on the samples prepared following identical steps, making it difficult to investigate the effect of modifications. The measured depths of triangular patterns without and with streptavidin modification on the DNA

nanostructures did not show significant difference when the negative-tone patterns were directly measured by AFM.

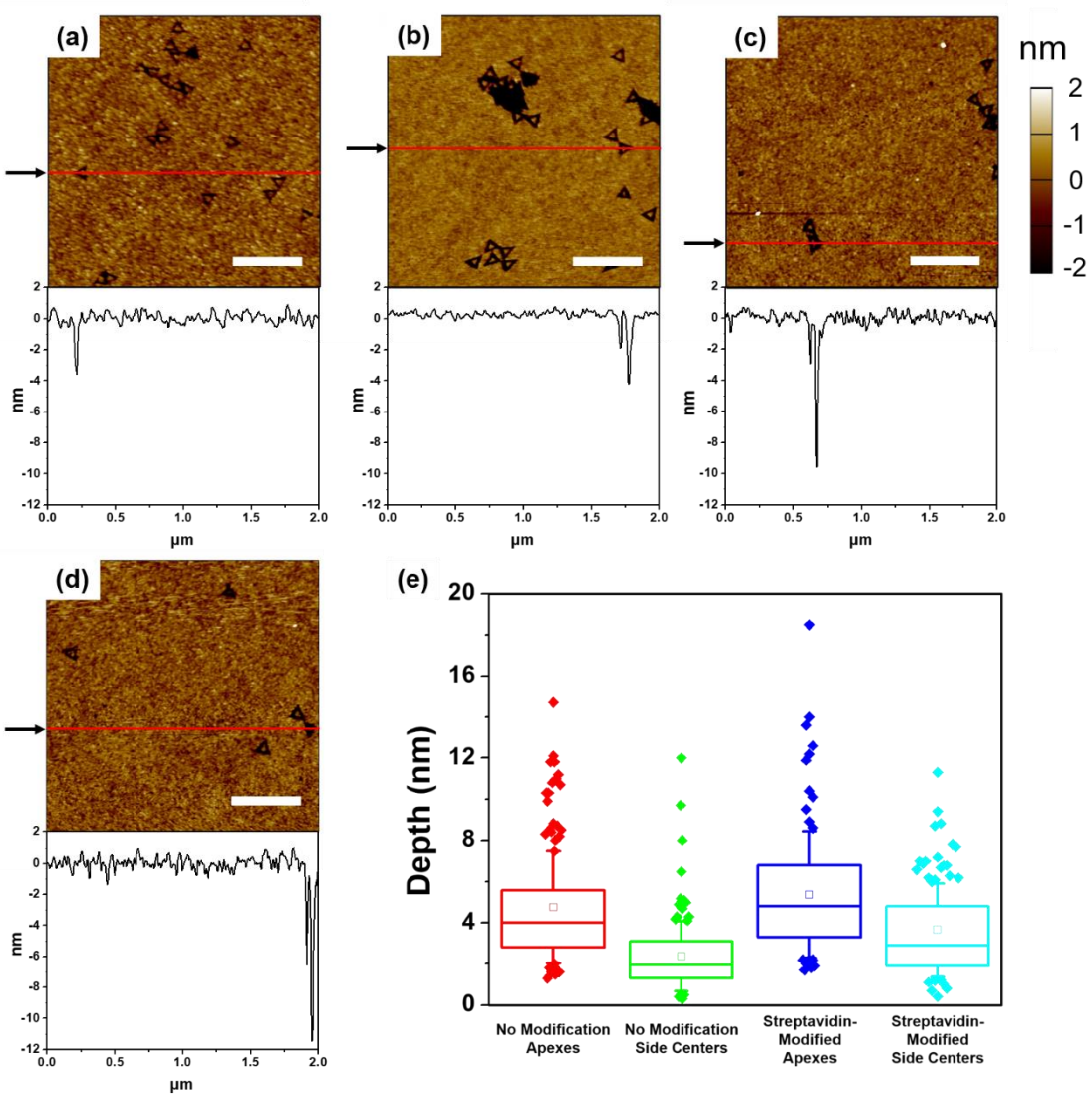

Figure 20. AFM images and corresponding cross sections of HF etched SiO_2/Si substrates deposited with: (a) and (b) triangular-shaped DNA origami nanostructures without modification; (c) and (d) triangular-shaped DNA origami nanostructures with streptavidin modification. Scale bars denote 500 nm. (e) Box plots of etched depth distribution at the apexes and the linear side centers for HF etched SiO_2/Si substrates deposited with two different types of DNA nanostructures. In each set of box plot, the hollow square represents the average; the box represents the 25% percentile to 75% percentile range; the whiskers represent one standard deviation lower and higher than the average value; the solid dots represent outliers outside the whiskers range.

The overall observations from the negative-tone pattern AFM images were consistent with previous trends. Within one triangular pattern, it was generally observed that the depths at the apexes and the linear side centers were different with the apexes generally being deeper (**Figure 20**). It was well known in our previous research and explained by the fact that the narrow width provided limited sampling points in AFM scanning and thus might not reflect the true topography.[112] It was not determined whether there was intrinsic difference in the topography depths at the apexes and the linear side centers in the triangular patterns. However, this trend was not always true when the depth values were compared across different triangular patterns. One piece of evidence was that in **Figure 20(e)**, we could not conclude a significant difference between the depth values at the apexes and at the linear side centers. Also, during the experiments, the depth of one particular triangular trench decreased dramatically as the AFM probe finished more scans. The measured topography profiles were not only related to the true etching behavior of the surfaces but also related to the quality and status of AFM probes. We believe that AFM artifacts, due to the limitation of AFM probe sharpness, made it challenging to reproducibly measure the true depth of the negative-tone nanoscale patterns. The depth of the patterns was underestimated due to the very narrow width, which prevented the AFM tip to probe the bottom of the trench. AFM artifacts contributed to the large variations in the measurements and made it impossible to investigate the effect of streptavidin modification using the negative-tone pattern AFM images.

2.4.7 AFM artifacts and influence on negative pattern imaging

When an AFM probe moves over a hole (negative pattern) on a surface, it may not reach the bottom of the hole if the width of the probe is larger than the diameter of the hole. The hole appears smaller and shallower due to this AFM artifacts.[221] The AFM artifacts have strong

influence to the pattern topography when the hole size is small along the scan direction. To prove that the variation in our negative-tone AFM images was due to the AFM artifacts, we performed AFM scanning at the same location in different scan directions (0°, 120°, 240°) and compared the topography images. As a triangular shaped pattern, the overall appearance of the pattern does not change for the three selected scan directions. However, the position of a specific linear side of the triangular pattern rotates as demonstrated in **Figure 21**. Three examples were selected in **Figure 22** for comparison purpose. Arrows of one specific color indicate the same linear side of a specific triangular pattern in three AFM images. The depth values of the linear side centers were measured and recorded in **Table 2**. We observed that the deepest linear side of the three in a specific triangular pattern was always the one that had the smallest angle with scan direction (*i.e.*, the *x* axis), regardless of the intrinsic depth of the pattern. The three examples here were randomly selected and represented the majority of the triangular patterns created by the HF etching reaction. AFM artifacts contributed to the variations of measured depth values dramatically. We also noticed that with one AFM probe, the negative patterns turned shallower as the number of scans increased, suggesting that the sharpness of the AFM probe decreases with more scans.

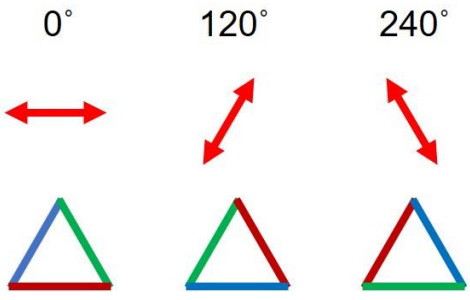

Figure 21. Demonstration of topography AFM images of a triangular pattern with different scan directions.

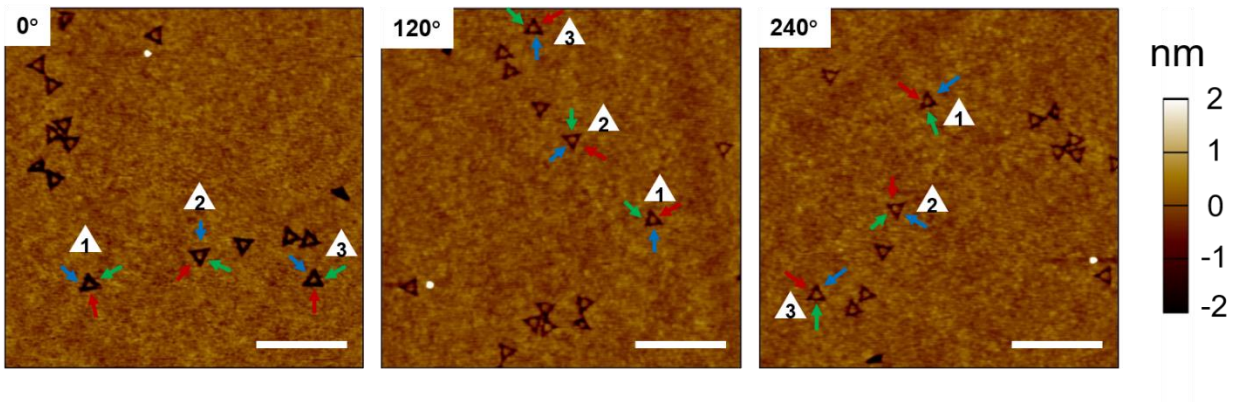

Figure 22. AFM images of a same piece of SiO_2/Si substrate at the same location using different scan directions. Marks and arrows indicate the same triangular patterns across the three images. Scale bars denote 500 nm.

Table 2. Depth values of triangular patterns in **Figure 22**. (Unit: nm)

Scan Direction	0°			120°			240°		
Linear Side	Red	Green	Blue	Red	Green	Blue	Red	Green	Blue
1	5.89	4.59	2.61	0.89	1.22	1.26	0.61	1.6	1.02
2	2.33	1.76	3.63	0.6	0.8	0.71	1.38	0.84	0.68
3	6.63	4.34	3.35	1.02	1.01	1.68	0.54	1.19	0.63

2.4.8 Pattern transfer from negative-tone SiO_2/Si surface to positive-tone PLLA film

In order to accurately measure the topography of the transferred pattern, the negative patterns created on the SiO_2/Si surface were transferred through a polymer imprinting technique onto a PLLA film (**Figure 23**).[189] In the imprinting process, PLLA was dissolved into dichloromethane and spin coated onto the SiO_2/Si surface, filling the negative trenches on the SiO_2/Si surface. Then the PLLA film was peeled off and the inverted positive patterns were imaged by AFM. By scanning the positive patterns and measuring the heights of the triangular patterns on

PLLA films, we can determine the depth of the negative triangular patterns on SiO_2/Si samples. **Figure 24(a)** shows that the triangular patterns were successfully transferred onto PLLA films through the polymer imprinting process. Following the similar methods used to analyze the negative-tone patterns, we obtained the height values of the triangular patterns at the apexes and also at the linear side centers. Based on the measurements of 20 randomly selected positive-tone triangular patterns, the overall average height was 28.1 nm (**Figure 24(d)**), which is approximately 5 times greater than the average depth of triangular trenches measured from the negative pattern samples (**Figure 20**). There was no significant difference between the measured height at the apexes and at the linear sides of the triangular patterns (**Figure 24(d)**). The measured height values also showed much less variation, indicating that the etching process produced uniform contrast. The triangular-shaped DNA nanostructure was made by folding the long scaffold DNA strand using hundreds of staple strands. With the only exception of the 97-nucleotide loop structure on one side (which also partly forms double-stranded hairpin structure), the triangular-shaped DNA origami nanostructure was composed of a single-layer DNA double helix. The design of the triangular-shaped DNA nanostructure has several 5 nm voids at the apexes.[44] However, the height of the apex (28.6 nm) was slightly higher than that of the middle of the edge (27.5 nm), indicating a negligible effect of the small voids on the apexes and that the contrast of the pattern transfer is only related to the local density of DNA materials (or other materials that can alter the local wettability).

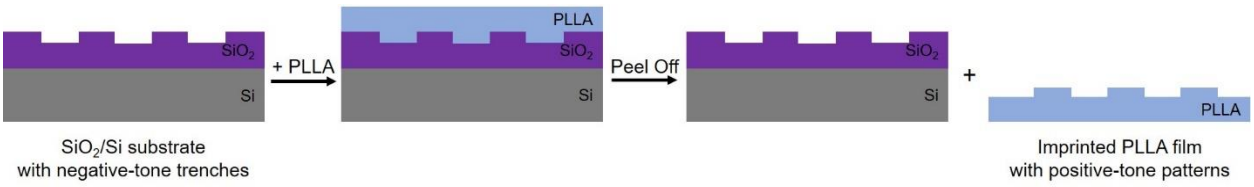

Figure 23. Fabrication of positive-tone patterned PLLA film using negative-tone patterned SiO_2/Si substrate as template.

Next, we studied the effect of streptavidin modification on the pattern transfer process. Following the same polymer imprinting process, the negative trenches obtained using two different types of modified DNA templates (with biotin modifiers only and with streptavidin modification) were converted into positive-tone patterns on PLLA films. AFM images were acquired and analyzed, as shown in **Figure 24(b)-(c)**. The triangular patterns obtained using the biotin-modified DNA nanostructures were very similar to those obtained using unmodified DNA nanostructures. The attachment of biotin modifiers onto the DNA nanostructures altered the DNA density of the local edge but the difference was small (less than 15% of a monolayer). Presumably, such a small change in the density of DNA does not induces a significant change in the etching rate. However, the triangular patterns obtained using streptavidin-modified DNA samples (**Figure 24(c)**) always showed uneven heights among the three linear sides. In each triangular pattern, there was one side significantly higher than the other two, which had similar heights. Note that because the orientation of the triangular-shaped DNA nanostructures was not controlled during the deposition, the higher linear side could be any one of the three.

To statistically evaluate the effect of modification on the etching process, we measured 20 triangular patterns (*i.e.*, 60 edge height values) obtained with each type of templates (unmodified, biotin-modified and streptavidin-modified). The height data were divided into two groups, in which one group contained the highest values of the three edge measurements from the same

triangular pattern and the other group contained the two lower values. We found that for the patterns obtained from the unmodified DNA templates, there was no statistical difference between the two groups of data. However, a significant difference was observed for the patterns developed using the streptavidin-modified DNA templates (**Figure 24(e)**, left panel, red bars). The average height of the modified edges was 34.2 nm, 25% higher than the average height of the edges without modification (27.5 nm). The patterns obtained using the biotin-modified templates showed intermediate results in which a slight enhancement effect could be observed but such difference was not statistically significant.

Considering that the etching process might not be uniform across the entire SiO_2/Si substrate surface and across different substrates, we also normalized the three height measurements of each triangular pattern with respect to the smallest value of the three. This process removed any potential heterogeneity in the pattern transfer across different regions of the wafer. The normalized heights were shown in **Figure 24(e)** in blue bars (right panel). With this approach, the average normalized height was 1.44, 35% higher than that from the patterns without modification (1.07). These data indicate that the streptavidin modification significantly and locally altered the rate of HF etching, creating 35% deeper negative trenches. This result is consistent with our hypothesis that streptavidin increases the local concentration of surface-adsorbed water and hence increasing the contrast of pattern transfer.

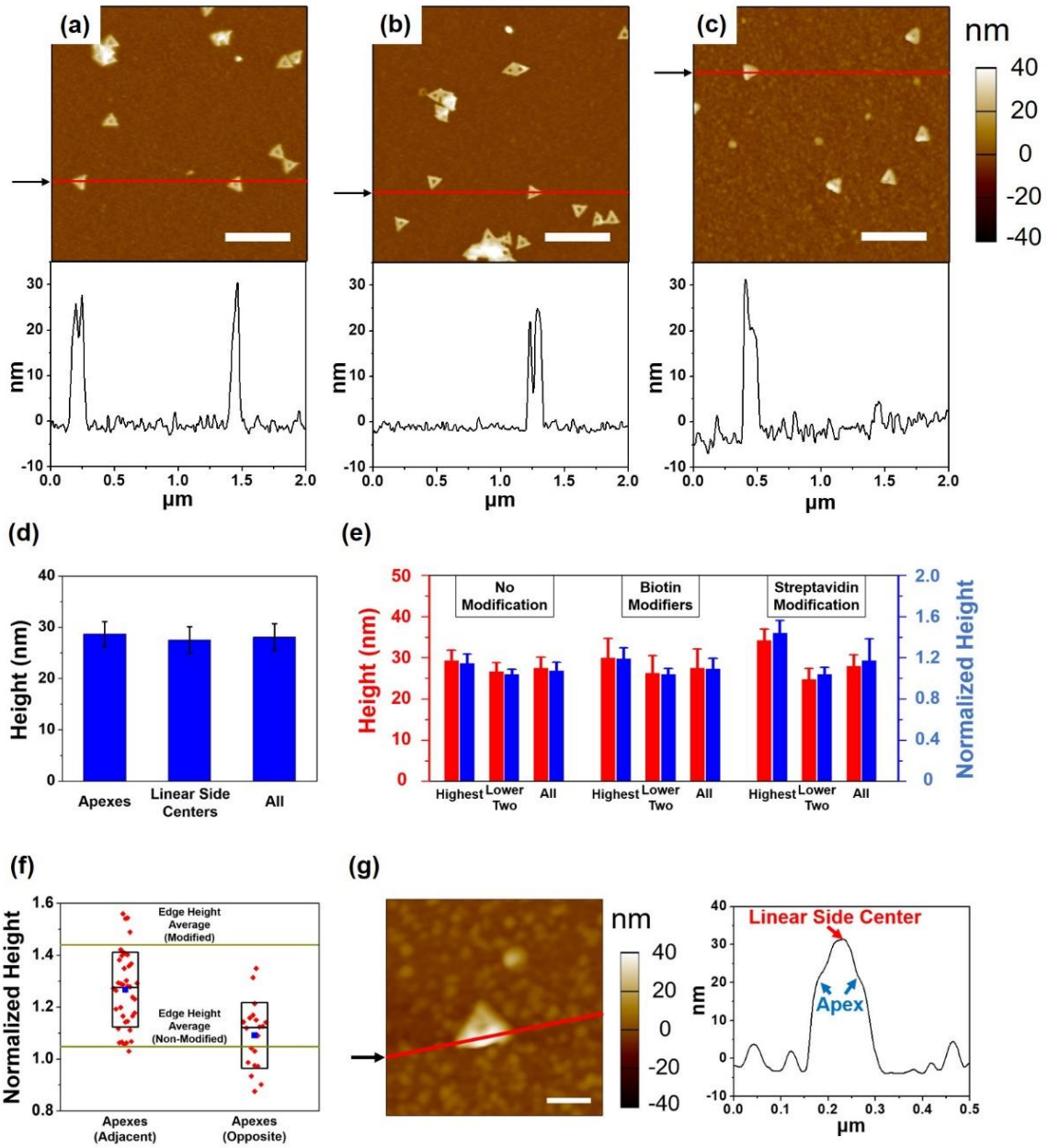

Figure 24. Analysis of positive-tone triangular patterns on PLLA films. AFM images and corresponding cross sections of transferred PLLA films from HF etched SiO_2/Si substrates deposited with: (a) triangular-shaped DNA nanostructures without modification; (b) triangular-shaped DNA nanostructures with only biotin modifiers; (c) triangular-shaped DNA nanostructures with streptavidin modification. Red horizontal lines indicate where the cross sections were determined. Scale bars denote 500 nm. (d) Average height values of the triangular patterns at the apexes and the linear side centers. The data were measured from patterns created by unmodified DNA nanostructures. Error bars represent the standard deviations of the data sets. (e) Height (left

panel) and normalized height (right panel) of the patterns produced by three different types of DNA nanostructures. For each type of triangular pattern, the highest value of the three linear sides was classified into one group while the other lower two values were classified into the other group. Error bars represent the standard deviations of the data sets. (f) Box plots of apex height values for patterns created by streptavidin-modified DNA nanostructures. In each box plot, the blue square represents the average and the box represents the standard deviation range of the data. All data points are plotted. The yellow lines represent the average normalized height values for edges without and with modification. (g) AFM image and corresponding cross section of a positive-tone triangular pattern on PLLA film along its modified linear side. Red line indicates where the cross section was determined. Scale bar denotes 100 nm.

An important question is how localized the effect of streptavidin on the contrast is. To answer this question, we also performed two more sets of data analysis. We first investigated how far the effect of modification could spread. We modified 21 discrete sites on the DNA nanostructure to attach streptavidin molecules. The distance between each two adjacent modification sites is approximately 4.6 nm vertically and 10.6 nm horizontally, with respect to the modified edge. Considering that streptavidin molecules were attached to the DNA origami nanostructures via a 20-bp long free DNA strand and also a hydrocarbon chain spacer, the freedom of movement for the streptavidin molecules on the surface is greater than 6 nm. With such structural freedom, the streptavidin molecules can potentially cover the entire surface of the modified linear side and the effect of individual streptavidin cannot be resolved after the etching process. Indeed, from our AFM images (**Figure 24(c)**), we didn't observe individual holes on the linear side of the triangular-shaped patterns created from modified DNA nanostructure (high resolution AFM image in **Figure 25**). Instead, the overall etching behavior on the entire linear side was homogeneous.

Next, we analyzed the heights of the apexes of the triangular patterns. We found that the apexes adjacent to the modified linear sides were generally higher than the one opposite to the modified linear side (**Figure 24(f)**). However, the average height of the adjacent apexes was still lower than the modified linear side centers. **Figure 24(g)** shows a cross section along the modified linear side of a triangular pattern, where a clear height difference could be observed between the apexes (unmodified) and the middle portion of the side (modified). This outcome was expected because all the streptavidin molecules were modified within the middle portion of the side of the triangle, with a minimum 10 nm distance from the apexes. This data shows that the effect of modification to the surface wettability is localized and can be controlled to the 10s of nm scale.

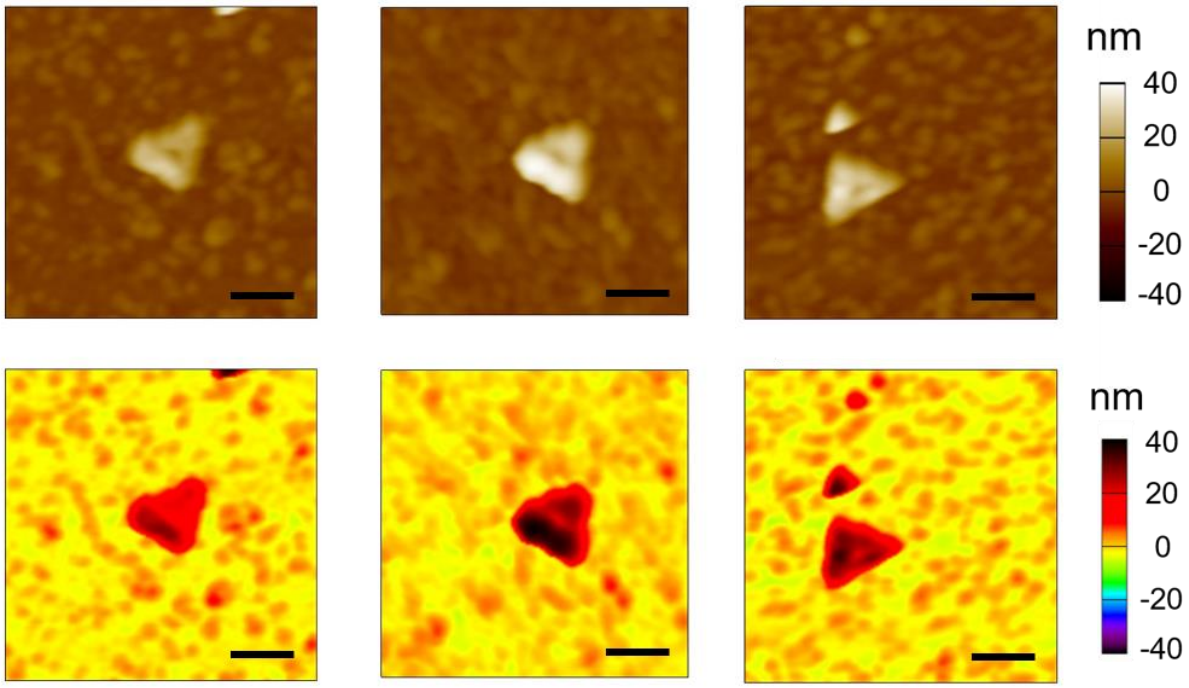

Figure 25. High resolution AFM images of positive triangular-shaped patterns on PLLA film. Top row images are in mud color map and the corresponding bottom row images are in spectrum black color map. Scale bars denote 100 nm.

2.4.9 Using AFM to measure the widths of the transferred triangular patterns

We measured the widths of the transferred patterns (both on SiO_2/Si and PLLA). A cross section was drawn through the linear side center and the opposite apex and the peak curve of the linear side was fit by Gaussian fitting. The FWHM (full width at half maximum) reading from the fitting curve was defined as the width of the linear side. For the positive triangular patterns on PLLA film, we also measured the central width of the linear sides of the triangular patterns following the same procedure. It was observed that the width value of the positive triangular pattern was significantly larger than that of the negative patterns on the SiO_2/Si substrate (**Figure**

26). This observation was expected and also indicated that the AFM artifact led to remarkable errors when scanning the negative patterns. At the same time, similar to the artifacts observed in the AFM images of negative patterns, the positive patterns were also affected by the tip-sample convolution effect. The boundary between the peak of the apex and the peak of the linear side center was vague in the cross section profile. With the width underestimated in a negative pattern, AFM could also overestimate the width in a positive pattern in a similar way. Another technique was required to fully understand the width change in the etching process due to the modification of streptavidin molecules.

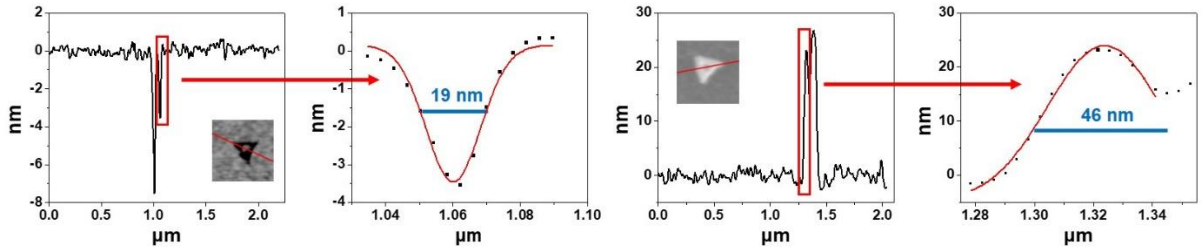

Figure 26. Comparison of pattern width between negative-tone pattern on SiO_2/Si substrate and positive-tone pattern on PLLA film.

2.4.10 SEM images of SiO_2/Si substrates etched with a different working condition

We found that the streptavidin modification did not decrease the resolution of the pattern transfer. AFM has limited accuracy in measuring width of patterns due to the tip-sample convolution effect. To obtain accurate measurement of the resolution, we used scanning electron microscopy (SEM) to image the negative-tone patterns on the SiO_2/Si substrates. To reduce the surface charging effect, a milder etching condition was used to prepare the samples for SEM

measurements. **Figure 27** presents two SEM images of SiO_2/Si substrates etched with the previous best working conditions [35 °C, N_2 flow rate = 55 sccm, N_2-carried H_2O flow rate = 15 sccm, N_2-carried 48% HF flow rate = 10 sccm, reaction time 20 min]. The charging effect significantly affected the image quality to create surrounding artifacts around the true triangular patterns and the measurement of width values from those images was difficult.

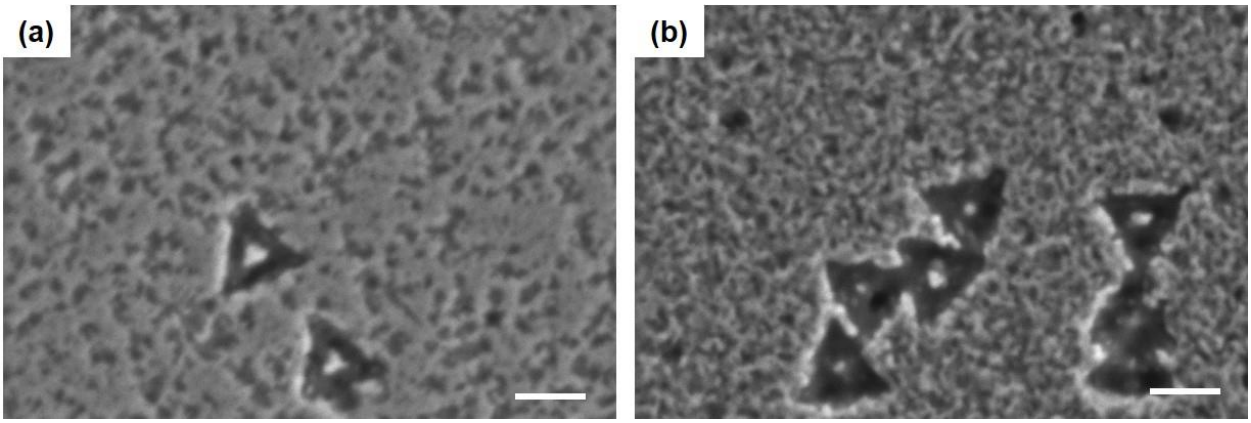

Figure 27. SEM images of SiO_2/Si substrates etched with the previous best working conditions [35 °C, N_2 flow rate = 55 sccm, N_2-carried H_2O flow rate = 15 sccm, N_2-carried 48% HF flow rate = 10 sccm, reaction time 20 min]. The substrates were deposited with different DNA templates: (a) Triangular-shaped DNA origami nanostructure without modification; (b) Triangular-shaped DNA origami nanostructure with streptavidin modification. Scale bars denote 100 nm.

2.4.11 Effect of modification on the width of the patterns

We used scanning electron microscopy (SEM) to image the negative-tone patterns on the SiO_2/Si substrates created by different DNA nanostructure templates. Two different methods were used to measure the three linear side width values of a randomly selected triangular pattern from an SEM image (**Figure 28**). To measure the width value of a specific linear side, a control line

was drawn through the opposite apex and the linear side center. This control line was perpendicular to the linear side of interest. In the first method, the grey value profile of the control line could be acquired. A Gaussian fitting was performed and the width value was defined as full FWHM of the peak (**Figure 29**). In the second method, the width was read manually by selecting the two cross points between the linear side and the perpendicular control line and measuring the distance between them (**Figure 30**).

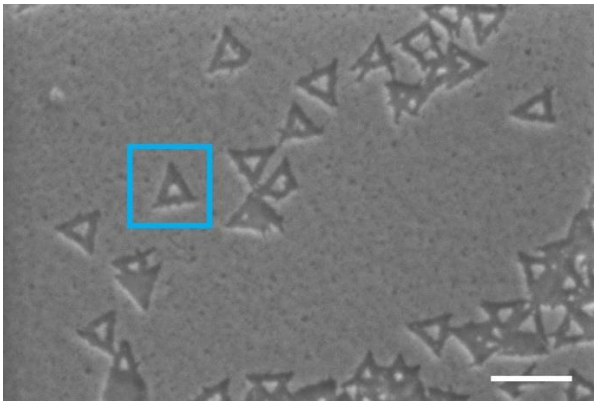

Figure 28. A randomly selected triangular pattern on an SEM image of HF etched SiO_2/Si substrate for comparison between different width analysis methods. Scale bar denotes 200 nm.

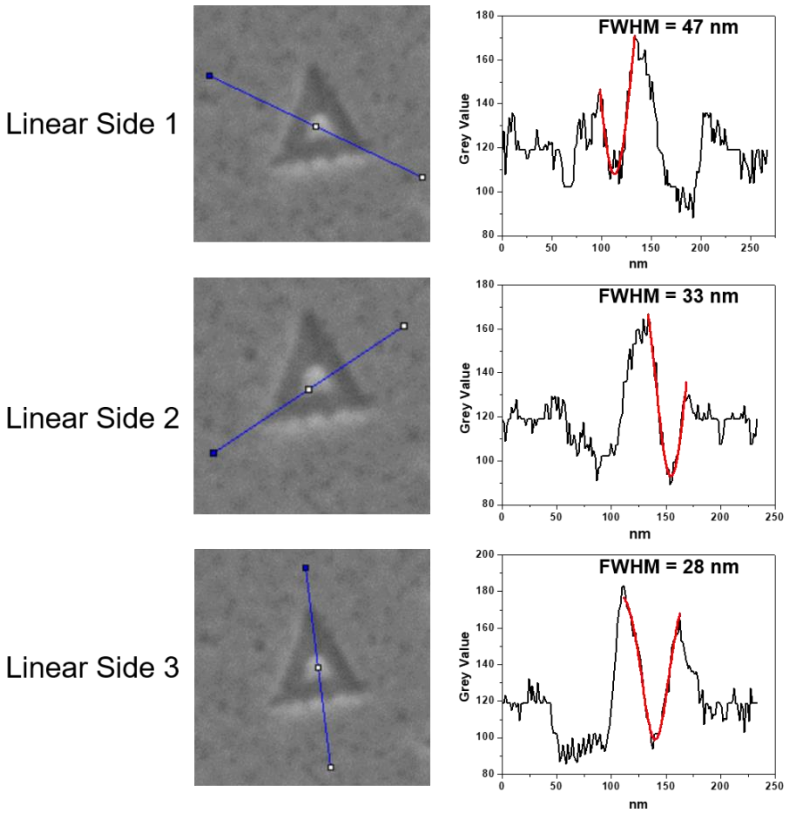

Figure 29. Width values of a randomly selected triangular pattern determined by Gaussian fitting of grey value profiles and measurements of FWHM.

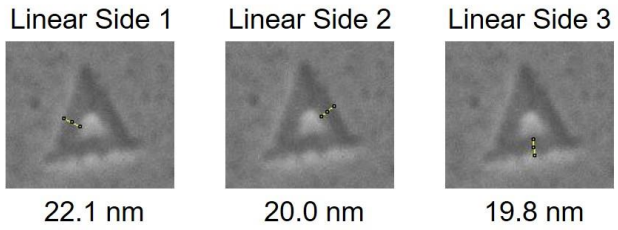

Figure 30. Width values of a randomly selected triangular pattern read directly from SEM image.

The width values read by the second method (**Figure 30**) were at least 30% shorter than the FWHM values (**Figure 29**). We evaluated the grey value curves in Figure **29** and discovered one phenomenon that the area around the triangular patterns were brighter than the bare SiO_2/Si substrate background baselines on the SEM images (**Figure 31**). We attributed this to the charging effect on the non-conductive sample surface, in this case, the SiO_2 oxide layer. At the border lines of the triangular pattern, vertical SiO_2 surface was exposed to the electrons and the charging effect was more severe. This artifact leads to an overestimate of the peak height and FWHM of the Gaussian fitting. We believe that the width values directly read from SEM images were more accurate because the borderlines between the triangular-shaped patterns were clear on the SEM images. This method was used to generate the statistical data below.

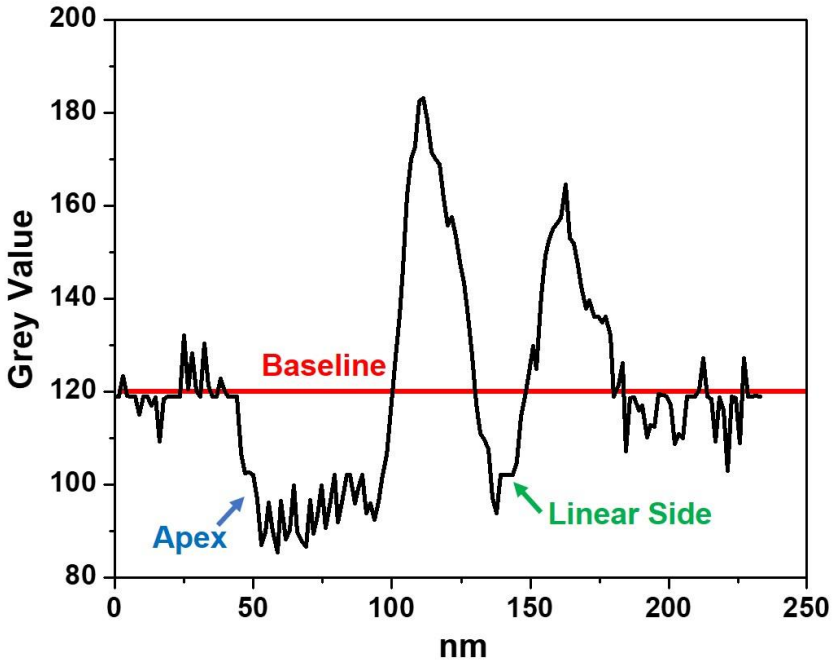

Figure 31. Influence of charging effect on the measurement of FWHM.

In **Figure 32(c)**, we show the statistical results obtained from 20 triangular patterns for two types of DNA nanostructure templates. The patterns obtained from unmodified templates showed an average width of 22 nm with a 20% variation. The average width is similar to the theoretical width of the triangular-shaped DNA nanostructure (20.6 nm).

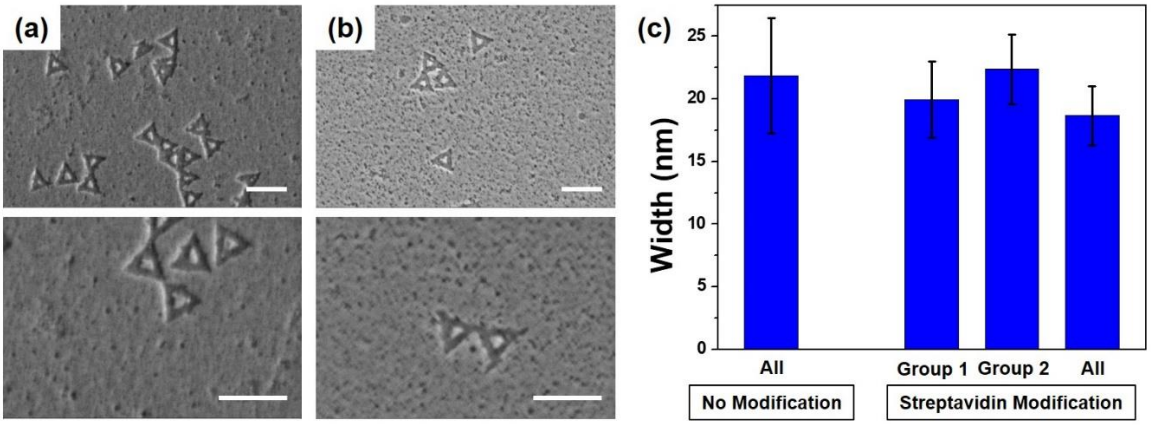

Figure 32. Analysis of edge widths of negative-tone triangular patterns on SiO_2/Si substrates by SEM. SEM images of HF etched SiO_2/Si substrates deposited with (a) unmodified DNA nanostructures and (b) streptavidin-modified DNA nanostructures. Scale bars denote 200 nm. (c) Column plot width comparison between patterns from different types of DNA nanostructures. For a specific triangular pattern, the highest width value of three linear sides was classified into Group 1 while the other two values were classified into Group 2. Error bars represent the standard deviations of the data sets.

For the triangular-shaped patterns created by the streptavidin-modified DNA nanostructures, the three width values from each pattern were again divided into two groups, with the widest in Group 1 and the other two in Group 2. However, the two groups did not show significant difference as in the case of height measurement (**Figure 32(e)**). In addition, the width values from the modified DNA nanostructures (20 nm in average) were not significantly different

from the ones without modification. From the above observation, we conclude that the streptavidin modification significantly increased the depth of the transferred pattern without increasing the width.

2.4.12 Observation of 'tail' structures from negative-tone triangular patterns

An interesting observation from the SEM images was related to the small 97-nucleotide loop on one side of the triangular DNA origami nanostructure. Evidence of the negative pattern etched by the loop was previously observed under AFM with limited resolution. The small 'tail' was only observed in AFM images in several cases with 2.0 ± 0.4 nm in depth and 7 ± 1 nm in length.[112] Here we have consistently observed the SiO_2 trenches patterned by the loop. Using the unmodified DNA template, about 65% of the triangular patterns were observed with small 'tails' at the center of only one linear side (**Figure 33**). The width of these 'tails' was no more than 6 nm, limited by the resolution of SEM due to the charging effect. This observation indicates that our method can be potentially used for pattern transfer from a single DNA strand with ultra-high resolution of as low as sub-10 nm.

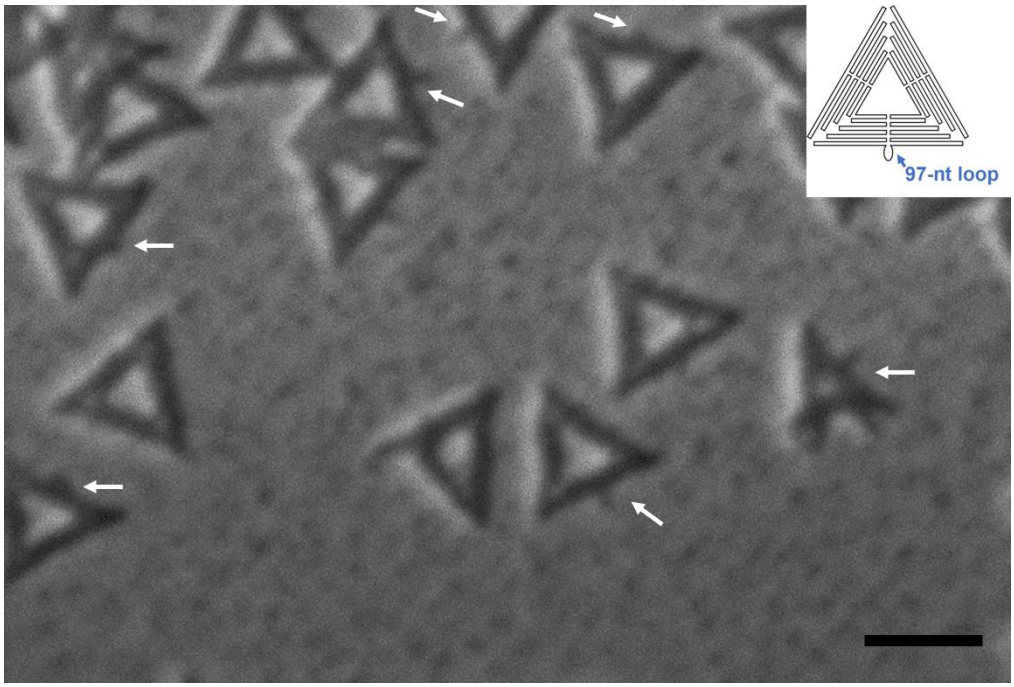

Figure 33. SEM images of triangular-shaped trenched on SiO_2/Si substrate. Arrows indicate the 'tails' created by the loop structure in the DNA origami nanostructures. Scale bar denotes 100 nm. Inset shows the 97-nucleotide loop structure of triangular-shaped DNA nanostructure.

2.5 Conclusion

We have studied the effect of chemical modification of DNA nanostructures on the nanoscale pattern transfer using HF etching of SiO_2. We attached streptavidin molecules onto one side of the triangular-shaped DNA nanostructures. The unmodified DNA templates produce negative-tone patterns of *ca.* 27 nm in depth and *ca.* 22 nm in width. We found that streptavidin locally promotes the HF etching reaction, increasing vertical contrast of the transferred pattern by 35% without noticeable increase in the width. The effect is consistent with the idea that hydrophilic molecules locally increase the HF-etching reaction rate by increasing surface-adsorbed water. Given the many different kinds of modifications that can be applied to DNA nanostructures, our result suggests that complex 3D patterns can be prepared by using a modified 2D DNA template in a single pattern transfer step. The knowledge obtained from this study highlight the potential of applying DNA nanostructures to wider nanofabrication applications, with the advantages of low cost, high contrast, and high resolution.

3.0 HF-Induced DNA Damage during Negative-Tone Pattern Transfer Process from DNA Nanostructures to SiO_2

3.1 Chapter Preface

Materials contained in this chapter are in preparation for publication as a research article.

List of Authors: Anqin Xu and Haitao Liu

Author Contributions: A.X. and H.L. designed and directed the experiments. A.X. conducted the experiments. A.X. and H.L. discussed the results and wrote the manuscript.

3.2 Introduction

The development of DNA nanotechnology has made it possible to construct arbitrary-shaped 2D or 3D DNA nanostructures.[3, 5-11, 14, 29-32, 37, 39, 206-207] Scaffolded DNA origami nanostructures, since their invention in 2006,[44] opened up a new field of bottom-up nanofabrication. With the advantages of high resolution and relatively low cost, DNA nanostructures have been widely used as nanoscale lithography templates in nanofabrication of metals,[88, 182-184] semiconductors,[186, 188] carbon materials[84, 190, 195, 208] and polymers.[189, 191] However, the stability of DNA nanostructures in the harsh chemical conditions used for pattern transfer methods has always been a concern.

In 2011, our group reported a nanoscale negative-tone pattern transfer method from DNA nanostructure to SiO_2 **(1.4.4)**.[188] The method could reproducibly produce with sub-10 nm resolution (**Figure 11(b)**)[192] or high vertical contrast (>10 nm, with sub-20 nm resolution).[112] Recent progress also indicated that complex 3D patterns can be prepared by using a modified 2D DNA template in a single pattern transfer step (**Chapter 2**).

Although our previous studies established a promising approach for high resolution, high contrast and high complexity pattern transfer from DNA nanostructures to SiO_2. One important scientific question was left unsolved about the reusability of DNA nanostructure templates. If the template remains intact, they may be used for other purposes (*e.g.*, sensing, directed material deposition) after nanofabrication. In addition, reusing the templates can further reduce the fabrication cost.

Hydrofluoric acid is not a strong acid, but it is a highly corrosive acid, which is known to induce DNA damage under high temperature and high concentration.[122, 132] In the vapor-phase HF etching system, gas phase HF was used instead of liquid phase HF, meaning that most HF

molecules present as HF instead of H^+ and F^- ions even with the small amount of water presented in the reaction chamber. The relative amount of HF in the system is significantly lower than the previously reported cases.[132] The experimental conditions are also milder.

In the previous studies, it was claimed that DNA nanostructures remained on the wafer surface after HF etching pattern transfer process.[188] The claim was made for the pattern transfer process under low relative humidity environment, in which positive-tone patterns were transferred. Heating and washing steps, which were believed to remove DNA residues,[110] were able to decrease the height of the positive patterns by 1-2 nm, consistent with the height of triangular DNA origami nanostructures (**Figure 34(a)**).[188] Another report by Diagne and co-workers made the same conclusion by monitoring the surface topography change throughout the entire HF etching process (**Figure 34(b)**). However, in this case, the height drop after removal of DNA nanostructure was only 2.6 nm, which was only half of the height of the DNA origami nanostructure (5.7 nm). Neither of the studies provided more insight into the damage of DNA nanostructures during the pattern transfer process. Also, in our follow-up study, we mainly focused on the high relative humidity conditions and the negative pattern transfer process, in which higher contrast could be created and the etching reaction was better controlled.[112] With more water in the system, HF could induce damage to DNA. There is by far no direct evidence on the fate of DNA after this pattern transfer process. Here we investigate the integrity of DNA nanostructures after their use as templates in HF etching of SiO_2.

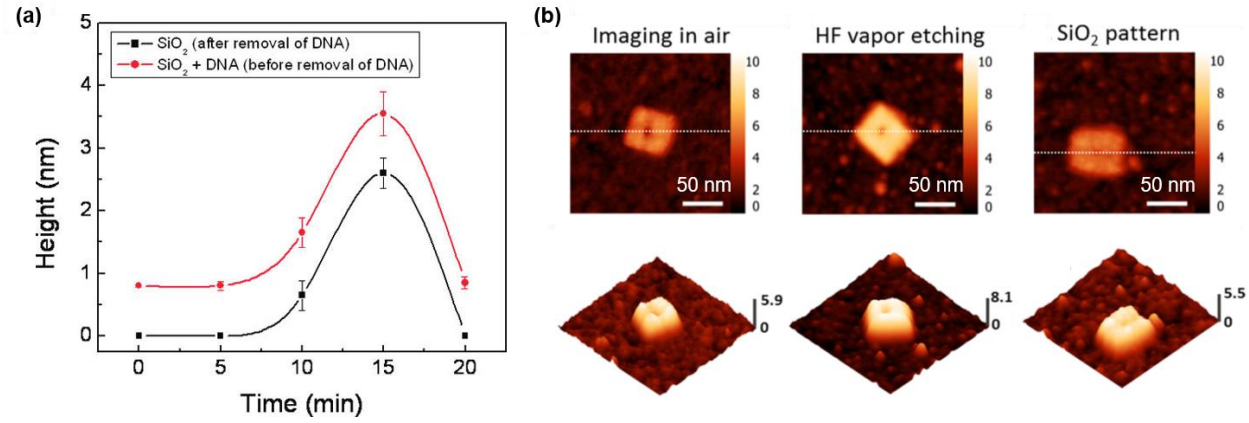

Figure 34. Comparation of pattern heights before and after removal of DNA nanostructure templates. (a) Temporal evolution of the height of the ridges obtained from the positive-tone pattern transfer process. Measurements were carried out before (SiO_2 + DNA; black) and after (SiO_2 only; red) cleaning of the surface via heating and piranha solution treatments. (b) AFM images (2D representation on top and 3D representation on bottom) of DNA origami nanostructures in air, SiO_2 pattern after 30 s HF vapor etching but before removal of DNA templates and SiO_2 after removal of DNA templates. Reprinted with permission from: (a) Reference 188, copyright © 2011, American Chemical Society; (b) Reference 192, copyright © 2016, American Chemical Society.

3.3 Experimental Section

3.3.1 Materials

(100)-oriented silicon wafers with 300 nm of thermal oxide layer was purchased from Addison Engineering, Inc. These wafers will be referred to as SiO_2/Si substrates. 2-Amino-2-(hydroxymethyl)-1,3-propanediol (Trizma base or Tris, ≥ 99.9%), ethylenediaminetetraacetic acid (EDTA, ≥ 99%), acetic acid (≥ 99.7%), magnesium acetate tetrahydrate (≥ 99%), sulfuric acid (95.0% - 98.0%), hydrogen peroxide solution (30% wt. % in water), hydrofluoric acid (HF, 48%) and potassium hydroxide (reagent grade, flakes, ≥ 90%) were purchased from Sigma-Aldrich, USA and used as received without further purification. Ethanol (200 proof) and 10 × TBE buffer (Tris-Borate-EDTA) was purchased from Thermo Fisher Scientific and diluted 10 times with water before use to make 1 × TBE buffer. *Taq* DNA polymerase (recombinant, with matched 10 × *Taq* buffer and 50 mM $MgCl_2$ solution) and GeneAmp dNTP blend (2.5 mM each) were also purchased from Thermo Fisher Scientific. PCR 20 bp low ladder was purchased from Sigma-Aldrich and used without purification. Gel loading buffer (containing bromophenol blue) was purchased from Sigma-Aldrich as well. SYTO 9 green fluorescent nucleic acid stain (DNA excitation at 485 nm and emission at 498 nm) was purchased from Thermo Fisher Scientific. SYBR Green I nucleic acid gel stain (10,000 × in DMSO, excitation at 490 nm and emission at 502 nm) was purchased from Sigma-Aldrich. Water (18.2 MΩ) was filtered by a water purification system (Barnstead MicroPure Standard, Thermo Scientific, Waltham, MA) and used throughout the entire experiment for the preparation of chemical solutions and in the cleaning of the experimental apparatus.

3.3.2 DNA materials

DNA nanotube strand (5'-CCAAGCTTGGACTTCAGGCCTGAAGTGGTCATTCGAA TGACCTGAGCGCTCA-3')[207] was purchased from Integrated DNA Technology, Inc. (IDT) and purified by Polyacrylamide Gel Electrophoresis (PAGE) by the manufacturer. Polymerase Chain Reaction (PCR) strands (**Table 3**) were also purchased from IDT and purified by PAGE by IDT. All the DNA samples were used as received without further purification. DNA powders were dissolved in deionized water and concentrations were measured and calculated by 260 nm UV absorbance measured by NanoDrop 2000c spectrophotometer (Thermal Scientific, Inc.).

Table 3. PCR DNA strands sequences.

Name	Sequence (5'-3')
ForwardPrimer25	GCACCTTAGTCTTTCTTTGAAGCAG
FP25-Comp	CTGCTTCAAAGAAAGACTAAGGTGC
ReversePrimer25	TACTTACTCTCGTCTCCTGCAACAC
PCR1	GCACCTTAGTCTTTCTTTGAAGCAGTTATGGACAACAGTCAA ACACAATTCAAATTATGGAGTATGTGTTGCAGGAGACGAGA GTAAGTA
PCR2	TACTTACTCTCGTCTCCTGCAACACATACTCCATAATTTGAAT TGTGTTTGACTGTTGTCCATAACTGCTTCAAAGAAAGACTAA GGTGC
PCR3	GCACCTTAGTCTTTCTTTGAAGCAGTTAGGACACGTCAACCA TTCAATAGGGTATGTGTTGCAGGAGACGAGAGTAAGTA
PCR4	TACTTACTCTCGTCTCCTGCAACACATACCCTATTGAATGGTT GACGTGTCCTAACTGCTTCAAAGAAAGACTAAGGTGC

3.3.3 Preparation of buffer solution for DNA nanostructure synthesis

10 × TAE/Mg buffer solution was prepared by dissolving trizma base (tris), EDTA, acetic acid and magnesium acetate tetrahydrate in water in which the concentrations of the reagents were tris-acetic acid 400 mM, EDTA 10mM, magnesium acetate 125 mM and pH was 8.0. The buffer solution was further diluted ten times with water to make 1 × TAE/Mg buffer solution.

3.3.4 Synthesis of DNA nanotubes

DNA nanotubes were synthesized following a previously published method.[207] DNA nanotubes were formed by mixing the single DNA nanotube strand solution (in water) with 10 × TAE/Mg buffer to achieve a final concentration of 2 μM for single strands in a total volume of 200 μL. The mixture underwent a slow annealing process in a 1-liter beaker with boiling water (about 100 ℃) kept in a plastic insulation box. The cooling down process from 100 ℃ to room temperature took about 48 hr. The sample was then transferred into a 4℃ refrigerator for further cooling and storage. The DNA nanotubes were used without further purification.

3.3.5 Annealing of complementary DNA double helix templates

OligoDNA PCR1 and PCR2 were annealed to make a complementary DNA double helix templates, which served as a 90-bp standard band for agarose gel electrophoresis. PCR1 (100 nM, 45 μL) and PCR 2 (100 nM, 45 μL) were mixed thoroughly with 10 μL of 10 × TAE/Mg buffer solution at room temperature. Then the mixture went through a rapid annealing process in a thermal cycler (MiniCycler™, MJ Research). The mixture was heated up to 94 ℃ rapidly and held steady

at that temperature for 2 min. Then the temperature decreased to 20 ℃ in 15 min. OligoDNA PCR3 and PCR4 were annealed following the same procedure to make an 80-bp standard band for agarose gel electrophoresis.

In the cases for high concentration DNA deposition, PCR1-PCR2, PCR3-PCR4 and ForwardPrimer25-FP25-comp double helix mixtures were annealed in a 1 × TAE/Mg buffer solution (final concentration) to make the highest possible concentration depending on the batches of the OligoDNA samples. Then the mixtures were annealed using the same procedure as described in the previous paragraph. The final concentrations were in the range of 10-50 μM.

3.3.6 Deposition of samples onto SiO_2/Si substrates

A SiO_2/Si substrate (0.4 cm × 0.8 cm size) was cleaned by immersing it in a newly prepared piranha solution (3/7 (v/v) 30% hydrogen peroxide/ 94% sulfuric acid solution) in a covered glass petri dish on a 50 ˚C heating plate for 30 min. *Warning: Piranha solution is a strong oxidizing reagent and can detonate unexpectedly; extra caution in handling is required.* The substrate was then thoroughly washed with water and dried with a N_2 stream. In some experiments, SiO_2/Si substrates were pre-incubated in 10 × TAE/Mg buffer to achieve higher density of DNA deposition. To perform pre-incubation, a SiO_2/Si substrate was immersed in 10 × TAE/Mg buffer for 24 hr and dried with a N_2 stream. Then the substrate was immersed into a 9/1 (v/v) ethanol/water solution for 5 s to remove salt impurities and dried again using a N_2 stream. To ensure complete removal of the salt residues on the surface, the immersion and drying steps were repeated two times.

DNA sample solution (20 μL) was pipetted onto the clean and dry SiO_2/Si substrate and left in a plastic petri dish without interruption for 30 min. A wet Kimwipe was inserted between the cover and the bottom of the plastic petri dish to maintain humidity inside and reduce

evaporation of water from DNA sample. After 30 min, the substrate was dried with a N_2 stream. Then the substrate was immersed into a 9/1 (v/v) ethanol/water solution for 5 s to remove salt impurities and dried again using a N_2 stream. To ensure complete removal of the salt residues, the immersion and drying steps were repeated two times.

3.3.7 HF etching of SiO_2 using DNA templates

After deposition of DNA sample, the SiO_2/Si substrate was transferred into a home-built HF etching system for further HF etching reaction (**Figure 13**). *Warning: Hydrofluoric acid (HF) is a highly corrosive liquid and a contact poison to human bodies; extra caution in handling is required.* The SiO_2/Si substrate was pasted onto the reaction boat at the marked position and transferred into the heating block (**Figure 13**). Vapors of HF and water were supplied by passing N_2 gas through the respective containers so there were totally three streams of N_2 gas in the system – pure N_2 gas, N_2 gas with HF vapor and N_2 gas with water vapor, which were controlled by the three mass flow controllers, respectively. Note that hydrofluoric acid used here was a 48% solution so the N_2 gas stream with HF vapor also contained water vapor. Three streams of N_2 gas combined before entering the chamber and went through the reaction chamber continuously. The flow rate of the three streams of N_2 gas carrier determined the partial pressure of each reagent. The best working condition [35 °C, N_2 flow rate = 55 sccm, N_2-carried H_2O flow rate = 15 sccm, N_2-carried 48% HF flow rate = 10 sccm, reaction time 20 min] was used throughout the experiments except otherwise specified.

In a typical HF etching process, after the SiO_2/Si substrate was placed in the reaction chamber, pure N_2 gas stream and N_2 gas with water vapor stream were first introduced into the chamber for 20 min to achieve equilibrium of water between the substrate surface and the gas flow.

N_2 gas carrier for HF vapor was shut off during this preparation process. Then all three streams were open and introduced together into the reaction chamber for the set reaction time (20 min). After 20 min, the N_2 gas carriers for water vapor and HF vapor were immediately shut off. Only high flow rate (*ca.* 180 sccm) of pure N_2 gas was used to clean up any leftover HF on SiO_2/Si substrate and in the reaction system before the substrate was taken out.

To evaluate the HF-induced DNA damage, the etched substrates underwent an optional washing and heating steps as described below, depending on the purpose of experiments. To test the existence of DNA templates after etching process, the etched substrates were used directly for characterization or sample preparation without any cleaning process. The standard cleaning process was that the sample was washed by water, acetone and then water again (30 s for each step) after taken out from the chamber and then dried using a N_2 stream. To remove the organic residues on the substrate, the sample was heated in a 400 ℃ furnace in air for 1 hr and rinsed with water for 1 min and then dried using a N_2 stream. After heating process, the sample was cleaned in a Novascan PSD digital UV/O_3 cleaner for 60 min and washed with piranha solution in a covered glass petri dish on a heating plate (50 ℃) for 30 min. Finally, the sample was rinsed with water thoroughly and dried using a N_2 stream before characterization.

3.3.8 Retrieval of DNA samples from SiO_2/Si substrates

DNA samples were retrieved from SiO_2/Si substrates with the help of water. In a 2 mL microcentrifuge tube, the SiO_2/Si substrate piece was inserted to the bottom and 100 μL of water was added to fully immerse the substrate surface. The closed microcentrifuge tube was kept undisturbed under room temperature for 24 hr to ensure the complete retrieval of DNA samples.

Then the SiO_2/Si substrate was removed from the liquid. The solution with DNA samples were refrigerated before further use.

3.3.9 Polymerase Chain Reaction (PCR)

PCR was used to help determine the sequence integrity of DNA strands after HF etching pattern transfer process. Artificial synthetic PCR templates and primers were listed in **Table 3**. In a 500 µL microcentrifuge tube, a 100 µL reaction mixture was prepared. ForwardPrimer25 and ReversePrimer25 were added to achieve final concentrations of 12.5 µM each. *Taq* reaction buffer, $MgCl_2$ solution, dNTP solution and *Taq* DNA polymerase were added to achieve final amounts of 1×, 1.5 mM, 200 µM and 0.5 U, respectively. PCR3 and PCR4 strands, for which the concentrations depended on the source, were also added to the system. Deionized water was added last to make up the volume difference. PCR program was set into 2 segments: (1) 94 °C, 180 s; (2) (35 cycles) 94 °C, 15 s/ 58 °C, 30 s/ 72 °C, 15 s. During the optimization process, different number of cycles were tested as specially indicated. Segment 2 here was the main PCR reaction segment. The second temperature in segment 2 (called 'annealing temperature') was estimated by the melting temperature of primers and tested through the study.

3.3.10 Fluorescence microscopy sample preparation and image scanning

SiO_2/Si substrates with different samples under dry state were incubated with 5 µL diluted (1 µM in water) SYTO 9 green fluorescent nucleic acid stain for 5 min. The substrates were then rapidly blown dry with N_2 flow and fluorescence microscopy images were taken within 1 hr to minimize the effect of photobleaching to fluorescence dye. The images were acquired with an

Olympus BX 51 WI microscope equipped with Fluorescein isothiocyanate (FITC) dichroic filter, 40 × lens and a Hamamatsu EM-CCD camera. Fluorescence microscopy images were processed with ImageJ software for better contrast presentation. The exposure time for bright field images was set to 0.0006 s. For fluorescence images, the exposure time was set to 5 s.

3.3.11 Agarose gel electrophoresis

Agarose gel electrophoresis was used to analyze fragments of DNA samples with a Mini-Sub cell GT cell system by Bio-Rad. To make 3% agarose gel, 1.5 g of agarose was mixed with 50 mL 1 × TBE buffer in a 250 mL Erlenmeyer flask and heated by a 1000 W microwave oven for 1 min for complete dissolution. The solution was cooled down to about 70 ℃ before 5 µL of SYBR Green I nucleic acid gel stain was added to the system. The mixture was then poured into a preset agarose gel mold and the air bubbles were removed before the gel cooled down to room temperature in 20 min. The agarose gel was then loaded into the cell tank. Adequate amount of 1 × TBE buffer was added to the cell tank to immerse the entire agarose gel. DNA sample (20 µL) was mixed with 4 µL of Sigma-Aldrich gel loading buffer thoroughly and the mixture was loaded into one well of the agarose gel. The loading process was repeated for each sample. For PCR 20 bp low ladder, 5 µL of DNA ladder was mixed with 1 µL Sigma-Aldrich gel loading buffer thoroughly and loaded into the agarose gel. The cell was then connected to a Bio-Rad PowerPac™ Basic Power Supply and ran at 75 V for 2 hr. The gel images were taken with ChemiDoc Imaging Systems (BIO-RAD) using 'UV – SYBR Green' mode and the exposure time was set to automatic. Gel image analysis was achieved with ImageJ software. In the case of 25-bp DNA sample analysis, 4% agarose gel was prepared with 2.0 g of agarose following the same procedure. Also, 50% (v/v)

glycerol-water solution was used as gel loading buffer to eliminate the effect of bromophenol blue to the sample bands.

3.4 Results and Discussion

3.4.1 Calculation of HF concentration inside the reaction chamber

A theoretical calculation was performed to estimate the equivalent concentration of HF inside the reaction chamber so that the HF-induced damage during vapor-phase HF etching reaction could be compared to the previous reports in HF solution. The containers of water and HF and also all the tubes to deliver gas into the etching chamber were stored at room temperature (20-25 ° C average). The saturation vapor pressure of H_2O at 2666 °C is 2339 Pa.[219] The equilibrium vapor pressure of 48% HF solution is 2666 Pa of HF and 666 Pa of H_2O.[112] From our previous studies, we can assume that N_2 gas got into equilibrium with the liquid phase after bubbling through the containers. The total pressure inside the etching chamber was around 1 atm since the system was balanced with outer atmosphere. The partial pressure of each vapor inside the chamber was proportional to the flow rate of N_2 through its container. For total vapor = 80 sccm and N_2 gas with HF vapor = 10 sccm, the partial pressure of HF was calculated as followed:

$$\text{HF: } p_{HF} = 10/80 \times 2666 = 333 \text{ Pa} = 2.5 \text{ mmHg}$$

The temperature inside the reaction chamber was set to 35 °C so we could estimate that the percentage of HF inside the chamber at liquid-gas equilibrium was 25 - 30% (**Figure 35**).[220] That means, if the 333 Pa (2.5 mmHg) HF partial pressure in the etching chamber reaches an equilibrium with the SiO_2/Si substrate surface, a thin layer of 25-30% HF solution (equivalent to 15-20 M) was condensed on the SiO_2/Si substrates and react over time in the chamber. This is considered a relatively high concentration of HF and the corresponding pH of the solution is <1. This concentration is significantly larger than 90 μg/mL, which is believed to induce significant damage for DNA (**Figure 7(a)**).

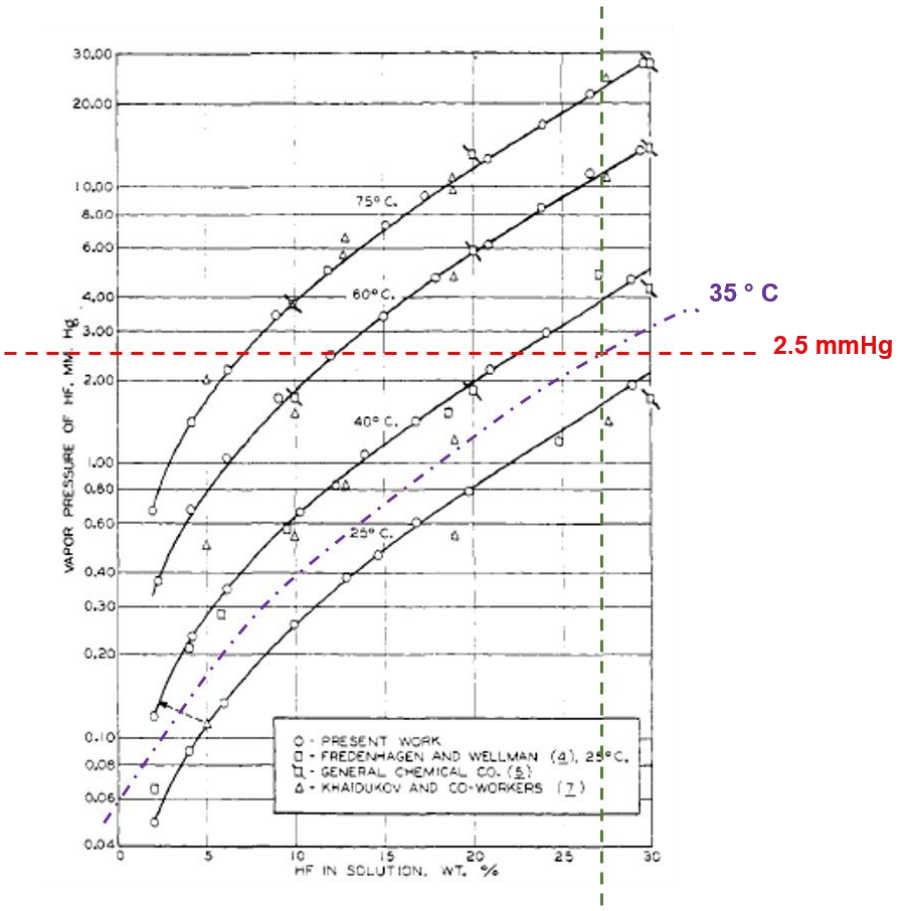

Figure 35. Isotherms of the partial pressure of hydrogen fluoride over solutions of hydrofluoric acid. Reprinted and adapted with permission from Reference 220, copyright © 1947, American Chemical Society.

3.4.2 Observation of DNA templates under fluorescence microscope

An in-situ method to directly visualize DNA on the SiO_2/Si substrates was to stain substrates with fluorescence dye and observe the surfaces with fluorescence microscopy. DNA nanotubes were selected for this part of the experiments due to their large structures in micrometer scale. SYTO 9 green fluorescence nucleic acid dye has a high affinity for DNA.[222] It is believed to have multiple binding modes, including intercalation and charge interaction with the phosphate

backbone, as well as binding to the groove of the DNA double helix.[223] SYTO 9 can be used to determine the chain integrity of DNA double helix molecules. The clean wafers (blank control) didn't show much background fluorescence signal and no tube-shape signals were observed. Then DNA nanotubes were deposited on a clean SiO_2/Si substrate and fluorescence microscopy images were taken for the sample (**Figure 36**). DNA nanotubes were clearly visible from the fluorescence images but not visible under bright field due to the low contrast.

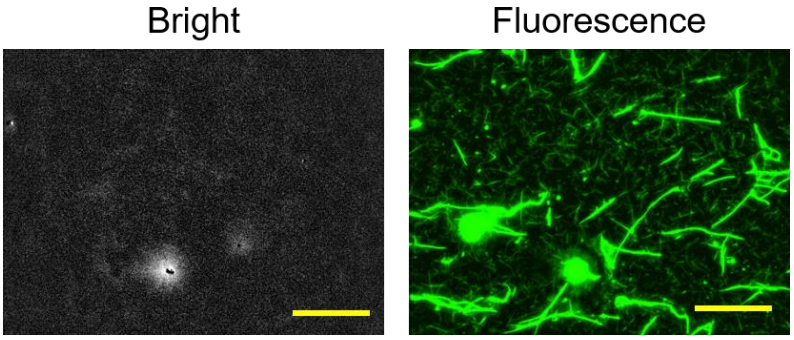

Figure 36. Fluorescence microscopy images of DNA nanotubes deposited on SiO_2/Si substrate under bright field and FITC channel (fluorescence) at the same location. Scale bars denote 40 μm.

Then we moved onto the measurements of etched SiO_2/Si substrates. The positions of negative trenches and the position of fluorescent nanotubes were compared by overlapping the images under bright field (white light) and FITC channel (fluorescence) of the same area. Each SiO_2/Si substrate was deposited with DNA nanotubes and etched using the listed conditions (**Table 4**). No washing steps were performed. The sample was directly stained with SYTO 9 and fluorescence microscopy images were obtained (**Figure 37**). Exposure time was set to 5 s in all these images.

Table 4. Etching conditions for DNA nanotubes samples on SiO_2/Si substrates (**Figure 37**).

Sample #	Temperature (°C)	N_2 flow rate (sccm)	N_2-carried H_2O flow rate (sccm)	N_2-carried 48% HF flow rate (sccm)	Reaction Time (min)
1	35	55	15	10	20
2	35	45	25	10	20
3	35	35	35	10	20

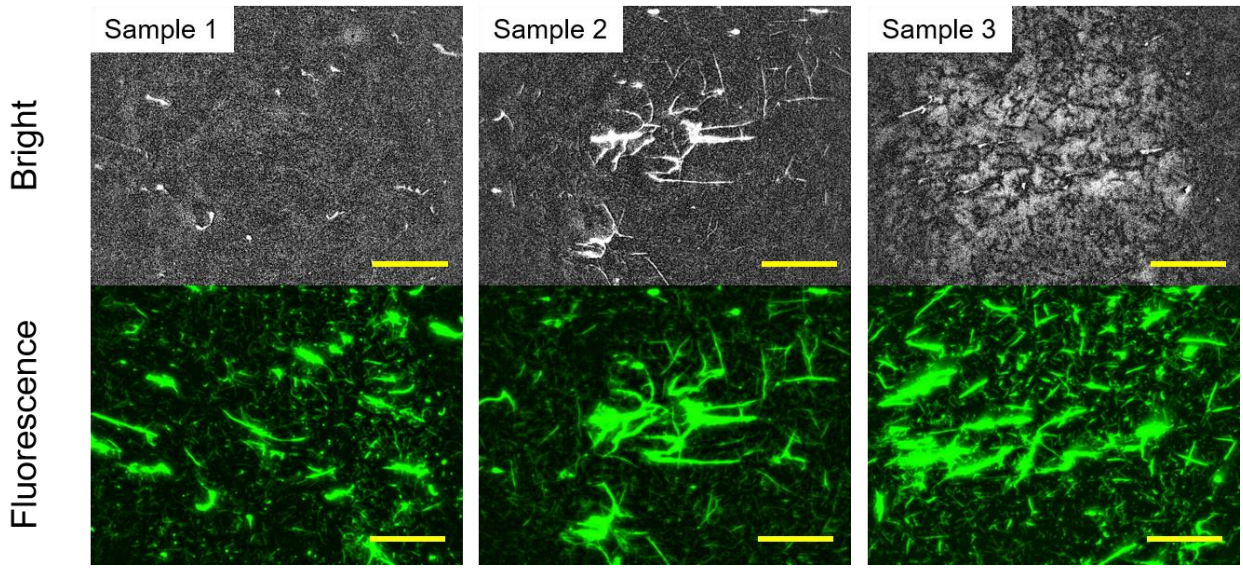

Figure 37. Fluorescence microscopy images of Sample #1 - #3 (**Table 4**) under bright field and FITC channel (fluorescence) at the same locations. Scale bars denote 40 μm.

The nanotube-shaped patterns in bright field images and fluorescence images in **Figure 37** were consistent with each other, suggesting that the DNA nanotubes were preserved after the HF etching process. Note that there were more tube-shaped patterns shown in the fluorescence images than in the bright field images. We attributed this to the fact that fluorescence signals had a lower detection limit than bright field images. The contrast provided by the nanometer scale trenches on the SiO_2/Si substrate was too small for optical microscopy. Only the DNA nanotube bundles could create large scale and deep trenches visible under bright field. It was observed that in general,

deeper trenches showed higher contrast for bright field microscopy images. However, sample #3 had an overall rough surface and the observation of trenches under bright field was not easy. The etching condition [35 °C, N_2 flow rate = 45 sccm, N_2-carried H_2O flow rate = 25 sccm, N_2-carried 48% HF flow rate = 10 sccm, reaction time 20 min] showed the best results.

DNA is believed to hold poor thermal stability for long time. Based on literature, bulk DNA decomposition started at 230 °C with two maxima rate at 233 and 300 °C measured by thermogravimetric analysis (TGA). A residue weight of 53% was observed after heating at 500 °C.[113] Another report focused on the topography of dry-deposited DNA origami nanostructures under high temperature thermal treatment (300 °C) in air or argon. The shapes of nanostructures were well maintained while the heights decreased dramatically (50%).[110] It was believed that the remaining residues were inorganic, which could be easily removed by rinsing with adequate amount of water. Washing and heating steps after HF etching pattern transfer process were believed to remove DNA residues (both inorganic and organic).[110]

To make sure that the fluorescence signals arose from the existing DNA nanotubes instead of artifacts created by the trenches, we prepared another three samples (**Table 5**) and this time, a complete series of washing steps were performed after the HF etching step. The exposure time was set to 5 s in these fluorescence images (**Figure 38**). Nanotube-shaped trenches could still be observed under bright field. However, no corresponding fluorescence signals were observed in the fluorescence images. The removal of DNA through the washing steps was efficient. Some random fluorescence signals were observed in the images, which might arise from the leftover stains after the sample was blown dried with N_2 stream. It can be concluded that DNA nanostructures can be preserved after the HF etching pattern transfer process and then be removed with heating and washing steps. This conclusion is valid for all the tested conditions including the best working

condition [35 °C, N_2 flow rate = 55 sccm, N_2-carried H_2O flow rate = 15 sccm, N_2-carried 48% HF flow rate = 10 sccm, reaction time 20 min]. Considering that the DNA damage in HF solution of equivalent concentration (25-30%) is more severe, we believe that there is a different mechanism between vapor phase HF and dry-deposited DNA samples with limited amount of water condensed on the surface.

Table 5. Etching conditions for DNA nanotubes samples on SiO_2/Si substrates (**Figure 38**).

Sample #	Temperature (°C)	N_2 flow rate (sccm)	N_2-carried H_2O flow rate (sccm)	N_2-carried 48% HF flow rate (sccm)	Reaction Time (min)
4	35	55	15	10	20
5	35	45	25	10	20
6	35	35	35	10	20

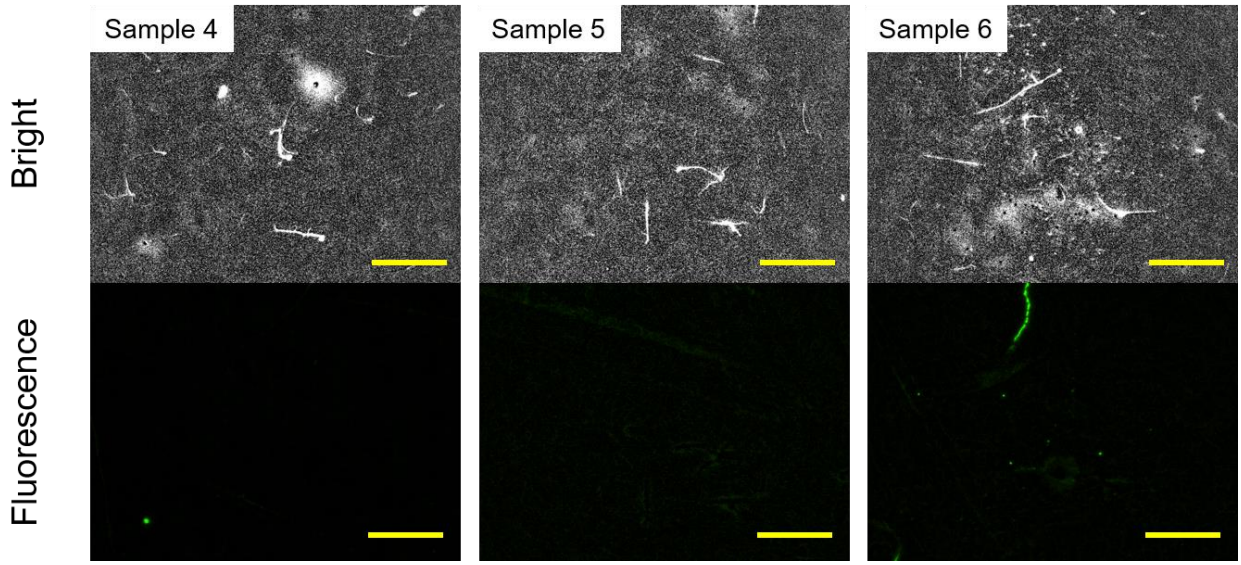

Figure 38. Fluorescence microscopy images of Sample #4-6 (**Table 5**) under bright field and FITC channel (fluorescence) at the same locations. Scale bars denote 40 μm.

3.4.3 Agarose gel electrophoresis of DNA strands retrieved directly from SiO_2/Si substrates

Water is believed to remove DNA nanostructures from SiO_2/Si surface due to the desorption of Mg^{2+}.[110] DNA strands were deposited on the SiO_2/Si substrates and retrieved from the surface using water after or without HF etching reaction. The retrieved DNA samples were directly analyzed with agarose gel electrophoresis. A 90-bp ds-DNA solution was prepared by annealing the mixture of PCR1 and PCR2 to achieve a final concentration of 9.9 μM for ds-DNA. The solution was deposited on two pieces of pre-incubated SiO_2/Si substrates. One piece was kept clean at room temperature while the other piece went through the etching reaction. Then DNA samples were retrieved from both substrates and analyzed by agarose gel electrophoresis (**Figure 39**). Lane 1 was loaded with PCR 20 bp low ladder. Lane 2 and Lane 3 were loaded with DNA samples retrieved from SiO_2/Si substrates without and with etching reaction, respectively. Lane 4 was loaded with the standard sample of 45 nM 90-bp ds-DNA. Comparing the band strength of Lane 2 to Lane 4, we can estimate that Lane 2 contained 70 nM of ds-DNA sample and Lane 3 contained 30 nM of ds-DNA sample. No smaller pieces of DNA strands were observed from agarose gel. After etching, less amount of DNA samples could be retrieved from the SiO_2/Si substrates. We speculate that DNA has a higher affinity to the etched trenches due to the larger area for electrostatic interaction.

Even though no broken pieces were observed on the agarose gel, there was still possible damage in DNA molecules. The detection limit of agarose gel electrophoresis was determined by the dye used in the system – SYBR Green I in this case. SYBR Green I is able to detect 1- 2 ng of 24-mer synthetic DNA on a 5% polyacrylamide gel electrophoresis (PAGE).[224] Lane 3 contained 30 nM of 90-bp ds-DNA with a loading volume of 20 μL. Converting to grams, we estimated that there were 32 ng of 90-bp ds-DNA in the sample. With a detection limit of 1 ng, we also estimated

that no more than 3% of broken pieces of the same length existed in the sample. Considering that phosphodiester bonds had the same possibility of being broken at any location within the DNA chain, a 90-bp ds-DNA had 89 potential broken pieces of different lengths. Even with 3% possibility for each of them, the possible total percentage of breakage was still very high. It was also possible that the broken pieces were too small and ran out of the gel under the running conditions.

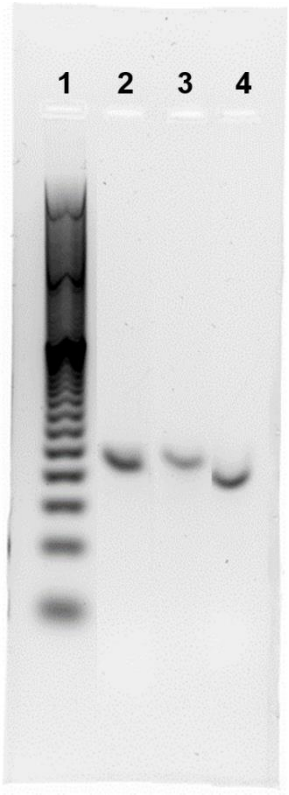

Figure 39. Agarose gel electrophoresis analysis of 90-bp ds-DNA samples retrieved from SiO_2/Si substrates without and after HF etching reaction.

The 90-bp ds-DNA experiment was repeated with different etching conditions. Four pieces of pre-incubated SiO_2/Si substrates were deposited with 9.9 μM ds-DNA solution in 1 × TAE/Mg buffer. One piece was kept clean at room temperature while the other three pieces went through

the etching reactions under different conditions (**Table 6**). Then DNA samples were retrieved from the substrates and analyzed by agarose gel electrophoresis (**Figure 40**). Lane 1 and Lane 8 were both loaded with PCR 20 bp low ladder. Lane 2, 3, 4 and 5 were loaded with DNA samples retrieved from SiO_2/Si substrates without and with etching reaction, respectively. Lane 6 and 7 were loaded with the standard sample of 45 nM and 5 nM 90-bp ds-DNA standard samples, respectively. Only a vague band was observed for the DNA samples retrieved from SiO_2/Si substrates without etching reaction. No DNA bands were observed from any of the three samples retrieved from SiO_2/Si substrates after etching reaction. The deposition of DNA onto SiO_2/Si substrates could be affected by numerous factors including the humidity of the environment and then the retrieval process was also affected. Comparing **Figure 39** and **Figure 40**, it was observed that the efficiency of deposition and retrieval of DNA templates varies dramatically from case to case.

Table 6. Etching conditions for 90-bp ds-DNA samples deposited on SiO_2/Si substrates (**Figure 40**).

Lane #	Temperature (°C)	N_2 flow rate (sccm)	N_2-carried H_2O flow rate (sccm)	N_2-carried 48% HF flow rate (sccm)	Reaction Time (min)
2	No Etching				
3	35	55	15	10	20
4	35	45	25	10	20
5	35	35	35	10	20

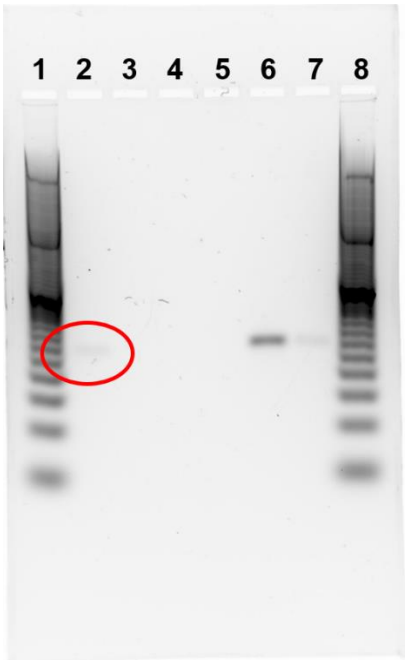

Figure 40. Agarose gel electrophoresis analysis of 90-bp ds-DNA samples retrieved from SiO_2/Si substrates without and after HF etching reactions of different conditions. The red circle indicates the vague band in Lane 2.

As an effort to increase the concentration of broken pieces for better imaging and observation, we shortened the ds-DNA samples to 25-mer. A 25-bp ds-DNA sample was prepared with ForwardPrimer25 and its complimentary strand FP25-comp. Four pieces of pre-incubated SiO_2/Si substrates were deposited with 19.8 μM ds-DNA solution in 1 × TAE/Mg buffer. One piece was kept clean at room temperature while the other three pieces went through the etching reactions under different conditions (**Table 7**). Then DNA samples were retrieved from the substrates and analyzed by agarose gel electrophoresis (**Figure 41**). Lane 1 and Lane 8 were both loaded with PCR 20 bp low ladder. Lane 2, 3, 4 and 5 were loaded with DNA samples retrieved from SiO_2/Si substrates without and with etching reactions, respectively. Lane 6 and 7 were loaded with the standard sample of 1.25 μM and 50 nM 25-bp ds-DNA, respectively. A clear band was observed for Lane 6 with 1.25 μM ds-DNA standard samples. A vague band was also observed

for Lane 7 with 50 nM ds-DNA standard samples. However, no visible bands were observed for Land 2-5, indicating that there was little amount of DNA retrieved from the SiO_2/Si substrates. Shorter DNA strands are usually more difficult to be deposited on the SiO_2/Si substrates, providing that fewer affinity sites are provided in each molecule. It was not of surprise that no visible DNA strands could be retrieved from the SiO_2/Si substrates on which only little amount of DNA strands were initially adsorbed. Even if the method provided a new route for direct observation, the practical difficulty due to the limitation of detection sensitivity made it impossible to draw any useful conclusion. With the data from direct fluorescence observation in **3.4.2**, we may also conclude that the reusable DNA templates were difficult to be recollected using conventional methods.

Table 7. Etching conditions for 25-bp ds-DNA samples deposited on SiO_2/Si substrates (**Figure 41**).

Lane #	Temperature (°C)	N_2 flow rate (sccm)	N_2-carried H_2O flow rate (sccm)	N_2-carried 48% HF flow rate (sccm)	Reaction Time (min)
2	No Etching				
3	35	55	15	10	20
4	35	45	25	10	20
5	35	35	35	10	20

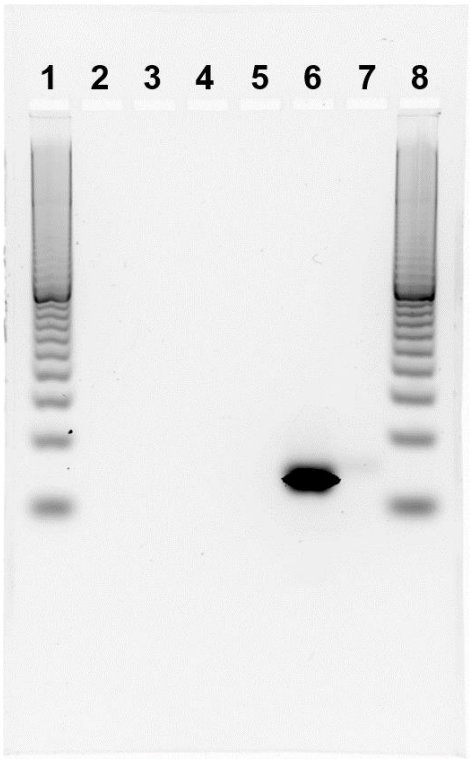

Figure 41. Agarose gel electrophoresis of 25-bp ds-DNA samples retrieved from SiO_2/Si substrates.

3.4.4 PCR amplification of DNA templates retrieved from SiO_2/Si substrates

An artificial PCR system was designed to amplify the DNA templates to ensure the sequence integrity of the DNA samples retrieved from SiO_2/Si substrates. A set of 80-bp complimentary strands PCR3 and PCR4 were designed as the templates of the PCR system. ForwardPrimer25 and ReversePrimer25 served as pair of PCR primers. To determine the best number of PCR cycles for the PCR system, we compared the results of blank control, 5 nM templates and 10 pM templates with different PCR cycles (**Table 8** and **Figure 42**). The low concentration of 10 pM templates served as a good simulation of the DNA samples retrieved from SiO_2/Si substrates. In each gel, Lane 1 was loaded with PCR 20 bp low ladder. Lane 2-6 were

loaded with PCR products after different numbers of cycles with Lane 2 as the most and Lane 6 as the least. Lane 7 was loaded with the positive control with 50 nM standard 80-bp bands. The PCR system was expected to yield ~ 50 nM 80-bp ds-DNA products when all the primers were consumed. Lane 8 was loaded with either a positive control (for blank control gel and 10 pM templates gel) or a negative control (for 5 nM templates gel) for the purpose of comparison between PCR products and primer dimers. No visible bands were observed in the blank control sample before 50 cycles. After 50 cyclers, a shorter strand of DNA band appeared on the gel with low concentration. This behavior accorded with primer dimers. On the other hand, even for 10 pM templates, 30 cycles were sufficient to achieve complete amplification in the PCR reaction. Number of cycles was set at 35 for the following experiments.

Table 8. Contents of lanes in the agarose gels of blank control, 5 nM templates and 10 pM templates to determine the best cycle number (**Figure 42**).

Cycle number (Template Concentration)	Blank Control	5 nM Templates	10 pM Templates
Lane 1	PCR 20 bp low ladder		
Lane 2	60 cycles (0)	60 cycles (5 nM)	60 cycles (10 pM)
Lane 3	50 cycles (0)	50 cycles (5 nM)	50 cycles (10 pM)
Lane 4	40 cycles (0)	40 cycles (5 nM)	40 cycles (10 pM)
Lane 5	30 cycles (0)	30 cycles (5 nM)	30 cycles (10 pM)
Lane 6	20 cycles (0)	20 cycles (5 nM)	20 cycles (10 pM)
Lane 7	50 nM 80-bp templates (no PCR) – positive control		
Lane 8	60 cycles (5 nM)	60 cycles (0)	60 cycles (5 nM)

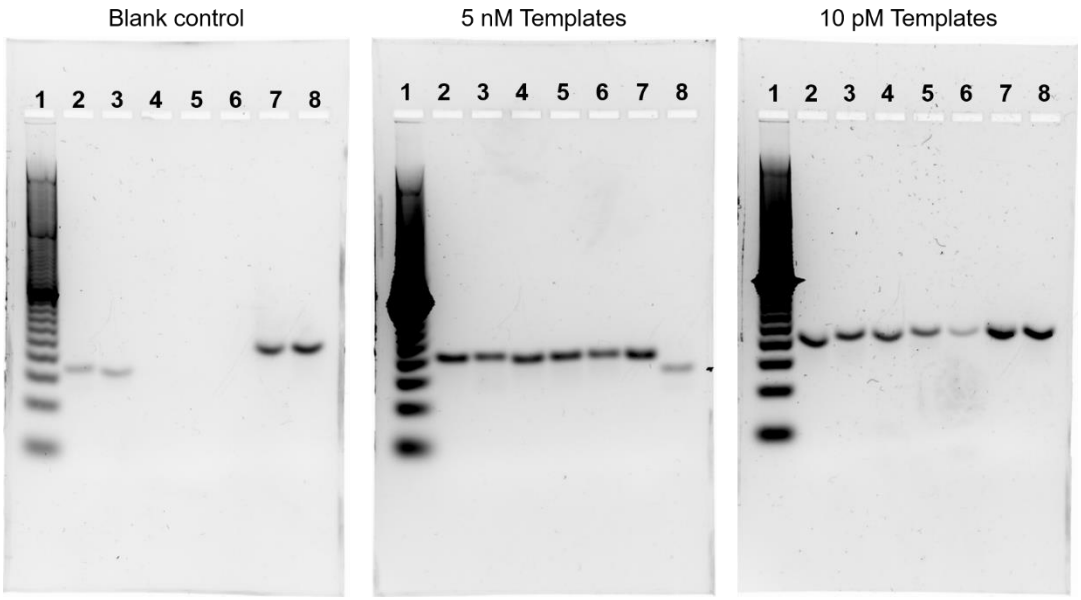

Figure 42. Determination of cycles for PCR amplification using blank control, 5 nM templates and 10 pM templates.

Then the method was applied to the analysis of DNA samples retrieved from SiO_2/Si substrates without or with etching reactions. Blank SiO_2/Si substrates were first used as blank control (**Table 9** and **Figure 43(a)**) after the reaction chamber was cleaned thoroughly. No DNA samples were deposited on any of the SiO_2/Si substrates. Lane 1 was loaded with PCR 20 bp low ladder. Lane 2 to 6 were loaded with samples retrieved from SiO_2/Si substrates without or with etching reactions (**Table 9**). Lane 7 was loaded with a freshly prepared blank control sample, *i.e.*, the PCR products without any templates. Lane 8 was loaded with the standard sample of 50 nM 80-bp ds-DNA as a positive control. No obvious DNA bands were observed for Lane 2 – 7. The blank control result was reproducible, indicating no contamination was introduced into the system. Also, blank SiO_2/Si substrates were not contaminated with DNA samples from chamber or the deposition area.

Table 9. Etching conditions for blank SiO_2/Si substrates (**Figure 43(a)**).

Lane #	Temperature (°C)	N_2 flow rate (sccm)	N_2-carried H_2O flow rate (sccm)	N_2-carried 48% HF flow rate (sccm)	Reaction Time (min)
2	No Etching				
3	No Etching				
4	35	55	15	10	20
5	35	45	25	10	20
6	35	35	35	10	20

Table 10. Etching conditions for SiO_2/Si substrates with DNA samples (**Figure 43(b)** and **(c)**).

Lane #	Temperature (°C)	N_2 flow rate (sccm)	N_2-carried H_2O flow rate (sccm)	N_2-carried 48% HF flow rate (sccm)	Reaction Time (min)
2	No Etching				
3	35	55	15	10	20
4	35	45	25	10	20
5	35	35	35	10	20

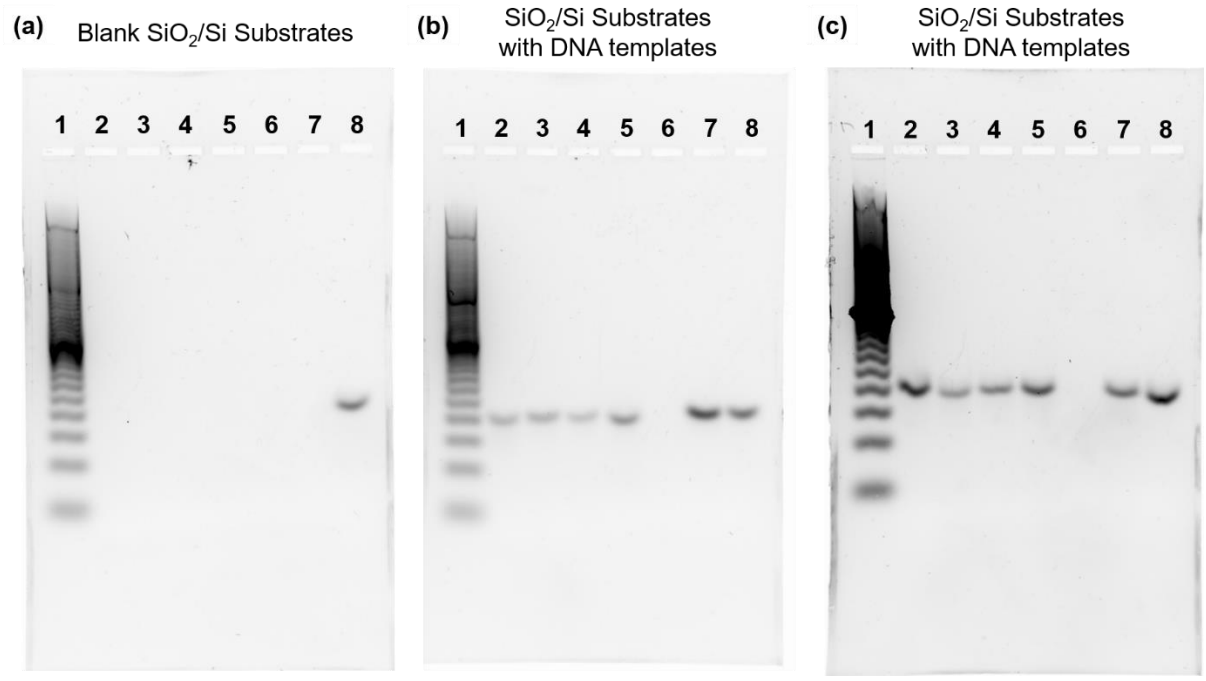

Figure 43. Agarose gel electrophoresis of PCR products from samples retrieved from blank SiO_2/Si substrates and SiO_2/Si substrates deposited with DNA templates, without or with etching reactions (**Table 9** and **Table 10**). (b) and (c) were two parallel tests.

The mixture of PCR3 and PCR4 was annealed to achieve a final concentration of 21.7 μM. The ds-DNA solution was deposited on four pieces of pre-incubated SiO_2/Si substrates. One piece was kept at room temperature while the other three pieces went through the etching reactions under different conditions (**Table 10**). Then DNA samples were retrieved from the substrates and analyzed through agarose gel electrophoresis (**Figure 43 (b)**). Lane 1 was loaded with PCR 20 bp low ladder. Lane 2- 5 were loaded with DNA samples retrieved from SiO_2/Si substrates without and with etching reaction, respectively (**Table 10**). Lane 6 was loaded with a freshly prepared blank control sample, *i.e.*, the PCR products without any templates. Lane 7 was loaded with the PCR products from 5 nM standard 80-bp templates. Lane 8 was loaded with the standard sample of 50 nM 80-bp ds-DNA. The experiment was repeated once (**Figure 43(c)**). The blank control

again showed clean lane on the agarose gel. Lane 2 to 5 all showed bands at the 80-bp mark, indicating that 80-bp DNA templates could be well preserved after the deposition and etching process. Using ImageJ software, we calculated the relative densities of the bands. The band densities were roughly 10-110% compared to Lane 8 and showed large variations across the lanes and parallel samples. For most of the cases, the band densities were less than 50% compared to Lane 8, meaning that the retrieved concentrations of DNA templates from the SiO_2/Si substrates were significantly lower than 10 pM. Assuming a monolayer of 80-bp ds-DNA templates on the substrate initially, we could estimate the amount of DNA deposited and thus estimate the retrieval yield. An 80-bp ds-DNA strand with B-DNA structure maintains cylinder shape with a diameter of 2.0 nm.[225] Each bp of ds-DNA raises around 0.34 nm[225] so the total length of the ds-DNA strand is 27.2 nm. With the cylinder lying on the substrate, the surface area of one ds-DNA strand is 2.0 nm × 27.2 nm = 54.4 nm^2. For a wafer of 4 mm × 8 mm, there were about 5.9×10^{11} molecules in a monolayer coverage, which is equivalent to 9.8×10^{-13} mol. If all the DNA templates were retrieved at 100% yield in 100 µL water, the concentration in the retrieved solution would be 9.8 nM and the concentration in PCR reaction would be 4.9 nM. The recovery yield is less than 0.2%. According to this number, it is possible that the retrieval method we used was not effective enough to recover DNA templates from SiO_2/Si substrates. This is also supported by the large variation in the amount of DNA retrieved among different parallel experiments. It is also possible that large amount of DNA strands was indeed damaged and could not be amplified by PCR reaction. Even without any possible damage, the data shows that it is difficult to recover DNA samples and reuse them into another nanofabrication process. However, the success of PCR amplification means that the whole sequence of the templates could be well preserved. These results, combined with our fluorescence microscopy observations for DNA nanotubes, confirmed our hypothesis that the

DNA nanostructures can be preserved after the HF etching pattern transfer process. There is still long way to go before the DNA nanostructures can be considered reusable nanomaterials for fabrication purpose, at least in the HF-etching reaction.

One interesting phenomenon was that with more severe etching, the SiO_2/Si substrate showed slightly better retrieval yield and thus slightly higher amount of product after PCR process. The HF etching process created negative-tone trenches on the SiO_2 substrate and the deposited DNA samples were supposed to have a better adhesion to the substrate via electrostatic force due to the larger contact area available in the 3D trenches. It was also generally accepted that the DNA samples might undergo more damages under harsh etching conditions, meaning Lane 5 was supposed to hold the least amount of integrated DNA templates. All these contradictions indicated that the retrieval efficiency, other than the damage from the HF etching process, played the key role in the process. It is impossible to quantitatively calculate the percentage of damage of the DNA samples through this PCR amplification method. A more effective retrieval method must be developed to achieve the recycling of DNA templates.

3.5 Conclusion

DNA nanostructures have served as templates for various nanofabrication applications. One major concern is the stability of DNA nanostructures in the harsh chemical conditions used for pattern transfer methods. Here we investigated the stability and reusability of DNA nanostructure templates after the HF etching negative-tone pattern transfer process. With the help of SYTO 9 fluorescent nucleic acid stain and fluorescence microscopy, a direct observation of DNA nanotubes presence after HF etching reaction and their disappearance after washing steps was achieved. These results confirmed that DNA nanostructures can be preserved after the HF etching pattern transfer process. A PCR amplification system was designed and used for amplification of the retrieved PCR templates from the HF etched SiO_2/Si substrates. The results further confirmed the sequence integrity of at least minor amount of DNA strands. We can conclude that the DNA nanostructures can be preserved after the HF etching pattern transfer process. The lack of effective retrieval method makes it almost impossible to quantitatively investigate the percentage of damaged DNA templates after the HF etching process. It is also the bottleneck to achieve recycling and reusing of the DNA templates. There is still long way to go before the reusability of DNA nanostructures as nanofabrication templates can be fully realized.

4.0 Deposition of DNA Nanostructures on Highly Oriented Pyrolytic Graphite (HOPG)

4.1 Chapter Preface

Materials contained in this chapter were published as a research article in *Langmuir*; materials and figures used in this chapter have been reprinted with permission from: Ricardo, K. B.; Xu, A.; Salim, M.; Zhou, F.; Liu, H., Deposition of DNA nanostructures on highly oriented pyrolytic graphite. *Langmuir* **2017,** *33* (16), 3991-3997.

List of Authors: Karen B. Ricardo, Anqin Xu, Muhammad Salim, Feng Zhou and Haitao Liu. Karen B. Ricardo and Anqin Xu contributed equally to the work.

Author Contributions: K.B.R, A.X. and H.L. designed and directed the experiments. K.B.R. and A.X. conducted the experiments and analyzed the results together with help from M.S. for XPS characterization and F.Z. for CVD. Specifically, A.X. was responsible for the results and discussions presented in part of **4.4.2**, all of **4.4.3**, part of **4.4.4**, part of **4.4.5**, all of **4.4.6** and part of **4.4.7**. All authors discussed the results. K.B.R., A.X. and H.L. wrote the manuscript with input from all authors.

Materials contained in this chapter was used in the doctoral dissertation of Karen B. Ricardo (University of Pittsburgh, 2017). All the materials in the research article are included in this dissertation for the completeness of entire research project and as one of my efforts to develop the applications of DNA nanostructures.

4.2 Introduction

DNA nanostructures have been a useful template for patterning at the nanometer length scale.[105, 226] Programmable structures can be created using synthetic, short strand DNA with or without a single strand viral scaffold DNA to form 2D and 3D shapes,[37, 50, 64, 227] making them useful for a wide variety of applications that include, but are not limited to, metallization,[182] growth of oxides,[186] and nanomaterial positioning.[228-229]

The sp^2 carbon materials have been widely studied because of their excellent mechanical, thermal and electrical properties.[230-232] Among the many different types of carbon materials (*e.g.*, graphite, semiconducting and metallic carbon nanotubes, and single and multilayer graphene), HOPG is often used as the model to understand the basic properties of extended sp^2 carbons in wetting,[233] adsorption,[234] tribology,[235] biosensing,[236] and surface chemistry.[237] Therefore, a fundamental understanding of the interaction between DNA nanostructure and HOPG will pave the way to integrating DNA nanostructure with a broad range of sp^2 carbon materials.

The interaction between graphitic surfaces with DNA has been studied for many years.[238-240] Husale, *et al*. reported a strong binding interaction between single-stranded DNA (ss-DNA) and exfoliated graphene and demonstrated preferential orientation of the ss-DNA towards the graphene lattice.[241] They also attempted to deposit DNA origami on graphene but the origami structures were not stable because they did not add Mg^{2+} in the buffer. Regarding DNA - HOPG interactions, all deposition procedures in literature involved surface modification,[208] applying a voltage,[242-243] or the modification of the DNA origami. Recently, DNA nanostructures have been deposited on graphene; however, most of these efforts involve a modification of the substrate to enhance DNA-carbon interaction, such as doping,[195, 244] and assisted immobilization.[182] It was recently reported that cross-shaped DNA origami structure was deformed when deposited onto

graphene.[245] In contrast, on 1-pyrenemethylamine modified graphene, DNA nanostructures were deposited without such deformation and were successfully used for subsequent metallization.[182] A related study also investigated the deposition of a cross shaped DNA nanostructure on pristine and 1-pyrenemethylamine-modified MoS_2 surfaces.[246] Similar to the case of graphene, the origami was found to deform upon contact with the pristine MoS_2 surface but the shape could be preserved by adding a layer of 1-pyrenemethylamine to the MoS_2 substrate. These preliminary reports points to the need to better understand and control the interaction between graphitic surface and DNA nanostructures.

Recently, it was reported that freshly exfoliated HOPG presented a water contact angle of 64.4˚,[247] much smaller than the previously accepted value of 86˚. It was further shown that the commonly observed hydrophobicity of graphite is due to adventurous airborne hydrocarbon contamination.[248] This finding points to a previously unknown factor that could impact graphitic carbon-DNA interaction and opens new opportunities to control the deposition of DNA nanostructures onto graphitic substrates.

Herein we report a detailed study of the deposition of triangular DNA origami nanostructures on exfoliated HOPG without any surface or DNA nanostructure modification. Atomic force microscopy (AFM) was used to analyze the DNA origami. The results showed that the deposition was accompanied by a structural reconfiguration of the DNA origami to maximize Van der Waals interaction between the DNA bases and the substrate. Surface contamination of HOPG by airborne hydrocarbons did not significantly impact the outcome of the deposition. Despite the structural change, the morphology of the DNA nanostructure remained unchanged on the HOPG surface for at least a week, comparable to the stability of DNA nanostructures deposited on other substrates, such as SiO_2.[110] This result provides new insight into the interaction between

graphitic carbon and DNA nanostructures and could aid the development of biosensors and electrochemistry applications.

4.3 Experimental Section

4.3.1 Materials

(100)-oriented silicon wafers with 300 nm of thermal oxide layer (SiO_2/Si substrates) were purchased from University Wafers, USA. HOPG (SPI-2 grade) was purchased from SPI Supplies. 2-Amino-2-(hydroxymethyl)-1,3-propanediol (Trizma base or Tris, ≥ 99.9%), acetic acid (≥ 99.7%), ethylenediaminetetraacetic acid (EDTA, ≥ 99%), magnesium acetate tetrahydrate (≥ 99%), sulfuric acid (95.0%-98.0%), hydrogen peroxide solution (30% wt. % in water), hexane (anhydrous, 95%), isopropanol (≥ 99.5 %) and acetone (ACS reagent, ≥ 99.5%) were purchased from Sigma-Aldrich, USA and used as received without further purification. Tetraethyl orthosilicate (98%, Arcos Organics), ammonia (NH_4OH, 28.0-30.0 %, J.T. Baker) and ethanol (200 proof) was purchased from Fisher Scientific, USA. M13mp18 single stranded phage DNA was purchased from Bayou Biolabs and used as the scaffold DNA strand for DNA origami nanostructure synthesis. Synthetic DNA strands were purchased from Integrated DNA Technology, Inc. The complete sequence profile of all 232 staple strands is listed in **2.3.3 DNA Sequence Profile**. Water (18.2 MΩ·cm) was filtered by a water purification system (Barnstead MicroPure Standard, Thermo Scientific™, USA) and used throughout the entire experiment for the preparation of chemical solutions and in the cleaning of the experimental apparatus.

4.3.2 Synthesis of DNA origami nanostructures

Triangular-shaped DNA origami nanostructures were synthesized using a previously published method[44] by mixing 15.0 μL of DNA staples (300 nM for each staple), 8.60 μL of M13mp18 DNA (454 nM), 77 μL of DI water and 181.0 μL of a TAE/Mg buffer. The stock TAE/Mg buffer solution contained the following reagents with its respective concentrations: 150.0 mM of $Mg(OAc)_2$, 2.0 mM of acetic acid, 2.0 mM of EDTA, and 40 mM of tris. The stock solution was then diluted for all the experiments and the concentrations were 12.5 mM of $Mg(OAc)_2$, 0.17 mM of acetic acid, 0.17 mM of EDTA and 3.33 mM of tris after dilution. The diluted TAE/Mg solution with the DNA was then heated to 95 ˚C and slowly cooled down to 25 ˚C at a rate of 1 ˚C/min. After the cooling process was completed, the sample (*ca.* 280 μL) was divided equally and transferred into two separate 30 kDa MW centrifugal devices (Nanosep Centrifugal Devices with Omega™ Membrane, Pall Corporation, Port Washington, NY). Additional *ca.* 400 μL of diluted buffer solution was added into each centrifugal device and the mixtures were centrifuged at a speed of 6000 rpm using a single speed benchtop microcentrifuge (Fisher Scientific, USA) to remove the excess DNA staple strands. The DNA origami solution was centrifuged until 1/3 to 1/4 of the original volume was left to ensure that the solution was not completely centrifuged to dryness. The process of adding buffer and centrifuging was repeated five times. The final DNA triangle solution was stored inside plastic vials at 4 ˚C. Different concentrations and volumes of M13mp18 DNA scaffold strands were used where noted for the purpose of comparing different staple-to-scaffold ratios.

Another TAE/Mg (TAE/Mg-2) buffer stock solution was also prepared for comparison purpose and contained the following reagents with their respective concentrations: 125 mM of $Mg(OAc)_2$, 200 mM of acetic acid, 10 mM of EDTA and 400 mM of tris. TAE/Mg-2 buffer had a

higher acetic acid concentration and overall buffer concentration. The stock solution was then diluted for all the experiments and the concentrations were 12.5 mM of $Mg(OAc)_2$, 20 mM of acetic acid, 1 mM of EDTA and 40 mM of tris. The synthesis and purification steps for DNA origami nanostructures in TAE/Mg-2 buffer were the same as in TAE/Mg buffer.

4.3.3 Preparation of mixture of DNA nanostructures and irrelevant ss-DNA

The concentration of triangular-shaped DNA origami nanostructures was determined by a UV-Vis spectrophotometer NanoDrop 2000c (Thermo Scientific, Wilmington, DE). Triangular-shaped DNA origami nanostructures were thoroughly mixed with different concentrations of an irrelevant ss-DNA in 1 × TAE/Mg buffer. The irrelevant DNA single strand was purchased from Integrated DNA Technology, Inc. and was used without further purification. The sequence of the strand was 5'-ACATTCCTAAGTCTGAAACATTACAGCTTGCTACACGAGAAGAGCCGC CATAGTA -3'. This ss-DNA was considered irrelevant because it does not have longer than 8 nucleotide complimentary sequence with M13mp18 single stranded phage DNA and any of the staple strands.

4.3.4 Cleaning of SiO_2/Si substrate

A clean Si wafer with 300 nm of oxide (SiO_2/Si substrate) was used as a support for the HOPG samples or as a substrate for the deposition of DNA nanostructures. In order to preserve a clean sample, the wafer was immersed in a piranha solution (3/7 (v/v) 30% hydrogen peroxide/ 98% sulfuric acid solution) in a covered glass petri dish on a 50 ˚C heating plate for 30 min. *Warning: Piranha solution is a strong oxidizing reagent and can detonate unexpectedly; extra*

caution in handling is required. The sample was then removed and copiously rinsed with DI water (>10 mL) and blow-dried with N_2 gas.

4.3.5 Exfoliation of HOPG

HOPG with a dimension of 20 mm × 20 mm × 1 mm was cleaved following the Scotch tape method[249] using double-sided tape (Scotch by 3M). Once the tape was attached to the HOPG, it was gently massaged to remove any air bubbles present. The tape was then slowly removed and a continuous layer of HOPG was obtained. This tape was then attached to a clean SiO_2/Si substrate for support. The HOPG layer on the tape was exposed to air and used as a substrate for the following experiments.

4.3.6 Deposition of DNA nanostructures on HOPG and SiO_2/Si substrate

The synthesized DNA origami solution was diluted with the TAE/Mg buffer (except otherwise noted) and 20 μL was deposited using a pipet to a HOPG substrate prepared using the procedure in **4.3.4**. The purpose of the dilution was to ensure that no more than monolayer of DNA origamis were deposited on the HOPG surface. The HOPG was then left undisturbed for 40 min in a plastic Petri dish. To keep a humid environment and avoid evaporation, a wet Kimwipe was put between the cover and the bottom of the Petri dish. The HOPG substrate was then slowly dried using a rubber tube to flow N_2 gas. Then the substrate was completely covered with 20 μL 9/1 (v/v) ethanol/water solution for 10 s and blown dry again with N_2 flow. The process was repeated three times to remove any residues present from the buffer solution. In the optimization process, multiple solvents were tested to clean the HOPG substrates, including water, 9/1 (v/v)

ethanol/water solution, ethanol, acetone and hexane. The same deposition and cleaning methods were used for the deposition of DNA nanostructures onto SiO_2/Si substrates.

4.3.7 Chemical Vapor Deposition (CVD) growth of SiO_2 using DNA origami on HOPG as a template

The CVD growth of SiO_2 was carried out on a 300 cm^3 chamber with 2.0 mL of each reagent, in accordance to our previous work:[186] water, TEOS (98%, Acros Organics), NH_4OH (28.0-30.0 % J.T. Baker) and isopropanol (≥ 99.5 %, Sigma Aldrich). The distance between substrate and the surface of each reagent was approximately 2 cm. After four hours, the sample was removed.

4.3.8 Atomic Force Microscopy (AFM) characterization

AFM measurements were taken with a Digital Instruments Nanoscope IIIA from Veeco Systems in tapping mode in air using HQ:NSC15/Al BS AFM probes (325 kHz, 40 N/m) purchased from μmasch (NanoAndMore, USA). Some AFM images, where specifically noted, were collected using an Asylum MFP-3D Atomic Force Microscope (Oxford Instruments, UK) by AC mode in air. Images were analyzed by Igor Software (Version 6.3.7.2) equipped with Asylum Research package. All images collected had a scan rate of 1.0 Hz and 512 data points per line with scan size identified by scale bars.

4.3.9 X-ray Photoelectron Spectroscopy (XPS) characterization

XPS measurements for the samples were conducted with a Thermo Scientific™ Escalab 250Xi. X-Ray source was monochromatic and used an Al anode with a spot size of 0.2 mm for the deposition experiments and 0.4 mm for the CVD experiments, with a takeoff angle of 45˚. A minimal of 3 survey scans (10 scans for CVD experiments) were employed for good signal to noise ratio. Higher resolution scans were performed with a minimum of 64 scans. Measurements were acquired, peaks deconvoluted, and analyzed using the Thermo Scientific TM Avantage Data System or the XPSPEAK 4.1 software. Peak fitting allowed for Lorentzian-Gaussian ratio control as well as difference spectra optimization, with the Smart method being implemented to calculate the background spectrum.

4.4 Results and Discussion

4.4.1 Morphology change of DNA origami nanostructures upon deposition onto HOPG

A schematic illustration of the deposition process of the DNA triangle origami onto HOPG is shown in **Figure 44(a)**. A previous report attempted to deposit DNA origami triangles on HOPG for imaging purposes but observed no deposition.[250] Contrary to that report, we found that the deposition of DNA nanostructures was achieved after depositing approximately 20 µL of the DNA origami solution onto HOPG. In this experiment, HOPG was exfoliated and immediately used (within 30s of exfoliation) for DNA deposition. Great care was taken whenever rinsing the HOPG substrate since the interaction of the DNA origami with the HOPG substrate is different from other substrates (*e.g.,* SiO_2/Si). It was important to determine the best rinsing process because AFM is a very sensitive characterization method and a clean surface is essential to obtain high quality images. The solvents tested ranged from polar to non-polar. It was discovered that having a 9/1 (v/v) ethanol/water solution was optimal (**Figure 45**), as shown elsewhere.[110] This solution removed the salt residues from the deposition without losing the origami structures.

AFM imaging was performed to examine the morphology of the DNA triangle. We found that the overall shape of the origami was preserved, but the lateral segments of the triangle were significantly deformed (**Figure 44(b)**) when compared to the ones deposited on a SiO_2/Si substrate (**Figure 44(c)**). We analyzed the cross section of 10 DNA nanostructures to extract the full width at half maximum (FWHM) values of the lateral triangle sides (**Figure 44(d)**). The DNA nanostructures deposited on HOPG were *ca.* 2.1 times wider in size compared to the ones deposited on SiO_2/Si. Note, in this analysis, the effects of AFM tip convolution and tip-sample interaction were neglected.[221] It was also found that *ca.* (74.7 ± 5.0) % of the DNA nanostructures conserved

their triangular shapes (*i.e.,* structures having a hole surrounded by three deformed edges). XPS elemental analysis showed the presence of Mg in the sample (**Figure 44(e)**), which was present in the buffer solution, and P atom from the DNA backbone (**Figure 44(h)**). Other elements such as nitrogen and oxygen were also found, but they were not quantified due to likely contribution from airborne contamination (**Figure 44(f)** and **(g)**).

To understand the observed shape deformation of DNA nanostructures, we note that ss-DNA interacts strongly with graphitic materials such as graphene[241] and carbon nanotubes.[251] Computational simulations of DNA nanostructures have also demonstrated that under aqueous conditions, the DNA origami goes through spontaneous dehybridization with a length of 3-6 base pairs.[252] One explanation for our observation is that the interaction between the DNA origami and the HOPG surface involved partial structural rearrangement and partial dehybridization of the DNA duplex, exposing the DNA bases to create π-π a stacking interaction with HOPG.[195, 251, 253] This conformation change caused the expansion of the lateral size of the DNA nanostructure.

To test if the above hypothesis was correct, we studied the effect of temperature on the deposition. We reasoned that the DNA dehybridization would be suppressed at lower temperature and thus the morphology of DNA nanostructure would be better preserved. Indeed, when the deposition was conducted in an ice bath, the average FWHM of the lateral size of the DNA nanostructure deposited on HOPG was smaller (33.5 ± 5.6 nm) than the value for samples deposited on HOPG samples at room temperature (**Figure 46**). Surprisingly, the density of the DNA nanostructure also increased, suggesting that entropy might also play a significant role in the deposition process.

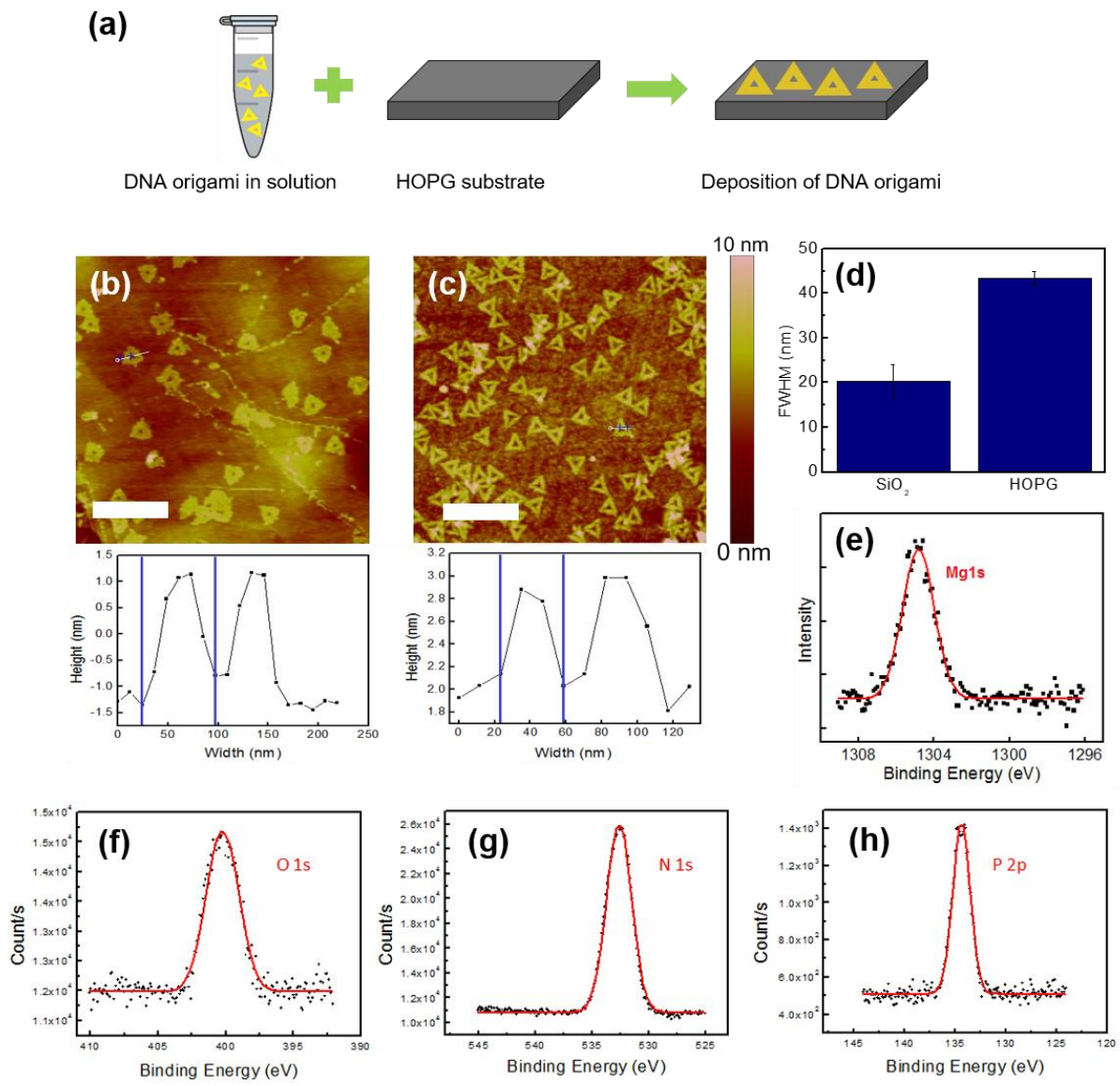

Figure 44. (a) Schematics of the deposition process. Representative AFM images of the triangular-shaped DNA origami nanostructures deposited on HOPG (b) and SiO_2/Si (c). The scale bars represent 500 nm. The cross sections below show the height profiles of selected DNA nanostructures in the image (marked by white lines). (d) Comparison of FWHM values of the lateral triangle sides of triangular-shaped DNA origami nanostructures deposited on two different substrates. (e-h) XPS spectrum (Mg 1s, O 1s, N 1s, P 2p) of the deposited triangular-shaped DNA origami nanostructures on HOPG.

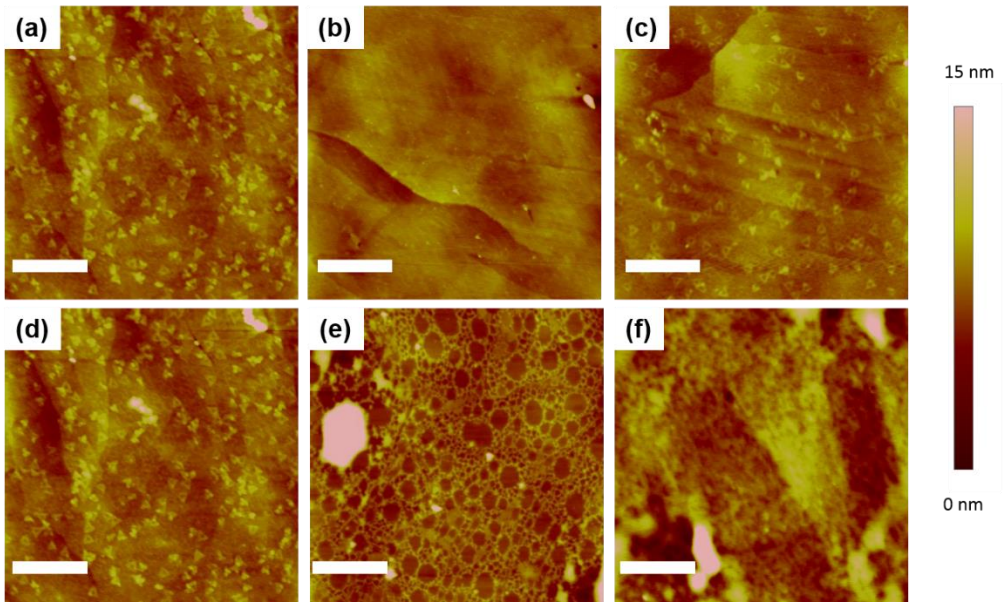

Figure 45. Representative AFM images of the DNA nanostructures deposited onto HOPG after being rinsed with different solvents: (a) No rinse. (b) Water. (c) 9/1 (v/v) ethanol/water solution. (d) Ethanol. (e) Acetone. (f) Hexane. The scale bars denote 750 nm.

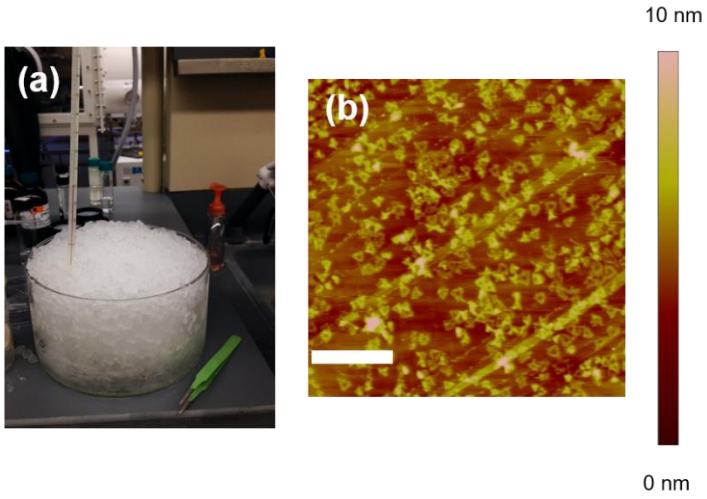

Figure 46. Effect of low temperature on the deposition process. (a) Photographic image of the experimental setup. (b) Representative AFM image of the deposited origami. The scale bar denotes 750 nm.

4.4.2 Comparison of deposition density between HOPG and SiO_2/Si substrates

SiO_2/Si is one of the most often used substrates for studying DNA nanostructures. The interaction between the DNA origami and the HOPG is promoted by strong Van der Waals forces while its interaction with a SiO_2/Si substrate has an electrostatic nature, using Mg^{2+} as an intermediate.[245] It was of interest to analyze the qualitative magnitude of the interaction between DNA and the two substrates. To this end, we exfoliated the HOPG substrate and exposed it to air for different periods of time (5 s to 1 hr) before using it for the deposition of DNA nanostructure. AFM images of the deposited DNA nanostructure were taken at 4 locations, 20 μm apart from each other. The results showed that the density of the DNA triangle did not change among these samples (**Figure 47** and **Table 11**). However, the ratio between the density of triangles found on HOPG and SiO_2/Si was *ca.* 1:2, demonstrating that the interactions between DNA and the two substrates were significantly different. A similar experiment was performed by adjusting the ionic strength of the buffer by increasing the Mg^{2+} solution concentration from 12.5 mM to 125.0 mM. In this case, although the amount of deposited DNA nanostructures decreased, the ratio of density of triangles between the HOPG and the SiO_2/Si substrate remained *ca.* 1:2, indicating that the ionic interaction between DNA and SiO_2/Si was again stronger under this condition (**Figure 48**).

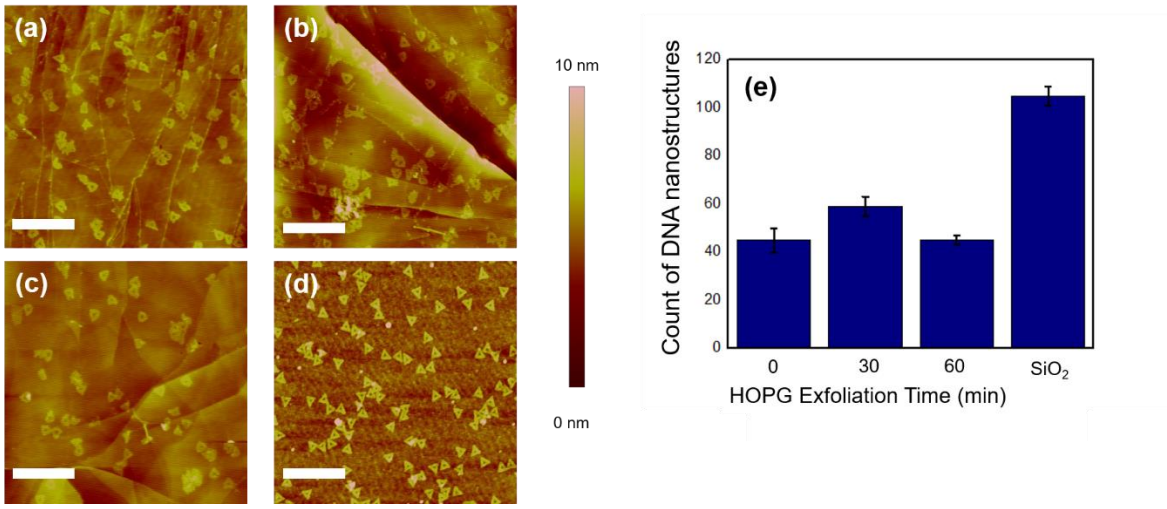

Figure 47. Representative AFM images of the DNA nanostructures deposited on different substrates. These images represent one of the four images taken per sample: (a) Fresh HOPG (~ 5 s), (b) HOPG with 30 min of air exposure, (c) HOPG with 60 min of air exposure, and (d) SiO_2/Si. The scale bars denote 750 nm. (e) Histogram graph representing the number of DNA nanostructures per AFM image (3 µm × 3 µm). Error bars represent the standard deviations out of 4 images per sample (**Table 11**).

Table 11. The number of DNA origami nanostructures presented at each 3 µm × 3 µm AFM image scanned for 4 samples (or 3 samples) with 12.5 mM Mg^{2+} buffer solution (**Figure 47**).

	Location 1	**Location 2**	**Location 3**	**Location 4**	**Average ± Standard Deviation**
Fresh HOPG	47	36	59	38	45 ± 5
30 min HOPG	51	66	54	63	59 ± 4
60 min HOPG	49	46	41	--	45 ± 2
SiO_2/Si	102	115	98	103	105 ± 4

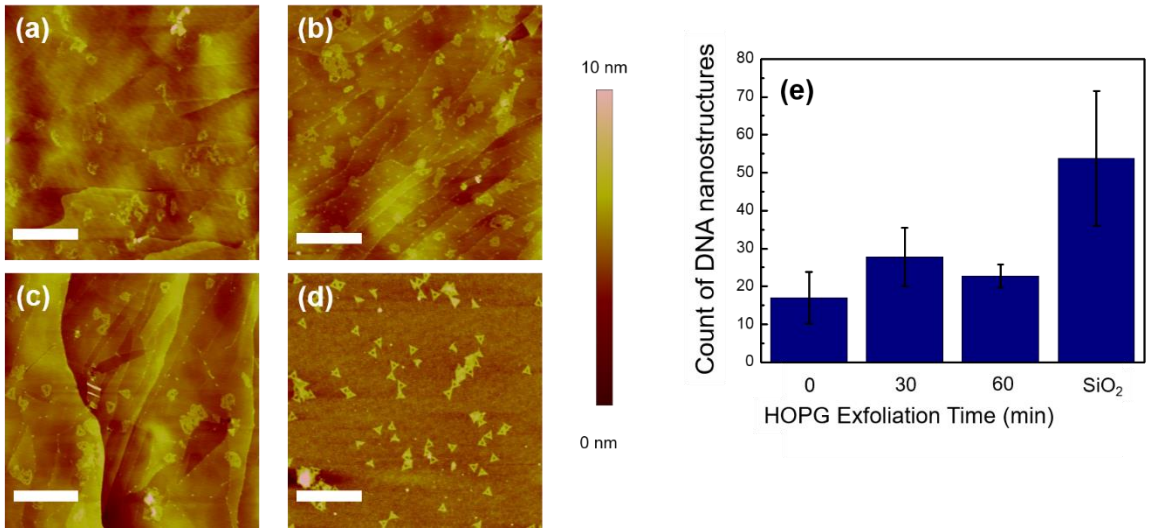

Figure 48. Representative AFM images of the DNA nanostructures deposited on different substrates when the concentration of Mg^{2+} in the buffer solution increased from 12.5 mM to 125.0 mM. These images represent one of the four images taken per sample: (a) Fresh HOPG (~ 5 s), (b) HOPG with 30 min of air exposure, (c) HOPG with 60 min of air exposure, and (d) SiO_2/Si. The scale bars denote 750 nm. (e) Histogram graph representing the number of DNA nanostructures per AFM image (3 μm × 3 μm). Error bars represent the standard deviations out of 4 images per sample.

4.4.3 Deposition of DNA origami synthesized with TAE/Mg-2 buffer onto HOPG

AFM images in **4.4.3** were collected using Asylum MFP-3D Atomic Force Microscope. Triangular-shaped DNA origami nanostructures were prepared using TAE/Mg-2 buffer, diluted to the same concentration, deposited on freshly exfoliated HOPG and characterized following the same process. Despite the difference between the buffer solutions used, a similar deposition behavior was observed. The overall shape of the origami was preserved in both cases with significant deformation (**Figure 49**). FWHM measurements for TAE/Mg DNA nanostructures and

TAE/Mg-2 DNA nanostructures were (45 ± 3) nm and (50 ± 3) nm, respectively, showing no statistical difference between the deposition using different buffers。

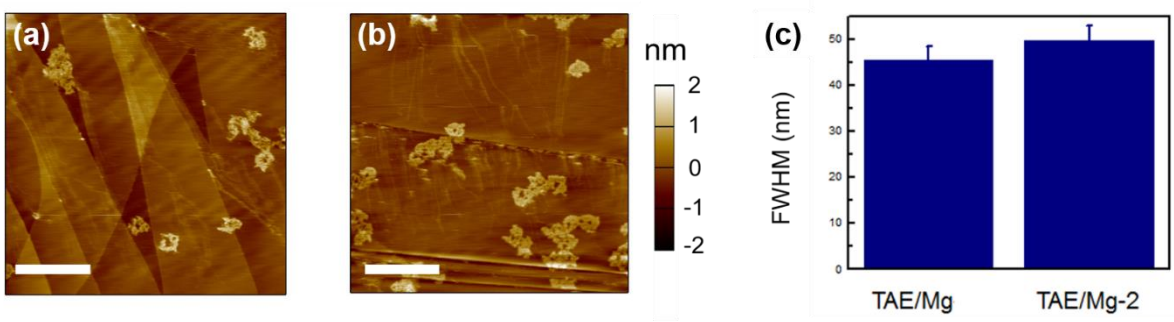

Figure 49. AFM images of the DNA nanostructures synthesized with different buffer solutions on HOPG: (a) TAE/Mg-2 buffer solution and (b) TAE/Mg buffer solution. Scale bars denote 500 nm. (c) Comparison of FWHM values of the lateral triangle sides of triangular-shaped DNA origami nanostructures synthesized with different buffer solutions when deposited on HOPG.

Another quantitative experiment to compare the deposition of triangular-shaped DNA origami nanostructures prepared with two buffer solutions was to calculate the percentage of DNA origami nanostructures that conserved their triangular shapes on the HOPG surface. The shape conservation percentages for TAE/Mg and TAE/Mg-2 buffer solutions were (74.7 ± 5.0) % and (50.0 ± 7.6) %, respectively. Based on the previous discussion, buffer solutions could affect the overall shape preservation of DNA nanostructures on HOPG. If the shape was preserved, the deformation of DNA triangle was not significantly affected by the buffer solutions.

Triangular-shaped DNA origami nanostructures synthesized with TAE/Mg buffer solutions were deposited onto different substrates (HOPG, SiO_2/Si, mica) and their densities on the surface were compared (**Figure 50**). AFM images showed that the density of DNA nanostructures on three substrates followed the trend: Mica > SiO_2/Si > HOPG. The density

comparison between HOPG and SiO_2/Si was consistent with the previous discussion (**Figure 47**) and only about half DNA nanostructures were observed on HOPG when compared to SiO_2/Si.

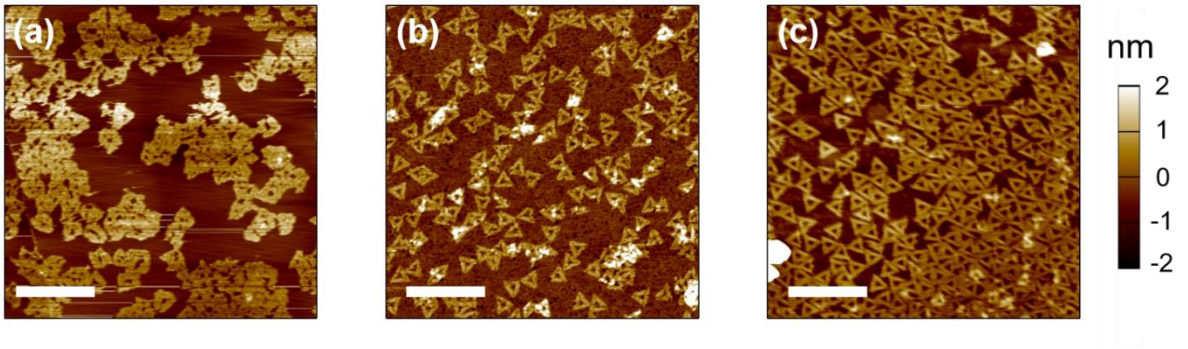

Figure 50. AFM images of deposition of triangular-shaped DNA origami nanostructures prepared with TAE/Mg buffer solution onto different substrates: (a) HOPG, (b) Mica and (c) SiO_2/Si. Scale bars denote 500 nm.

Deposition of DNA nanostructures synthesized using the TAE/Mg-2 buffer without dilution was also performed. AFM images showed that the densities of DNA nanostructures on HOPG and mica were high and more than one layer of nanostructures were observed (**Figure 51**). However, the density of DNA nanostructures on SiO_2/Si was significantly lower. Dilution and deposition of DNA nanostructures in TAE/Mg-2 buffer showed comparable densities on HOPG and mica substrates (**Figure 52**, **Table 12**) but the DNA nanostructures on SiO_2/Si were difficult to find (data not shown due to the extremely low density).

The data shown indicated that the relative DNA nanostructure density on different substrates (both HOPG and SiO_2/Si) was highly affected by the detailed composition of the buffer solution used to prepare and dilute DNA nanostructures. For example, increasing the final concentration of acetic acid (from 0.17 mM to 20 mM) and Tris (from 3.33 mM to 40 mM) resulted in an increase density of deposited DNA nanostructure on HOPG but a decrease on SiO_2/Si.

However, in any case, DNA nanostructure could be deposited on HOPG and a reasonable density was observed.

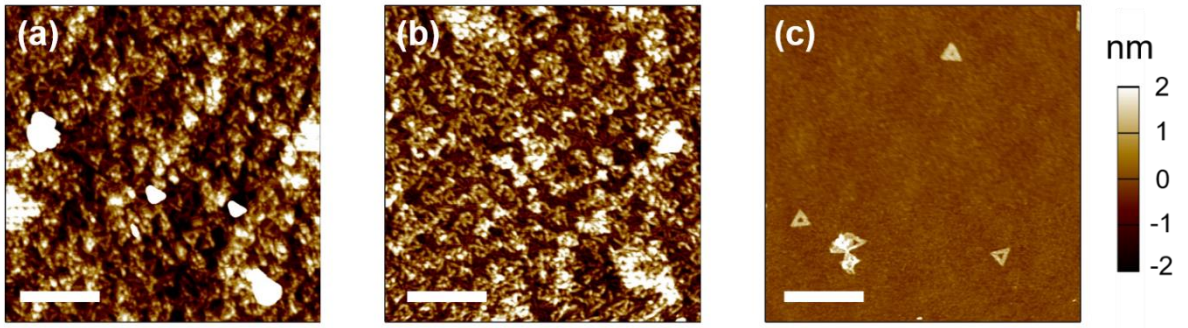

Figure 51. AFM images of deposition of triangular-shaped DNA origami nanostructures prepared with TAE/Mg-2 buffer solution (without dilution) onto different substrates: (a) HOPG, (b) Mica and (c) SiO_2/Si. Scale bars denote 500 nm.

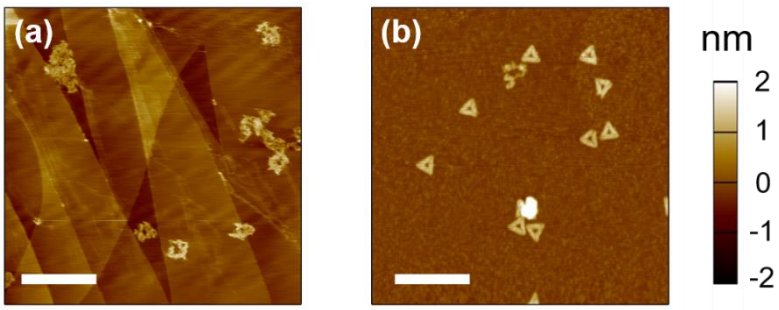

Figure 52. AFM images of deposition of triangular-shaped DNA origami nanostructures prepared with TAE/Mg-2 buffer solution (after dilution) onto different substrates: (a) HOPG and (b) Mica. Scale bars denote 500 nm.

Table 12. The number of triangular-shaped DNA origami nanostructures prepared by TAE/Mg-2 buffer solution (after dilution) present at each 2 μm × 2 μm AFM image scanned for 2 samples for each substrate (**Figure 52**).

	Location 1	Location 2	Average
Fresh HOPG	16	10	13
Mica	10	15	12

4.4.4 Effect of wettability of HOPG

In the above experiments, the HOPG substrate was used immediately (< 30 s) after exfoliation. As discussed in the introduction, the wettability of graphitic surfaces can be significantly impacted by airborne hydrocarbons contamination. Given this recent development, it was of interest to analyze if the deposition of DNA nanostructure can be achieved when the HOPG surface was exposed to air for longer periods of time. The longer the HOPG is exposed to air, the more hydrocarbon contamination present in the atmosphere can adsorb onto HOPG, making it more hydrophobic.[247] Preliminary results in **Figure 47** didn't show significant deposition behavior difference for HOPG substrates exfoliated within 1 hr. Here, freshly exfoliated HOPG substrates were left exposed to air ranging from 5 s up to 4 hr. We previously showed that exposing a freshly cleaved HOPG to air for > 1 hour will render its surface hydrophobic (water contact angle > 80˚). [247-248] The result showed that the exposure time of the HOPG did not significantly affect the deposition outcome. After 4 hours of air exposure the deposition of DNA nanostructure was still observed (**Figure 53**). FWHM analysis of the cross sections of 10 representative triangular shapes on 5 s and 4 hr samples showed that the lateral side width was slightly smaller in the case of air-aged HOPG but the difference was close to the error bar (**Figure 53(g)**). Since the airborne contamination did not significantly affect the deposition process, we concluded that the interaction

between the DNA origami nanostructure and the HOPG was not dictated by the wettability of the substrate.

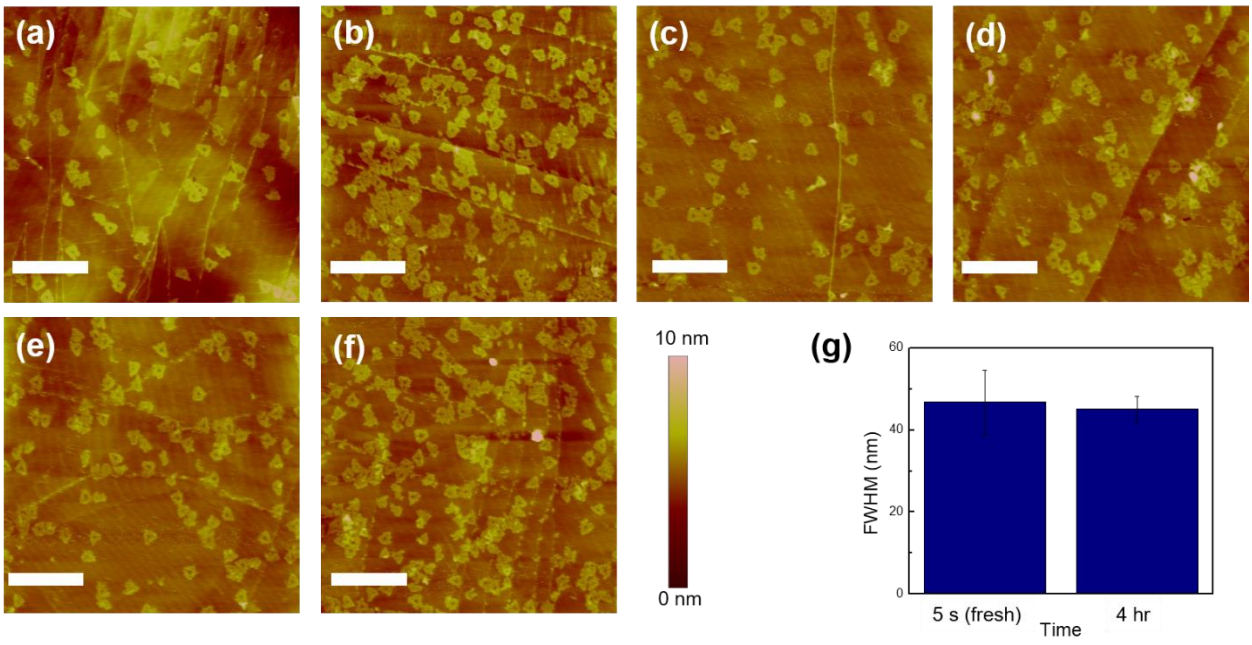

Figure 53. AFM images of the triangular-shaped DNA origami nanostructures deposited onto HOPG exfoliated and exposed to air for different times: (a) ~ 5 s (fresh); (b) 30 min; (c) 1 hr; (d) 2 hr; (e) 3 hr; (F) 4 hr. The scale bars denote 750 nm. (g) Comparison of FWHM values of the lateral triangle sides of triangular-shaped DNA origami nanostructures deposited on HOPG exfoliated for different times. The analysis was performed for 10 DNA nanostructures on each image in (a) and (f).

Similar experiments were repeated with DNA nanostructures prepared using TAE/Mg-2 buffer. Different HOPG samples were left exposed to air for ~ 5 s (fresh) and 4 hr before deposition of DNA nanostructures prepared with TAE/Mg-2 buffer solution. The result (**Figure 54**) showed that again the exposure time of the HOPG did not affect the deposition process, meaning that buffer

solution didn't significantly affect the deposition of DNA nanostructures on HOPG surface. AFM images in **Figures 54** were collected using Asylum MFP-3D Atomic Force Microscope.

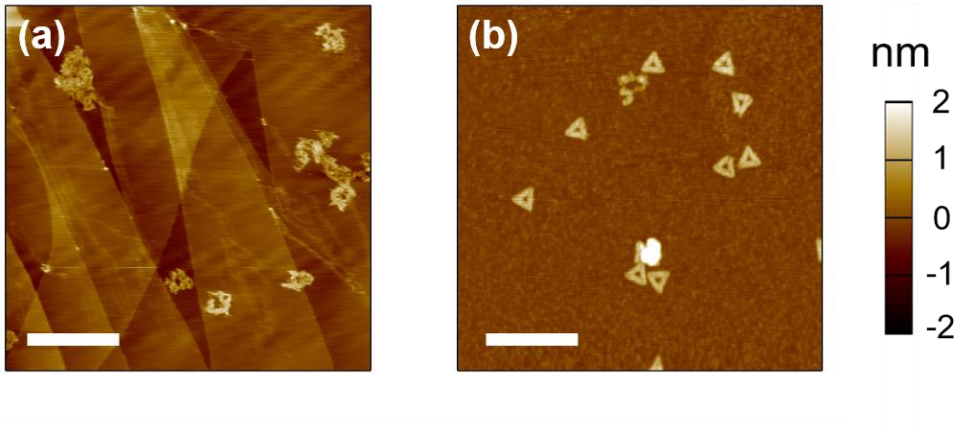

Figure 54. AFM images of the triangular-shaped DNA origami nanostructures deposited onto HOPG exfoliated and exposed to air for different times: (a) ~ 5 s (fresh); (b) 4 hr. The scale bars denote 500 nm.

4.4.5 Stability of deposited DNA nanostructures

Having established the successful deposition of DNA nanostructures on HOPG, we moved our attention to the stability of deposited DNA nanostructures in air. Same-location AFM images were taken after the sample was exposed to air for up to a week (**Figure 55**). It was observed that the average FWHM of the lateral triangle sides of triangular-shaped DNA origami nanostructures remained unchanged, indicating the absence of diffusion of the DNA backbone on HOPG in the dry state. A similar result was also observed when the DNA nanostructures were deposited in a SiO_2/Si wafer (**Figure 56**).

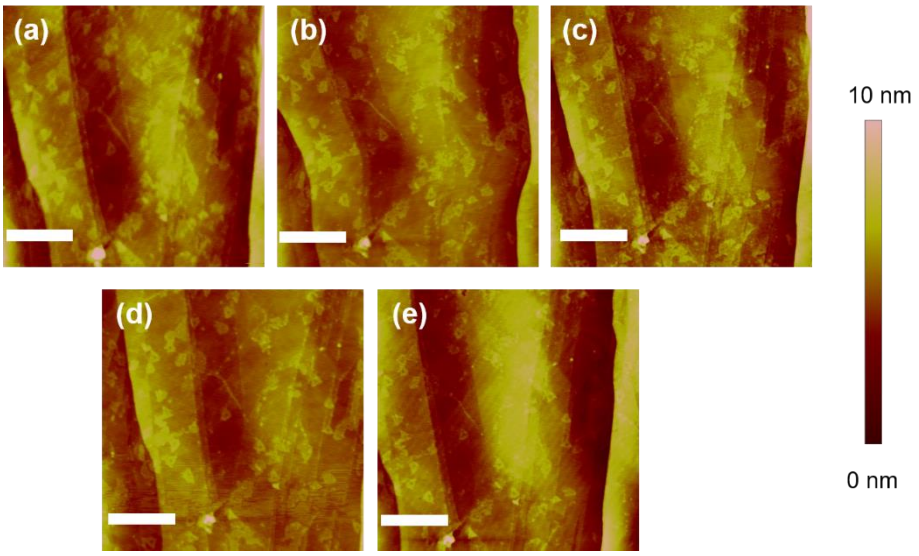

Figure 55. Same location AFM images of the DNA nanostructures at different times after the deposition on HOPG. (a) Fresh (~ 2 hr). (b) 2 days. (c) 4 days. (d) 5 days. (e) 7 days. The scale bars denote 750 nm.

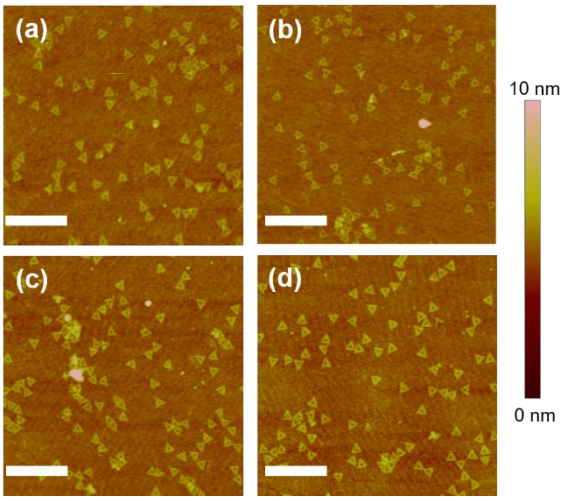

Figure 56. Same area AFM images of the DNA nanostructures at different times after the deposition on SiO_2/Si substrate. (a) Fresh (~2 hours). (b) 2 days. (c) 5 days. (d) 7 days. The scale bars denote 750 nm.

4.4.6 Role of single stranded DNA

Single stranded DNA (ss-DNA) is known to strongly adsorb onto HOPG.[254-256] Large excess amount of ss-DNA was used in the synthesis of DNA origami nanostructures. Although most of these ss-DNA was removed by the purification process, it was important to understand the effect of ss-DNA on the deposition process. For this purpose, DNA origami nanostructures with different staple-to-scaffold ratios (1:1 to 10:1) were successfully synthesized via thermal annealing process and purified by the same methods (**Table 13**). The corresponding AFM images on mica (**Figure 57(a)**) show the well-defined DNA origami structures. Then DNA origami nanostructures were deposited on the freshly cleaved HOPG surface. The deposition of the DNA nanostructures was achieved on HOPG no matter what staple-to-scaffold ratio was used in synthesis. Immediately after the deposition process, AFM imaging was performed to examine the shapes of the DNA nanostructures (**Figure 57(b)**) and the results showed that the triangular shapes of DNA origami nanostructures were similar in all cases. However, all the AFM images showed the deformation of lateral segments of the triangular-shaped DNA origami nanostructures, consistent with our earlier observations. No significant difference was observed between samples with different staple-to-scaffold ratios. As discussed above, ss-DNA has a strong interaction with HOPG surface, which presumably causes the structural deformation of DNA nanostructures when deposited on the HOPG surface. At the largest staple-to-scaffold ratio, more single stranded staples were left over in the sample after the purification step, meaning that more single strands could be deposited on HOPG surface. However, even at a 10:1 staple-to-scaffold ratio, the remaining single strands did not affect the spontaneous DNA nanostructure deposition process on HOPG. AFM images in **Figures 57** were collected using an Asylum MFP-3D Atomic Force Microscope.

Table 13. Different reagent concentrations used for the synthesis of DNA origami nanostructures for the comparison between different staple-to-scaffold ratios.

Reagent Volume/ µL	**#1**	**#2**	**#3**	**#4**	**#5**
M13mp18 single stranded phage DNA solution (1 mg/mL = 454 nM)	8.57	0	0	3.00	9.00
M13mp18 single stranded phage DNA solution (52. 8 nM)	0	8.57	14.3	0	0
DNA staple strand mixture solution (300 nM each)	15.0	15.0	15.0	15.0	15.0
Deionized water (µL)	77	77	71	82	76
1 × TAE/Mg buffer (µL)	181	181	181	181	181
Staples : Scaffold Ratio	1.2:1	10:1	6:1	3:1	1:1

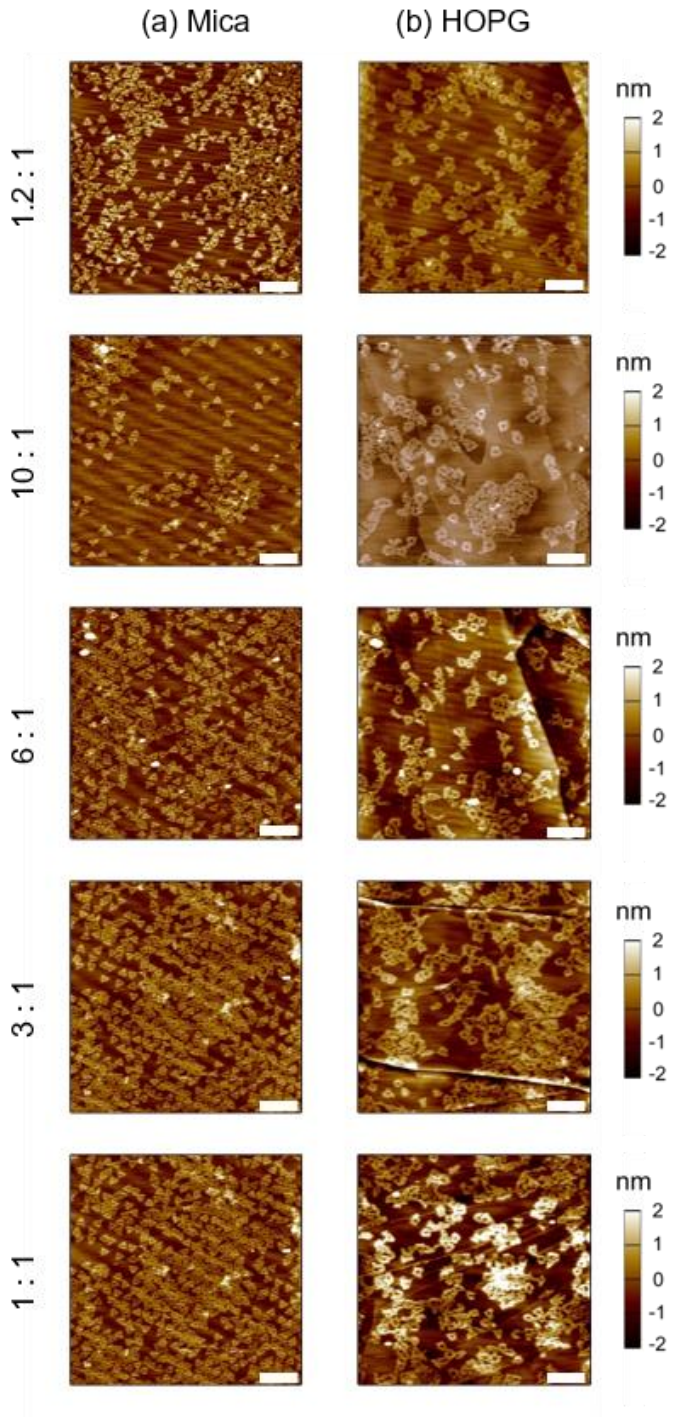

Figure 57. AFM images of triangular-shaped DNA origami nanostructures synthesized with different staple-to-scaffold ratios (**Table 13**) and deposited onto mica (a) and HOPG (b). Scale bars denote 500 nm.

Another approach we used was the addition of non-hybridizing irrelevant ss-DNA to the DNA origami solution. This ss-DNA does not contain a complimentary sequence longer than 8 nucleotides with respect to the M13mp18 single stranded phage DNA or any of the staple strands. The mixture (ratio of ss-DNA : DNA origami = 0 - 5) was deposited on the freshly cleaved HOPG substrate. The AFM images of these samples showed similar morphology, demonstrating that the added ss-DNA did not significantly affect the deposition of the DNA nanostructures on HOPG (**Figure 58** and **Table 14**). We have also used other types of DNA and DNA nanostructures such as λ-DNA and DNA tile nanostructures for the deposition (**Figure 59**). Surprisingly, the deposition of these DNA nanostructures onto HOPG was not successful. A possible explanation could be due to limited surface area of these DNA structures, leading to much smaller van der Waals interaction between DNA structures and the HOPG surface.

Table 14. Molar concentrations of DNA origami nanostructures and irrelevant DNA ss-DNA in different experiments.

Experiment #	**1**	**2**	**3**	**4**
DNA origami nanostructures (nM)	1.2	1.2	1.2	1.2
Irrelevant ss-DNA (nM)	0	1.2	3.0	6.0
Ratio of ss-DNA : DNA origami	0	1:1	2.5:1	5:1

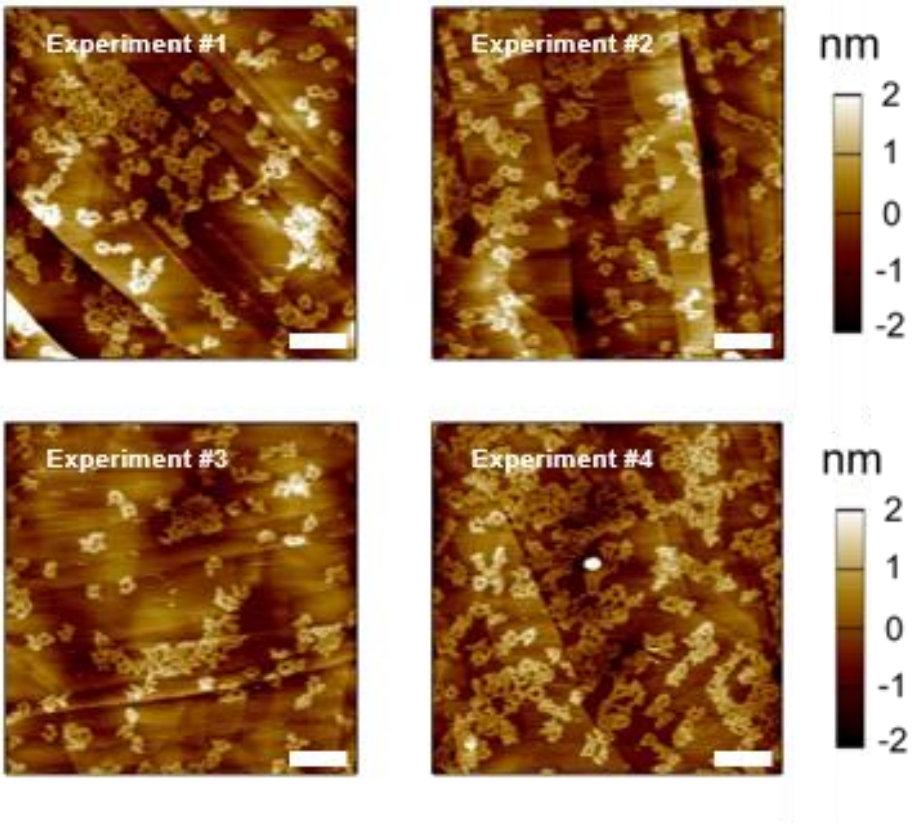

Figure 58. AFM images for mixture of DNA origami nanostructures with different amounts of irrelevant ss-DNA. The image numbers correspond to the sample numbers in **Table 14**. Scale bars denote 500 nm.

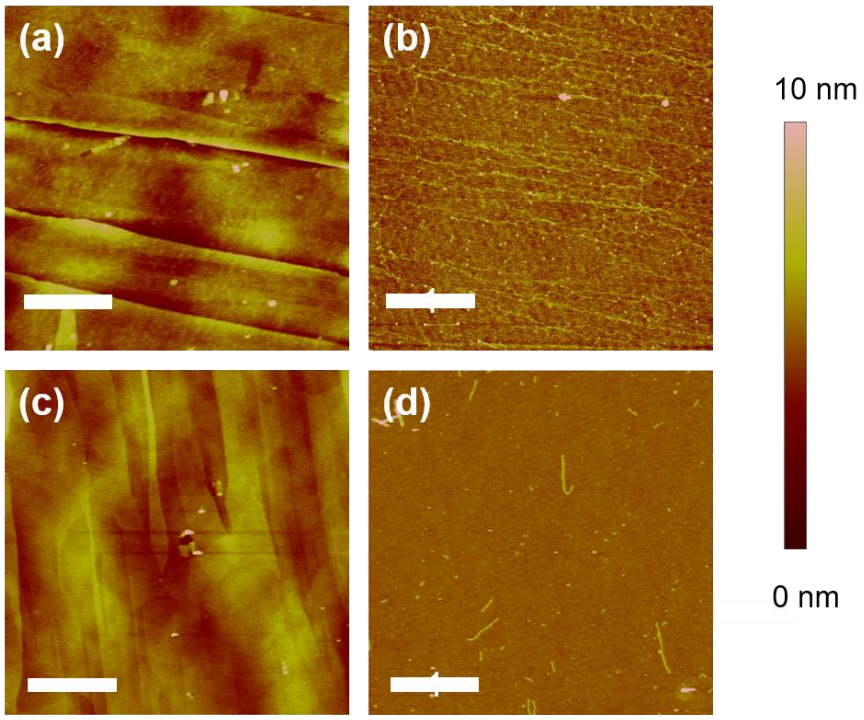

Figure 59. AFM images of the deposition of other DNA samples on HOPG and SiO_2/Si substrates. (a) λ-DNA on HOPG. (b) λ-DNA on SiO_2/Si. (c) Tile DNA nanostructures on HOPG. (d) Tile DNA nanostructures on SiO_2/Si. The synthesis of the DNA tile was detailed elsewhere.[37] Scale bars denote 750 nm.

4.4.7 Application in area-selective CVD

HOPG is one of the most common substrates used for imaging and deposition of nanomaterials.[257-258] More importantly, with the exception of step edges, the basal plan of HOPG is chemically inert. This particular feature makes HOPG a desirable substrate if one wishes to initiate chemical transformation on and only on the deposited DNA nanostructures. As an example, we previously reported that DNA nanostructures could promote chemical vapor deposition (CVD) of inorganic oxides (*e.g.*, SiO_2).[186] In that work, the DNA nanostructures were supported on a

SiO_2/Si substrate, which was also active for CVD. As a result, it was difficult to confine the CVD of SiO_2 only on DNA nanostructures.

We carried out CVD growth of SiO_2 on the DNA origami deposition on HOPG using TEOS, NH_4OH, water, and isopropanol and the growth of SiO_2 was successful (**Figure 60**). The average SiO_2 growth was *ca.* 8.5 nm, as shown in the cross-section analysis (**Figure 60(a)**). XPS data confirmed the presence of SiO_2 after the CVD growth, with a surface Si coverage of (4.35 ± 0.76) atom% (**Figure 60(b)**). The thickness of CVD-grown SiO_2 was much higher compared to our previous report of SiO_2 growth on DNA nanostructures deposited on a SiO_2/Si substrate (*ca.* 2 nm). We attributed the improvement to the inertness of the HOPG substrate, which improved the spatial selectivity and also allowed more aggressive reaction conditions to be used. XPS analysis of the carbon peak before and after the CVD growth were similar, demonstrating that the CVD process was selective and that most of the HOPG surface was not covered by SiO_2 (**Figure 60(c)**). The CVD growth of TiO_2 was also explored but was not as successful due to the high reactivity of the TiO_2 precursor, which leads to TiO_2 deposition at the reactive step edges of HOPG.[259]

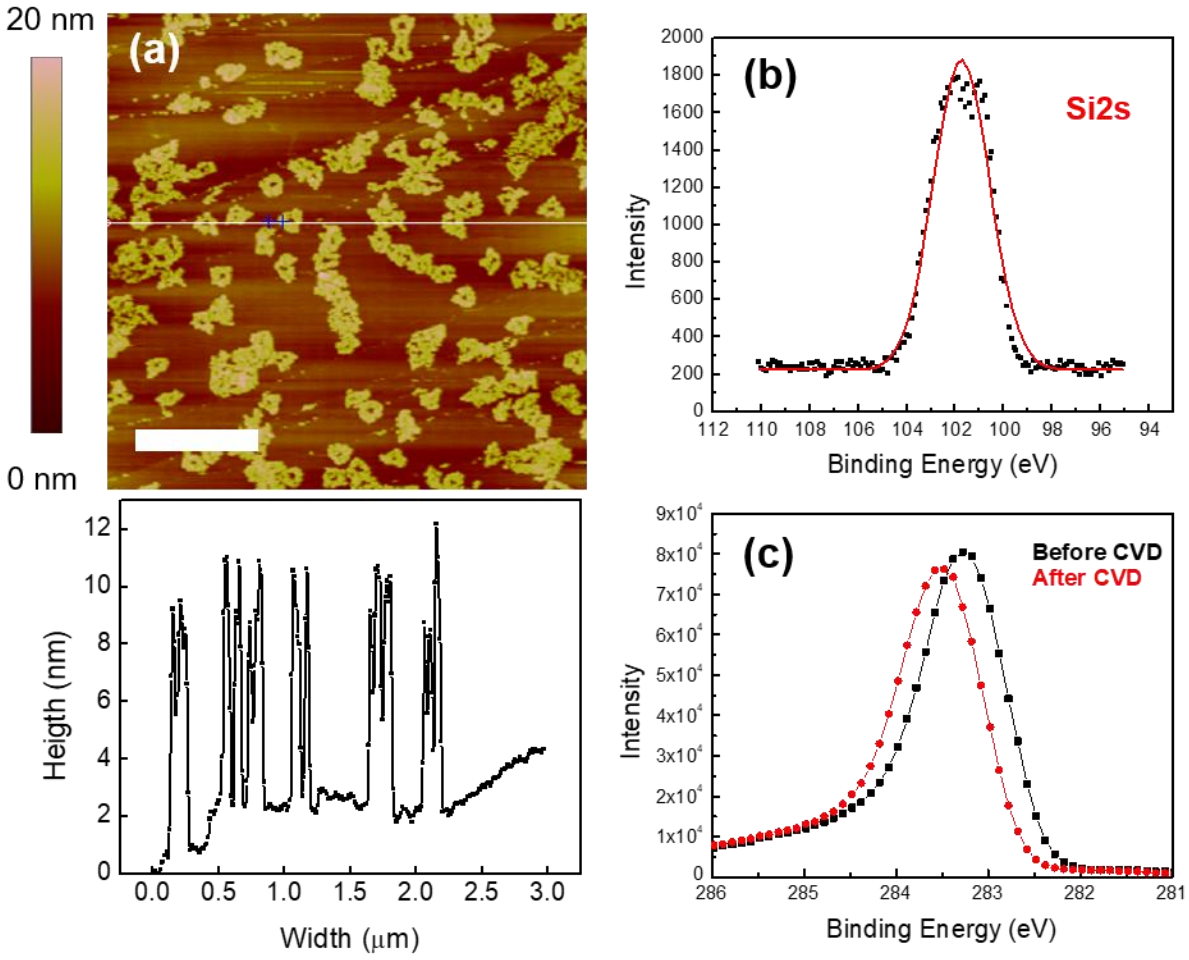

Figure 60. (a) AFM image and cross section analysis of the CVD growth of SiO_2 on the DNA nanostructures deposited on the HOPG surface. While horizontal line indicates where the cross section was determined. The scale bar denotes 750 nm. (b) XPS spectrum (Si 2s) of the sample after CVD of SiO_2. (c) XPS C 1s (Black) before CVD deposition and (Red) after CVD deposition of SiO_2.

4.5 Conclusion

In summary, we have studied the deposition of DNA nanostructures onto HOPG from an aqueous buffer solution. No surface modification on the HOPG or modification of the DNA nanostructures was needed to achieve the deposition. We observed significant structural deformation of the DNA nanostructures, which we attribute to the π-π interaction between the DNA bases and the HOPG substrate. The deposition was not sensitive to the surface contamination of the HOPG surface by airborne hydrocarbon. The deposited DNA nanostructures were stable for at least a week. As a demonstration for nanofabrication application, the DNA nanostructures on HOPG substrate was used as templates to promote site-selective chemical vapor deposition of SiO_2. We hope this study will expand the use of DNA nanostructure in a broader range of surface-related studies and applications.

5.0 Photochemical Active DNA Tetrahedron Nanostructure

5.1 Chapter Preface

Materials contained in this chapter are in preparation for publication as a research article.

List of Authors: Anqin Xu, James Hemphill, Alexander Deiters and Haitao Liu

Author Contributions: A.X., A.D. and H.L. designed and directed the experiments. A.X. conducted the experiments with help from J.H. for synthesis and supply of oligonucleotide strands with photo-cleavable linkers. All authors discussed the results. A.X. and H.L. wrote the manuscript with input from all authors.

5.2 Introduction

A single-step synthesis method of DNA tetrahedron structure was first reported by Goodman and co-workers in 2004 (**Figure 61(a)**).[31] The design of the DNA tetrahedron nanostructure is simple, in which each of the four component oligonucleotides runs around one face of the tetrahedron and hybridizes with each other to form edges of double helices. Since then, a family of DNA tetrahedron nanostructures, either regular or irregular, were designed and synthesized through self-assembly process.[260] The high-yield synthesis of the DNA tetrahedron nanostructures is conveniently achieved by mixing the four component oligonucleotides of equimolar quantities and performing a rapid thermal annealing process. The DNA tetrahedron structure is the simplest possible 3D DNA polyhedron structure. The structure is mechanically robust and rigid with braced geometry. The range of configurations the structure can adopt is well controlled. All these intrinsic structural features make it a potential geometrical building block. By extending the oligonucleotides beyond the vertices, different DNA tetrahedrons can hybridize via the sticky ends, creating a larger structure with face-to-face or vertex-to-vertex tetrahedrons (**Figure 61(b)**).[31, 260] The reversible reconfiguration of DNA tetrahedron nanostructure was also demonstrated by adding a specially designed hairpin structure into one of the edges (**Figure 61(c)**). By adding a complementary 'fuel' strand to the system, the hairpin structure can be opened and the DNA tetrahedron nanostructure is expanded.[206]

The DNA tetrahedron nanostructure is one of the most popular DNA materials for biosensing[150-154] and drug delivery.[169, 174, 261] The current drug delivery applications of DNA tetrahedron nanostructures allows the selective delivery of doxorubicin, especially to drug resistant cells. Recently, Zhang and co-workers also managed to probe and regulate apurinic/apyrimidinic endonuclease (APE1) in cells via inserting an apurinic/apyrimidinic (AP) site in the DNA

tetrahedron nanostructure.[262] Meanwhile, each DNA tetrahedron structure has a well-defined inner pocket in nanometer scale. The edge of each DNA tetrahedron nanostructure was less than 10 nm so its inner pocket has a diameter of about 2-3 nm. This is a suitable size for hosting some large molecules, including proteins. One reported application demonstrated the encapsulation of a single molecule of cytochrome *c* (a 12.4 kDa protein) within this rigid DNA tetrahedral cage (**Figure 61(d)**).[263] The DNA cages may allow functional control of proteins.

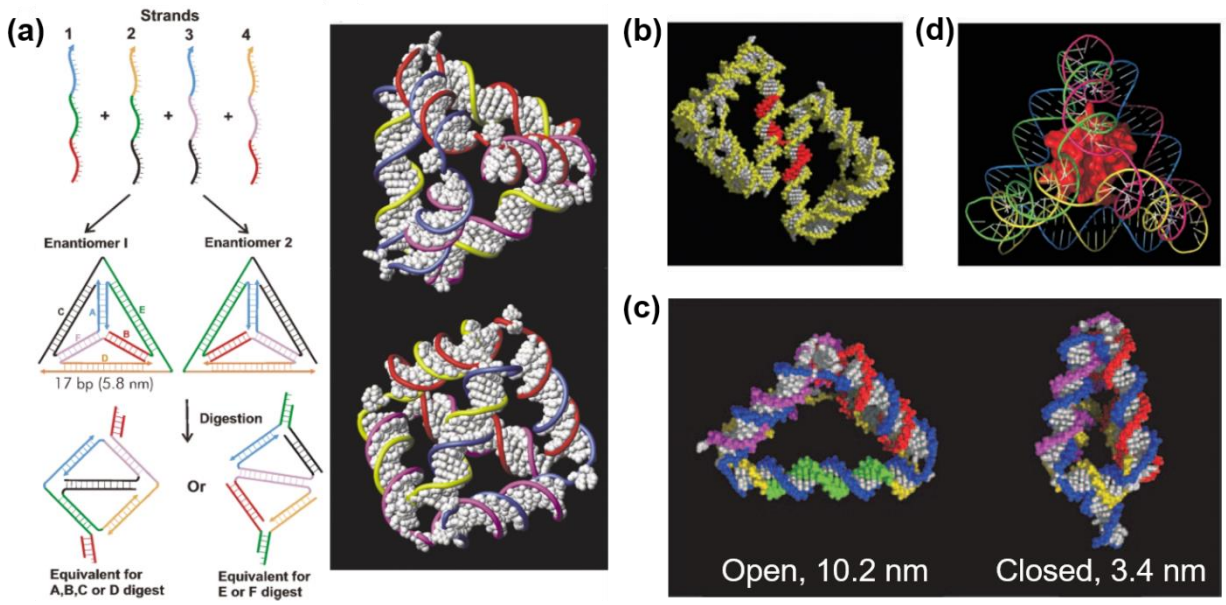

Figure 61. DNA tetrahedron nanostructures. (a) Synthetic scheme of the first DNA tetrahedron nanostructure, with representations of the final product illustrating both possible enantiomers. (b) DNA tetrahedron dimer. (c) Reconfigurable DNA tetrahedron with views of the open and closed states.wile (d) Encapsulation of cytochrome *c* inside DNA tetrahedron nanostructure Reprinted with permission from: (a) Reference 31, copyright © 2004, Royal Society of Chemistry; (b) Reference 260, copyright © 2005, American Association for the Advancement of Science; (c) Reference 206, copyright © 2008, Springer Nature; (d) Reference 263, copyright © 2006, Wiley-VCH Verlag GmbH & Co. KGaA, Weinheim.

Light has been widely used by chemists to provide energy and regulate reaction. As an external source, light can be precisely controlled spatially and temporally.[94] Insertion and photo-activation of a photo-cleavable linker can lead to photo-regulation of oligonucleotide function and thus the structural or functional change of a DNA nanostructure. Several designs of photochemical active cages have been demonstrated for cell uptake and molecule delivery.[100-101] However, the nanocages used in those cases were larger than 50 nm, which may lead to potential problems with the function control of the encapsulated molecules, especially when the molecule is significantly smaller than the cavity of the nanocage. The encapsulation of protein and enzyme inside a DNA nanostructure is often achieved by site-specific modifications[264] so the encapsulation efficiency is generally higher for the more compact DNA nanostructure of smaller size. Meanwhile, the biosafety of DNA nanostructures uptake into cells has always been a concern for scientists. It is believed that the amount of DNA inside a cell is strictly maintained at a certain level. Larger DNA nanostructures can cause a significant increase in the amount of exogenous DNA in cells, which may lead to unexpected problems.[265]

Here we want to demonstrate a sub-10 nm photochemical active DNA tetrahedron structure which can be partially or completely opened by light control. This will broaden the applications of DNA tetrahedron nanostructures for drug delivery by adding another method for selective targeting *in vivo*.

5.3 Experimental Section

5.3.1 Materials

Unmodified oligonucleotides used for regular DNA tetrahedron synthesis (**Table 15, Figure 62**) were purchased from IDT and used without further purification. Oligonucleotide strands with photo-cleavable linkers (**Table 16, Figure 62**) for photochemical active DNA tetrahedron synthesis were synthesized by Dr. Alexander Deiter's group (Department of Chemistry, University of Pittsburgh) and purified with polyacrylamide gel electrophoresis (PAGE). The photo-cleavable linker (**Figure 62**) is sensitive to 365 nm irradiation. DNA strand gets cut off at the linker position when exposed to 365 nm light.

2-Amino-2-(hydroxymethyl)-1,3-propanediol (Trizma base or Tris, ≥ 99.9%), Ethylenediaminetetraacetic Acid (EDTA, ≥ 99%), magnesium chloride hexahydrate (≥ 99.0%), hydrochloric acid (ACS reagent, 37%), Tris-Borate-EDTA buffer (TBE buffer, 10 × concentrate), acrylamide/ bis-acrylamide (29:1, 30% solution), ammonium persulfate (APS, ≥ 98.0%), N,N,N',N'-Tetramethylethylenediamine (TEMED, ~ 99%), PCR 20-bp low ladder (200 μg/mL), gel loading buffer (containing bromophenol blue as an indicator of pH and mobility), stains-all (~ 95%), formamide (≥ 99.5%) and glycerol (≥ 99.0%) were purchased from Sigma-Aldrich, USA and used as received without further purification. Stains-all can be used to stain different biological molecules: DNA – blue; RNA – Purple; Protein – Red. Here, DNA was the only target molecule in our gel so the bands given by a black-white gel imager were all DNA signals. Water (18.3 MΩ) was filtered by a water purification system (Barnstead MicroPure Standard, Thermo Scientific, Waltham, MA) and used throughout the entire experiment for the preparation of chemical solutions and in the cleaning of the experimental apparatus.

Table 15. Sequences of oligonucleotides used to form regular DNA tetrahedron.

Strand Number	Sequences of Oligonucleotides (5'-3')
1	ACATTCCTAAGTCTGAAACATTACAGCTTGCTACACGAGAAGAGCCGCCATAGTA
2	TATCACCAGGCAGTTGACAGTGTAGCAAGCTGTAATAGATGCGAGGGTCCAATAC
3	TCAACTGCCTGGTGATAAAACGACACTACGTGGGAATCTACTATGGCGGCTCTTC
4	TTCAGACTTAGGAATGTGCTTCCCACGTAGTGTCGTTTGTATTGGACCCTCGCAT

Table 16. Sequences of oligonucleotides with photo-cleavable linkers used to form photochemical active DNA tetrahedron.

Strand Number	Sequences of Oligonucleotides with Photo-cleavable Linkers (5'-3')
1*	ACATTCCTAAGTCTGAA-(linker)-CATTACAGCTTGCTACAC-(linker)-AGAAGAGCCGCCATAGTA
2*	TATCACAGGCAGTTGA-(linker)-AGTGTAGCAAGCTGTAAT-(linker)-GATGCGAGGGTCCAATAC
3*	TCAACTGCCTGGTGATA-(linker)-AACGACACTACGTGGGAA-(linker)-CTACTATGGCGGCTCTTC
4*	TTCAGACTTAGGAATGT-(linker)-CTTCCCACGTAGTGTCGT-(linker)-TGTATTGGACCCTCGCAT

5.3.2 Preparation of buffer solution

Synthesis buffer solution was prepared by mixing trizma base, hydrochloric acid, EDTA, and magnesium chloride. The concentrations of tris, EDTA and Mg^{2+} are 100 mM, 10 mM, and

200 mM, respectively and hydrochloric acid was added to adjust the pH of the buffer to 8.0. The buffer is termed the standard 10 × TEM buffer, which means it is 10 times concentration of 1 × TEM buffer. The buffer was used in the synthesis of DNA tetrahedrons and it was diluted to 1 × TEM buffer when used to make the synthesis mixture with oligonucleotide strands.

5.3.3 Synthesis of regular DNA tetrahedron nanostructure

Regular DNA tetrahedrons were constructed following reference[31] but the annealing time was extended for a better synthesis result. Equimolar quantities (1 μM) of oligonucleotides #1 to #4 (**Table 15**) were mixed in 1 × TEM buffer. The mixture was put into a thermal cycler (MiniCycler™, MJ Research). The temperature was raised to 95 °C and kept at 95 °C for 2 minutes, and then reduced to 20 °C over 15 min (**Figure 62**). The 100% yield of DNA tetrahedrons was 1 μM.

5.3.4 Synthesis of photochemical active DNA tetrahedron nanostructure

Oligonucleotides with photo-cleavable linkers #1* to #4* (**Table 16**) were used instead of oligonucleotides #1 to #4 in **5.3.3** to synthesize photochemical active DNA tetrahedron (**Figure 62**). For the 'partially' photochemical active DNA tetrahedron, a mixture of oligonucleotide with and without photo-cleavable linkers were used.

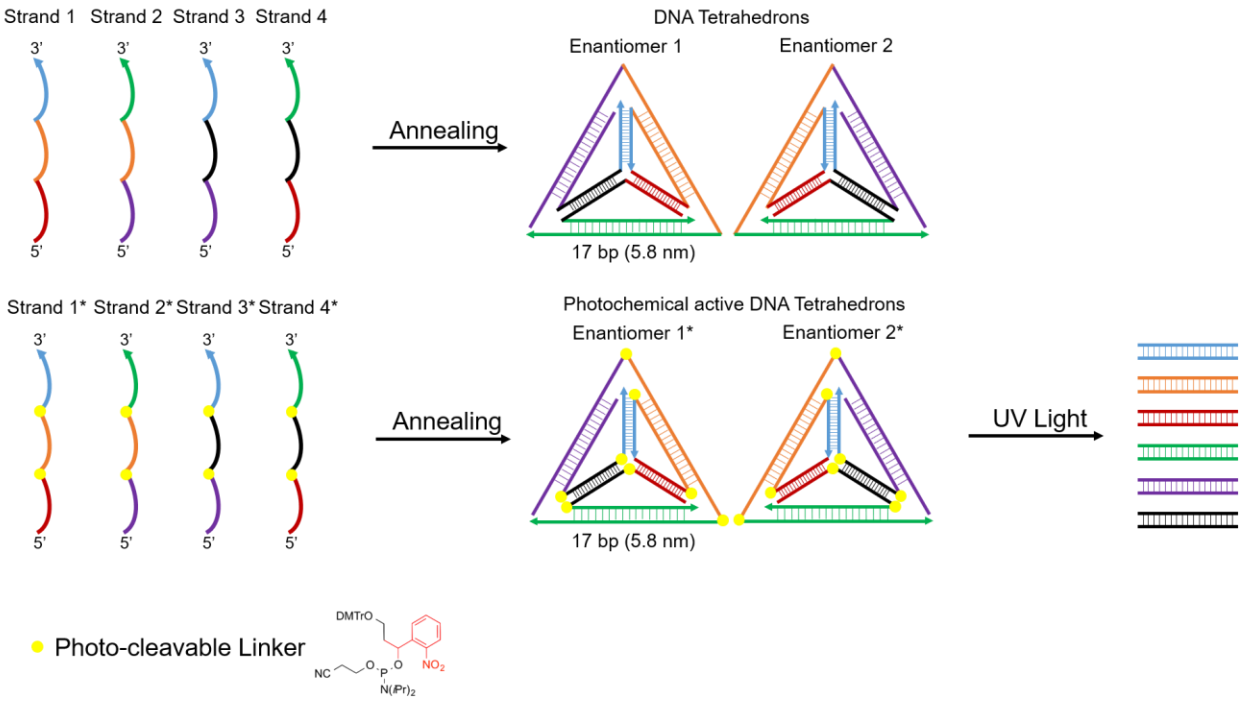

Figure 62. Scheme of DNA tetrahedron nanostructure synthesis and the photochemical cleavage of photochemical active DNA tetrahedron.

5.3.5 Irradiation of DNA tetrahedron nanostructures

The samples were transferred into individual UV-transparent plastic microcuvettes for irradiation with the photo illuminator with 365 nm wavelength. The microcuvettes were lied down on the illumination plate to achieve the highest irradiation efficiency.

5.3.6 Polyacrylamide Gel Electrophoresis (PAGE) analysis

Polyacrylamide Gel Electrophoresis (PAGE) analysis was carried out by a set of BIO-RAD Mini-PROTEAN Tetra Cell with 0.75 mm thickness gel plates. The power supply was a PowerPac

Basic Power Supply from BIO-RAD. PAGE gel at a gel concentration of 12.5% was used to analyze all the samples. Acrylamide (4.2 mL, 30%), 10 × TBE buffer (1.0 mL), deionized water (3.8 mL), APS (6.4 mg) were mixed thoroughly in a 50 mL centrifuge tube. Then 5.0 μL of TEMED was added to the solution immediately before the solution was transferred in between the gel plates using a micropipette. The gel was left undisturbed for 1 hr for complete solidification.

The concentration of DNA sample used for PAGE analysis was either 10 μM for oligonucleotides or 1 μM for the synthesized DNA tetrahedrons. DNA sample was mixed with gel loading buffer before deposited into a gel well. Two types of gel loading buffers were used in the experiment. The first type was purchased from Sigma-Aldrich and referenced herein as 'Sigma-Aldrich gel loading buffer'. It contained bromophenol blue as an indicator of pH and mobility. Bromophenol blue showed up as a band around 15-20 bp position on a 12.5% PAGE gel. To use Sigma-Aldrich gel loading buffer for DNA sample loading, 20 μL of DNA sample was thoroughly mixed with 4 μL of gel loading buffer and then transferred into a gel well using a micropipette. The sample and gel loading buffer volumes were decreased to 5 μL and 1 μL, respectively, for the loading of PCR 20 bp low ladder. Sigma-Aldrich gel loading buffer was used throughout the experiment unless otherwise specified.

The second type of gel loading buffer was made by mixing equal amount of glycerol and water and referenced herein as 'A.X. gel loading buffer'. To use A.X. gel loading buffer for DNA sample loading, 20 μL of DNA sample was thoroughly mixed with 2 μL of gel loading buffer and then transferred into a gel well using a micropipette. The sample and gel loading buffer volumes were decreased to 5 μL and 0.5 μL, respectively, for the loading of PCR 20 bp low ladder.

After samples of suitable volumes were loaded to different gel lanes, the gel electrophoresis is performed in 1 × TBE buffer at 200 V for about 1.5 hours. Then the gel was carefully removed

from the gel plates and stained with stains-all solution (0.005 g stains-all dissolved in 22.5 mL formamide and 27.5 mL water) for 15 min. The staining process was carried out in dark to avoid photolysis of the dye. After removed from the staining solution, the gel was carefully washed with water to clean up the dye residues on the gel surface. Finally, the gel images were taken with ChemiDoc Imaging Systems (BIO-RAD) using 'white' mode.

5.3.7 Atomic Force Microscopy (AFM) characterization

The structure of DNA tetrahedron was scanned using an Asylum MFP-3D Atomic Force Microscope by AC mode in air with HQ:NSC15/Al BS AFM probes (325 kHz, 40 N/m) purchased from μmasch (NanoAndMore USA). Images were analyzed by Igor Software (Version 6.3.7.2) equipped with Asylum Research package. The image was collected at a scan rate of 1 Hz and 512 data points per line with the scan size identified by scale bar.

5.4 Results and Discussion

5.4.1 Formation of DNA tetrahedron nanostructures

Oligonucleotide strands #1 - #4 (without photo-cleavable linkers), #1* - #4* (with photo-cleavable linkers) were loaded to PAGE gel with formed regular DNA tetrahedrons and photochemical active DNA tetrahedrons. Gel electrophoresis analysis showed the successful formation of both regular DNA tetrahedrons and photochemical active DNA tetrahedrons (**Figure 63(a)** and **(b)**). The four oligonucleotide strands went through a 1:1:1:1 reaction and almost no reagent was left over after the reaction since there were no visible bands in Lane 6-9 corresponding to the bands in Lane 2-5 in both gels. Pure products were formed with thick bands shown on PAGE gel, indicating the formation of the expected DNA tetrahedrons. Defining 200 bp ladder as the standard, the relative mobility of each DNA sample was presented in **Figure 63(c)**. No significant difference in relative mobility was observed for the two types of DNA tetrahedrons. The substitution of regular nucleotides in DNA strands by the photo-cleavable linkers didn't affect the formation of DNA tetrahedrons.

One note here is that DNA tetrahedron was much slower than a typical 102-bp ds-DNA in the gel when compared to PCR 20 bp low ladder in Lane 1, in which the sixth band from the bottom indicated a standard 120-bp ds-DNA sample. This is because the 3D structure of DNA tetrahedron reduced the molecule's mobility and made the structure more difficult to travel through the gel, which was also the reason for smeared bands observed in Lane 6-9 in both gels. Another note is that more than one bands were observed for oligonucleotide strands, especially the ones without photo-cleavable linkers. We attributed these vague bands to impurities in the samples of nucleotides due to the lack of purification of oligonucleotides by the manufacturer, the random

aggregation of DNA strands and the natural degradation of oligonucleotides. The same behavior was later observed in all the PAGE gels.

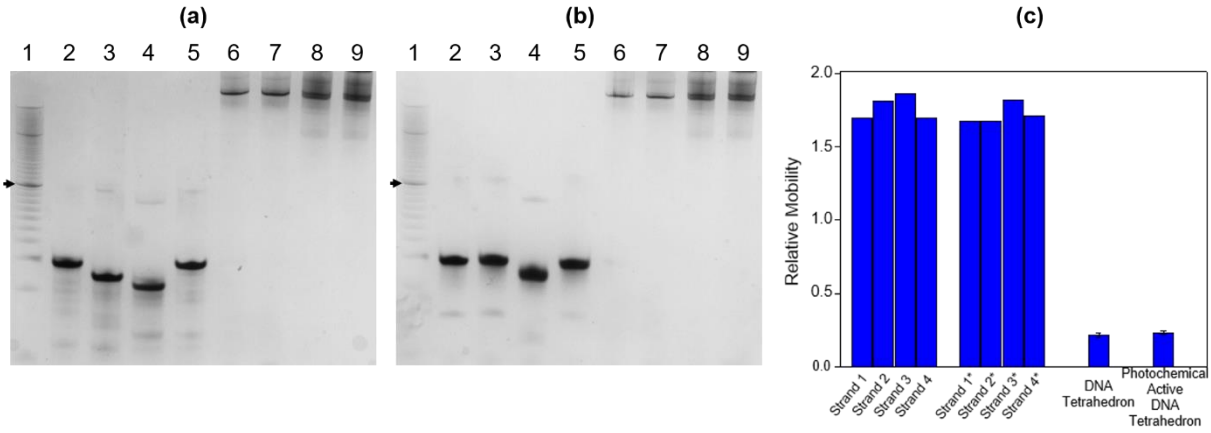

Figure 63. Gel electrophoresis results for synthesis of the DNA tetrahedrons. (a) Lane 1: PCR 20 bp low ladder. Lane 2-5: Oligonucleotide strands #1 - #4. Lane 6: regular DNA tetrahedrons. Lane 7: regular DNA tetrahedrons. Lane 8: photo-cleavable DNA tetrahedrons. Lane 9: photo-cleavable DNA tetrahedrons. (b) Lane 1: 20-bp ladder. Lane 2-5: Oligonucleotide strands with photo-cleavable linkers #1* - #4*. Lane 6: regular DNA tetrahedrons. Lane 7: regular DNA tetrahedrons. Lane 8: photo-cleavable DNA tetrahedrons. Lane 9: photo-cleavable DNA tetrahedrons. (c) Comparison of relative mobility of different DNA samples using 200 bp ladder (marked with arrows in (a) and (b) gels) as the standard.

ACAir mode AFM was also used to characterize the formation of DNA tetrahedrons. AFM images (height and phase) and corresponding cross section result are shown in **Figure 64**. The shapes seen on the AFM images were blurry and did not reveal any tetrahedral (or triangular) shapes. The observed structure had a height 0.5 nm and a width of about 30 nm, which were relatively far away from the true structure size of around 6 nm. Considering that DNA tetrahedron structures was flattened in air on a substrate, the observed features are most likely a result of tip-

convolution effect. ACWater mode AFM or ultrasharp AFM probe may help with the scanning but they were technically difficult to achieve on our Asylum MFP-3D instrument.

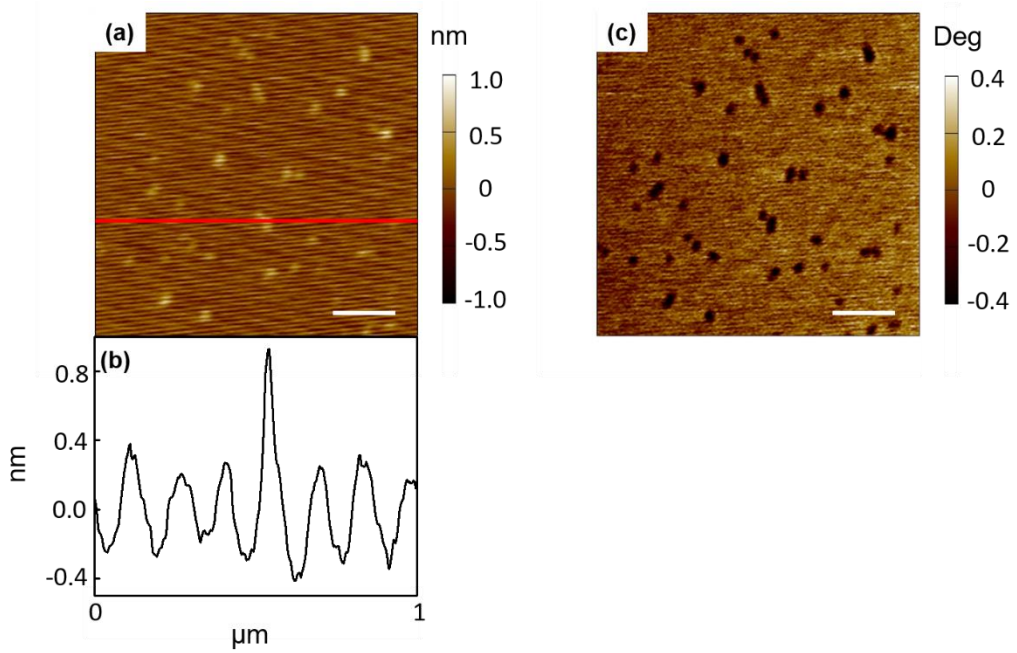

Figure 64. ACAir AFM images of DNA tetrahedrons. (a) Height image. White horizontal line indicates where the cross section was determined. Scale bar: 200 nm; (b) Corresponding cross section; (c) Phase image. Scale bar: 200 nm.

5.4.2 Photochemical activity of DNA tetrahedron nanostructures

Based on the sequence design in **Table 16**, two photo-cleavable linkers were introduced into each of the four oligonucleotides used to construct the DNA tetrahedron. The photo-cleavable linkers were purposely placed at each vertex of DNA tetrahedron to achieve best cleavage efficiency and to minimize the influence of photo-cleavable linkers on the synthesis of DNA

tetrahedron. A total of eight photo-cleavable linkers existed in one DNA tetrahedron made with oligonucleotides #1* - #4*. The estimated melting temperature of a 17-bp ds-DNA in 1 × TEM buffer is over 40 °C.[108] In other words, after 365 nm irradiation at room temperature, the 3D DNA tetrahedron structure should break to 6 double-strand DNA (**Figure 62**). The newly formed strands after irradiation should be 17-bp ds-DNA (the edge length of the DNA tetrahedron) with one unpaired nucleotide on each side of the strand.

Oligonucleotide strands #1 - #4 (without photo-cleavable linkers), #1* - #4* (with photo-cleavable linkers) were irradiated individually under 365 nm light for 10 min and then analyzed with PAGE gel (**Figure 65**). Oligonucleotides #1 - #4 remained unchanged after irradiation while Oligonucleotides with photo-cleavable linkers #1* - #4* disintegrated after irradiation. Almost no band was seen at the single strand locations for Lane 6 - 9, suggesting high efficiency of linker cleavage. The broken pieces were too small and ran out of the gel. The bottom band (around 15 - 20 bp) was from bromophenol blue in the gel loading buffer.

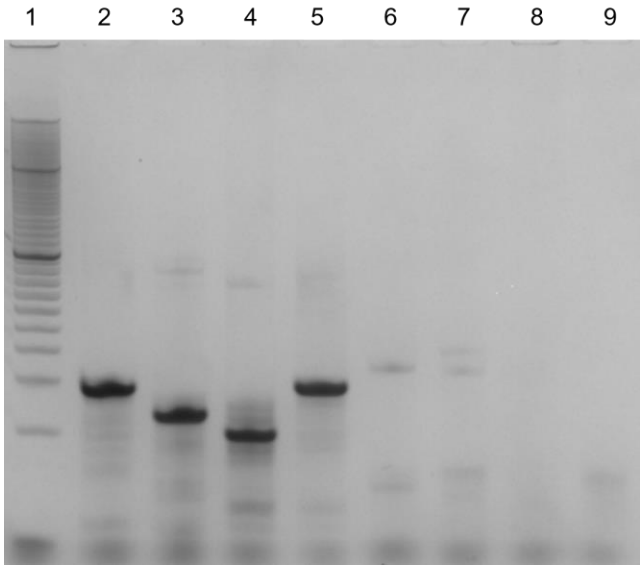

Figure 65. PAGE gel analysis of oligonucleotides after 10 min 365 nm irradiation. Lane 1: PCR 20 bp low ladder. Lane 2 - 5: Oligonucleotide #1 - #4 (**Table 15**) after 10 min 365 nm irradiation. Lane 6 - 9: Oligonucleotide with photo-cleavable linkers #1* - #4* (**Table 16**) after 10 min 365 nm irradiation.

The regular DNA tetrahedron and photo-cleavable DNA tetrahedron were also irradiated for 10 min at 365 nm. The gel image in **Figure 66** showed the comparison of DNA tetrahedrons before and after irradiation (Lane 2 - 5). Regular DNA tetrahedron maintained the same band position after irradiation while photochemical active DNA tetrahedron band disappeared from gel after irradiation. This indicated that the shape and structure of regular DNA tetrahedron didn't change after irradiation. However, the structure of photochemical active DNA tetrahedron changed and the produced pieces were much smaller so they travelled out of the gel in the 1.5 hr running time.

Oligonucleotides after irradiation were also used to synthesize DNA tetrahedrons. Oligonucleotides #1 - #4 after irradiation were mixed together and went through the standard annealing process before gel electrophoresis analysis. Parallelly, oligonucleotides with photo-cleavable linkers #1* - #4* were also mixed and went through the standard annealing process (**Figure 67**). These two processes made up the samples in Lane 6 and 7 in **Figure 66**.

From the results of Lane 6 and 7 in **Figure 66**, regular oligonucleotides #1 - #4 were still able to form a DNA tetrahedron by base pair recognition after irradiation. However, oligonucleotides with photo-cleavable linkers #1* - #4* were not able to form a 3D tetrahedral structure after irradiation. These results further confirmed the photochemical behaviors of the DNA tetrahedron with photo-cleavable linkers and eliminated the other possibilities leading to the breakdown of the structure.

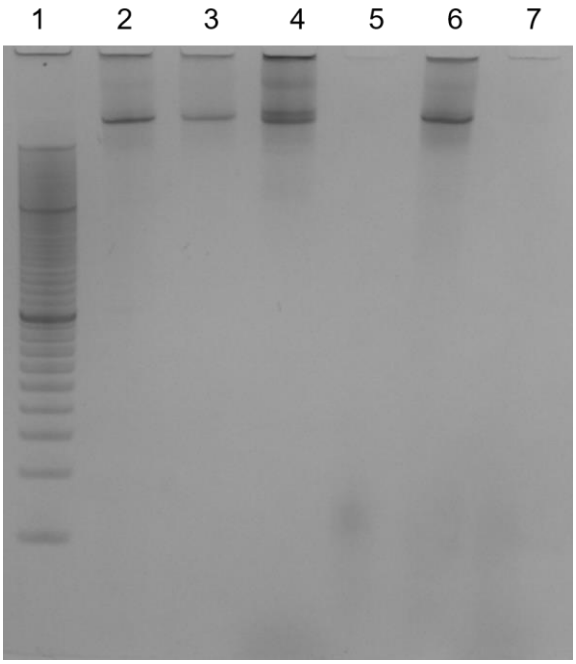

Figure 66. PAGE gel analysis of DNA tetrahedrons before/ after 365 nm irradiation. Lane 1: PCR 20 bp low ladder. Lane 2 - 3: Regular DNA tetrahedron before and after irradiation. Lane 4 - 5: Photochemical Active DNA tetrahedron before and after irradiation. The samples loaded in Lane 6 - 7 are described in **Figure 67**.

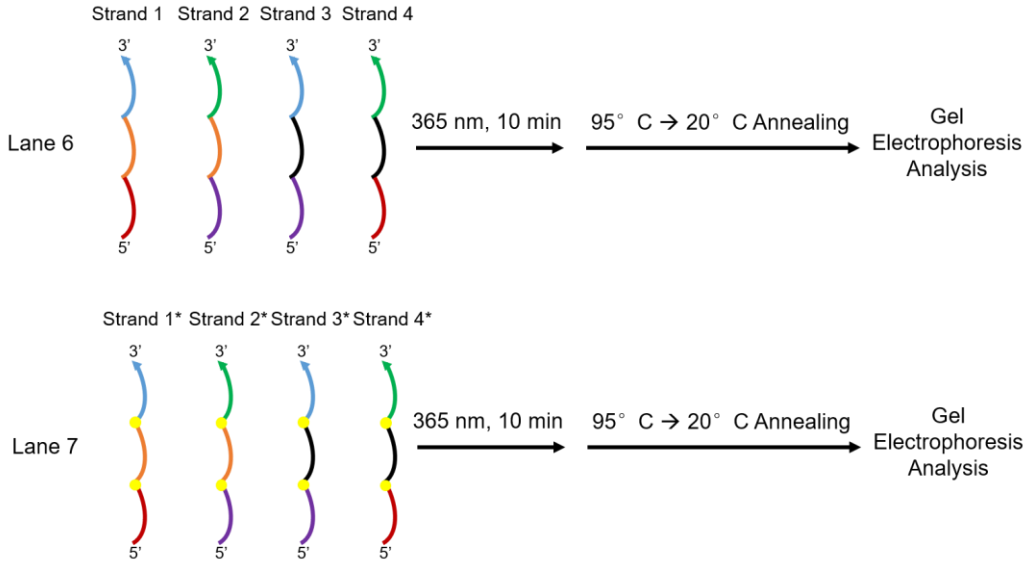

Figure 67. Sample preparation scheme of Lane 6 and 7 samples in **Figure 66**.

Finally, to confirm the size of the broken pieces, A.X. gel loading buffer was used to load samples. As mentioned before, the broken pieces of the DNA tetrahedron after irradiation should be 17-bp ds-DNA. Bromophenol blue also showed up at around 15 - 20 bp for 12.5% PAGE gel. Removal of bromophenol blue should reveal the broken pieces in the samples. Different samples including oligonucleotides #1 - #4, photochemical active DNA tetrahedron before and after irradiation were loaded to the gel with A.X. gel loading buffer for comparison. Oligonucleotide #1 - #4 were used here to indicate the positions of the reactants. From **Figure 63**, oligonucleotides #1 - #4 and oligonucleotides with photo-cleavable linkers #1* - #4* were confirmed to have identical gel electrophoresis behaviors. At the same time, a sample of Sigma-Aldrich gel loading buffer (with bromophenol blue) was diluted 5 times with 1 × TBE buffer and loaded to Lane 8 of the gel for comparison (**Figure 68**). Lane 7 in **Figure 68** clearly showed the band for broken pieces, which corresponds to 15 - 20-bp standard ds-DNA when compared to the PCR 20 bp low ladder bands in Lane 1 and bromophenol blue band in Lane 8. The experimental result here was consistent with our expectation, in which 17-bp ds-DNA were left over after irradiation. It was also observed that the band for Lane 7 was much wider than the band of DNA tetrahedron in Lane 6 even if the amount of DNA were the same in two samples. This was because the broken pieces were a mixture of 6 different sequences of ds-DNA whose mobility might be slightly different.

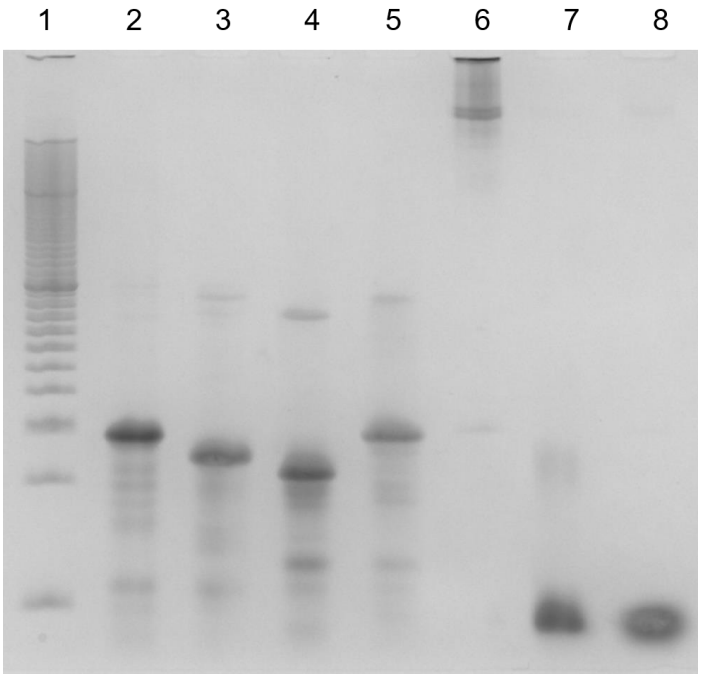

Figure 68. PAGE gel analysis of broken pieces from the DNA tetrahedron nanostructures after irradiation. Lane 1: PCR 20 bp low ladder loaded with A.X. gel loading buffer. Lane 2 - 5: oligonucleotides #1 - #4 (**Table 15**) loaded with A.X. gel loading buffer. Lane 6 - 7: Photochemical active DNA tetrahedron before and after 365 nm irradiation loaded with A.X. gel loading buffer. Lane 8: Sigma-Aldrich gel loading buffer (containing bromophenol blue).

5.4.3 Optimization of irradiation time

Different irradiation times (3 min, 5 min, 7 min) were tested for photochemical active DNA tetrahedrons. PAGE gel analysis (**Figure 69**) showed that 3 min was enough for complete breakdown of the tetrahedral structure, indicating that the reaction was highly efficient.

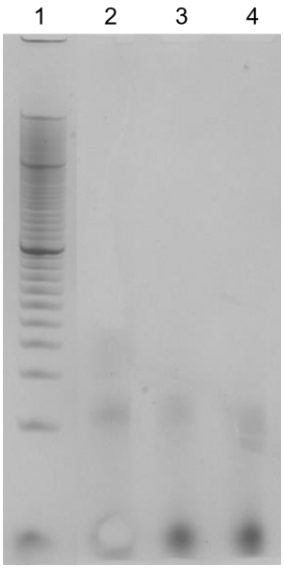

Figure 69. PAGE gel analysis of DNA tetrahedrons after different irradiation time. Lane 1: PCR 20 bp low ladder. PAGE gel analysis of DNA tetrahedrons after different irradiation times. Lane 2: 3 min. Lane 3: 5 min. Lane 4: 7 min.

5.4.4 Partial and complete breakdown of DNA tetrahedron nanostructure

Combination of oligonucleotides #1 - #4 (**Table 15**) and oligonucleotides with photo-cleavable linkers #1* - #4* (**Table 16**) also gave opportunity to achieve partial breakdown of DNA tetrahedron structures. In those cases, only some of the vertex connections were 'unlocked', producing different 2D structures. Based on geometrical estimation, **Table 17** lists a theoretical summary of the structure sizes after irradiation when combining oligonucleotides #1 - #4 (**Table 15**) and oligonucleotides with photo-cleavable linkers #1* - #4* (**Table 16**). Here, the symbol '∼' indicates an approximation due to the fact that there are unpaired nucleotides at the vertexes of the DNA tetrahedron structure not counted into the number of base pairs. **Figure 70** presents the predicted DNA structures after irradiation.

Table 17. Theoretical summary of structure sizes after irradiation.

# of Photo-cleavable Strands / # of Regular Strands	# of Photo-cleavable Linkers	Structure after Irradiation
0 / 4	0	~ 102 bp, 3D Structure
1 / 3	2	~ 102 bp, 2D Structure with a little more flexibility
2 / 2	4	~ 85 bp + ~ 17 bp, 2D Structure
3 / 1	6	~ 51 bp + 3 × ~ 17 bp, 1D Structure
4 / 0	8	6 × ~ 17 bp bp, 1D Structure

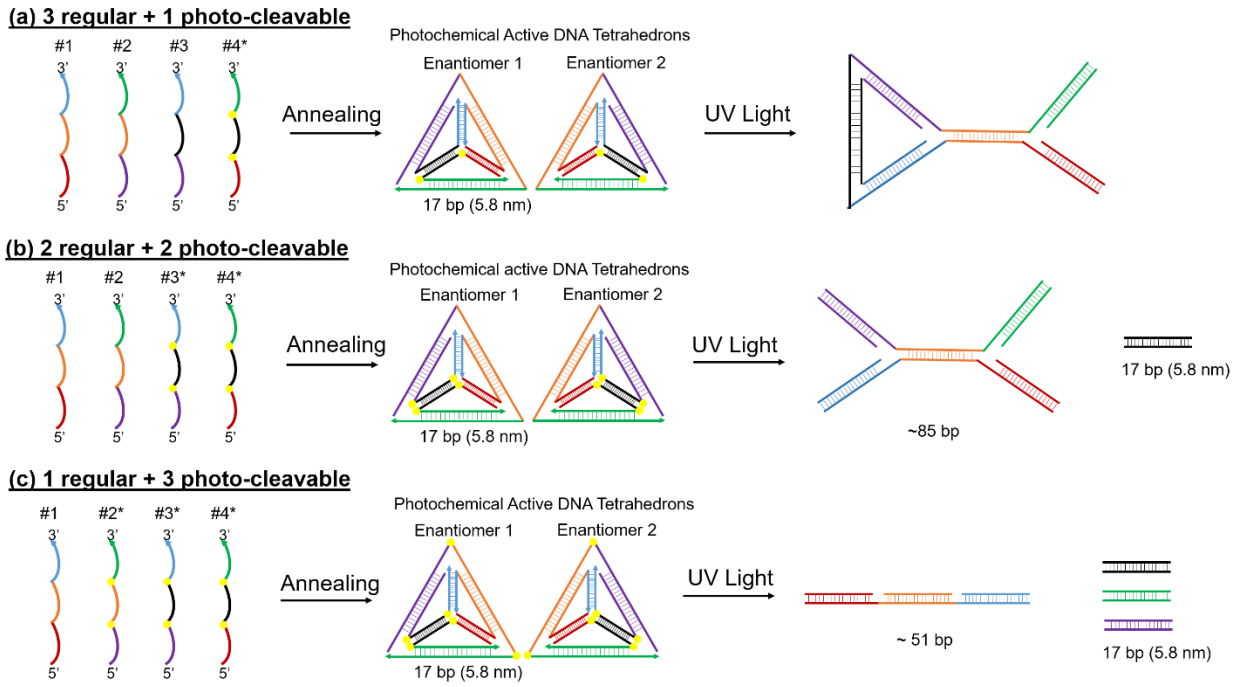

Figure 70. Scheme of synthesis and partial breakdown of different types of photochemical active DNA tetrahedron nanostructures.

In the experiment, oligonucleotides #1 - #4 (**Table 15**) and oligonucleotides with photo-cleavable linkers #1* - #4* (**Table 16**) were first mixed together to synthesize the DNA tetrahedrons. Here the DNA tetrahedron with 6 photo-cleavable linkers was made with

oligonucleotides #1* + #2* + #3 + #4*. The DNA tetrahedron with 4 photo-cleavable linkers was made with oligonucleotides #1 + #2* + #3 + #4*. The DNA tetrahedron with 2 photo-cleavable linkers was made with oligonucleotides #1* + #2 + #3 + #4*. Then the DNA tetrahedrons were irradiated at 365 nm for 10 min. The products were loaded to PAGE gel with A.X. gel loading buffer and the gel image is provided in **Figure 71 (b)**. For comparison purpose, gel electrophoresis analysis of regular DNA tetrahedron and photochemical active DNA tetrahedron with 8 photo-cleavable linkers was also performed with A.X. gel loading buffer used instead of Sigma-Aldrich gel loading buffer (**Figure 71(a)**). Relative mobility analysis in **Figure 71(c)** confirms the partial breakdown of DNA tetrahedrons with larger leftover pieces when the number of oligonucleotides with photo-cleavable linkers went down. Again, due to the 2D and 3D structures of the broken pieces, the bands didn't show up at the same distance as the standard samples of same molecular weight in PCR 20 bp low ladder.

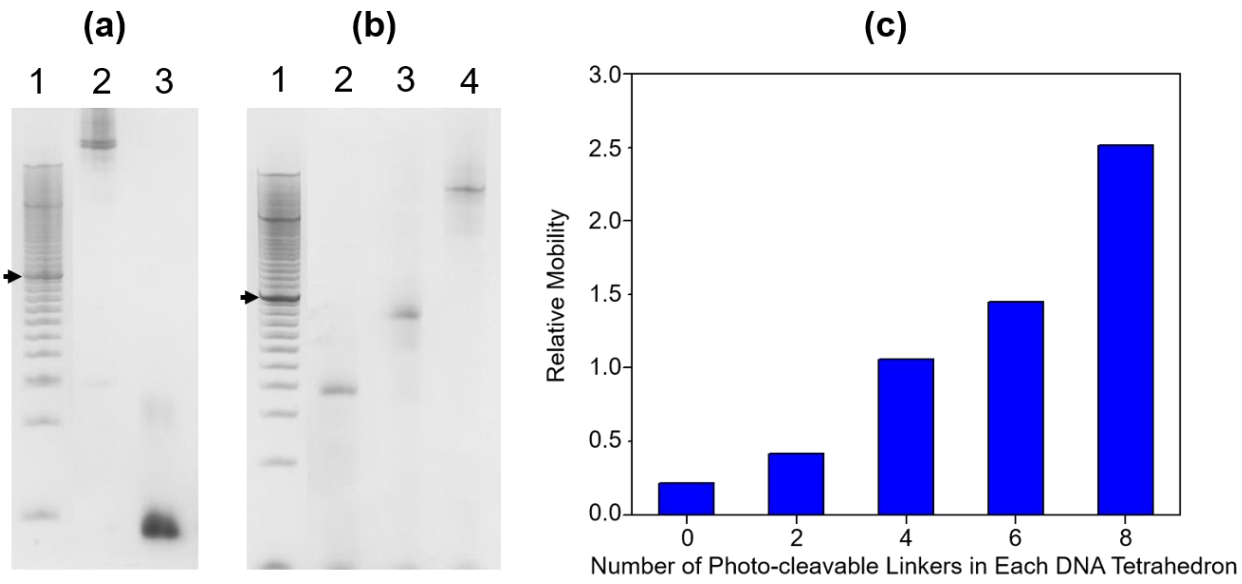

Figure 71. Gel electrophoresis results for photochemical activities of the photochemical active DNA tetrahedrons. (a) Lane 1: PCR 20 bp low ladder. Lane 2: Regular DNA tetrahedrons after light irradiation. Lane 3: Photochemical active DNA tetrahedrons synthesized with strands 1*+2*+3*+4* (totally 8 photo-cleavable linkers) after light irradiation. (b) Lane 1: PCR 20 bp low ladder. Lane 2: Photochemical active DNA tetrahedrons synthesized with strands 1*+2*+3+4* (totally 6 photo-cleavable linkers) after light irradiation. Lane 3: Photochemical active DNA tetrahedrons synthesized with strands 1+2*+3+4* (totally 4 photo-cleavable linkers) after light irradiation. Lane 4: Photochemical active DNA tetrahedrons synthesized with strands 1+2+3+4* (totally 2 photo-cleavable linkers) after light irradiation. (c) Comparison of relative mobility of UV treatment products of Photochemical active DNA tetrahedrons with different numbers of photo-cleavable linkers using 200 bp ladder (marked with arrows in (a) and (b) gels) as the standard.

5.5 Conclusion

In this study, we designed a photochemical active DNA tetrahedron structure. Regular DNA tetrahedron and photochemical active DNA tetrahedron were both successfully synthesized using an easy, one-step annealing reaction with high yield. The photochemical activities of both types of DNA tetrahedrons were tested. Photochemical active DNA tetrahedron broke down after as short as 3 min of 365 nm irradiation while the regular DNA tetrahedron maintained its 3D structure. The breakdown of DNA tetrahedron was caused by cleavage of photo-cleavable linkers via UV light irradiation. Combination of regular single strands and photo-cleavable single strands leads to DNA tetrahedron structures that could be partially broken down upon irradiation. Larger pieces were left over when fewer photo-cleavable linkers were introduced in the structure. Our study demonstrated a successful design of photo-regulated 3D DNA nanostructure within sub-10 nm scale. This photochemical active DNA tetrahedron can be potentially applied for selective and controlled molecule encapsulation and delivery using precise UV light activation.

6.0 Conclusions and Prospective

In this dissertation, I have described my research on the development of DNA nanotechnology. I have demonstrated several approaches to chemically modify DNA nanostructures that are motived by their potential applications in nanofabrication and drug delivery. Multiple types of DNA nanostructure have been utilized or modified in my research work, including DNA origami nanostructures, DNA nanotubes and unscaffolded DNA tetrahedron nanostructures. Nanofabrication methods have been demonstrated for both SiO_2 substrates and carbon materials (HOPG). My research provided new insight into the applications of DNA nanotechnology and will serve as a foundation for more innovative opportunities in the future. In this section, I will provide brief summaries of my projects and discuss some potential future directions.

6.1 DNA-Based 3D Lithography Using 2D Templates

In Chapter 2, I have studied the effect of chemical modification of DNA nanostructures on the nanoscale pattern transfer using HF etching of SiO_2. Streptavidin is a one of the most commonly used modifiers on DNA nanostructures thanks to its strong and specific interaction with biotin. Streptavidin is a hydrophilic protein and it is expected to increase the HF-etching reaction rate by increasing the amount of surface-adsorbed water. The unmodified DNA templates produced negative-tone patterns of *ca.* 27 nm in depth and *ca.* 22 nm in width. Streptavidin molecules were modified onto one side of the triangular-shaped DNA origami nanostructure and was able to locally promote the HF etching reaction. The vertical contrast of the transferred pattern was increased by 35% while no noticeable increase in the width was observed. The knowledge obtained from this study suggests the possibility of utilizing DNA nanostructures for wider range of nanofabrication applications, with the advantages of low cost, high contrast, and high resolution.

Given the many different kinds of modifications that can be applied to DNA nanostructures, our result suggests that the future direction of the method can be focused on creating complex 3D patterns for semiconductor electronic devices. The goal can be achieved by a single pattern transfer step using a 2D DNA template modified with various types of functional groups. Following a similar approach as described in Chapter 2, the effect of other types of modifications, including both hydrophilic and hydrophobic ones, such as polymers, metal nanoparticles, and carbon nanotubes, on the pattern transfer process can be investigated and compared. With the combination of two or more types of modifications, the promotional and inhibitive effects can be achieved within one single DNA nanostructure and hence highly complex patterns can be created on a SiO_2 substrate (**Figure 72**). The patterns created using the preceding method can further be used to fabricate field-effect transistors. For example, two deeply etched pockets, which open up the

connection to the bottom substrate, can be converted into the source and drain electrodes, while the less etched areas in between will be used as the gate dielectric.[266] This approach may establish a new pathway to the scalable fabrication of nanoscale electronics.

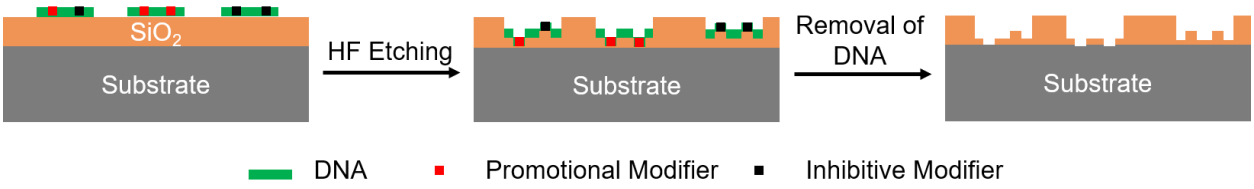

Figure 72. Scheme of DNA-mediated pattern transfer process with two promotional and/or inhibitive modifiers.

6.2 HF-Induced DNA Damage during Negative-Tone Pattern Transfer Process from DNA Nanostructures to SiO_2

In chapter 3, I investigated the stability and reusability of DNA nanostructure templates after the HF etching negative-tone pattern transfer process. With the help of SYTO 9 fluorescent nucleic acid stain and fluorescence microscopy, a direct observation of DNA nanotubes presence after HF etching reaction and their disappearance after washing steps was achieved. These results confirmed that DNA nanostructures can be preserved after the HF etching pattern transfer process. Using PCR amplification, we were able to confirm the sequence integrity of some remaining DNA strands. Considering that the DNA damage in HF solution of equivalent concentration (25-30%) is more severe, the results suggest a different mechanism between vapor phase HF and dry-deposited DNA samples with limited amount of water condensed on the surface, which may be of interest for further investigation in the future. The lack of effective retrieval method made it almost impossible to quantitatively investigate the percentage of damage to the DNA templates after the HF etching process. It is also the bottleneck to achieve recycling and reusing of the DNA templates for other nanofabrication processes. The research work provided several standard methods to study the reusability of DNA nanostructure templates and suggested that DNA nanostructures are more chemically stable than expected.

For future research, a key issue is to find an efficient and cost-effective retrieval method for DNA templates. A preliminary test using buffer solution failed, which is understandable due to the high concentration of Mg^{2+} within the buffer solution. Other solution-based methods may be performed and compared in the future. Another approach is to pre-modify the DNA nanostructure templates with magnetic beads before applying them for nanofabrication process.[267-268] Then the DNA nanostructure templates can be easily recollected after each fabrication cycle.

However, a lot of issues may arise from this technique including the cost of modification, the effect of magnetic beads to the fabrication reaction and the interaction between the beads and the substrate. The last approach, which is very specific to the presented SiO_2 patterning system, is to use a milder method to remove the top layer of the SiO_2 substrate and free the deposited DNA nanostructures. Buffered oxide etch solution (HF/NH_4F mixture, 48%/ 40%, 1:6) has been tried in the preliminary test but ended up leading to DNA damage. Different methods may have to be developed for different fabrication systems. Without removing DNA templates from the substrate surface, an alternative approach to realize the reusability of DNA templates is to develop in-situ reutilization methods to use the DNA molecules as templates for other applications including another round of nanofabrication of different materials (*e.g.*, metals) or biochemical signal transduction. There is still long way to go before the reusability of DNA nanostructure templates can be fully realized. Solving this problem will potentially lead to broader industrial applications of DNA nanostructures in the future.

6.3 Deposition of DNA Nanostructures on Highly Oriented Pyrolytic Graphite (HOPG)

In Chapter 4, we have successfully deposited DNA nanostructures onto HOPG from an aqueous buffer solution and the deposition process was carefully investigated. No surface modification on the HOPG was needed to achieve the deposition. Significant structural deformation of the DNA nanostructure occurred, exposing the DNA bases to the HOPG substrate to maximize the π-π interaction. Surface contamination of HOPG did not affect the deposition process and the deposited DNA nanostructures were stable for at least a week. As a demonstration for application, the DNA nanostructure templates on HOPG can promote site-selective chemical vapor deposition of SiO_2. This study will expand the use of DNA nanostructure in a broader range of surface-related studies and applications.

It will be of interest to design more applications for the DNA-deposited HOPG system, especially using DNA nanostructures as templates for organizing and depositing other molecules or materials. Efforts have been made to achieve CVD growth of TiO_2 on HOPG surface. However, due to the high chemical reactivity of titanium chloride ($TiCl_4$) and titanium isopropoxide precursors, the preliminary trials also led to significant growth of TiO_2 on the step edges of HOPG surface. Other titanium precursors can be investigated and the experimental conditions can be optimized to achieve CVD growth of TiO_2. Metal nanoparticles (*e.g.*, gold)[269] and other inorganic materials (*e.g.*, Al_2O_3)[270] may also lead to potential applications like electrocatalysis or fabrication of nanoelectronics when deposited on HOPG substrates. DNA nanostructures may also serve as templates for HOPG patterning via oxygen plasma etching.[271] I hope this work can lead to broader applications of using DNA nanostructures as templates for fabrication of carbon materials.

6.4 Photochemical Active DNA Tetrahedron Nanostructure

In Chapter 5, I designed and successfully synthesized a photochemical active DNA tetrahedron structure through an easy, one-step annealing reaction with high yield. The photochemical activities of the photochemical active DNA tetrahedrons were investigated and its complete dissociation occurred after as short as 3 min of 365 nm irradiation. Partial breakdown and structural change of DNA tetrahedron nanostructure was achieved by altering the number of photo-cleavable linkers in the design. This photochemical active DNA tetrahedron can be potentially applied for selective and controlled molecule encapsulation and delivery using precise UV light activation.

In the follow-up experiments, the applications of the photochemical active DNA tetrahedron could be explored. The size of the DNA tetrahedron is suitable for encapsulation of proteins. Using cytochrome *c* as an example, we can demonstrate the selective delivery of molecules. Encapsulation of other molecules can also be achieved by designing the capturing ligands inside the tetrahedron structure. It will be critical to show the function control of the encapsulated molecule via UV light irradiation. Another idea is to use the photochemical active DNA tetrahedron nanostructure to selectively regulate enzyme activities like APE1. It has been reported that insertion of AP site in DNA tetrahedron structure leads to regulation of APE1 activity, which can help enhance the efficiency of cancer treatment drugs. Light irradiation can be used to selectively inhibit APE1 in cancer tissues but remain the activity of APE 1 in healthy cells, leading to selective treatment by cancer drugs.[262]

6.5 Final Remarks

In summary, I have demonstrated several approaches to chemically modify DNA nanostructures and proposed their potential applications for nanofabrication, drug delivery or biosensing. DNA nanostructures provide abundant structural and chemical information and can be used for broad fields in material science and biochemistry. I hope these results will serve as a stepping stone for the future development of DNA nanotechnology.

Abbreviation

AFM	Atomic force microscopy
ALD	Atomic Layer Deposition
ATP	Adenosine triphosphate
CVD	Chemical vapor deposition
DNA	Deoxyribonucleic acid
ds-DNA	Double-stranded DNA
DOX	Doxorubicin
EDTA	Ethylenediaminetetraacetic acid
FITC	Fluorescein isothiocyanate
FWHM	Full width at half maximum
GOx	Glucose oxidase
HPLC	High-performace liquid chromatography
HOPG	Highly oriented pyrolytic graphite
HRP	Horseradish peroxidase (HRP)
MDR	Multidrug resistance
miRNA	microRNA
OTM	Olive tail moment
PAGE	Polyacrylamide gel electrophoresis
PCR	Polymerase chain reaction
PDGF	Platelet-derived growth factor
PDMS	Polydimethylsiloxane

P*f*LDH	*Plasmodium falciparum* lactate dehydrogenase
PLLA	Poly(*L*-lactide)
PMMA	Poly(methyl methacrylate)
PSA	Prostate-specific antigen
RCA	Rolling circle amplification
RNA	Ribonucleic acid
ROS	Reactive oxygen species
TGA	Thermogravimetric analysis
TMB	3,3',5,5'-tetra-methylbenzidine
SCGE	Single cell gel electrophoresis
SDS	Sodium dodecyl sulfate
SEM	Scanning electron microscopy
siRNA	Small interfering RNA
SNP	Single nucleotide polymorphism
ss-DNA	Single-stranded DNA
TEMED	Tetramethylethylenediamine
TEOS	Tetraethyl orthosilicate
XPS	X-Ray photoelectron spectroscopy
UV	Ultraviolet
UV-Vis	Ultraviolet-Visible

Bibliography

1. Dahm, R., Discovering DNA: Friedrich Miescher and the early years of nucleic acid research. *Human Genetics* **2008,** *122* (6), 565-581.

2. Watson, J. D.; Crick, F. H. C., Molecular structure of nucleic acids: A structure for deoxyribose nucleic acid. *Nature* **1953,** *171* (4356), 737-738.

3. Nangreave, J.; Han, D.; Liu, Y.; Yan, H., DNA origami: a history and current perspective. *Current Opinion in Chemical Biology* **2010,** *14* (5), 608-615.

4. Seeman, N. C., Nucleic acid junctions and lattices. *Journal of Theoretical Biology* **1982,** *99* (2), 237-247.

5. Seeman, N. C.; Sleiman, H. F., DNA nanotechnology. *Nature Reviews Materials* **2017,** *3* (1), 17068.

6. Chidchob, P.; Sleiman, H. F., Recent advances in DNA nanotechnology. *Current Opinion in Chemical Biology* **2018,** *46*, 63-70.

7. Arora, A. A.; de Silva, C., Beyond the smiley face: applications of structural DNA nanotechnology. *Nano Reviews & Experiments* **2018,** *9* (1), 1430976.

8. Nummelin, S.; Kommeri, J.; Kostiainen, M. A.; Linko, V., Evolution of structural DNA nanotechnology. *Advanced Materials* **2018,** *30* (24), e1703721.

9. Fu, J.; Liu, M.; Liu, Y.; Yan, H., Spatially-interactive biomolecular networks organized by nucleic acid nanostructures. *Accounts of Chemical Research* **2012,** *45* (8), 1215-1226.

10. Seeman, N. C., Nanomaterials based on DNA. *Annual Review of Biochemistry* **2010,** *79*, 65-87.

11. Zhang, G.; Surwade, S. P.; Zhou, F.; Liu, H., DNA nanostructure meets nanofabrication. *Chemical Society Reviews* **2013,** *42* (7), 2488-2496.

12. Seeman, N. C., DNA in a material world. *Nature* **2003,** *421* (6921), 427-431.

13. Fu, T.-J.; Tse-Dinh, Y.-C.; Seeman, N. C., Holliday Junction Crossover Topology. *Journal of Molecular Biology* **1994,** *236* (1), 91-105.

14. Petrillo, M. L.; Newton, C. J.; Cunningham, R. P.; Ma, R.-I.; Kallenbach, N. R.; Seeman, N. C., The ligation and flexibility of four-arm DNA junctions. *Biopolymers* **1988,** *27* (9), 1337-1352.

15. Li, H.; Labean, T. H.; Leong, K. W., Nucleic acid-based nanoengineering: novel structures for biomedical applications. *Interface Focus* **2011,** *1* (5), 702-724.

16. Fu, T.-J.; Seeman, N. C., DNA double-crossover molecules. *Biochemistry* **1993,** *32* (13), 3211-3220.

17. Ge, Z.; Gu, H.; Li, Q.; Fan, C., Concept and development of framework nucleic acids. *Journal of the American Chemical Society* **2018,** *140* (51), 17808-17819.

18. Zhang, S.; Seeman, N. C., Symmetric holliday junction crossover isomers. *Journal of Molecular Biology* **1994,** *238* (5), 658-668.

19. Ding, B.; Sha, R.; Seeman, N. C., Pseudohexagonal 2D DNA crystals from double crossover cohesion. *Journal of the American Chemical Society* **2004,** *126* (33), 10230-10231.

20. He, Y.; Chen, Y.; Liu, H.; Ribbe, A. E.; Mao, C., Self-assembly of hexagonal DNA two-dimensional (2D) arrays. *Journal of the American Chemical Society* **2005,** *127* (35), 12202-12203.

21. Yan, H.; Park, S. H.; Finkelstein, G.; Reif, J. H.; LaBean, T. H., DNA-templated self-assembly of protein arrays and highly conductive nanowires. *Science* **2003,** *301* (5641), 1882-1884.

22. Mao, C.; Sun, W.; Seeman, N. C., Designed two-dimensional DNA holliday junction arrays visualized by atomic force microscopy. *Journal of the American Chemical Society* **1999,** *121* (23), 5437-5443.

23. Lin, C.; Ke, Y.; Liu, Y.; Mertig, M.; Gu, J.; Yan, H., Functional DNA nanotube arrays: bottom-up meets top-down. *Angewandte Chemie International Edition* **2007,** *46* (32), 6089-6092.

24. Lo, P. K.; Karam, P.; Aldaye, F. A.; McLaughlin, C. K.; Hamblin, G. D.; Cosa, G.; Sleiman, H. F., Loading and selective release of cargo in DNA nanotubes with longitudinal variation. *Nature Chemistry* **2010,** *2* (4), 319-328.

25. He, Y.; Mao, C., Balancing flexibility and stress in DNA nanostructures. *Chemical Communications* **2006,** (9), 968-969.

26. Rothemund, P. W. K.; Ekani-Nkodo, A.; Papadakis, N.; Kumar, A.; Fygenson, D. K.; Winfree, E., Design and characterization of programmable DNA nanotubes. *Journal of the American Chemical Society* **2004,** *126* (50), 16344-16352.

27. Mathieu, F.; Liao, S.; Kopatsch, J.; Wang, T.; Mao, C.; Seeman, N. C., Six-helix bundles designed from DNA. *Nano Letters* **2005,** *5* (4), 661-665.

28. Ma, R.-I.; Kallenbach, N. R.; Sheardy, R. D.; Petrillo, M. L.; Seeman, N. C., Three-arm nucleic acid junctions are flexible. *Nucleic Acids Research* **1986,** *14* (24), 9745-9753.

29. Chen, J.; Seeman, N. C., Synthesis from DNA of a molecule with the connectivity of a cube. *Nature* **1991,** *350* (6319), 631-633.

30. Zhang, Y.; Seeman, N. C., Construction of a DNA-truncated octahedron. *Journal of the American Chemical Society* **1994,** *116* (5), 1661-1669.

31. Goodman, R. P.; Berry, R. M.; Turberfield, A. J., The single-step synthesis of a DNA tetrahedron. *Chemical Communications* **2004,** *12* (12), 1372-1373.

32. Shih, W. M.; Quispe, J. D.; Joyce, G. F., A 1.7-kilobase single-stranded DNA that folds into a nanoscale octahedron. *Nature* **2004,** *427* (6975), 618-621.

33. Li, Z.; Wei, B.; Nangreave, J.; Lin, C.; Liu, Y.; Mi, Y.; Yan, H., A replicable tetrahedral nanostructure self-assembled from a single DNA strand. *Journal of the American Chemical Society* **2009,** *131* (36), 13093-13098.

34. He, Y.; Ye, T.; Su, M.; Zhang, C.; Ribbe, A. E.; Jiang, W.; Mao, C., Hierarchical self-assembly of DNA into symmetric supramolecular polyhedra. *Nature* **2008,** *452*, 198-202.

35. Zhang, C.; Su, M.; He, Y.; Zhao, X.; Fang, P.-a.; Ribbe, A. E.; Jiang, W.; Mao, C., Conformational flexibility facilitates self-assembly of complex DNA nanostructures. *Proceedings of the National Academy of Sciences* **2008,** *105* (31), 10665-10669.

36. Zheng, J.; Birktoft, J. J.; Chen, Y.; Wang, T.; Sha, R.; Constantinou, P. E.; Ginell, S. L.; Mao, C.; Seeman, N. C., From molecular to macroscopic via the rational design of a self-assembled 3D DNA crystal. *Nature* **2009,** *461* (7260), 74-77.

37. Wei, B.; Dai, M.; Yin, P., Complex shapes self-assembled from single-stranded DNA tiles. *Nature* **2012,** *485* (7400), 623-626.

38. Mathur, D.; Henderson, E. R., Complex DNA nanostructures from oligonucleotide ensembles. *ACS Synthetic Biology* **2013,** *2* (4), 180-185.

39. Ke, Y.; Ong, L. L.; Shih, W. M.; Yin, P., Three-dimensional structures self-assembled from DNA bricks. *Science* **2012,** *338* (6111), 1177-1183.

40. Wei, B.; Dai, M.; Myhrvold, C.; Ke, Y.; Jungmann, R.; Yin, P., Design space for complex DNA structures. *Journal of the American Chemical Society* **2013,** *135* (48), 18080-18088.

41. Ong, L. L.; Hanikel, N.; Yaghi, O. K.; Grun, C.; Strauss, M. T.; Bron, P.; Lai-Kee-Him, J.; Schueder, F.; Wang, B.; Wang, P.; Kishi, J. Y.; Myhrvold, C.; Zhu, A.; Jungmann, R.; Bellot, G.; Ke, Y.; Yin, P., Programmable self-assembly of three-dimensional nanostructures from 10,000 unique components. *Nature* **2017,** *552* (7683), 72-77.

42. Wang, W.; Chen, S.; An, B.; Huang, K.; Bai, T.; Xu, M.; Bellot, G.; Ke, Y.; Xiang, Y.; Wei, B., Complex wireframe DNA nanostructures from simple building blocks. *Nature Communications* **2019,** *10* (1), 1067.

43. Huang, K.; Yang, D.; Tan, Z.; Chen, S.; Xiang, Y.; Mi, Y.; Mao, C.; Wei, B., Self-assembly of wireframe DNA nanostructures from junction motifs. *Angewandte Chemie International Edition* **2019,** *58* (35), 12123-12127.

44. Rothemund, P. W., Folding DNA to create nanoscale shapes and patterns. *Nature* **2006,** *440* (7082), 297-302.

45. Douglas, S. M.; Marblestone, A. H.; Teerapittayanon, S.; Vazquez, A.; Church, G. M.; Shih, W. M., Rapid prototyping of 3D DNA-origami shapes with caDNAno. *Nucleic Acids Research* **2009,** *37* (15), 5001-5006.

46. Andersen, E. S.; Dong, M.; Nielsen, M. M.; Jahn, K.; Lind-Thomsen, A.; Mamdouh, W.; Gothelf, K. V.; Besenbacher, F.; Kjems, J., DNA origami design of dolphin-shaped structures with flexible tails. *ACS Nano* **2008,** *2* (6), 1213-1218.

47. Castro, C. E.; Kilchherr, F.; Kim, D. N.; Shiao, E. L.; Wauer, T.; Wortmann, P.; Bathe, M.; Dietz, H., A primer to scaffolded DNA origami. *Nature Methods* **2011,** *8* (3), 221-229.

48. Han, D.; Pal, S.; Nangreave, J.; Deng, Z.; Liu, Y.; Yan, H., DNA origami with complex curvatures in three-dimensional space. *Science* **2011,** *332* (6027), 342-346.

49. Ke, Y.; Sharma, J.; Liu, M.; Jahn, K.; Liu, Y.; Yan, H., Scaffolded DNA origami of a DNA tetrahedron molecular container. *Nano Letters* **2009,** *9* (6), 2445-2447.

50. Douglas, S. M.; Dietz, H.; Liedl, T.; Hogberg, B.; Graf, F.; Shih, W. M., Self-assembly of DNA into nanoscale three-dimensional shapes. *Nature* **2009,** *459* (7245), 414-418.

51. Zhang, H.; Chao, J.; Pan, D.; Liu, H.; Huang, Q.; Fan, C., Folding super-sized DNA origami with scaffold strands from long-range PCR. *Chemical Communications* **2012,** *48* (51), 6405-6407.

52. Zhao, Z.; Yan, H.; Liu, Y., A route to scale up DNA origami using DNA tiles as folding staples. *Angewandte Chemie International Edition* **2010,** *49* (8), 1414-1417.

53. Zhao, Z.; Liu, Y.; Yan, H., Organizing DNA origami tiles into larger structures using preformed scaffold frames. *Nano Letters* **2011,** *11* (7), 2997-3002.

54. Endo, M.; Sugita, T.; Katsuda, Y.; Hidaka, K.; Sugiyama, H., Programmed-assembly system using DNA jigsaw pieces. *Chemistry: A European Journal* **2010,** *16* (18), 5362-5368.

55. Rajendran, A.; Endo, M.; Katsuda, Y.; Hidaka, K.; Sugiyama, H., Programmed two-dimensional self-assembly of multiple DNA origami jigsaw pieces. *ACS Nano* **2011,** *5* (1), 665-671.

56. Endo, M.; Sugita, T.; Rajendran, A.; Katsuda, Y.; Emura, T.; Hidaka, K.; Sugiyama, H., Two-dimensional DNA origami assemblies using a four-way connector. *Chemical Communications* **2011,** *47* (11), 3213-3215.

57. Liu, W.; Zhong, H.; Wang, R.; Seeman, N. C., Crystalline two-dimensional DNA-origami arrays. *Angewandte Chemie International Edition* **2011,** *50* (1), 264-267.

58. Woo, S.; Rothemund, P. W., Programmable molecular recognition based on the geometry of DNA nanostructures. *Nature Chemistry* **2011,** *3* (8), 620-627.

59. Woo, S.; Rothemund, P. W., Self-assembly of two-dimensional DNA origami lattices using cation-controlled surface diffusion. *Nature Communications* **2014,** *5*, 4889.

60. Iinuma, R.; Ke, Y.; Jungmann, R.; Schlichthaerle, T.; Woehrstein, J. B.; Yin, P., Polyhedra self-assembled from DNA tripods and characterized with 3D DNA-PAINT. *Science* **2014,** *344* (6179), 65-69.

61. Yang, Y. R.; Liu, Y.; Yan, H., DNA nanostructures as programmable biomolecular scaffolds. *Bioconjugate Chemistry* **2015,** *26* (8), 1381-1395.

62. Wilner, O. I.; Willner, I., Functionalized DNA nanostructures. *Chemical Reviews* **2012,** *112* (4), 2528-2556.

63. Gothelf, K. V., Chemical modifications and reactions in DNA nanostructures. *MRS Bulletin* **2017,** *42* (12), 897-903.

64. Sacca, B.; Niemeyer, C. M., DNA origami: the art of folding DNA. *Angewandte Chemie International Edition* **2012,** *51* (1), 58-66.

65. Modifications of oligonucleotides. www.idtdna.com/site/Catalog/Modifications (accessed August, 2019).

66. Sandström, P.; Boncheva, M.; Åkerman, B., Nonspecific and thiol-specific binding of DNA to gold nanoparticles. *Langmuir* **2003,** *19* (18), 7537-7543.

67. Cárdenas, M.; Barauskas, J.; Schillén, K.; Brennan, J. L.; Brust, M.; Nylander, T., Thiol-specific and nonspecific interactions between DNA and gold nanoparticles. *Langmuir* **2006,** *22* (7), 3294-3299.

68. González, M.; Bagatolli, L. A.; Echabe, I.; Arrondo, J. L. R.; Argaraña, C. E.; Cantor, C. R.; Fidelio, G. D., Interaction of biotin with streptavidin: Thermostability and conformational changes upon binding. *Journal of Biological Chemistry* **1997,** *272* (17), 11288-11294.

69. Chhabra, R.; Sharma, J.; Ke, Y.; Liu, Y.; Rinker, S.; Lindsay, S.; Yan, H., Spatially addressable multiprotein nanoarrays templated by aptamer-tagged DNA nanoarchitectures. *Journal of the American Chemical Society* **2007,** *129* (34), 10304-10305.

70. Wong, N. Y.; Zhang, C.; Tan, L. H.; Lu, Y., Site-specific attachment of proteins onto a 3D DNA tetrahedron through backbone-modified phosphorothioate DNA. *Small* **2011,** *7* (10), 1427-1430.

71. Lund, K.; Liu, Y.; Lindsay, S.; Yan, H., Self-assembling a molecular pegboard. *Journal of the American Chemical Society* **2005,** *127* (50), 17606-17607.

72. Kuzuya, A.; Kimura, M.; Numajiri, K.; Koshi, N.; Ohnishi, T.; Okada, F.; Komiyama, M., Precisely programmed and robust 2D streptavidin nanoarrays by using periodical nanometer-scale wells embedded in DNA origami assembly. *Chembiochem* **2009,** *10* (11), 1811-1815.

73. Mastroianni, A. J.; Claridge, S. A.; Alivisatos, A. P., Pyramidal and chiral groupings of gold nanocrystals assembled using DNA scaffolds. *Journal of the American Chemical Society* **2009,** *131* (24), 8455-8459.

74. Pal, S.; Dutta, P.; Wang, H.; Deng, Z.; Zou, S.; Yan, H.; Liu, Y., Quantum efficiency modification of organic fluorophores using gold nanoparticles on DNA origami scaffolds. *The Journal of Physical Chemistry C* **2013,** *117* (24), 12735-12744.

75. Ding, B.; Deng, Z.; Yan, H.; Cabrini, S.; Zuckermann, R. N.; Bokor, J., Gold nanoparticle self-similar chain structure organized by DNA origami. *Journal of the American Chemical Society* **2010,** *132* (10), 3248-3249.

76. Deng, Z.; Samanta, A.; Nangreave, J.; Yan, H.; Liu, Y., Robust DNA-functionalized core/shell quantum dots with fluorescent emission spanning from UV-vis to near-IR and compatible with DNA-directed self-assembly. *Journal of the American Chemical Society* **2012,** *134* (42), 17424-17427.

77. Maune, H. T.; Han, S. P.; Barish, R. D.; Bockrath, M.; Goddard, W. A., III; Rothemund, P. W.; Winfree, E., Self-assembly of carbon nanotubes into two-dimensional geometries using DNA origami templates. *Nature Nanotechnology* **2010,** *5* (1), 61-66.

78. Fu, J.; Liu, M.; Liu, Y.; Woodbury, N. W.; Yan, H., Interenzyme substrate diffusion for an enzyme cascade organized on spatially addressable DNA nanostructures. *Journal of the American Chemical Society* **2012,** *134* (12), 5516-5519.

79. Stephanopoulos, N.; Liu, M.; Tong, G. J.; Li, Z.; Liu, Y.; Yan, H.; Francis, M. B., Immobilization and one-dimensional arrangement of virus capsids with nanoscale precision using DNA origami. *Nano Letters* **2010,** *10* (7), 2714-2720.

80. Sacca, B.; Meyer, R.; Erkelenz, M.; Kiko, K.; Arndt, A.; Schroeder, H.; Rabe, K. S.; Niemeyer, C. M., Orthogonal protein decoration of DNA origami. *Angewandte Chemie International Edition* **2010,** *49* (49), 9378-9383.

81. Rinker, S.; Ke, Y.; Liu, Y.; Chhabra, R.; Yan, H., Self-assembled DNA nanostructures for distance-dependent multivalent ligand-protein binding. *Nature Nanotechnology* **2008,** *3* (7), 418-422.

82. Wilner, O. I.; Weizmann, Y.; Gill, R.; Lioubashevski, O.; Freeman, R.; Willner, I., Enzyme cascades activated on topologically programmed DNA scaffolds. *Nature Nanotechnology* **2009,** *4* (4), 249-254.

83. Shimada, J.; Maruyama, T.; Kitaoka, M.; Yoshinaga, H.; Nakano, K.; Kamiya, N.; Goto, M., Programmable protein-protein conjugation via DNA-based self-assembly. *Chemical Communications* **2012,** *48* (50), 6226-6228.

84. Rahman, M.; Neff, D.; Green, N.; Norton, M. L., DNA origami reorganizes upon interaction with graphite: Implications for high-resolution DNA directed protein patterning. *Nanomaterials* **2016,** *6* (11), 196.

85. Mangalum, A.; Rahman, M.; Norton, M. L., Site-specific immobilization of single-walled carbon nanotubes onto single and one-dimensional DNA origami. *Journal of the American Chemical Society* **2013,** *135* (7), 2451-2454.

86. Lin, C.; Jungmann, R.; Leifer, A. M.; Li, C.; Levner, D.; Church, G. M.; Shih, W. M.; Yin, P., Submicrometre geometrically encoded fluorescent barcodes self-assembled from DNA. *Nature Chemistry* **2012,** *4* (10), 832-839.

87. Pilo-Pais, M.; Goldberg, S.; Samano, E.; Labean, T. H.; Finkelstein, G., Connecting the nanodots: programmable nanofabrication of fused metal shapes on DNA templates. *Nano Letters* **2011,** *11* (8), 3489-3492.

88. Kuzyk, A.; Schreiber, R.; Fan, Z.; Pardatscher, G.; Roller, E. M.; Hogele, A.; Simmel, F. C.; Govorov, A. O.; Liedl, T., DNA-based self-assembly of chiral plasmonic nanostructures with tailored optical response. *Nature* **2012,** *483* (7389), 311-314.

89. Zhang, Z.; Yang, Y.; Pincet, F.; Llaguno, M. C.; Lin, C., Placing and shaping liposomes with reconfigurable DNA nanocages. *Nature Chemistry* **2017,** *9* (7), 653-659.

90. Knudsen, J. B.; Liu, L.; Bank Kodal, A. L.; Madsen, M.; Li, Q.; Song, J.; Woehrstein, J. B.; Wickham, S. F.; Strauss, M. T.; Schueder, F.; Vinther, J.; Krissanaprasit, A.; Gudnason, D.; Smith, A. A.; Ogaki, R.; Zelikin, A. N.; Besenbacher, F.; Birkedal, V.; Yin, P.; Shih, W. M.; Jungmann, R.; Dong, M.; Gothelf, K. V., Routing of individual polymers in designed patterns. *Nature Nanotechnology* **2015,** *10* (10), 892-898.

91. Jean, J. M.; Hall, K. B., 2-Aminopurine fluorescence quenching and lifetimes: Role of base stacking. *Proceedings of the National Academy of Sciences* **2001,** *98* (1), 37-41.

92. Carmody, M. W.; Vary, C. P., Inhibition of DNA hybridization following partial dUTP substitution. *Biotechniques* **1993,** *15* (4), 692-699.

93. Ordoukhanian, P.; Taylor, J.-S., Design and synthesis of a versatile photocleavable DNA building block. Application to phototriggered hybridization. *Journal of the American Chemical Society* **1995,** *117* (37), 9570-9571.

94. Liu, Q.; Deiters, A., Optochemical control of deoxyoligonucleotide function via a nucleobase-caging approach. *Accounts of Chemical Research* **2014,** *47* (1), 45-55.

95. Tallafuss, A.; Gibson, D.; Morcos, P.; Li, Y.; Seredick, S.; Eisen, J.; Washbourne, P., Turning gene function ON and OFF using sense and antisense photo-morpholinos in zebrafish. *Development* **2012,** *139* (9), 1691-1699.

96. Tang, X.; Maegawa, S.; Weinberg, E. S.; Dmochowski, I. J., Regulating gene expression in zebrafish embryos using light-activated, negatively charged peptide nucleic acids. *Journal of the American Chemical Society* **2007,** *129* (36), 11000-11001.

97. Ouyang, X.; Shestopalov, I. A.; Sinha, S.; Zheng, G.; Pitt, C. L. W.; Li, W.-H.; Olson, A. J.; Chen, J. K., Versatile synthesis and rational design of caged morpholinos. *Journal of the American Chemical Society* **2009,** *131* (37), 13255-13269.

98. Tang, X.; Su, M.; Yu, L.; Lv, C.; Wang, J.; Li, Z., Photomodulating RNA cleavage using photolabile circular antisense oligodeoxynucleotides. *Nucleic Acids Research* **2010,** *38* (11), 3848-3855.

99. Yamazoe, S.; Shestopalov, I. A.; Provost, E.; Leach, S. D.; Chen, J. K., Cyclic caged morpholinos: Conformationally gated probes of embryonic gene function. *Angewandte Chemie International Edition* **2012,** *51* (28), 6908-6911.

100. Kohman, R. E.; Han, X., Light sensitization of DNA nanostructures via incorporation of photo-cleavable spacers. *Chemical Communications* **2015,** *51* (26), 5747-5750.

101. Tohgasaki, T.; Shitomi, Y.; Feng, Y.; Honna, S.; Emura, T.; Hidaka, K.; Sugiyama, H.; Endo, M., A photocaged DNA nanocapsule for controlled unlocking and opening inside the cell. *Bioconjugate Chemistry* **2019,** *30* (7), 1860-1863.

102. Derr, N. D.; Goodman, B. S.; Jungmann, R.; Leschziner, A. E.; Shih, W. M.; Reck-Peterson, S. L., Tug-of-war in motor protein ensembles revealed with a programmable DNA origami scaffold. *Science* **2012,** *338* (6107), 662-665.

103. Kohman, R. E.; Cha, S. S.; Man, H. Y.; Han, X., Light-triggered release of bioactive molecules from DNA nanostructures. *Nano Letters* **2016,** *16* (4), 2781-2785.

104. Asanuma, H.; Liang, X.; Nishioka, H.; Matsunaga, D.; Liu, M.; Komiyama, M., Synthesis of azobenzene-tethered DNA for reversible photo-regulation of DNA functions: hybridization and transcription. *Nature Protocol* **2007,** *2* (1), 203-212.

105. Yang, Y.; Endo, M.; Hidaka, K.; Sugiyama, H., Photo-controllable DNA origami nanostructures assembling into predesigned multiorientational patterns. *Journal of the American Chemical Society* **2012,** *134* (51), 20645-20653.

106. Kuzyk, A.; Yang, Y.; Duan, X.; Stoll, S.; Govorov, A. O.; Sugiyama, H.; Endo, M.; Liu, N., A light-driven three-dimensional plasmonic nanosystem that translates molecular motion into reversible chiroptical function. *Nature Communications* **2016,** *7*, 10591.

107. Yang, Y.; Goetzfried, M. A.; Hidaka, K.; You, M.; Tan, W.; Sugiyama, H.; Endo, M., Direct visualization of walking motions of photocontrolled nanomachine on the DNA nanostructure. *Nano Letters* **2015,** *15* (10), 6672-6676.

108. OligoAnalyzer. www.idtdna.com/calc/analyzer (accessed August, 2019).

109. Subirana, J. A.; Soler-Lopez, M., Cations as hydrogen bond donors: a view of electrostatic interactions in DNA. *Annual Review of Biophysics and Biomolecular Structure* **2003,** *32*, 27-45.

110. Kim, H.; Surwade, S. P.; Powell, A.; O'Donnell, C.; Liu, H., Stability of DNA origami nanostructure under diverse chemical environments. *Chemistry of Materials* **2014,** *26* (18), 5265-5273.

111. Pillers, M. A.; Lieberman, M., Thermal stability of DNA origami on mica. *Journal of Vacuum Science & Technology B* **2014,** *32* (4), 040602.

112. Zhou, F.; Michael, B.; Surwade, S. P.; Ricardo, K. B.; Zhao, S.; Liu, H., Mechanistic study of the nanoscale negative-tone pattern transfer from DNA nanostructures to SiO_2. *Chemistry of Materials* **2015,** *27* (5), 1692-1698.

113. Aoi, K.; Takasu, A.; Okada, M., DNA-based polymer hybrids Part 1. Compatibility and physical properties of poly(vinyl alcohol)/DNA sodium salt blend. *Polymer* **2000,** *41* (8), 2847-2853.

114. Alongi, J.; Di Blasio, A.; Milnes, J.; Malucelli, G.; Bourbigot, S.; Kandola, B.; Camino, G., Thermal degradation of DNA, an all-in-one natural intumescent flame retardant. *Polymer Degradation and Stability* **2015,** *113*, 110-118.

115. Gates, K. S., An overview of chemical processes that damage cellular DNA: spontaneous hydrolysis, alkylation, and reactions with radicals. *Chemical Research in Toxicology* **2009,** *22* (11), 1747-1760.

116. Lindahl, T., Instability and decay of the primary structure of DNA. *Nature* **1993,** *362* (6422), 709-715.

117. An, R.; Jia, Y.; Wan, B.; Zhang, Y.; Dong, P.; Li, J.; Liang, X., Non-enzymatic depurination of nucleic acids: factors and mechanisms. *PLOS ONE* **2015,** *9* (12), e115950.

118. Kielar, C.; Xin, Y.; Shen, B.; Kostiainen, M. A.; Grundmeier, G.; Linko, V.; Keller, A., On the stability of DNA origami nanostructures in low-magnesium buffers. *Angewandte Chemie International Edition* **2018,** *57* (30), 9470-9474.

119. Hahn, J.; Wickham, S. F. J.; Shih, W. M.; Perrault, S. D., Addressing the instability of DNA nanostructures in tissue culture. *ACS Nano* **2014,** *8* (9), 8765-8775.

120. Stellwagen, E.; Muse, J. M.; Stellwagen, N. C., Monovalent cation size and DNA conformational stability. *Biochemistry* **2011,** *50* (15), 3084-3094.

121. Ponnuswamy, N.; Bastings, M. M. C.; Nathwani, B.; Ryu, J. H.; Chou, L. Y. T.; Vinther, M.; Li, W. A.; Anastassacos, F. M.; Mooney, D. J.; Shih, W. M., Oligolysine-based coating protects DNA nanostructures from low-salt denaturation and nuclease degradation. *Nature Communications* **2017,** *8*, 15654.

122. Seo, E.-J.; Lee, M.-Y., Amelioration of hydrofluoric acid-induced DNA damage by phytochemicals. *Toxicology and Environmental Health Sciences* **2014,** *5* (4), 201-206.

123. Wong, A.; Greene, S.; Robinson, J., Hydrofluoric acid poisoning: data from the victorian poisons information centre. *Emergency Medicine Australasia* **2012,** *24* (1), 98-101.

124. Carney, S. A.; Hall, M.; Lawrence, J. C.; Ricketts, C. R., Rationale of the treatment of hydrofluoric acid burns. *British Journal of Industrial Medicine* **1974,** *31* (4), 317-321.

125. Vanderborgh, N. E., Evaluation of the lanthanum fluoride membrane electrode response in acidic solutions: The determination of the pK_a of hydrofluoric acid. *Talanta* **1968,** *15* (10), 1009-1013.

126. Burgher, F.; Mathieu, L.; Lati, E.; Gasser, P.; Peno-Mazzarino, L.; Blomet, J.; Hall, A. H.; Maibach, H. I., Experimental 70% hydrofluoric acid burns: histological observations in an established human skin explants *ex vivo* model. *Cutaneous and Ocular Toxicology* **2011,** *30* (2), 100-107.

127. Anderson, W. J.; Anderson, J. R., Hydrofluoric acid burns of the hand: Mechanism of injury and treatment. *The Journal of Hand Surgery* **1988,** *13* (1), 52-57.

128. Kirkpatrick, J. J. R.; Enion, D. S.; Burd, D. A. R., Hydrofluoric acid burns: a review. *Burns* **1995,** *21* (7), 483-493.

129. Andem, A.; Agbor, R.; Ekpo, I., Review on Comet assay: a reliable tool for assessing DNA damage in animal models. *Journal of Current Research in Science* **2013,** *1* (6), 405-427.

130. Liao, W.; McNutt, M. A.; Zhu, W. G., The comet assay: a sensitive method for detecting DNA damage in individual cells. *Methods* **2009,** *48* (1), 46-53.

131. Kumaravel, T. S.; Vilhar, B.; Faux, S. P.; Jha, A. N., Comet assay measurements: a perspective. *Cell Biology and Toxicology* **2009,** *25* (1), 53-64.

132. Catania, J.; Keenan, B. C.; Margison, G. P.; Fairweather, D. S., Determination of 5-methylcytosine by acid hydrolysis of DNA with hydrofluoric acid. *Analytical Biochemistry* **1987,** *167* (2), 347-351.

133. Hui, L.; Zhang, Q.; Deng, W.; Liu, H., DNA-based nanofabrication: pathway to applications in surface engineering. *Small* **2019**, e1805428.

134. Wang, P.; Meyer, T. A.; Pan, V.; Dutta, P. K.; Ke, Y., The beauty and utility of DNA origami. *Chem* **2017,** *2* (3), 359-382.

135. Praetorius, F.; Kick, B.; Behler, K. L.; Honemann, M. N.; Weuster-Botz, D.; Dietz, H., Biotechnological mass production of DNA origami. *Nature* **2017,** *552* (7683), 84-87.

136. Pei, H.; Zuo, X.; Zhu, D.; Huang, Q.; Fan, C., Functional DNA nanostructures for theranostic applications. *Accounts of Chemical Research* **2014,** *47* (2), 550-559.

137. Chao, J.; Zhu, D.; Zhang, Y.; Wang, L.; Fan, C., DNA nanotechnology-enabled biosensors. *Biosensors and Bioelectronics* **2016,** *76*, 68-79.

138. Ke, Y.; Lindsay, S.; Chang, Y.; Liu, Y.; Yan, H., Self-assembled water-soluble nucleic acid probe tiles for label-free RNA hybridization assays. *Science* **2008,** *319* (5860), 180-183.

139. Han, S.; Liu, W.; Yang, S.; Wang, R., Facile and label-free electrochemical biosensors for microrna detection based on DNA origami nanostructures. *ACS Omega* **2019,** *4* (6), 11025-11031.

140. Zhang, Z.; Wang, Y.; Fan, C.; Li, C.; Li, Y.; Qian, L.; Fu, Y.; Shi, Y.; Hu, J.; He, L., Asymmetric DNA origami for spatially addressable and index-free solution-phase DNA chips. *Adv Mater* **2010,** *22* (24), 2672-2675.

141. Subramanian, H. K.; Chakraborty, B.; Sha, R.; Seeman, N. C., The label-free unambiguous detection and symbolic display of single nucleotide polymorphisms on DNA origami. *Nano Letters* **2011,** *11* (2), 910-913.

142. Zhang, Z.; Zeng, D.; Ma, H.; Feng, G.; Hu, J.; He, L.; Li, C.; Fan, C., A DNA-Origami chip platform for label-free SNP genotyping using toehold-mediated strand displacement. *Small* **2010,** *6* (17), 1854-1858.

143. Kuzuya, A.; Sakai, Y.; Yamazaki, T.; Xu, Y.; Komiyama, M., Nanomechanical DNA origami 'single-molecule beacons' directly imaged by atomic force microscopy. *Nature Communications* **2011,** *2*, 449.

144. Ke, Y.; Meyer, T.; Shih, W. M.; Bellot, G., Regulation at a distance of biomolecular interactions using a DNA origami nanoactuator. *Nature Communications* **2016,** *7*, 10935.

145. Kuzuya, A.; Watanabe, R.; Yamanaka, Y.; Tamaki, T.; Kaino, M.; Ohya, Y., Nanomechanical DNA origami pH sensors. *Sensors* **2014,** *14* (10), 19329-19335.

146. Koirala, D.; Shrestha, P.; Emura, T.; Hidaka, K.; Mandal, S.; Endo, M.; Sugiyama, H.; Mao, H., Single-molecule mechanochemical sensing using DNA origami nanostructures. *Angewandte Chemie International Edition* **2014,** *53* (31), 8137-8141.

147. Godonoga, M.; Lin, T. Y.; Oshima, A.; Sumitomo, K.; Tang, M. S. L.; Cheung, Y. W.; Kinghorn, A. B.; Dirkzwager, R. M.; Zhou, C.; Kuzuya, A.; Tanner, J. A.; Heddle, J. G., A DNA aptamer recognising a malaria protein biomarker can function as part of a DNA origami assembly. *Scientific Reports* **2016,** *6*, 21266.

148. Yan, J.; Hu, C.; Wang, P.; Liu, R.; Zuo, X.; Liu, X.; Song, S.; Fan, C.; He, D.; Sun, G., Novel rolling circle amplification and DNA origami-based DNA belt-involved signal amplification assay for highly sensitive detection of prostate-specific antigen (PSA). *ACS Applied Materials & Interfaces* **2014,** *6* (22), 20372-20377.

149. Fu, Y.; Zeng, D.; Chao, J.; Jin, Y.; Zhang, Z.; Liu, H.; Li, D.; Ma, H.; Huang, Q.; Gothelf, K. V.; Fan, C., Single-step rapid assembly of DNA origami nanostructures for addressable nanoscale bioreactors. *Journal of the American Chemical Society* **2013,** *135* (2), 696-702.

150. Pei, H.; Lu, N.; Wen, Y.; Song, S.; Liu, Y.; Yan, H.; Fan, C., A DNA nanostructure-based biomolecular probe carrier platform for electrochemical biosensing. *Advanced Materials* **2010,** *22* (42), 4754-4758.

151. Wen, Y.; Pei, H.; Shen, Y.; Xi, J.; Lin, M.; Lu, N.; Shen, X.; Li, J.; Fan, C., DNA nanostructure-based Interfacial engineering for PCR-free ultrasensitive electrochemical analysis of microRNA. *Scientific Reports* **2012,** *2*, 867.

152. Pei, H.; Wan, Y.; Li, J.; Hu, H.; Su, Y.; Huang, Q.; Fan, C., Regenerable electrochemical immunological sensing at DNA nanostructure-decorated gold surfaces. *Chemical Communications* **2011,** *47* (22), 6254-6256.

153. Wen, Y.; Pei, H.; Wan, Y.; Su, Y.; Huang, Q.; Song, S.; Fan, C., DNA nanostructure-decorated surfaces for enhanced aptamer-target binding and electrochemical cocaine sensors. *Analytical Chemistry* **2011,** *83* (19), 7418-7423.

154. Pei, H.; Liang, L.; Yao, G.; Li, J.; Huang, Q.; Fan, C., Reconfigurable three-dimensional DNA nanostructures for the construction of intracellular logic sensors. *Angewandte Chemie International Edition* **2012,** *51* (36), 9020-9024.

155. Huang, R.; He, N.; Li, Z., Recent progresses in DNA nanostructure-based biosensors for detection of tumor markers. *Biosensors and Bioelectronics* **2018,** *109*, 27-34.

156. Linko, V.; Ora, A.; Kostiainen, M. A., DNA nanostructures as smart drug-delivery vehicles and molecular devices. *Trends Biotechnology* **2015,** *33* (10), 586-594.

157. Li, J.; Fan, C.; Pei, H.; Shi, J.; Huang, Q., Smart drug delivery nanocarriers with self-assembled DNA nanostructures. *Advanced Materials* **2013,** *25* (32), 4386-4396.

158. Xie, N.; Liu, S.; Yang, X.; He, X.; Huang, J.; Wang, K., DNA tetrahedron nanostructures for biological applications: biosensors and drug delivery. *Analyst* **2017,** *142* (18), 3322-3332.

159. Angell, C.; Xie, S.; Zhang, L.; Chen, Y., DNA Nanotechnology for precise control over drug delivery and gene therapy. *Small* **2016,** *12* (9), 1117-1132.

160. Ko, S.; Liu, H.; Chen, Y.; Mao, C., DNA nanotubes as combinatorial vehicles for cellular delivery. *Biomacromolecules* **2008,** *9* (11), 3039-3043.

161. Walsh, A. S.; Yin, H.; Erben, C. M.; Wood, M. J. A.; Turberfield, A. J., DNA cage delivery to mammalian cells. *ACS Nano* **2011,** *5* (7), 5427-5432.

162. Li, J.; Pei, H.; Zhu, B.; Liang, L.; Wei, M.; He, Y.; Chen, N.; Li, D.; Huang, Q.; Fan, C., Self-assembled multivalent DNA nanostructures for noninvasive intracellular delivery of immunostimulatory CpG oligonucleotides. *ACS Nano* **2011,** *5* (11), 8783-8789.

163. Hamblin, G. D.; Carneiro, K. M. M.; Fakhoury, J. F.; Bujold, K. E.; Sleiman, H. F., Rolling circle amplification-templated DNA nanotubes show increased stability and cell penetration ability. *Journal of the American Chemical Society* **2012,** *134* (6), 2888-2891.

164. Keum, J. W.; Bermudez, H., Enhanced resistance of DNA nanostructures to enzymatic digestion. *Chemical Communications* **2009,** (45), 7036-7038.

165. Mei, Q.; Wei, X.; Su, F.; Liu, Y.; Youngbull, C.; Johnson, R.; Lindsay, S.; Yan, H.; Meldrum, D., Stability of DNA origami nanoarrays in cell lysate. *Nano Letters* **2011,** *11* (4), 1477-1482.

166. Perrault, S. D.; Shih, W. M., Virus-inspired membrane encapsulation of DNA nanostructures to achieve *in vivo* stability. *ACS Nano* **2014,** *8* (5), 5132-5140.

167. Jiang, Q.; Song, C.; Nangreave, J.; Liu, X.; Lin, L.; Qiu, D.; Wang, Z. G.; Zou, G.; Liang, X.; Yan, H.; Ding, B., DNA origami as a carrier for circumvention of drug resistance. *Journal of the American Chemical Society* **2012,** *134* (32), 13396-13403.

168. Zhao, Y.-X.; Shaw, A.; Zeng, X.; Benson, E.; Nyström, A. M.; Högberg, B., DNA origami delivery system for cancer therapy with tunable release properties. *ACS Nano* **2012,** *6* (10), 8684-8691.

169. Kim, K. R.; Kim, D. R.; Lee, T.; Yhee, J. Y.; Kim, B. S.; Kwon, I. C.; Ahn, D. R., Drug delivery by a self-assembled DNA tetrahedron for overcoming drug resistance in breast cancer cells. *Chemical Communications* **2013,** *49* (20), 2010-2012.

170. Lee, H.; Lytton-Jean, A. K.; Chen, Y.; Love, K. T.; Park, A. I.; Karagiannis, E. D.; Sehgal, A.; Querbes, W.; Zurenko, C. S.; Jayaraman, M.; Peng, C. G.; Charisse, K.; Borodovsky, A.; Manoharan, M.; Donahoe, J. S.; Truelove, J.; Nahrendorf, M.; Langer, R.; Anderson, D. G., Molecularly self-assembled nucleic acid nanoparticles for targeted *in vivo* siRNA delivery. *Nature Nanotechnology* **2012,** *7* (6), 389-393.

171. Liu, X.; Xu, Y.; Yu, T.; Clifford, C.; Liu, Y.; Yan, H.; Chang, Y., A DNA nanostructure platform for directed assembly of synthetic vaccines. *Nano Letters* **2012,** *12* (8), 4254-4259.

172. Douglas, S. M.; Bachelet, I.; Church, G. M., A logic-gated nanorobot for targeted transport of molecular payloads. *Science* **2012,** *335* (6070), 831-834.

173. Crawford, R.; Erben, C. M.; Periz, J.; Hall, L. M.; Brown, T.; Turberfield, A. J.; Kapanidis, A. N., Non-covalent single transcription factor encapsulation inside a DNA cage. *Angewandte Chemie International Edition* **2013,** *52* (8), 2284-2288.

174. Chen, N.; Qin, S.; Yang, X.; Wang, Q.; Huang, J.; Wang, K., "Sense-and-Treat" DNA nanodevice for synergetic destruction of circulating tumor cells. *ACS Applied Materials & Interfaces* **2016,** *8* (40), 26552-26558.

175. Xu, A.; Harb, J. N.; Kostiainen, M. A.; Hughes, W. L.; Woolley, A. T.; Liu, H.; Gopinath, A., DNA origami: The bridge from bottom to top. *MRS Bulletin* **2017,** *42* (12), 943-950.

176. Wu, S.; Lin, C. Y.; Chiang, M. C.; Liaw, J. J.; Cheng, J. Y.; Yang, S. H.; Tsai, C. H.; Chen, P. N.; Miyashita, T.; Chang, C. H.; Chang, V. S.; Pan, K. H.; Chen, J. H.; Mor, Y. S.; Lai, K. T.; Liang, C. S.; Chen, H. F.; Chang, S. Y.; Lin, C. J.; Hsieh, C. H.; Tsui, R. F.; Yao, C. H.; Chen, C. C.; Chen, R.; Lee, C. H.; Lin, H. J.; Chang, C. W.; Chen, K. W.; Tsai, M. H.; Chen, K. S.; Ku, Y.; Jang, S. M. In *A 7nm CMOS platform technology featuring 4th generation FinFET transistors with a 0.027um2 high density 6-T SRAM cell for mobile SoC applications*, 2016 IEEE International Electron Devices Meeting (IEDM), 3-7 Dec. 2016; 2016; pp 2.6.1-2.6.4.

177. Chen, Z.; Liu, C.; Cao, F.; Ren, J.; Qu, X., DNA metallization: principles, methods, structures, and applications. *Chemical Society Reviews* **2018,** *47* (11), 4017-4072.

178. Braun, E.; Eichen, Y.; Sivan, U.; Ben-Yoseph, G., DNA-templated assembly and electrode attachment of a conducting silver wire. *Nature* **1998,** *391* (6669), 775-778.

179. Gu, Q.; Cheng, C.; Haynie, D. T., Cobalt metallization of DNA: toward magnetic nanowires. *Nanotechnology* **2005,** *16* (8), 1358-1363.

180. Mertig, M.; Colombi Ciacchi, L.; Seidel, R.; Pompe, W.; De Vita, A., DNA as a selective metallization template. *Nano Letters* **2002,** *2* (8), 841-844.

181. Geng, Y.; Pearson, A. C.; Gates, E. P.; Uprety, B.; Davis, R. C.; Harb, J. N.; Woolley, A. T., Electrically conductive gold- and copper-metallized DNA origami nanostructures. *Langmuir* **2013,** *29* (10), 3482-3490.

182. Jin, Z.; Sun, W.; Ke, Y.; Shih, C. J.; Paulus, G. L.; Hua Wang, Q.; Mu, B.; Yin, P.; Strano, M. S., Metallized DNA nanolithography for encoding and transferring spatial information for graphene patterning. *Nature Communications* **2013,** *4*, 1663.

183. Schreiber, R.; Kempter, S.; Holler, S.; Schuller, V.; Schiffels, D.; Simmel, S. S.; Nickels, P. C.; Liedl, T., DNA origami-templated growth of arbitrarily shaped metal nanoparticles. *Small* **2011,** *7* (13), 1795-1799.

184. Liu, J.; Geng, Y.; Pound, E.; Gyawali, S.; Ashton, J. R.; Hickey, J.; Woolley, A. T.; Harb, J. N., Metallization of branched DNA origami for nanoelectronic circuit fabrication. *ACS Nano* **2011,** *5* (3), 2240-2247.

185. Pearson, A. C.; Liu, J.; Pound, E.; Uprety, B.; Woolley, A. T.; Davis, R. C.; Harb, J. N., DNA origami metallized site specifically to form electrically conductive nanowires. *The Journal of Physical Chemistry B* **2012,** *116* (35), 10551-10560.

186. Surwade, S. P.; Zhou, F.; Wei, B.; Sun, W.; Powell, A.; O'Donnell, C.; Yin, P.; Liu, H., Nanoscale growth and patterning of inorganic oxides using DNA nanostructure templates. *Journal of the American Chemical Society* **2013,** *135* (18), 6778-6781.

187. Liu, X.; Zhang, F.; Jing, X.; Pan, M.; Liu, P.; Li, W.; Zhu, B.; Li, J.; Chen, H.; Wang, L.; Lin, J.; Liu, Y.; Zhao, D.; Yan, H.; Fan, C., Complex silica composite nanomaterials templated with DNA origami. *Nature* **2018,** *559* (7715), 593-598.

188. Surwade, S. P.; Zhao, S.; Liu, H., Molecular lithography through DNA-mediated etching and masking of SiO_2. *Journal of the American Chemical Society* **2011,** *133* (31), 11868-11871.

189. Tian, C.; Kim, H.; Sun, W.; Kim, Y.; Yin, P.; Liu, H., DNA nanostructures-mediated molecular imprinting lithography. *ACS Nano* **2017,** *11* (1), 227-238.

190. Ricardo, K. B.; Xu, A.; Salim, M.; Zhou, F.; Liu, H., Deposition of DNA nanostructures on highly oriented pyrolytic graphite. *Langmuir* **2017,** *33* (16), 3991-3997.

191. Kim, H.; Arbutina, K.; Xu, A.; Liu, H., Increasing the stability of DNA nanostructure templates by atomic layer deposition of Al2O3 and its application in imprinting lithography. *Beilstein Journal of Nanotechnology* **2017,** *8*, 2363-2375.

192. Diagne, C. T.; Brun, C.; Gasparutto, D.; Baillin, X.; Tiron, R., DNA origami mask for sub-ten-nanometer lithography. *ACS Nano* **2016,** *10* (7), 6458-6463.

193. Zhao, S.; Liu, H., Bottom-up nanofabrication through catalyzed vapor phase HF etching of SiO_2. *Nanotechnology* **2015,** *26* (1), 015301.

194. Kershner, R. J.; Bozano, L. D.; Micheel, C. M.; Hung, A. M.; Fornof, A. R.; Cha, J. N.; Rettner, C. T.; Bersani, M.; Frommer, J.; Rothemund, P. W.; Wallraff, G. M., Placement and orientation of individual DNA shapes on lithographically patterned surfaces. *Nature Nanotechnology* **2009,** *4* (9), 557-561.

195. Yun, J. M.; Kim, K. N.; Kim, J. Y.; Shin, D. O.; Lee, W. J.; Lee, S. H.; Lieberman, M.; Kim, S. O., DNA origami nanopatterning on chemically modified graphene. *Angewandte Chemie International Edition* **2012,** *51* (4), 912-915.

196. Gopinath, A.; Rothemund, P. W. K., Optimized assembly and covalent coupling of single-molecule DNA origami nanoarrays. *ACS Nano* **2014,** *8* (12), 12030-12040.

197. Hui, L.; Xu, A.; Liu, H., DNA-Based Nanofabrication for Antifouling Applications. *Langmuir* **2019,** *35* (38), 12543-12549.

198. Han, M.; Lee, W.; Lee, S.-K.; Lee, S. S., 3D microfabrication with inclined/rotated UV lithography. *Sensors and Actuators A: Physical* **2004,** *111* (1), 14-20.

199. Hong, Y.; Zhao, D.; Liu, D.; Ma, B.; Yao, G.; Li, Q.; Han, A.; Qiu, M., Three-dimensional in situ electron-beam lithography using water ice. *Nano Letters* **2018,** *18* (8), 5036-5041.

200. Sun, K.; Wei, T. S.; Ahn, B. Y.; Seo, J. Y.; Dillon, S. J.; Lewis, J. A., 3D printing of interdigitated Li-ion microbattery architectures. *Advanced Materials* **2013,** *25* (33), 4539-4543.

201. Tan, G.; Wu, F.; Yuan, Y.; Chen, R.; Zhao, T.; Yao, Y.; Qian, J.; Liu, J.; Ye, Y.; Shahbazian-Yassar, R.; Lu, J.; Amine, K., Freestanding three-dimensional core-shell nanoarrays for lithium-ion battery anodes. *Nature Communications* **2016,** *7*, 11774.

202. Huang, W.; Yu, X.; Froeter, P.; Xu, R.; Ferreira, P.; Li, X., On-chip inductors with self-rolled-up SiN_x nanomembrane tubes: a novel design platform for extreme miniaturization. *Nano Letters* **2012,** *12* (12), 6283-6288.

203. Tian, B.; Liu, X.; Tu, B.; Yu, C.; Fan, J.; Wang, L.; Xie, S.; Stucky, G. D.; Zhao, D., Self-adjusted synthesis of ordered stable mesoporous minerals by acid-base pairs. *Nature Materials* **2003,** *2* (3), 159-163.

204. Zhang, H.; Yu, X.; Braun, P. V., Three-dimensional bicontinuous ultrafast-charge and -discharge bulk battery electrodes. *Nature Nanotechnology* **2011,** *6* (5), 277-281.

205. Ahn, B. Y.; Duoss, E. B.; Motala, M. J.; Guo, X.; Park, S.-I.; Xiong, Y.; Yoon, J.; Nuzzo, R. G.; Rogers, J. A.; Lewis, J. A., Omnidirectional printing of flexible, stretchable, and spanning silver microelectrodes. *Science* **2009,** *323* (5921), 1590-1593.

206. Goodman, R. P.; Heilemann, M.; Doose, S.; Erben, C. M.; Kapanidis, A. N.; Turberfield, A. J., Reconfigurable, braced, three-dimensional DNA nanostructures. *Nature Nanotechnology* **2008,** *3* (2), 93-96.

207. Liu, H.; Chen, Y.; He, Y.; Ribbe, A. E.; Mao, C., Approaching the limit: can one DNA oligonucleotide assemble into large nanostructures? *Angewandte Chemie International Edition* **2006,** *45* (12), 1942-1945.

208. Campos, R.; Zhang, S.; Majikes, J. M.; Ferraz, L. C.; LaBean, T. H.; Dong, M. D.; Ferapontova, E. E., Electronically addressable nanomechanical switching of i-motif DNA origami assembled on basal plane HOPG. *Chemical Communications* **2015,** *51* (74), 14111-14114.

209. Dong, J.; Liu, J.; Kang, G.; Xie, J.; Wang, Y., Pushing the resolution of photolithography down to 15 nm by surface plasmon interference. *Scientific Reports* **2014,** *4*, 5618.

210. Wagner, C.; Harned, N., Lithography gets extreme. *Nature Photonics* **2010,** *4* (1), 24-26.

211. Cord, B.; Yang, J.; Duan, H.; Joy, D. C.; Klingfus, J.; Berggren, K. K., Limiting factors in sub-10 nm scanning-electron-beam lithography. *Journal of Vacuum Science & Technology B: Microelectronics and Nanometer Structures* **2009,** *27* (6), 2616-2621.

212. Grigorescu, A. E.; Hagen, C. W., Resists for sub-20-nm electron beam lithography with a focus on HSQ: state of the art. *Nanotechnology* **2009,** *20* (29), 292001.

213. Mojarad, N.; Gobrecht, J.; Ekinci, Y., Beyond EUV lithography: a comparative study of efficient photoresists' performance. *Scientific Reports* **2015,** *5*, 9235.

214. Whidden, T. K.; Allgair, J.; Ryan, J. M.; Kozicki, M. N.; Ferry, D. K., Catalyzed HF vapor etching of silicon dioxide for micro - and nanolithographic masks. *Journal of the Electrochemical Society* **1995,** *142* (4), 1199-1205.

215. Allgair, J.; Ryan, J. M.; Song, H. J.; Kozicki, M. N.; Whidden, T. K.; Ferry, D. K., Nanoscale patterning of silicon dioxide thin films by catalyzed HF vapor etching. *Nanotechnology* **1996,** *7* (4), 351-355.

216. Anguita, J.; Briones, F., HF/H_2O vapor etching of SiO_2 sacrificial layer for large-area surface-micromachined membranes. *Sensors and Actuators A: Physical* **1998,** *64* (3), 247-251.

217. Kang, J. K.; Musgrave, C. B., The mechanism of HF/H_2O chemical etching of SiO_2. *Journal of Chemical Physics* **2002,** *116* (1), 275-280.

218. Neish, C. S.; Martin, I. L.; Henderson, R. M.; Edwardson, J. M., Direct visualization of ligand-protein interactions using atomic force microscopy. *British Journal of Pharmacology* **2002,** *135* (8), 1943-1950.

219. Vapor pressure of water. http://en.wikipedia.org/wiki/Vapour_pressure_of_water (accessed August, 2019).

220. Brosheer, J.; Lenfesty, F.; Elmore, K., Vapor pressure of hydrofluoric acid solutions. *Industrial & Engineering Chemistry* **1947,** *39* (3), 423-427.

221. Allen, M. J.; Hud, N. V.; Balooch, M.; Tench, R. J.; Siekhaus, W. J.; Balhorn, R., Tip-radius-induced artifacts in AFM images of protamine-complexed DNA fibers. *Ultramicroscopy* **1992,** *42-44*, 1095-1100.

222. Monis, P. T.; Giglio, S.; Saint, C. P., Comparison of SYTO9 and SYBR Green I for real-time polymerase chain reaction and investigation of the effect of dye concentration on amplification and DNA melting curve analysis. *Analytical Biochemistry* **2005,** *340* (1), 24-34.

223. Tarnok, A., SYTO dyes and histoproteins--myriad of applications. *Cytometry Part A* **2008,** *73* (6), 477-479.

224. SYBR® Green I nucleic acid gel stain. www.sigmaaldrich.com/catalog/product/sial/s9430 (accessed August, 2019).

225. Nucleic acid double helix. http://en.wikipedia.org/wiki/Nucleic_acid_double_helix (accessed August, 2019).

226. Peng, Z.; Liu, H., Bottom-up nanofabrication using DNA nanostructures. *Chemistry of Materials* **2016,** *28* (4), 1012-1021.

227. Aldaye, F. A.; Palmer, A. L.; Sleiman, H. F., Assembling materials with DNA as the guide. *Science* **2008,** *321* (5897), 1795-1799.

228. Zhang, X.; Hu, H., DNA molecules site-specific immobilization and their applications. *Central European Journal of Chemistry* **2014,** *12* (10), 977-993.

229. Gu, H.; Chao, J.; Xiao, S. J.; Seeman, N. C., Dynamic patterning programmed by DNA tiles captured on a DNA origami substrate. *Nature Nanotechnology* **2009,** *4* (4), 245-248.

230. Geim, A. K.; Novoselov, K. S., The rise of graphene. In *Nanoscience and Technology*, Co-Published with Macmillan Publishers Ltd, UK: 2009; pp 11-19.

231. Chung, D. D. L., Review graphite. *Journal of Materials Science* **2002,** *37* (8), 1475-1489.

232. Patel, A. N.; Collignon, M. G.; O'Connell, M. A.; Hung, W. O. Y.; McKelvey, K.; Macpherson, J. V.; Unwin, P. R., A new view of electrochemistry at highly oriented pyrolytic graphite. *Journal of the American Chemical Society* **2012,** *134* (49), 20117-20130.

233. Ashraf, A.; Wu, Y.; Wang, M. C.; Aluru, N. R.; Dastgheib, S. A.; Nam, S., Spectroscopic investigation of the wettability of multilayer graphene using highly ordered pyrolytic graphite as a model material. *Langmuir* **2014,** *30* (43), 12827-12836.

234. Kwon, S.; Vidic, R.; Borguet, E., Enhancement of adsorption on graphite (HOPG) by modification of surface chemical functionality and morphology. *Carbon* **2002,** *40* (13), 2351-2358.

235. Martínez-Martínez, D.; Kolodziejczyk, L.; Sánchez-López, J. C.; Fernández, A., Tribological carbon-based coatings: An AFM and LFM study. *Surface Science* **2009,** *603* (7), 973-979.

236. Diculescu, C. V.; Paquim, C. A.-M.; Brett, O. A. M., Electrochemical DNA sensors for detection of DNA damage. *Sensors* **2005,** *5* (6), 377-393.

237. Chiorcea, A.-M.; Oliveira Brett, A. M., Atomic force microscopy characterization of an electrochemical DNA-biosensor. *Bioelectrochemistry* **2004,** *63* (1), 229-232.

238. Clemmer, C. R.; Beebe, T. P., Graphite: a mimic for DNA and other biomolecules in scanning tunneling microscope studies. *Science* **1991,** *251* (4994), 640-642.

239. Chiorcea, A. M.; Oliveira-Brett, A. M., Scanning probe microscopic imaging of guanine on a highly oriented pyrolytic graphite electrode. *Bioelectrochemistry* **2002,** *55* (1), 63-65.

240. Tao, N. J.; Shi, Z., Monolayer guanine and adenine on graphite in NaCl solution: a comparative STM and AFM study. *The Journal of Physical Chemistry* **1994,** *98* (5), 1464-1471.

241. Husale, B. S.; Sahoo, S.; Radenovic, A.; Traversi, F.; Annibale, P.; Kis, A., ssDNA binding reveals the atomic structure of graphene. *Langmuir* **2010,** *26* (23), 18078-18082.

242. Oliveira Brett, A. M.; Chiorcea, A.-M., Effect of pH and applied potential on the adsorption of DNA on highly oriented pyrolytic graphite electrodes. Atomic force microscopy surface characterisation. *Electrochemistry Communications* **2003,** *5* (2), 178-183.

243. Oliveira Brett, A. M.; Chiorcea, A.-M., Atomic force microscopy of DNA immobilized onto a highly oriented pyrolytic graphite electrode surface. *Langmuir* **2003,** *19* (9), 3830-3839.

244. Mudedla, S. K.; Balamurugan, K.; Kamaraj, M.; Subramanian, V., Interaction of nucleobases with silicon doped and defective silicon doped graphene and optical properties. *Physical Chemistry Chemical Physics* **2016,** *18* (1), 295-309.

245. Green, N. S.; Norton, M. L., Interactions of DNA with graphene and sensing applications of graphene field-effect transistor devices: a review. *Analytica Chimica Acta* **2015,** *853*, 127-142.

246. Zhang, X.; Rahman, M.; Neff, D.; Norton, M. L., DNA origami deposition on native and passivated molybdenum disulfide substrates. *Beilstein Journal of Nanotechnology* **2014,** *5*, 501-506.

247. Kozbial, A.; Li, Z.; Sun, J.; Gong, X.; Zhou, F.; Wang, Y.; Xu, H.; Liu, H.; Li, L., Understanding the intrinsic water wettability of graphite. *Carbon* **2014,** *74*, 218-225.

248. Li, Z.; Wang, Y.; Kozbial, A.; Shenoy, G.; Zhou, F.; McGinley, R.; Ireland, P.; Morganstein, B.; Kunkel, A.; Surwade, S. P.; Li, L.; Liu, H., Effect of airborne contaminants on the wettability of supported graphene and graphite. *Nature Materials* **2013,** *12* (10), 925-931.

249. Novoselov, K. S.; Geim, A. K.; Morozov, S. V.; Jiang, D.; Zhang, Y.; Dubonos, S. V.; Grigorieva, I. V.; Firsov, A. A., Electric field effect in atomically thin carbon films. *Science* **2004,** *306* (5696), 666-669.

250. Alloyeau, D.; Ding, B.; Ramasse, Q.; Kisielowski, C.; Lee, Z.; Jeon, K. J., Direct imaging and chemical analysis of unstained DNA origami performed with a transmission electron microscope. *Chemical Communications* **2011,** *47* (33), 9375-9377.

251. Zheng, M.; Jagota, A.; Semke, E. D.; Diner, B. A.; McLean, R. S.; Lustig, S. R.; Richardson, R. E.; Tassi, N. G., DNA-assisted dispersion and separation of carbon nanotubes. *Nature Materials* **2003,** *2* (5), 338-342.

252. Yoo, J.; Aksimentiev, A., In situ structure and dynamics of DNA origami determined through molecular dynamics simulations. *Proceedings of the National Academy of Sciences* **2013,** *110* (50), 20099-20104.

253. Liu, Z.; Zhao, L.; Zu, Y.; Tan, S.; Wang, Y.; Zhang, Y., Unusual DNA structures formed on bare highly oriented pyrolytic graphite surfaces studied by atomic force microscopy. *Microscopy and Microanalysis* **2013,** *19* (3), 544-552.

254. Adamcik, J.; Klinov, D. V.; Witz, G.; Sekatskii, S. K.; Dietler, G., Observation of single-stranded DNA on mica and highly oriented pyrolytic graphite by atomic force microscopy. *FEBS Letters* **2006,** *580* (24), 5671-5675.

255. Akca, S.; Foroughi, A.; Frochtzwajg, D.; Postma, H. W., Competing interactions in DNA assembly on graphene. *PLOS One* **2011,** *6* (4), e18442.

256. Liu, Z.; Zhao, L.; Zhou, Z.; Sun, T.; Zu, Y., Assembly of single-stranded DNA onto HOPG surface at different temperature: atomic force microscopy study. *Scanning* **2012,** *34* (5), 302-308.

257. El Kirat, K.; Burton, I.; Dupres, V.; Dufrene, Y. F., Sample preparation procedures for biological atomic force microscopy. *Journal of Microscopy* **2005,** *218* (3), 199-207.

258. Clemmer, C. R.; Beebe, T. P., A review of graphite and gold surface studies for use as substrates in biological scanning tunneling microscopy studies. *Scanning microscopy* **1992,** *6* (2), 319-333.

259. Marichy, C.; Pinna, N., Carbon-nanostructures coated/decorated by atomic layer deposition: Growth and applications. *Coordination Chemistry Reviews* **2013,** *257* (23-24), 3232-3253.

260. Goodman, R. P.; Schaap, I. A. T.; Tardin, C. F.; Erben, C. M.; Berry, R. M.; Schmidt, C. F.; Turberfield, A. J., Rapid chiral assembly of rigid DNA building blocks for molecular nanofabrication. *Science* **2005,** *310* (5754), 1661-1665.

261. Liu, X.; Wu, L.; Wang, L.; Jiang, W., A dual-targeting DNA tetrahedron nanocarrier for breast cancer cell imaging and drug delivery. *Talanta* **2018,** *179*, 356-363.

262. Zhang, Y.; Deng, Y.; Wang, C.; Li, L.; Xu, L.; Yu, Y.; Su, X., Probing and regulating the activity of cellular enzymes by using DNA tetrahedron nanostructures. *Chemical Science* **2019,** *10* (23), 5959-5966.

263. Erben, C. M.; Goodman, R. P.; Turberfield, A. J., Single-molecule protein encapsulation in a rigid DNA cage. *Angewandte Chemie* **2006,** *118* (44), 7574-7577.

264. Chandrasekaran, A. R.; Levchenko, O., DNA Nanocages. *Chemistry of Materials* **2016,** *28* (16), 5569-5581.

265. Hu, Q.; Li, H.; Wang, L.; Gu, H.; Fan, C., DNA nanotechnology-enabled drug delivery systems. *Chemical Reviews* **2019,** *119* (10), 6459-6506.

266. Hofstein, S. R.; Heiman, F. P., The silicon insulated-gate field-effect transistor. *Proceedings of the IEEE* **1963,** *51* (9), 1190-1202.

267. Palecek, E.; Fojta, M., Magnetic beads as versatile tools for electrochemical DNA and protein biosensing. *Talanta* **2007,** *74* (3), 276-290.

268. Rudi, K.; Kroken, M.; Dahlberg, O. J.; Deggerdal, A.; Jakobsen, K. S.; Larsen, F., Rapid, universal method to isolate PCR-ready DNA using magnetic beads. *Biotechniques* **1997,** *22* (3), 506-511.

269. Brulle, T.; Ju, W.; Niedermayr, P.; Denisenko, A.; Paschos, O.; Schneider, O.; Stimming, U., Size-dependent electrocatalytic activity of gold nanoparticles on HOPG and highly boron-doped diamond surfaces. *Molecules* **2011,** *16* (12), 10059-10077.

270. Lee, B.; Park, S.-Y.; Kim, H.-C.; Cho, K.; Vogel, E. M.; Kim, M. J.; Wallace, R. M.; Kim, J., Conformal Al_2O_3 dielectric layer deposited by atomic layer deposition for graphene-based nanoelectronics. *Applied Physics Letters* **2008,** *92* (20), 203102.

271. Lu, X.; Huang, H.; Nemchuk, N.; Ruoff, R. S., Patterning of highly oriented pyrolytic graphite by oxygen plasma etching. *Applied Physics Letters* **1999,** *75* (2), 193-195.